Geomorphic controls on mineral weathering, elemental transport, carbon cycling, and production of mineral surface area in a schist bedrock weathering profile, Piedmont Pennsylvania

A Dissertation

SUBMITTED TO THE FACULTY OF

UNIVERSITY OF MINNESOTA

BY

Beth A. Fisher

IN PARTIAL FULFILLMENT OF THE REQUIREMENTS

FOR THE DEGREE OF

DOCTOR OF PHILOSOPHY

Kyungsoo Yoo

October 2016

Acknowledgements

Thank you to my advisor, Kyungsoo Yoo, for countless hours of mentorship, patience and willingness to repeat concepts as many times as I needed, and for giving me access to an exceptional set of resources and mentors.

Thank you to the team of mentors who allowed me to tap into their extensive and varied expertise: Brandy Toner, Deborah Allan, Tracy Twine, Peter Snyder, Diana Karwan, Anthony Aufdenkampe, Carl Rosen, Bill Seyfried, Carrie Jennings, Josh Feinberg, Brian Mahoney, Harry Jol, Scott Alexander, Kelton Barr, and Nathan Gruman. I would like to extend a special thank you for the bountiful mentorship and support from Ed Nater.

Thank you to Aaron Rendahl for gracefully transitioning from *friend* to *friend and colleague* and for your immeasurable assistance with statistics and coding of the Weathering Trends model and venturing into GitHub with me.

I would like to thank Dr. Phoebe Fisher, Brandywine Conservancy, and the team at Stroud Water Research Center, especially D. Montgomery, S. Hicks, S. Dix and J. Matkov for assistance with field and laboratory components of this project. Thank you to Fang Tan, Paul Imhoff, Holly Michael, and Yi Mi for drilling assistance.

For great discussions about biogeochemistry and many other things: Nic Jelinski, Brandi Cron-Kammermans, Sarah Nicholas, Keith Pelletier, Marta Roser, Julia Marquard, Adrian Wackett, Charlotte Riggs, and Amy Lyttle. For assistance in the laboratory: Lindsey Lepak, Justene Davis, Alex Dirr, Jennifer Wang, and Kalei Holt. For knowing how to do All The Things: Kari Jarcho and Marjorie Bonse.

Thank you to Michael Manno and Linda Sauer and the University of Minnesota Characterization Facility for training and assistance with XRD.

Thank you to the National Science Foundation for funding this work through the Christina River Basin Critical Zone Observatory (0724971 and 1331856).

Finally, thank you to my family and friends for believing in me.

Dedication

For Anders and Nils, with immense gratitude for your patience, endurance, forgiveness, support, humor, and encouragement beyond your years. Thank you for letting me be all that I can be; I hope to do the same for you.

For My Love, who helped me grab back onto The Rope more times than I care to count.

Table of Contents

List of Tables

List of Figures

1 Critical Link Between Weathering and Carbon Cycle: Mineral Surface Area

1.1 The Problem of Sequestering Carbon

Atmospheric carbon dioxide (CO_2) emissions are drastically above pre-civilization levels owing to land use changes and the combustion of fossil fuels (Hartmann et al., 2013). The reservoir of organic matter stored in soil is the largest active reservoir of carbon (Hartmann et al., 2013). Soil carbon can be rapidly transformed into atmospheric CO_2 unless it is protected from microbial oxidation by association within minerals or on mineral surfaces (Kleber et al., 2007; Wagai and Mayer, 2007). Over recent decades in organic matter research, the paradigm for understanding why organic matter persists in soils has shifted. The former paradigm held that the recalcitrance of organic matter in soils was due to intrinsic properties such as complex molecular structure preventing degradation of some types of organic matter. We now understand that various protective mechanisms, the most important being interaction with mineral surfaces, are responsible for the longevity of organic carbon in soils and sediments (Kleber et al., 2010; Schmidt et al., 2011).

1.2 Mineral Surface Area and Carbon

The ratio of organic matter concentration to mineral specific surface area (SSA) is consistently in the range of 0.5-1 mgC m^{-2} of mineral surface (Mayer, 1994a, 1994b; Wagai and Mayer, 2007), suggesting that SSA has a significant role in determining the potential of soils and sediments to stabilize organic matter (Keil and Mayer, 2014).

Organic matter attaches to mineral surfaces in patches rather than in smooth, homogeneous layers (Mikutta et al., 2009; Solomon et al., 2012; Thieme et al., 2010) by a number of mechanisms (Keil and Mayer, 2014), and the zone furthest from the mineral surface may turn over more rapidly than the inner zones (Kleber et al., 2007; Sollins et al., 2006). Instead of being released to the atmosphere as CO_2 upon erosion (Berhe et al., 2007; Van Oost et al., 2007), organomineral interaction and stabilization increases in response to soil mixing (Aufdenkampe et al., 2011; Lyttle et al., 2014) (*Figure 1.1*). By understanding the mechanisms for the persistence of organic matter from the mineral surface to whole soil scales, we are better able to leverage the protective mechanisms to store and sequester carbon in soils, preventing loss as atmospheric CO_2.

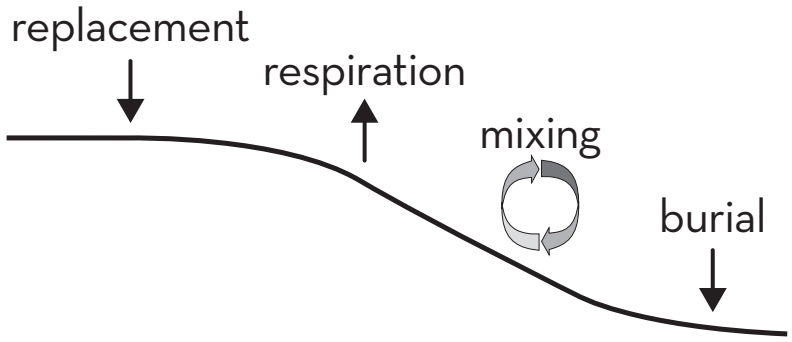

Figure 1.1. Processes acting on organic matter along an eroding hillslope include replacement of organic matter at the ridge. Erosion not only results in some respiration of organic matter as CO_2, but also the physical mixing of organic matter and mineral surfaces freshly exhumed by erosion promote new organomineral associations, which physically protect organic matter from respiration as CO_2. Finally, burial of organic matter, both as uncomplexed and mineral-associated complexes, often occurs at the toeslope, retaining most of the eroded organic matter within the same landscape.

Despite the potential utility of mineral SSA in understanding organic matter cycling and stabilization along with many other biogeochemical and hydrological

processes in soils, systematic understanding of the development of mineral SSA in weathering profiles is rare. For example, mineral dissolution rates have been normalized to mineral surface area in laboratory experiments and soil chronosequence studies (e.g. White and Brantley, 2003), but these studies focus on subsets of mineralogical groups rather than representing the total matrices of soils or chemically weathered bedrock. Additionally, SSA values reported for advancing our knowledge of mineral dissolution are often modeled parameters rather than laboratory measured values. Reactive transport models utilize SSA, estimated for each mineral, to calculate geochemical reaction rates based on the solubility and kinetics of the minerals (Moore et al., 2012; White and Brantley, 2003; White et al., 1996). However, these models suffer from the unknown nature of depth and topographic distribution of mineral SSA.

1.3 Investigating the Co-Evolution of Mineral Surface Area and Carbon

Working within the Christina River Basin Critical Zone Observatory, the following work seeks to address the CRB-CZO overarching goal of understanding how chemical and physical weathering interact with the organic carbon cycle. The production of SSA is a complex co-evolution of mineralogy, landscape processes, hydrology, and biogeochemistry. As SSA develops through weathering and pedogenesis, particularly as secondary minerals, the development of new SSA is often physically separate from inputs of organic matter near the ground surface and within the rhizosphere. Numerous pedon-scale mixing processes overcome physical separation and promote the association of organic matter and minerals, but this is a rate-limiting step in most natural soil

environments.

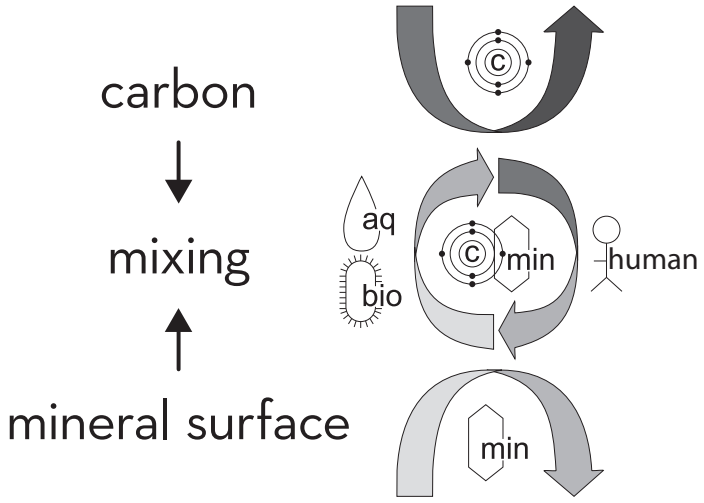

Figure 1.2. Production of organic matter is physically separate from the production of most mineral surface area. To promote organomineral associations, physical mixing, driven by a wide range of biological, hydrologic, and anthropogenic processes, overcomes separation.

In this work we seek to understand the relationship between organic matter and mineral weathering and surface area using an interdisciplinary, first-order watershed-scale investigation. We first investigate the development of mineral surface area in two deep weathering profiles at different landscape positions within the same bedrock and watershed (Chapter 2). In the investigation of deep weathering profiles, we identified the difficulties of assessing weathering on geochemically variable bedrock, and developed a statistical computational package for differentiating weathering from geochemical variability (Chapter 3), which is a critical process for delineating the subsurface topographies of the Critical Zone in nearly any bedrock context. Finally, we assess the movement of soils in the same first-order watershed to demonstrate how erosional mixing

promotes new organomineral associations that are deposited in the lower portions of the landscape (Chapter 4).

The following chapters detail the process and outcomes of demonstrating the importance of SSA, how to capture its development through weathering, and how SSA and organic matter distribute with landscapes.

2 Vertical and lateral distribution of mineral surface area reveals the importance of iron oxidation and oxygen gas penetration in chemical weathering

Submitted on June 9, 2016 to Journal of Geophysical Research-Earth Surface as: Paper #2016JF003988, Vertical and lateral distribution of mineral surface area reveals the importance of iron oxidation and oxygen gas penetration in chemical weathering.

Authors: B. A. Fisher, K. Yoo, A. K. Aufdenkampe, E. A. Nater, and J. E. Nyquist

Accepted with major revisions on August 22, 2016, due on October 6, 2016.

With K. Yoo, UMN—Advisor, A. K. Aufdenkampe, Stroud Water Research Center—Project Lead PI, field site, SSA assistance; E. A. Nater, UMN—XRD guidance; J. E. Nyquist, Temple University—geophysical field study.

2.1 Synopsis

Mineral specific surface area (SSA) is generated by chemical weathering as primary minerals weather and restructure into secondary phyllosilicate and oxide minerals. Mineral SSA is a measurable property that captures nearly all physical and chemical weathering processes in a single measurement. This first measurement of deep mineral SSA profiles at two landscape positions reveals clear vertical and lateral trends despite mineralogical variability caused by highly variable schist bedrock. We observe steep transitions in SSA at the depth of 3 meters that do not coincide with the soil-

weathered rock boundary or the water table, where we expected to observe the biggest changes in SSA production. Rather, we observe that the 3 meter boundaries coincide with the depth extent of secondary iron minerals and the detection of secondary silicate weathering products. We arrive at a first ever estimate for SSA production rates of 0.10-0.33 $m^2kg^{-1}yr^{-1}$ within the top 3 meters of the weathering profile. The SSA production rate at the ridge exceeds the production rate at the interfluve, yet the colluvium at the interfluve yields a higher depth-integrated inventory of SSA.

2.2 Introduction and hypotheses

Many critical biogeochemical and environmental reactions in terrestrial and aquatic ecosystems occur on the surfaces of minerals. In soil systems, traditional scientific focus on clays has been justified on the basis of chemical reactivity and large specific surface area (SSA) of clay minerals. Specific surface area of minerals is a significant parameter for understanding the capacity of soil and sediment to store moisture and regulate chemical reactions. Many biogeochemical reactions occur on mineral surfaces in soils. Mineral dissolution is a key factor determining chemical weathering rates, and chemical weathering releases nutrients and generates mineral surface area and these processes are foundational for regional to global geochemical and biogeochemical cycles. Carbon-mineral sorption is a key factor determining organic matter mineralization rates to carbon dioxide. Advancing our understanding of processes determining the production and distribution of mineral surfaces thus has implications for a broad range of questions related to all disciplines seeking to understand Critical Zone

evolution, structure, and function.

Because mineral SSA is highly sensitive to small changes in the presence and abundance of secondary phyllosilicate minerals and iron oxides, it may also serve as a useful indicator of the initiation of chemical weathering, particularly in places where bedrock or parent material have highly variable mineralogy. This is pertinent because one of the current frontiers of research is identifying the boundaries where process changes occur in the zone between soil and fresh bedrock (Parsekian et al., 2015; Rempe and Dietrich, 2014; Richter and Billings, 2015). Our literature-derived hypotheses suggest that morphologic boundaries should exhibit observable changes in chemical weathering. Most secondary phyllosilicate minerals boast an order of magnitude or more SSA than primary silicates, thus mineral SSA could be a highly sensitive intrinsic measure of chemically weathered material.

Despite the potential utility of mineral SSA in understanding many key biogeochemical and hydrological processes in soils, systematic measurement of mineral SSA in the context of the formation of weathering profiles is rare. For example, mineral dissolution rates have been normalized to mineral surface area in laboratory experiments and soil chronosequence studies (e.g. White and Brantley, 2003), but these studies focus on subsets of mineralogical groups rather than representing the total matrices of soils or chemically weathered bedrock. Additionally, SSA values reported for advancing our knowledge of mineral dissolution are often modeled parameters rather than laboratory measured values. Reactive transport models utilize SSA, estimated for each mineral, to

calculate geochemical reaction rates based on the solubility and kinetics of the minerals (Moore et al., 2012; White and Brantley, 2003; White et al., 1996). However, these models suffer from the unknown nature of depth and topographic distribution of mineral SSA. In research communities interested in the mechanisms of soil organic carbon stabilization, there has been a growing appreciation that interactions between organic matter and minerals may be a critical protective mechanism for organic matter in soils (Aufdenkampe et al., 2011; Berhe et al., 2007; Kleber et al., 2007; Schmidt et al., 2011; Yoo et al., 2011). The marine sediment community has used SSA as a proxy to understand the potential for mineral surfaces to stabilize associated organic matter (Hedges et al., 1999; Keil and Mayer, 2014; Mayer, 1994a).

Here our overarching goal is to measure and understand the development of mineral SSA during evolution of the critical zone. The critical zone itself is the part of the earth that extends from the top of the vegetation canopy to the deepest limits of actively cycling groundwater (Brantley et al., 2007a). It is the outer skin of the earth that is critical to sustaining life. There are many functional layers of the critical zone, ranging from soil to fresh bedrock, and some of the layers have been defined with multiple terms. We define bedrock as rock that has not been subject to alteration by physical or chemical weathering. We define weathered rock as the non-mobile layer above bedrock that has been weathered but has not been mobilized, as evidenced by the retention of rock structure. Weathered rock includes the commonly referenced saprolite and saprock (Graham et al., 2010; Lebedeva et al., 2010) and is described as C-horizon by

pedologists. We define soil to include the mobile layer above weathered rock, in which physical and chemical weathering processes are most active, and which develop genetic horizons, such as A- and B-horizons. We also consider soil to be synonymous with what geomorphologists recognize as the mobile regolith, which serves as a functional definition to describe material that has been physically mixed or displaced and no longer retains rock structure (Anderson et al., 2013). Thus, we define all material above the C-horizon as soil for the purposes of this discussion. The boundaries between soil, weathered rock, and fresh bedrock are shaped by complex interactions of geomorphic, geochemical, biological, and hydrological processes. These boundaries have been most actively studied, often across multiple disciplines, at the hillslope scale (e.g., Rempe and Dietrich, 2014; Hasenmueller et al., 2015), where the hillslope is selected because it is the fundamental unit of landscapes (Carson and Kirkby, 1972). Efforts to measure these boundaries as a function of hillslope topography using geophysical and geochemical methods abound, but we know of no previous efforts to measure the vertical and lateral distribution of SSA in a landscape.

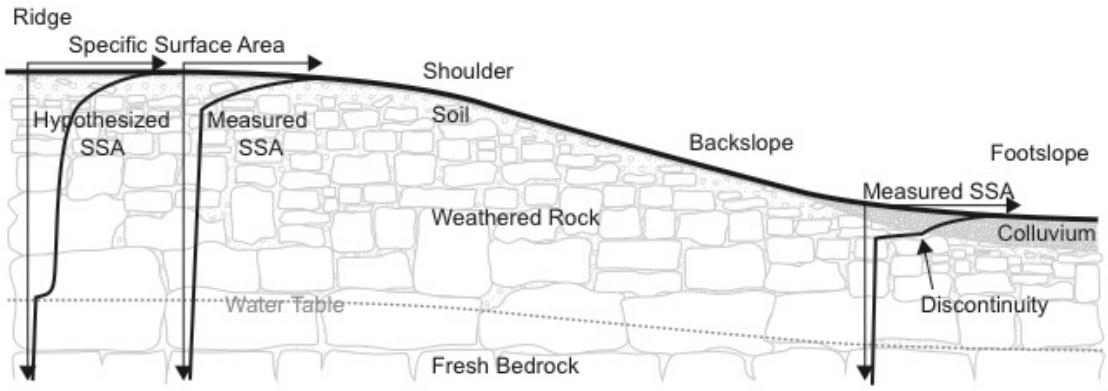

Figure 2.1. Conceptual model of a hillslope cross-section of the depth and topographic distribution of mineral specific surface area, revealing literature-derived hypothesized SSA and measured SSA. The three-layer model of the deep critical zone is composed of soil, weathered rock, and fresh bedrock. Relevant processes in each layer include the following: pedogenesis and colluvial transport in soil; vadose gases and pore water acidity drive dissolution and chemical weathering in weathered rock; fresh bedrock is saturated with groundwater where porosity may be minimal and vadose gases no longer dominate pore space. We also recognize that some of the boundaries have distinct processes, including the capillary fringe, where redox and dissolution processes occur immediately above the water table.

Current knowledge of how geochemical and geomorphic processes operate at hillslope scales have informed us to develop a conceptual model for the depth and topographic distribution of mineral SSA over a cross section of a hillslope transect (Figure 2.1), where we describe a suite of competing hypotheses for mineral surface area production. Our conceptual hillslope transect is continuously covered by soil and is underlain by chemically weathered but physically non-mobile rock that grades into fresh bedrock beneath. We presume the ground water table mimics the surface topography and coincides with the weathered rock to fresh bedrock boundary, and dominant weathering processes can be grouped into a three layer model of the deep critical zone (Figure 2.1), with each layer bounded by morphologic boundaries or features such as the water table. We then consider mineral surface area production at two contrasting hillslope positions: eroding (ridge) and depositional (footslope).

At the soil-weathered rock boundary, consolidated rock is physically and chemically broken down to unconsolidated soil that may be subject to gravity-driven colluvial transport (Carson and Kirkby, 1972; Dietrich et al., 1995; Heimsath et al.,

2005). The conversion from weathered rock to soil has been termed soil production (Heimsath et al., 1997). The chemical weathering rate within the soil is directly proportional to soil production rates, and thus the supply rate of fresh mineral surface area (Gilbert, 1909; Raymo and Ruddiman, 1992; Riebe et al., 2004; West et al., 2005). Given the active physical and chemical weathering processes within physically mixed soils, we attempt to establish how mineral SSA varies across this important boundary and test a hypothesis that mineral SSA and its production rates increase sharply across the weathered rock to soil boundary. Where colluvial processes deposit transported topsoil (footslope in Figure 2.1), we expect to observe a vertical discontinuity where deposited material is superimposed on in-situ soil.

The ability to quantify soil production rate—at the boundary between physically mixed soil and non-mobile weathered rock—was an important breakthrough in our understanding of hillslope evolution (Heimsath et al., 1997). It led to the inevitable question about identifying the lower boundary of weathering profiles where downward propagation of chemical weathering fronts occur (Susan L. Brantley et al., 2013) due to the equilibrium status of pore waters (Maher, 2010) or due to acidity of pore waters (S. L. Brantley et al., 2013; Hasenmueller et al., 2015). New synthesis models propose the depth of the groundwater table as a lower boundary of weathering profiles (Rempe and Dietrich, 2014). Temporal fluctuation of the groundwater table, in combination with the redox cycle controlling release of iron from primary minerals and subsequent precipitation of secondary oxides (Haberer et al., 2015), may contribute to the initiation

of the production of mineral surface area in the capillary fringe. Therefore we hypothesize that there is a significant change in the mineral surface area and its production rate at the groundwater table. Mechanisms for the termination of weathering at the groundwater table include that slow moving groundwater reaches equilibrium with bedrock (Rempe and Dietrich, 2014), and that the penetration of acidity into the formation is eventually exhausted with depths that may coincide with the groundwater table (S. L. Brantley et al., 2013).

This literature review and set of hypotheses highlight the imperative need for measuring mineral SSA through entire weathering profiles beyond the depth of water table at both eroding and depositional localities within a hillslope. Here we characterized the mineralogy, geochemistry, and specific surface area within a 100% forested watershed underlain by schist, by drilling and analyzing two 21 meter cores, one at ridge-top and the other in a convex depositional zone at intermediate elevation within the landscape, or interfluve. To our knowledge, this work provides a first ever quantification of mineral SSA within whole weathering profiles and their topographic distribution on a landscape scale.

We found that SSA is a measurable physical property that sums nearly all mineralogical weathering processes and thus may be an effective weathering indicator, especially where bedrock is geochemically and mineralogically too variable to detect weathering trends, such as in sedimentary and metasedimentary rocks. Our observations revealed that none of the morphologic boundaries generated the expected changes in

production of SSA. The groundwater table was not the terminal point of SSA production. The boundary between mobile soil and non-mobile weathered rock did not coincide with the drastic change observed in SSA. And the major weathering boundary that we observed through the lens of mineral SSA did not vary with landscape position. All of our unconfirmed literature-derived hypotheses lead us to carefully consider our available points of observation to present a new testable hypothesis about the driver of the weathering engine that we observe in the Laurels Schist and possibly many other formations. We hypothesize that oxidation of iron minerals and other oxidizable minerals (such as sulfur) by O_2, and thus the consumption and depth of ventilation of O_2 is the mechanism that initiates weathering and is the primary limitation on the advancement of the silicate weathering engine.

2.3 Study Site

The study site is the Spring Brook watershed (Figure 2.2) located in southeastern Pennsylvania and within the Christina River Basin Critical Zone Observatory (CRB-CZO). The bedrock in the site is the Laurels Schist, a foliated silvery gray-green quartz-plagioclase-muscovite-chlorite-garnet schist with minor biotite (mostly retrograded to chlorite) and accessory magnetite, epidote, tourmaline, apatite, and zircon (Blackmer, 2004). The foliations in the Laurels Schist weather to high-density, platy segments of rock that remain virtually unweathered. Weathering action appears to occur primarily in fractures and foliations between the plates.

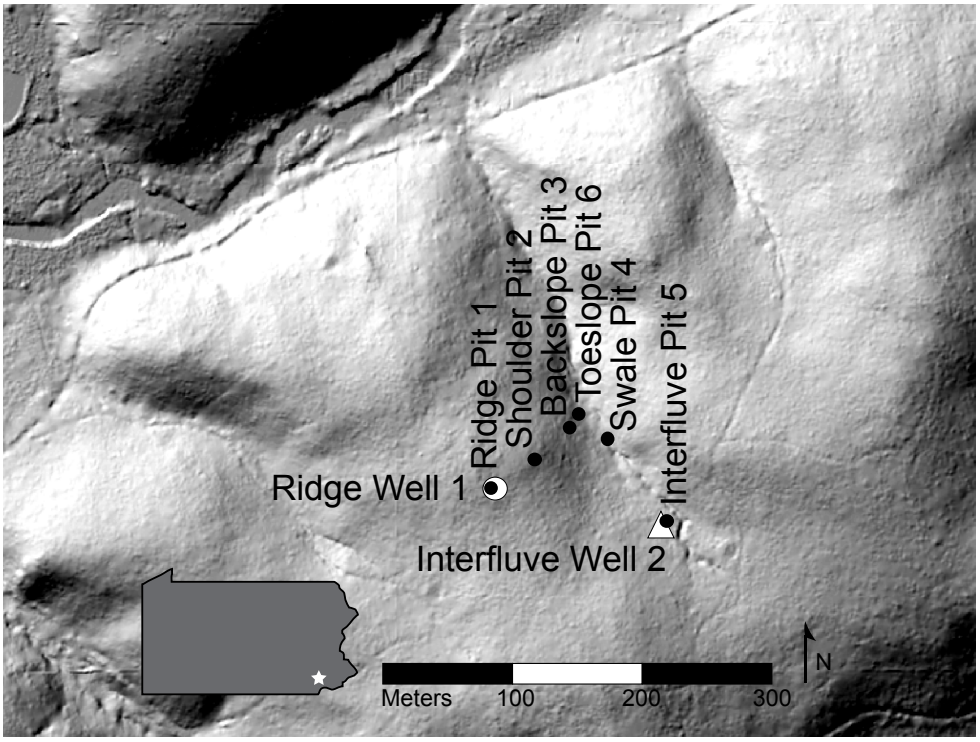

Figure 2.2. Ground returns Lidar hillshade image provides a site map with topographic information of the Spring Brook watershed in the Laurels Preserve in southeastern, Pennsylvania. In addition to Ridge Well 1 and Interfluve Well 2, we sampled a transect of soil pits to characterize the influence of landscape position on SSA and other biogeochemical properties.

Spring Brook is a first order watershed that covers 0.096 km^2, with a 250-meter long spring fed perennial stream. Up gradient from the stream is a 150-meter long, 1-meter deep historic gully that is no longer actively eroding but acts as a depositional swale with a developed A-horizon through the extent of the swale. The soils in Spring Brook are mapped as Manor Series soils (Staff and NRCS, 2012). These Typic Dystrudepts are known for weak structures, coarse loamy textures, and are highly micaceous. The abundant coarse fragments in all of the soils in Spring Brook are composed of angular schist channers (flat rocks).

The Spring Brook watershed is the only perennial stream watershed in the CRB-CZO that is 100% covered by mature forest and has no tilled agricultural history. The second growth mixed chestnut, oak, and hickory forest is approximately 120-150 years in age, and was likely logged for 1-2 cutting and planting cycles of 25-30 year old hardwood trees to provide charcoal for local smelting operations beginning around 1825 (Lesley, 1859; Shields and Benson, 2011). The property was purchased for hobby farming in the early 1900's, was used for cattle grazing beginning in 1946, and was dedicated as preserve land in 1967 (Shields and Benson, 2011). Since 1967 no grazing has occurred within the Preserve.

The climate in Spring Brook is Humid Continental with mean annual precipitation (MAP) of 1246 mm and a mean annual temperature (MAT) of 10.85°C, which ranges annually from -6 to 29°C (1961-1990, Coatesville, PA www.usclimatedata.com). Paleoclimate records from 18,000-12,000 ybp based on pollen type estimate annual lows of -12°C and highs of 16°C in the region during that period, which was experiencing these periglacial conditions until the Laurentide ice sheet began to retreat. By 9,000 ybp the temperatures were -4 to 22°C, with a gradual shift to present day temperature ranges (Prentice et al., 1991).

2.4 Methods

2.4.1 Rotosonic drilling

In order to capture the subsurface topography of weathered materials in the steep forested terrain, we selected the ridge top (143.886 MASL; 39.9195025°, -

075.7891562°°; IGSN:IESW10006) and interfluve (134.164 MASL; 39.9194885°, -075.7879179°; IGSN:IESW10007) for drilling. Two 21-meter deep boreholes were drilled into the Laurels Schist formation in August 2012. Drilling of additional boreholes was precluded by logistical and financial challenges in coordinating drilling operation in remote, densely forested, rugged topography. Samples were acquired using a Geoprobe Rotosonic (model 8140LC) mid-sized track-mounted drilling rig. The drilling method employed was the "4x6" method, which involves two hollow bits that yield a 4-inch (10.16 cm) sample diameter and a 6-inch (15.24 cm) borehole diameter. Sample intervals up to 10 m in Well 1 and to 5 m in Well 2 were drilled with air (i.e. no fluids) to maximize recovery and nearly eliminate contamination, while deeper intervals alternated between no drilling fluid and EZ-MUD® Polymer Emulsion (by Baroid IDP) to enable drilling to proceed in a timely manner. The drill segments were 152.4 cm and were inserted into a plastic sleeve immediately after recovery. While the cores were partially pulverized by the Rotosonic drilling action and broken, the recovered volumes were 68-100% for core segments drilled without fluid. Where EZ-MUD fluid was used, the recoveries ranged from 17-83%. In the lab the cores were opened and photographed and divided into intervals of approximately 10 cm. Samples were oven dried at 60°C, sieved to 2 mm where applicable, and weighed. The drilled wells were maintained with flexible liners (FLUTe™ Blank liners) that can be removed for measurements and future installations.

2.4.2 Soil sampling

In addition to drilling, soil pits were hand excavated to ~1-meter deep within a few meters of each well to allow samples to be collected by morphologic horizon (Pit 1, ridge: 143.932 MASL, 39.9194572°, -075.7892333°, IGSN:IESW10001; Pit 2, shoulder: 139.949 MASL, 39.919783°, -75.7888499°, IGSN:IESW10002; Pit 3, planar backslope: 129.989 MASL, 39.919926°, -75.7885518°, IGSN:IESW10003; Pit 6, toeslope: 123.096 MASL, 39.9200122°, -75.7883606°, IGSN:IESW10005; Pit 4, swale: 39.919863°, -75.788162°, IGSN:IESW1001C; Pit 5, interfluve: 133.108 MASL 39.9195557°, -075.7878866°, IGSN:IESW10004). After detailed soil description (Staff and NRCS, 2012), soil sample collection was guided by morphological horizons (Dataset S1). Soil materials were sampled across the entire width of the upslope side of the soil pit to integrate heterogeneities. Soil samples were homogenized in the lab, oven dried, and sieved to 2 mm, and weighed. We did not collect forest litter.

2.4.3 Specific surface area (SSA)

Samples from the fine fraction (<2 mm), which was mostly generated by the grinding from drilling action, were retained for measurement of specific surface area. Oven dried (60°C) samples were degassed at 150°C for a minimum of four hours in an N_2 environment, weighed, and analyzed using N_2 adsorption on a Micromeritics TriStar II 3020. Specific surface area (mineral surface area per unit mass of soil) was calculated using an 11 point isotherm using the BET multipoint isotherm method (Brunauer et al., 1938). For each sample, we measured SSA on three sample treatments to collect

information about organomineral associations and Fe oxides. Untreated samples that may contain organic matter associated with minerals were measured (SSA_{om}), then the samples were oxidized at 350°C for 12 hours to remove organic matter (Keil et al., 1997) to expose all mineral surfaces for N_2 adsorption (SSA_{tot}). Finally, Fe oxides were removed by Citrate-Dithionate method (Burt, 2004) to measure the SSA of primary and secondary silicate minerals (SSA_{Si}). The mean of replicate scans of each sample treatment are reported. We calculate the contribution of Fe oxides to SSA as the fraction of Fe_{cd} SSA, where Fe_{cd} SSA = $(SSA_{tot}-SSA_{Si})/SSA_{tot}$.

Method selection for organic matter removal from soils is a balancing act of weighing the efficiency of organic matter removal, alteration of minerals, and duration of treatment. We chose to oxidize our samples by muffling at 350°C partly because no wet chemical oxidation method completely removes organic matter from soils (Mikutta et al., 2005). We understand that elevated temperatures from our choice of muffling alters short range order minerals and may collapse some phyllosilicates, but we chose this method for its efficiency of complete organic matter removal and procedural simplicity given our large quantity of samples (Keil et al., 1997). Chemical oxidation not only fails to completely remove organic matter but also can result in mineral alteration. H_2O_2 can break down sheet silicate minerals, which are a major component of the studied soil (Heister, 2014). NaOCl leaves less destruction of oxides than muffling (Heister, 2014), but our experience with the NaOCl method indicated that substantial organic matter remained on mineral surfaces even after ten cycles of heating the NaOCl bath to 90°C.

$Na_2S_2O_8$ may dissolve feldspars, may alter short range order minerals, and can have lengthy reaction times (Mikutta et al., 2005). In addition to these mineral alterations by chemical oxidation, all of the chemically treated samples will require some extent of heat treatment by degassing (often 150-325°C) prior to SSA analysis, so they may be subject to heat alteration regardless of organic matter removal method.

2.4.4 Inventory of total mineral surface area

Specific surface area does not reveal the quantity of mineral surface area that is kept within a volume of a soil. The total surface area can be determined by calculating the inventory of mineral surface area. We determine the depth-integrated inventory of total mineral surface area per given ground surface area (surface area inventory, SAI, in unit dimensions of L^2L^{2-}) from the surface to the lower depth (z) limit of H as:

Equation 2.1 $$SAI = \int_{z=0}^{z=H} [SSA_z \rho_z (1 - f_z)] dz$$

Where SSA_z is the total mineral specific surface area (L^2M^{-1}) in the depth z, ρ is the bulk density of weathered material (ML^{-3}), and f is the coarse fraction (MM^{-1}). This inventory of total mineral surface area can be calculated to a depth of choice (i.e. z=H).

2.4.5 Bulk density

Bulk density measurements for Well 1 were directly measured from the ground surface using a soil recovery probe to the depth of 3.41 m from a nearly continuous set of 2.4 cm diameter cores that were collected from an excavated soil pit a few meters from the well. Bulk density for Well 2 was measured using the same method for the first 1.80 meters. Soil cores were segmented in the lab at intervals no greater than 10 cm, air dried,

oven dried for 48 hours at 60°C and weighed. The USDA standard drying temperature is 110°C (Burt and Staff, 2014), but we chose 60°C to minimize the degradation caused by heat on phyllosilicates and metastable oxide minerals.

We were not able to measure bulk density directly from depths of 5 m to 21 m at Well 1 and from 4 m to 21 m at Well 2. For these intervals we estimated the bulk density based on the density of rock chips. The specific gravity of rock chips was measured by water displacement: dry rock chips were weighed in air and in water, with 2-5 replicates for each interval. Because rock chips had low permeability we did not coat them with plastic or wax. Rock chip density values in each well did not vary systematically with depth. Average rock chip density for Well 1 (n=63) was 2.70±0.10 kg m^{-3} and for Well 2 (n=108) the average was 2.77±0.11 kg m^{-3}. Where we have both rock chip density measurements and bulk density cores in the top 3 meters, the bulk density ranged from 53-69% lower than rock chip density. Because we expect that the influence of weathering decreases with increasing depth, for the deeper samples we used the high end of this range to estimate bulk density as 68% of the rock chip density at each interval. As an additional cross-check, we received comparable bulk density values calculated from the recovered drill cores to those estimated using rock chips density.

2.4.6 Characterization of minerals

To examine the links between mineral surface area and chemical weathering, we characterized mineralogy of bulk samples using X-ray diffraction (XRD) on a Siemens D-500 Diffractometer with 2.2 kW sealed cobalt source at the University of Minnesota

Characterization Facility. Samples were pulverized on a tungsten carbide ring mill to 6 μm (D_{90}) and combined with a 10% zincite internal standard (Eberl, 2003). The mixture was combined using an agate mortar and pestle wetted with ethanol and was packed into a holder and x-rayed from 5 (machine minimum) to 75 degrees two-theta using Co K-alpha radiation with 0.02 degree steps and a dwell time of 2 seconds per step on a continuously rotating sample stage.

XRD spectra were converted to Cu K-alpha wavelengths using Jade 7.0 (Materials Data, Inc.) and exported as ASCII text for analysis. Peak intensities were manually normalized in spreadsheet form setting the zincite 2.476Å peak as 10%. Minerals were identified and quantified using non-interfering peaks and normalized by expected peak intensities: Quartz 1.8179Å (0.14 intensity), Plagioclase group 3.17-3.21Å (1), Muscovite 9.95Å (0.95), and Clinochlore (Chlorite group) 4.77Å (0.7).

2.4.7 Clay mineralogy

Given the expected disproportionate contributions of secondary phyllosilicate minerals to mineral SSA, we separately characterized their mineralogical compositions. The clay size fraction was isolated by gravity sedimentation using a suction apparatus (Jackson and Barak, 2005). Isolated clay sized fractions were pre-treated in multiple steps to remove carbonates (sodium acetate-acetic acid solution), organic matter (bleach method), and exchangeable iron oxides (citrate-dithionite) (Burt, 2004; Jackson and Barak, 2005). Clays were divided and saturated with potassium and magnesium and were oriented suspension mounted on glass coverslips. Potassium and magnesium saturated

samples were X-rayed from 5 to 18 and 5 to 36 degrees two-theta using Co K-alpha radiation, respectively. Potassium saturated samples were heated to 500°C for 1 hour and scanned again from 5 to 18 degrees two-theta. Magnesium saturated samples were further saturated with ethylene glycol and scanned from 5 to 18 degrees two-theta.

2.4.8 Iron mineralogy

On a small subset of specimens from Well 1 (n=12), we used rock magnetic measurements to characterize the iron mineral type, quantity, and size. Samples were pressed into 6-mm diameter pellets under pressure in a mixture of rock powder with SpectroBlend powder (81.0% C, 2.9% O, 13.5% H, 2.6% N). Room temperature and low temperature saturation isothermal remanence (RTSIRM, LTSIRM) was measured on five of the specimens using a Magnetic Properties Measurement System (MPMS, Quantum Designs). A room temperature Vibrating Sample Magnetometer (VSM, Princeton Measurements) was used to obtain hysteresis loops for all samples. We applied a 1.25 T maximum magnetic field and measured the hysteresis parameters, saturation magnetization (Ms), saturation remanence (Mr), coercivity (Hc), and coercivity of remanence (Hr).

2.4.9 Seismic Multichannel Analysis of Surface Waves (MASW)

Seismic Multichannel Analysis of Surface Waves (MASW) survey was performed (by Jonathan Nyquist) across the transect to connect Ridge Well 1 and Interfluve Well 2. MASW survey used a 16-lb sledge hammer as the seismic source in conjunction with a 24-channel Geometrics Geode seismograph and 4.5 Hz geophones.

The geophones were spaced 1.5 m apart (34.5 m spread) with a source offset of 10.5 m from the end the geophone spread to avoid near field effects in surface wave generation. At each shot location we stacked five hammer blows to boost the signal to noise ratio. The entire line was then shifted 3 m (2x the geophone spacing) and the process repeated for a total survey line length of 141 m. The seismic data were analyzed using SeisImager/2W[5].

2.5 Results

2.5.1 Morphology of weathering profiles

The Manor Series soils are coarse-loamy, micaceous, mesic Typic Dystrudepts and in Spring Brook they exhibit morphological differences associated with landscape position, with the primary contrast occurring between eroding zones (ridge, shoulder, backslope) and depositional zones (toeslope, swale, interfluve). Detailed morphology of the ridge and interfluve soils, which correspond with Wells 1 and 2, respectively, are tabulated in the supplementary material (Dataset S1). We identified the C-horizon at 84 cm at Ridge Well 1, and although Interfluve Well 2 was identified as BC horizon from 107-124 cm, the C-horizon was not visible to depth of hand excavation. The texture class in all soil intervals for these two soil pits is extremely channery sandy clay loam. Among the ubiquitous characteristics in the soils is a high concentration of platy schist rock fragments (Dataset S1). The coarse fragments at the ridge, shoulder, and backslope are supported in the soil by other rock clasts; in contrast, the coarse fragments in depositional zones (interfluve and toeslope) are fewer and supported by a matrix of sand, silt, and

clay. The eroding soils have weak structure, are highly micaceous, and the fine fraction (<2 mm) is largely composed of millimeters-thick layer of loose grains of sand, silt, and clay sized mica mantling each schist channer. Also in the eroding soils, the depth to hand auger refusal is 10-20 cm due to high rock content. By contrast, the depositional soils in Spring brook, such as in the interfluves and swale, will allow hand augering to 50 cm.

2.5.2 Mineral specific surface area

Measured values of total mineral specific surface area (SSA_{tot}) vs. depth (Figure 2.3A) reveal that there is a nominal difference between Ridge Well 1 and Interfluve Well 2, with the interfluve well displaying higher surface area at many depth intervals. The depth distribution reveals a sharp increase in total mineral specific surface area with decreasing depth, with SSA_{tot} ranging from 9-22 $m^2 g^{-1}$ in the upper 1.5 m, from 2-12 $m^2 g^{-1}$ from 1.5 to 3 m, and from 2-5 $m^2 g^{-1}$ below 3 m to 22 m. We observe that the Citrate-Dithionate extractable iron (Burt, 2004) contributes greater than 50% of the SSA found in samples within the top three meters at both landscape positions (Figure 2.3B) whereas the silicate SSA (Figure 2.3C) follows a depth trend similar to total SSA. The fraction of SSA contributed by iron oxides (Fe_{cd} $SSA=1-(SSA_{cd}/SSA_{tot})$), at Ridge Well 1 is 48-81% from 0-3 meters deep and 5-25% below 3 m. At the Interfluve Well 2 iron oxides contribute 36-77% of SSA from 0-1.5 m, 13-74% from 1.5-3 m and 10-15% below 3 m. Therefore SSA contributed by Fe oxides increases in direct proportion to those contributed by silicate minerals over the top three meters of the drill cores as statistically shown in Figure 2.4. All breakpoints for SSA_{tot}, Fe_{cd} SSA, and SSA_{Si} are deeper than the

boundaries from mobile soil to non-mobile weathered rock (84 cm & ~150 cm for ridge & interfluve respectively) and do not correlate with any morphologic observations from the drill cores.

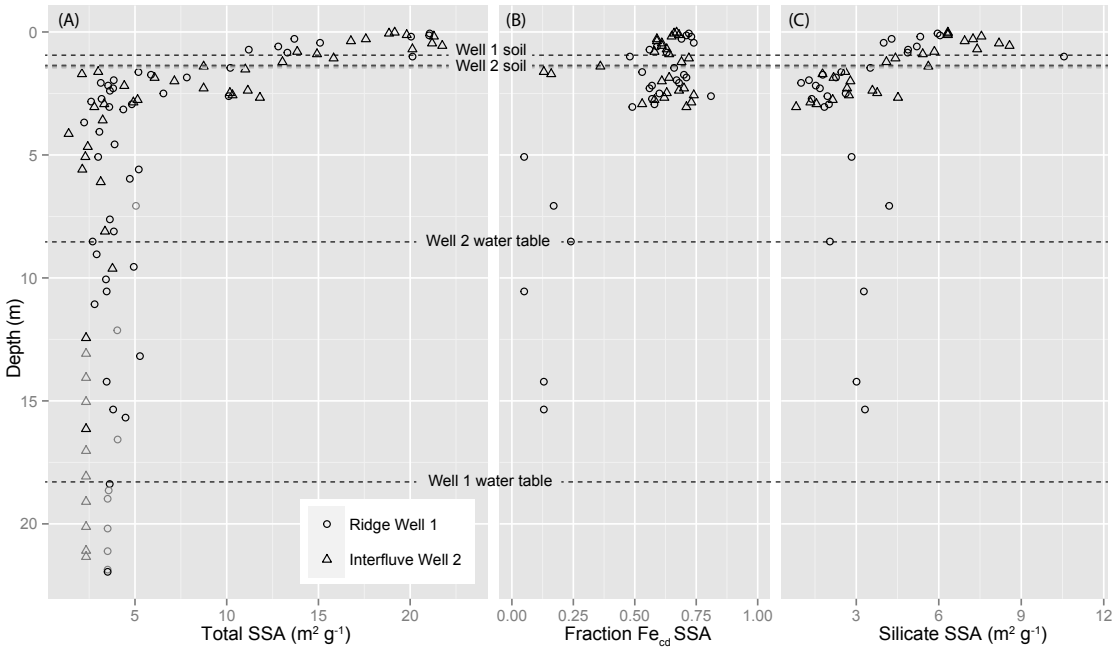

Figure 2.3. Total SSA vs depth (A), fraction of SSA contributed by Citrate-Dithionite extractable iron (Fe_{cd}, B), and silicate SSA (C) reveal that the total SSA increases toward the ground surface. Fe_{cd} SSA exhibits a sudden change with most intervals contributing over 50% of SSA above 3 meters, and below 3 meters, very little of the SSA is contributed by iron oxide minerals. Gray points are interpolated or estimated SSA.

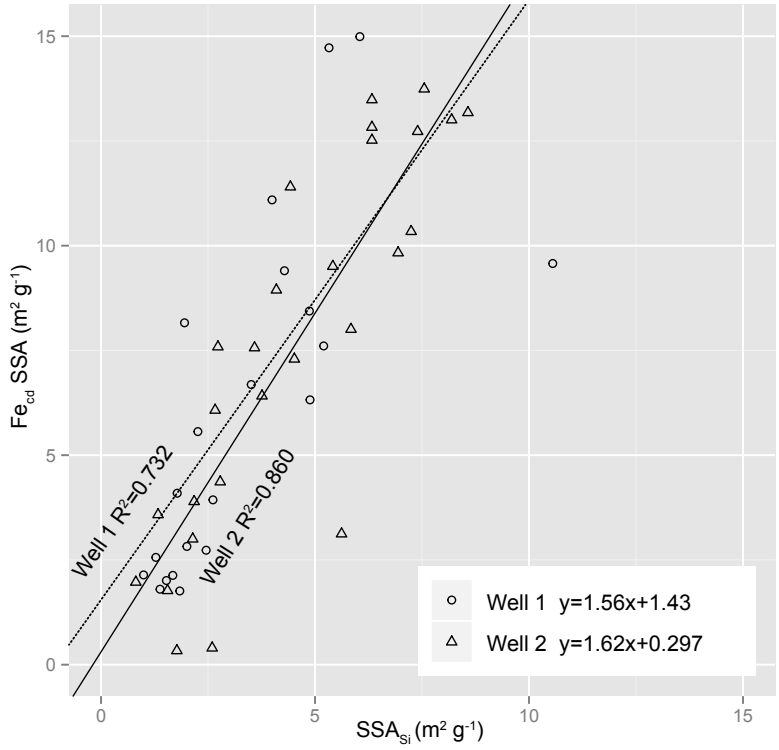

Figure 2.4. Correlation of Fe_{cd} SSA with silicate SSA for data from 0-3 meters reveals a strong positive correlation between iron and silicate SSA. The correlation holds true at Ridge Well 1 and Interfluve Well 2.

The depth-integrated inventory of total mineral surface area (SAI, Equation 2.1) shows the cumulative total mineral surface area from the ground surface to a variable lower depth limit for each of the drilled wells (Figure 2.5). This computation normalizes the mineral specific surface area with bulk density for each depth interval and helps differentiate between the natural measured variability of surface area and the broad patterns in the genesis of mineral surface area. Segmented linear regression provides an objective approach to determining intervals of similar slopes and breakpoints between these intervals (Muggeo, 2008). We applied the segmented linear regression model (Muggeo, 2008) iteratively for each SAI profile using SAI as the dependent variable in the regression analysis and depth as the independent variable, in order to objectively find

the depths of breakpoints and the slopes of SAI depth-trends between breakpoints, in units of square meter of mineral surface per cubic meter volume of soil or rock. Ridge Well 1 had two breakpoints at 1.50±0.08 and 3.11±0.07 meters deep (slope 1=$8.71x10^4$ m^2m^{-3}, slope 2=$4.81x10^4$ m^2m^{-3}, slope 3=$7.51x10^3$ m^2m^{-3}, R^2=0.9981). Interfluve Well 2 had three breakpoints at 1.02±0.03, 2.22±0.06, and 2.82±0.02 meters (slope 1=$1.35x10^5$ m^2m^{-3}, slope 2=$6.07x10^4$ m^2m^{-3}, slope 3=$1.06x10^4$ m^2m^{-3}, slope 4=$5.83x10^3$ m^2m^{-3}, R^2=0.9994). The number of break points presented represents the optimum fit for each well, and additional break points did not improve the regression.

These statistically calculated breakpoints do not correlate well with any morphologic features observed from the excavated soil pits or drill cores (Figure 2.5). The largest relative change in slopes within each profile occurred near 3 meters at both landscape positions. We interpret the slope of the surface area inventory as the rate of surface area production as a function of depth normalized to the volume of soil.

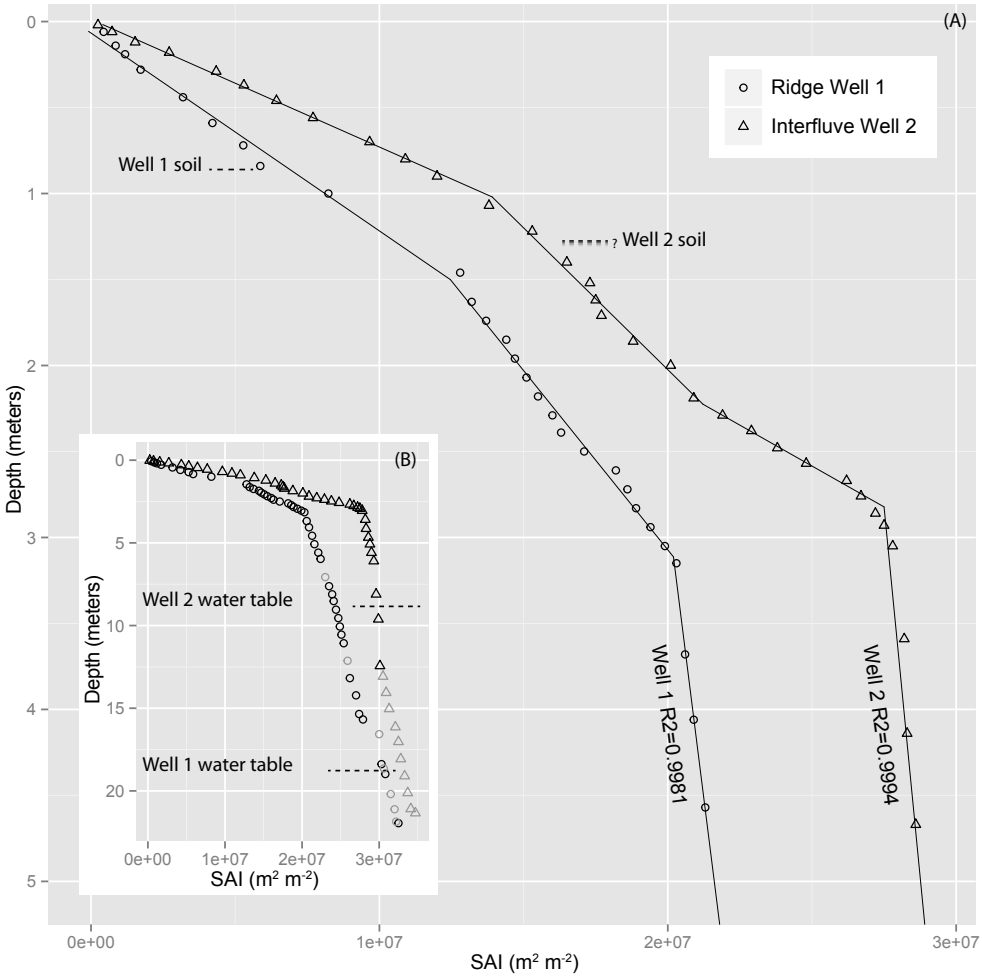

Figure 2.5. Surface area inventory, calculated by Equation 2.1, reveals trends in the accumulation of mineral surface area. The inset image (B) shows the full depth trend while the larger image (A) reveals the top five meters, where changes in the slope, once combined with erosion rates, may indicate different rates of SSA production. The segmented linear regressions reveal slope changes that do not represent morphologically identified boundaries. Morphological boundaries are noted as “Well 1 soil” and “Well 2 soil” indicate the depths were soils transition to weathered rock, although the transition to rock in Well 2 was not conclusively identified by excavation. Note that distinct change in the slope of the surface area inventory lines, which occurs near 3 meters, does not occur at the lower boundaries of soils or near the water table in either well (B). Gray points in the inset are calculated from interpolated or estimated SSA.

2.5.3 Mineralogy

Quantitative analysis of bulk XRD reveals that the Laurels Schist is mineralogically variable (Figure 2.6). The primary mineral matrix is composed of quartz, Ca-plagioclase, muscovite, and chlorite group minerals. In the clay-sized fraction of weathered materials, in addition to primary-derived micas and chlorites, we identified illite and vermiculite minerals, and minor amounts of kaolinite. In Ridge well 1, despite mineralogical variability, XRD of random mounts of the whole sample indicated a gradual decrease of primary plagioclase group minerals from 7 meters to the surface at the ridge and above 5 meters at the interfluve. Additionally, the muscovite and chlorite group minerals co-vary at most sample intervals in both wells.

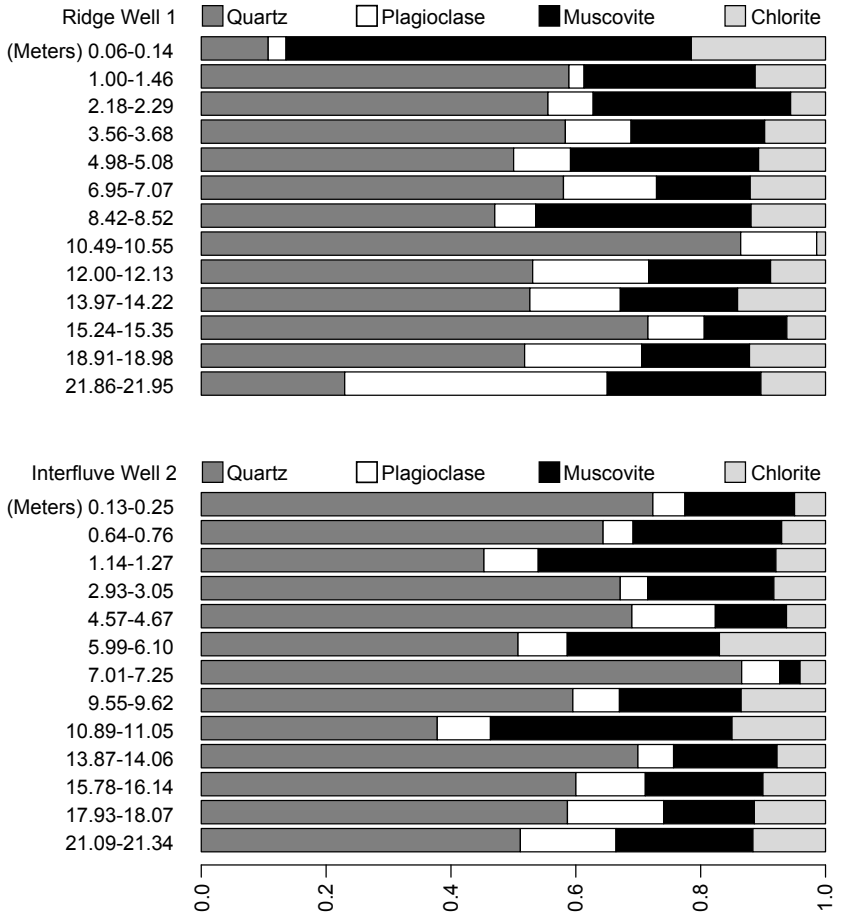

Figure 2.6. Four major mineral groups in the Laurels Schist Formation with quartz (dark gray), plagioclase group minerals (white), muscovite group minerals (black), and chlorite group minerals (light gray) normalized by fraction such that the four minerals comprise the whole rock. This illustrates how the mineralogy is variable with depth in both wells, lacking distinctive weathering trends apart from decrease in plagioclase group minerals (white) with decreasing depth in Ridge Well 1.

Detailed XRD analysis allowed identification of phyllosilicate mineral species that contributed to the observed mineral SSA. We identify both kaolinite and clay-sized chlorite from soil pits and push-cores in the top 1.5 meters at the ridge and the top 3 meters at the interfluve indicated by the destruction of the 7 Ångstrom peak upon heating

to 500°C (kaolinite) and the intensification of the 14 Ångstrom peak (chlorite) in the same treatment (Jackson and Barak, 2005). However, clear quantifcation of secondary phyllosilicate minerals was difficult with samples from greater depths collected from Rotosonic drill cores. Pulverization by sonic drilling action broke primary minerals into pieces small enough to separate with clays, inhibiting the secondary phyllosilicates from orienting parallel to the glass slides. The presence of kaolinite is thus difficult to identify in any rock where primary chlorite group minerals share diagnostic d-spacing.

2.5.4 Magnetic mineralogy

Magnetic Property Measurement System was applied to a small subset of Spring Brook samples from the ridge soil pit. The results universally reveal that magnetite dominates the magnetic properties of all of the Spring Brook samples such that the abundances of short range order iron minerals are extremely low. They are not below minimum detection limits for this procedure (ppm) (Özdemir et al., 2002), but removal of magnetite will be necessary to meaningfully characterize the presence of goethite and hematite among the iron oxides (Strehlau et al., 2014).

Seismic Multichannel Analysis of Surface Waves (MASW)

Seismic Multichannel Analysis of Surface Waves (MASW) survey revealed a gradual increase in seismic shear wave velocity with increasing depth, with the highest velocities reaching only 500 m s^{-1} for depths up to 17 meters, which is interpreted as soft rock (Lowrie, 1997). The soft rock velocities seem to conflict with rock chip densities, which average around 2.7 g cm^{-3} in both wells. Foliations in the Laurels Schist result in

discontinuous rock, which effectively slow seismic wave propagation, resulting in low velocities despite the high density rock chips (Clarke and Burbank, 2011, 2010). MASW surveys do not reveal the changes in mineral SSA we observed (Figure 2.3 and Figure 2.5), yet the MASW results clearly indicate an absence of abrupt change in rock properties over the remaining 14 meters. (MASW data interpretation from Jonathan Nyquist, personal communication.)

2.6 Discussion

2.6.1 Vertical and topographic distributions of total mineral specific surface area

The boundary where physically mixed soil transitions to physically *in situ* but chemically weathered rock (84 cm and ~150 cm for the ridge and interfluve respectively) did not coincide with the onset of total mineral SSA, Fe_{cd} SSA and silicate SSA (~3 m), indicating that the transition to physical mixing processes does not involve dramatic changes in mineral surface area production by chemical weathering. In the Laurels Schist, simplification of weathering profiles into this type of soil to weathered rock layered system (Dixon et al., 2009; Yoo and Mudd, 2008) is somewhat limited because soil materials often penetrate into the underlying densely layered rock clasts, offering what geophysically displays as a deep, gradual, transition between soil and weathered rock (Jonathan Nyquist, MASW survey interpretation via personal communication). Though the soil zone indeed has greater mineral SSA when compared to the underlying zone (Figure 2.3), our measurements do not support the hypothetically expected sharp change in SSA at the soil-weathered rock boundary. The quantity of measured total SSA

decreases with depth in each drill core, with the sharpest breakpoint in SAI occurring at 3.11±0.07 m in Ridge Well 1 and at 2.82±0.02 m in Interfluve Well 2 (Figure 2.5). The boundary from soil to C-horizon, however, was identifiable at 84 cm at the ridge, and drill core photographs (Figure S1) confirm a distinct color change in recovered material at this depth. While our confidence in morphologically determining the soil-weathered rock boundary is somewhat compromised at the interfluve, it is still evident that the morphologic boundary is distinct from the inflection depth of total mineral SSA. At the interfluve the soil pit was hand excavated to 124 cm, where colluvial material was observed for the entire excavation. Push cores into the bottom of the interfluve soil pit revealed what may be the boundary between colluvial material and weathered rock at approximately 150 cm that also occurs as a color change in the drill core. This depth of 150 cm was also expected due to the lateral continuity of this boundary to multiple adjacent cores in this soil pit. However, Interfluve Well 2 has a cluster of high SSA measurements at 2.5 meters deep (Figure 2.3), which may indicate that the thickness of colluvium and therefore the depth to weathered rock could approach 2.5 meters. In summary, the major vertical patterns in total mineral SSA cannot be explained by the transition of soil to weathered rock at both eroding and depositional topographic positions in the studied catchment.

Another hypothesis from the literature suggests that the groundwater table may mark the initiation of chemical weathering that might be reflected in depth profiles of mineral SSA. In a full year of observation in 2014, however, the water table at Ridge

Well 1 ranged from 17.7-20.3 meters below the ground surface and the range at Interfluve Well 2 was 6.8-8.3 meters. These depths are well below the depths of major changes in mineral SSA, thus we conclude that processes responsible for generating mineral SSA are not directly related to the groundwater table. Each well appears to have a minor change in SSA production rate (see below) at the respective water tables (Figure 2.5B), but low sampling resolution of dry cores at these depths make this observation difficult to statistically assess.

2.6.2 Mineralogical Sources of Mineral Surface Area

We expect mineral weathering to generate high SSA phyllosilicate at the expense of low SSA minerals (such as plagioclase). In the clay-sized fraction of weathered materials, illite, vermiculite, and kaolinite were present in the upper 1.5 to 3 m, in addition to primary-derived micas and chlorites. The primary mineral matrix includes magnetite that was identified using magnetic methods. The theoretical SSA of all minerals detected in our study, based on mineral structure and measurements of pure minerals (Essington, 2003), is shown along with their classical weathering progression (Jackson and Hseung, 1952; Jackson et al., 1948) in Figure 2.7.

The constructed weathering sequence of minerals from the Laurels Schist (Figure 2.7) reveals the primary and secondary minerals identified by XRD and rock magnetic techniques in the rocks and soils in this study. Plagioclase minerals weather directly to kaolinite following the progressive removal of cations. Muscovite weathering follows a more complex sequence, often involving the weathering of some layers to vermiculite

and illite, resulting in a disordered set of interlayered micaceous minerals that make identification by XRD difficult. We identify illite and vermiculite minerals in the same specimens as muscovite, indicating that there is either incomplete diagenetic transformation of muscovite during metamorphism or partial removal of muscovite by weathering processes. Regardless of the process the overall trend from muscovite to illite and vermiculite, in pure or interlayered forms, theoretically results in higher SSA minerals until the minerals ultimately weather to kaolinite. Chlorite group minerals follow a similar weathering pattern as mica group minerals, with interlayered vermiculite minerals increasing SSA and the octahedral occupation of weathering products inherited from the primary minerals. Through the depth extent of oxidation, iron bearing primary minerals (muscovite, chlinochlore, and magnetite) will oxidize and solubilize Fe^{2+}, leading to the production of maghemite, hematite, and goethite. These reactions in iron bearing minerals are important for generating porosity to promote further weathering (Buss et al., 2008; Navarre-Sitchler et al., 2009, 2013), and although we did not pursue characterization of low-abundance iron oxide minerals in our mineralogical analysis, we infer the presence of hematite and goethite due to the measured contribution of Citrate-Dithionite exchangeable iron oxides to SSA in the upper 3 meters (Figure 2.3), the coloration of drill core specimens above 3 meters (Figure S1 and Dataset S3), and the near ubiquitous presence of hematite and goethite in soils (Essington, 2003).

XRD of random mounts of the whole sample indicated a gradual decrease of primary plagioclase group minerals from 7 meters to the surface at the ridge and above 5

meters at the interfluve Figure 2.6). The conversion of plagioclase to kaolinite can increase SSA from 1 m^2g^{-1} to 10-20 m^2g^{-1} (Essington, 2003). We identify both chlorite and kaolinite in the top 1.5 meters at the ridge and the top 3 meters at the interfluve. Such observation of kaolinite does not contradict the presence of Inceptisols at the study site because of the deep subsurface weathering prior to the conversion of the weathered rock into the colluvial soils. Kaolinite formation is favored by acidic environments at the expense of the formation of smectite phases (Jackson, 1963; Jackson et al., 1948), which are absent in the studied samples.

Additional contributions to the near surface SSA increase may come from chemical weathering of muscovite (10-40 m^2g^{-1}) to illite (70-120 m^2g^{-1}), as evidenced by the increase in 5 Ångstrom peak intensity, a minor but distinguishing peak between the two minerals, at depths above 1.5 meters at the ridge and above 3 meters at the interfluve. Chlorite (70-150 m^2g^{-1}) transitioning to vermiculite (300-800 m^2g^{-1}), along with their interlayered intermediates, are present at depths above 1.5 meters at the ridge and above 3 meters at the interfluve. As each of these minerals chemically weathers to their secondary counterparts, they contribute to higher SSA (Figure 2.8).

Figure 2.7. Weathering sequence of minerals observed using clay and bulk XRD in the Laurels Schist. The list of minerals at the left of the diagram are the primary minerals observed in the Laurels Formation. The sequence follows their typical weathering progression to a variety of phyllosilicates with octahedral occupation inherited by primary minerals. Of particular note is the drastic increase in SSA as primary minerals weather to their secondary counterparts until they converge on their ultimate end products, which is often kaolinite. Notably kaolinite does not appear to be abundant in the Laurels Formation.

2.6.3 Production rates of mineral surface area

On soil covered eroding landscapes, as soils are eroded, underlying weathered rock and subsoil are incorporated into the soil, maintaining a mantle of soil on the landscape (Heimsath et al., 1997). Likewise, the zone of weathered rock is maintained by the balance of soil production and weathering front propagation into the underlying fresh bedrock (Dixon et al., 2009). In unglaciated landscapes such as our study site, we assume a steady state condition for the thickness of the weathering profile. This assumption, when combined with the depth profiles of mineral SSA and SAI, provides an opportunity to calculate the production rate of mineral surface area within weathering profiles. We calculate a denudation rate of 50 m/m.y. at the ridge in Spring Brook using meteoric ^{10}Be. Meteoric ^{10}Be-based denudation rate for the Shale Hills CZO site in Pennsylvania was estimated to be ~15-20 m/m.y., which resulted in the soil residence time of 9-10 k.y. (West et al., 2013). Given this range of denudation rates, it would take 60-150 k.y. to erode the upper 3 meters of the weathering profile where mineral SSA increases from 2 m^2/g to 22 m^2/g (Figure 2.3). Using the denudation rate for Spring Brook, this amounts to an annual mineral SSA production rate of 0.33 $m^2kg^{-1}yr^{-1}$ within the top 3 meters of the weathering profile with no significant changes associated with soil-weathered rock boundaries. Given the regional range of denudation rates, the range of SSA production rates is 0.10-0.33 $m^2kg^{-1}yr^{-1}$. This approach, when applied to the interfluve excluding the colluvial soil transported from upslope, results in a similar mineral SSA production rate.

This, to our knowledge, is the first estimate of mineral surface area production

rate within a weathering profile. Only a few related published values are available, but these are not directly comparable to our results. White and Brantley [2003] conducted a 6 year long laboratory batch experiment, where they reported changes in mineral surface area that result in a production of 35 $m^2kg^{-1}yr^{-1}$ for fresh granite and 280 $m^2kg^{-1}yr^{-1}$ for weathered granite under the same experimental conditions. The mineral dissolution rates from the same experiment showed the opposite trend, where weathered granite weathers at a rate that is an order of magnitude slower than the fresh granite lab rate. There are few reports of mineral surface area data from soil chronosequences (White and Brantley, 2003), but their focus on specific mineral groups make comparison with our work difficult. At a fundamental level, one should use caution in projecting our mineral SSA production rate to estimate changes in mineral surface area along soil chronosequences. While soil chronosequence studies compare soil materials at similar depths assuming that they differ only by their time exposed to weathering agents, our study focuses on describing vertical changes in mineral surface area within weathering profiles.

We observe little or no change in SSA production rate for the samples collected below 3 meters (Figure 2.5). The weathered rock in both wells exhibits a slope below 3 meters that simply represents accumulation of constant mineral surface area as shown in Figure 2.3A. Surface area inventory reveals that more surface area has accumulated at the interfluve, which is due to deposition of fine colluvial material and higher bulk density of the interfluve soils (bulk density in Dataset S2).

2.6.4 Contribution of iron oxides to mineral SSA

The contribution of crystalline and amorphous secondary iron oxide minerals to total SSA remains consistently between 50-75% of the total SSA over the top three meters of each drill core. We quantified iron oxide SSA using the difference between total SSA and SSA after citrate-dithonite extraction. Iron oxides are known to possess high SSA (Eusterhues et al., 2005; Keil and Mayer, 2014; Thompson et al., 2011), and we observed that the SSA contributed by Fe oxides increases in direct proportion to SSA from silicate minerals over the top three meters of the drill cores (Figure 2.4). Between 1.5-3 meters we observe the emergence of secondary phyllosilicates in both wells. Silicate SSA increases similarly in both wells, suggesting that secondary phyllosilicates may exist below the extent of our detection at 1.5 meter in Ridge Well 1. Immediately below this 3 meter boundary the iron contribution to SSA is nearly nonexistent. This boundary in iron oxides at 3 meters was matched by visible color changes (Figure S1 and Dataset S3) in the recovered drill core at both the interfluve and the ridge. Redox coloration is visible in core samples from 0-3 meters at both landscape positions.

Iron oxide minerals are ultimately a geological recorder of oxidation process and subsurface O_2 gas (Anderson et al., 2002; S. L. Brantley et al., 2013). Our iron oxide SSA data indicate that 3 meters may be the depth of the O_2 ventilation front at both landscape positions within the Spring Brook watershed, although we do not have soil gas data to confirm that 3 meters is the extent of O_2 penetration. The O_2 ventilation front does not directly account for the increase in silicate SSA while the emergence of secondary

phyllosilicate was also found at 3 meters. We postulate that iron oxidation on primary minerals could be the key to the initiation or acceleration of weathering of other elements from primary minerals and the formation of secondary phyllosilicate minerals and oxide minerals. We observe an abrupt, step function increase in SSA at 3 meters, well below the soil-weathered rock boundary, and this abrupt change suggests a connection between the observed changes in multiple weathering indicators and the depth extent of oxidation processes.

Extensively deep oxidation of iron and sulfur minerals is recorded throughout the literature. In steep forested Oregon Coastal Range, for instance, pyrite containing greywacke sandstone bedrock was pervasively oxidized to the depth of 4.5 meters at the ridge top, above which pyrite was no longer present (Anderson et al., 2002). At Shale Hills Critical Zone Observatory in Pennsylvania, pyrite oxidation extended as deep as 23 meters (Susan L. Brantley et al., 2013). Oxidation of biotite within quartz diorite was identified as a source of fracturing and the initiation of weathering in a mountainous landscape in Puerto Rico (Buss et al., 2008). At a granite ridge in the Piedmont, *Bazilevskaya et al.*, [2015] found that the depth of the lower boundary of weathering is controlled by biotite oxidation, which generates porosity and accelerates other chemical weathering processes by facilitating advective transport of water and oxygen. Our results suggest that these reported depths of oxidation may accompany abrupt changes in mineral SSA.

Our finding that 50-75% of SSA is contributed by iron oxides reveals that the

production of secondary phyllosilicate minerals is not the primary source of mineral SSA. Silicate SSA, the combined SSA of primary minerals and secondary phyllosilicate minerals, was responsible for only a maximum of 10 m^2g^{-1} of mineral SSA at the ridge and 9 m^2g^{-1} at the interfluve (Figure 2.3C). Silicate SSA is significant but smaller than SSA attributed to dithionite-citrate extractable iron minerals, which are as much as 15 m^2g^{-1} at the ridge and 14 m^2g^{-1} at the interfluve. Thus, mineral SSA production is derived by the production of not only iron oxides but also secondary phyllosilicate minerals, which are directly proportional and statically correlated with each other (Figure 2.4). This can be seen from the depth-independent relative contribution of iron oxides to mineral SSA within the top 3 meters (Figure 2.3B). The remaining contribution to the increasing mineral SSA with decreasing soil depth is largely from the production of secondary phyllosilicate minerals (Figure 2.3C).

The significance of the contribution of iron oxide minerals to SSA is multifaceted. The occurrence and depth distribution of iron oxides is the same at the ridge and interfluve (Figure 2.4), indicating that landscape position does not impart significant control on the oxidation reactions that generate iron oxides in this watershed. The abrupt transition from almost no SSA contribution by iron oxides to 50-75% at 3 meters deep records an abrupt change in oxidation reactions, which we understand to record the O_2 gas ventilation front. Below the O_2 ventilation front at 3 meters there is not only a halt in the oxidation of iron oxides, but there appears to be very little, if any, production of secondary phyllosilicate minerals. Thus the O_2 ventilation front may be the extent of the

silicate weathering engine, which implicates O_2 as the limiting factor for chemical weathering and oxidation reactions as the initiator of chemical weathering.

2.6.5 Processes that facilitate the infiltration of CO_2, O_2, and pore water

The processes that influence weathering are numerous and dynamic and often impossible to isolate in field settings. The interplay between several factors, including soil moisture, microbial respiration, soil texture, landscape position, tree rooting depth, and frost damage, influence the depth of O_2 penetration and the production of pCO_2 in soil and weathered rock (Davidson and Trumbore, 1995; Liptzin et al., 2011; Richter and Billings, 2015; Silver et al., 2005). In our studied weathering profiles, iron oxides and secondary phyllosilicate minerals are responsible for mineral SSA. Therefore, the question of how production of secondary iron oxide and secondary phyllosilicate minerals drive generation of mineral SSA may be substantially dependent on the capacity of the weathering profile to conduit water, oxygen, and CO_2 and the availability of organic acids.

Silicate weathering requires carbonic or organic acid. For example, chemical weathering of calcic plagioclase (~1 m^2g^{-1}), which is present in the Laurels schist, consumes CO_2 and ultimately leaves secondary kaolinite (10-20 m^2g^{-1}). The presence of kaolinite is measurable above 3 meters, which may contribute to the observed major change in surface area production at 3 meters. Acidic conditions promote silicate weathering, and a 7-10x increase in pCO_2 results in a 1 pH unit decrease in soil pH (Hasenmueller et al., 2015). Although we have not measured soil CO_2 in the Laurels

Schist, there are a number of published subsurface CO_2 depth profiles. Davidson and Trumbore [1995] observed pCO_2 to increase to ~70,000 ppm at 8 meters with no plateau. Landscape position can more significantly influence pCO_2 than depth, particularly where soil moisture is highly variable within a landscape, yet soil pCO_2 is invariably higher than atmospheric values (Hasenmueller et al., 2015). Groundwater released into rivers is shown to have elevated pCO_2 that decreases as it travels away from the groundwater source, indicating that soil and groundwater are supersaturated in CO_2 (Johnson et al., 2008). Waters supersaturated in CO_2 occur in significant quantities for global carbon fluxes in rivers of all scales, including small headwater streams (Argerich et al., 2016). These observations from the literature reveal that CO_2 and acidity are not limited at any depth; we see that pCO_2 in the subsurface is orders of magnitude higher than atmospheric pCO_2 and that processes that generate CO_2 can extend deep into weathering fronts.

If CO_2 is not a limitation at depth, and acidity from elevated pCO_2 is the favorable condition for silicate weathering, then we need to explain the presence of silicate weathering fronts, which represent the termination of silicate weathering at depth. Soil CO_2 is produced at the expense of O_2, so the depth profile of O_2 depletion is inversely proportional to pCO_2 (Liptzin et al., 2011; Richardson et al., 2013). We believe that the key limitation to chemical weathering may be the presence of O_2 in subsurface pores. Oxygen enables abiotic and microbially-mediated iron oxide formation and is a fundamental process for promoting silicate weathering. We propose a new hypothesis that the penetration depth of O_2 is a key factor in determining the depth of the chemical

weathering front in the critical zone.

Furthermore, we believe that the penetration depth of O_2 is determined by a combination of large scale physical weathering processes and biological processes. Physical weathering processes, such as frost damage and tree rooting, create a macro-pore network that controls the diffusion of gasses through the soil and weathered rock layers of the critical zone. Water content of the critical zone further reduces gas diffusion, especially below the water table. Biological processes, such as root respiration and microbial oxidation of organic matter and iron, controls the consumption of oxygen at depth and the resultant respiration of CO_2. These physical and biological processes combine to determine the ventilation front for the penetration of O_2. We hypothesize that this coupled system where O_2 promotes weathering of iron and respiration of CO_2 is the fundamental mechanism that drives the silicate weathering engine.

A number of publications indicate an association between physical weathering and chemical dissolution of silicate minerals that occur due to vascular plants (Alexandre et al., 1997; Andrews and Schlesinger, 2001; Berner and Cochran, 1998; Berner, 1992; Cochran and Berner, 1996; Drever, 1994; Moulton, 2000). Physical disruption caused by rooting and the rootwads of overturned tress (Roering et al., 2010) facilitates infiltration of O_2 giving biogeochemical processes access to fresh minerals (Drever, 1994). Physiochemical weathering at deeper zones and in the microenvironments surrounding roots can be further promoted by root and rhizosphere respiration of CO_2 and acidic secretions (Andrews and Schlesinger, 2001; Berner and Cochran, 1998; Cochran and

Berner, 1996; Moulton, 2000). The weathering influence by vascular plants can generate abrupt weathering boundaries evidenced by removal of minerals such as plagioclase (Cochran and Berner, 1996). Several of the tree species present in the Laurels Preserve are documented to root to at least 3 meters deep (including Q. rubra, Q. alba, L. tulipifera, C. cordiformis (Stone and Kalisz, 1991), and tree-throw pit-mound topographic features are common in Lidar data (Figure 2.2, DOI: 10.5069/G9T43R00). These observations suggest the important role that tree roots may have contributed to the observed depth profiles of mineral SSA.

The disruption by tree roots and the resulting generation of pores and cracks may have been enabled by frost damage when the studied region experienced periglacial climate conditions (Anderson et al., 2013; Marshall and Roering, 2014). Geomorphologists and pedologists have long been aware that periglacial environments during the last glacial maximum left a wide range of geomorphic legacy in the continental US that includes the Pennsylvania piedmont (Ciolkosz and Waltman, 1995; Ciolkosz et al., 1986; Clark and Ciolkosz, 1988; Gardner et al., 1991; Hancock and Kirwan, 2007). Modeling studies based on frost processes throughout the world reveal that frost damage of bedrock can extend as much as four meters deep where the frost cracking temperature window occurs between -3°C to -8°C (Andersen et al., 2015; Anderson et al., 2013; Hales and Roering, 2007). Anderson et al. [2013] understand frost damage and mobile regolith transport processes as climatic driven processes. That the 3 meter SSA inflection appears to occur regardless of landscape position or soil

morphology suggests that it may be a laterally continuous feature, which would be the result if periglacial frost damage was present on the entire landscape. If frost damage processes were active in our study site during periglacial times, they may have generated the conduits that could have directly facilitated transport of atmospheric oxygen, water, and soil CO_2 to the depth extent where we observe the changes in mineral surface area production.

2.7 Conclusions

Measuring mineral specific surface area is not currently part of the standard suite of measurements applied in weathering studies, despite its usefulness as a single, easy laboratory measurement that sums the effect of nearly all physical and mineralogical alterations, and its role in mineral dissolution and organic carbon stabilization. By applying this tool to assess the extent of weathering in two 21 m profiles at different landscape positions within an unglaciated schist lithology, we discovered that the morphologic boundaries within weathering profiles, namely the soil-weathered bedrock boundary and the water table, are not the morphologic features where mineral SSA exhibited significant changes. Total SSA, iron oxide SSA, and silicate SSA all exhibited abrupt changes at 3 m depth at both the ridge and interfluve, with no other abrupt change in surface area below. This finding is supported by mineralogy, rock chip densities, and geophysical survey. These findings warn against assuming these morphologic boundaries as critical depths where mineral surface characteristics change. Furthermore, our work shows the utility of mineral SSA measurements in identifying and determining the

initiation depth and extent of chemical weathering, which is more typically estimated through laboratory measurements of mass change of rock forming elements and their associated minerals, to understand critical hydro-biogeochemical fronts within weathering profiles.

The cause of the observed 3-meter interface is conclusively not the result of processes occurring due to the presence of the water table, which has been proposed to control the depth extent of weathering (Rempe and Dietrich, 2014). Decoupling of the water table and chemical weathering processes is surprising but suggests that co-location of the water table and a lower boundary of weathering profiles may not be a norm but instead requires a specific set of geomorphic, geochemical, and hydrological conditions over the course of landscape evolution. An informative venture for future research will be efforts to reconcile how the depths of oxidation (Bazilevskaya et al., 2014; Susan L. Brantley et al., 2013; Buss et al., 2008) and groundwater table (Rempe and Dietrich, 2014) are set by different suites of conditions and what determines their relative contributions to determine the vertical extent of weathering.

Our results demonstrate that greater mineral SSA in the upper 3 meters of the studied weathering profiles is the result of the formation of iron oxide and secondary phyllosilicate minerals. We expected silicate weathering to generate high SSA phyllosilicate minerals and we expected to be able to correlate the emergence of high SSA secondary minerals with the depletion of low SSA primary minerals (such as plagioclase). However, in this highly heterogeneous schist bedrock, the variability of

silicate minerals makes it difficult to observe the mineralogical changes associated with chemical weathering. The contribution of oxide minerals, which are difficult to detect by traditional mineralogical techniques, occur in low abundance but contribute substantial SSA to the weathering system. These ambiguous mineralogical results, combined with the clear indication of weathering presented by SSA results, demonstrate that mineral SSA is a highly sensitive indicator to the combined effects of chemical weathering. Namely, SSA measurements provided a better indication of the depth extent of secondary phyllosilicate and iron oxide mineral formation than classic mineralogical methods (this paper) or geochemical mass balance methods on this variable schist bedrock.

Our data suggest that the penetration depth of the O_2 ventilation front may determine the depth of the chemical weathering front. We propose a coupled system where O_2 promotes weathering of iron from primary minerals then in turn accelerates the silicate weathering engine. We arrive at this conclusion from: (1) the observation of a strong positive correlation between iron oxide SSA and silicate SSA in the upper 3 m (Figure 2.4); (2) the ubiquitous negative correlation of their respective geochemical weathering agents (i.e. O_2 for iron oxides and carbonic acid from elevated pCO_2 for phyllosilicates); (3) the ubiquitous trend of decreasing subsurface gas O_2 with depth to concentrations near zero at the depth where iron oxides appear and reduced iron minerals such as pyrite disappear; and (4) the typical trend of increasing subsurface pCO_2 with depth to concentrations that are typically 1-2 orders of magnitude higher than in the atmosphere. These two dynamic, bioactive gasses are critical controls for chemical

weathering, and we recommend future studies measure subsurface O_2, pCO_2, and SSA as highly useful tools to assess the vertical distribution and mechanisms of chemical weathering in all bedrock environments, including highly heterogeneous bedrock.

At least 60,000 years would be required for the erosion of the upper 3 meters of weathering profiles, where significant production of mineral SSA occurs. Given that this region was under periglacial climate conditions during the last glacial maximum, 20,000 years ago, it is entirely possible that the legacy of periglacial frost damage and colluvial transport have not eroded away and are integral to our observations of the weathering profiles. In fact, we hypothesize that periglacial frost damage down to the present 3 m depth may have created a fracture and macropore network that permitted root growth to those same depths. These large-scale physical and biological mechanisms together controlled the depth of ventilation of atmospheric gases and the depth of O_2 consumption and CO_2 production by root and organic matter respiration. Gas fluxes due to these physical and biological processes will typically dwarf the geochemical sinks of these two bioactive gases. Our data set presents an unexpected case study in the role of climatically originated disturbances and their contribution to the vertical and topographic distributions in mineral SSA.

3 Quantifying weathering on variable rocks, an extension of geochemical mass balance

Submitted on August 31, 2016 to Earth Surface Processes and Landforms as: Manuscript #ESP-16-0228, Quantifying weathering on variable rocks, an extension of geochemical mass balance.

Authors: B. A. Fisher, A. K. Rendahl, A. K. Aufdenkampe, and K. Yoo.

With A. K. Rendahl; UMN—Statistical model and coding; A. K. Aufdenkampe, Stroud Water Research Center—Project Lead PI, field site; and K. Yoo, UMN—Advisor.

3.1 Synopsis

We present a statistical model to assess weathering in deep profiles. The Weathering Trends (WT) model is presented as an extension of the geochemical mass balance model as an open-source R library (statistical model coding and statistical development by Aaron Rendhal https://github.com/AaronRendahl/WeatheringTrends). WT models log-transformed element concentration ratio data as a function of depth to determine the depth extent of weathering for measured elements, and confidence intervals on this depth to bedrock. WT displays the shape of weathering profiles of log-transformed geochemical data to capture the magnitude of changes on a scale proportional to first-order kinetics and thermodynamics. WT estimates average parent

material composition, average composition of the upper weathered zone, and fractional mass change of each element over the entire weathering profile, with confidence limits, with no prior assumptions regarding depth to bedrock. The WT model offers an enhanced opportunity to characterize biogeochemical weathering in heterogeneous rock types. We apply the model to two 21-meter cores from the Laurels Schist bedrock in the Christina River Basin Critical Zone Observatory in the Pennsylvania Piedmont. The Laurels Schist had inconclusive morphological and elemental indicators for the transition from weathering profile to fresh bedrock. The WT model differentiated between rock variability and weathering to delineate the maximum extent of weathering at 12.3 (CI 95% [9.2, 21.3]) meters in Ridge Well 1 and 7.2 (CI 95% [4.3, 13.0]) meters in Interfluve Well 2. The modeled depth to weathering is decoupled from the water table at the ridge, but coincides with the water table at the interfluve. We test statistical approaches to assess variability and correlation of immobile elements to identify the best immobile element for use in both models. We apply the WT model to published data where the geochemical mass balance was applied to demonstrate how the WT model provides additional information about weathering depth and weathering trends.

3.2 Introduction

Among the current frontiers in critical zone science is to delineate not only surficial topography, but also the topography of key geomorphic and hydrologic boundaries in the deep critical zone. The critical zone is the portion of the earth's surface that extends from the top of the vegetation canopy to the deepest limits of actively

cycling groundwater, and includes many functional layers both above and below the ground surface (Brantley et al., 2007b). Surficial topography is known to exhibit control on subsurface boundaries; for example, in the absence of bedrock confinement the groundwater table mimics the topography of the ground surface. Similarly, the boundaries between soil, weathered rock, and fresh bedrock are shaped by processes often driven at the earth's surface and include interactions between hydrology, biology, geomorphology, and geochemistry (Carson and Kirkby, 1972; Fisher et al., n.d.; Heimsath et al., 2009; Rempe and Dietrich, 2014). The spatial relationships between these boundaries are actively studied in interdisciplinary contexts because these boundaries influence erosion rates, organic matter cycling and atmospheric exchange, infiltration rates, primary productivity, and more (Fisher et al., n.d.; Hasenmueller et al., 2015; Parsekian et al., 2015; Rempe and Dietrich, 2014; Richter and Billings, 2015).

Despite the interest to associate the surface topography with subsurface features shaped by coupled earth surface processes, the progress toward this goal is often challenged at its most basic level, determining the depth where biogeochemical alteration of fresh bedrock material begins to occur. The significance of delineating depth to bedrock and providing the associated statistical uncertainties is probably most pronounced in the application of the geochemical mass balance model, which is widely used in quantitatively characterizing rock weathering and pedogenic alteration. The geochemical mass balance approach compares element concentrations of weathering profiles with element concentrations in the underlying fresh bedrock. By additionally

focusing on how element concentrations behave relative to a weathering-resistant element such as zirconium (Zr), the approach allows quantification of the losses or gains of elements due to biogeochemical alteration (Brimhall and Dietrich, 1987; Brimhall et al., 1988).

The success of the geochemical mass balance is highly dependent on our ability to correctly identify the transition from weathered materials to fresh bedrock, which requires characterizing the element concentrations of representative fresh bedrock in each weathering system. The assignment of parent material has a wide range of published methods, often based on logistical constraints to sampling representative unweathered rock, or parent material, at each study site. The parent material parameter may come from samples that were found at the bottom of a soil pit (Chadwick et al., 1990; Yoo et al., 2015), from a nearby outcrop or quarry exposure (Oh and Richter, 2005; Riebe et al., 2003), or from a drill core (Anderson et al., 2002; Jin et al., 2010). Parent material may be represented by the average concentration of a set of samples (Anderson et al., 2002; Jin et al., 2010). Assigning parent material composition is particularly challenging for variable bedrock, such as commonly found in sedimentary and metasedimentary lithologies, and such lithologies with expected high variability cover more than 90% of continental landmasses (Blatt and Jones, 1975; Suchet et al., 2003).

Here we present the statistically-based Weathering Trends (WT) model to address several of the needs of the deep critical zone community. In this model, weathering is defined as a set of processes that alter element concentrations and their ratios during the

transition of unweathered, fresh bedrock, through weathered rock to soil. The WT model extends the geochemical mass balance model by applying statistical approaches to evaluate changes in elemental ratios as a function of depth. WT offers robust identification of depth to unweathered bedrock, averages and confidence limits for geochemical composition of parent material, objective determination of the best immobile elements for use with geochemical mass balance, and a clear assessment and display of weathering trends in element data on a scale that is proportional to first-order geochemical kinetics and thermodynamics. The statistical method allows WT to differentiate between geochemical heterogeneity and weathering alteration. In addition to facilitating the clear identification of the depth to fresh bedrock, WT addresses the need to delineate other subsurface boundaries by differentiating a near-surface zone that is affected by soil formation processes such as mixing and enrichments from litter, fertilizer and atmospheric deposition, and by modeling the shape of the deeper weathering profile for each element over multiple orders of magnitude. WT thus facilitates assessment of subtleties in biogeochemical and weathering processes, identification of abrupt or gradual transitions, and indication of significant biogeochemical trends of increase, decrease, variability, and stability.

3.3 Weathering Trends statistical model

3.3.1 Geochemical mass balance model

The Weathering Trends (WT) model is derived from the geochemical mass balance model, so we briefly introduce its foundation and the formulation of the

fractional mass change, tau (τ) (Brimhall and Dietrich, 1987; Brimhall et al., 1988; Chadwick et al., 1990). In weathering systems the geochemical mass balance model compares the ratios of elements between weathered materials and fresh bedrock and quantifies the fractional mass change for each mobile element between these two materials. As mobile elements are removed from a weathering system, residual immobile elements exhibit an increase in concentration relative to the whole weathered rock. Thus the most meaningful way of assessing the variation of elements and the magnitude of their compositional changes is to assess the value of one element relative another, in ratio form (Aitchison and J. Egozcue, 2005; Buccianti, 2011).

Application of fractional mass change calculations to whole weathering profiles requires the knowledge of the boundary between weathered and fresh rock materials. The mass balance model also assumes that the parent material is geochemically homogeneous prior to enrichment or depletion and the immobile element must be resistant to removal by biogeochemical dissolution, leaching, or physical mobility (Brimhall and Dietrich, 1987; Brimhall et al., 1988). Unfortunately, these criteria are problematic to satisfy for many non-plutonic rocks, yet the intrusive igneous complexes that are most likely to be geochemically homogeneous comprise only 9% of rocks exposed on the continents (Blatt and Jones, 1975; Suchet et al., 2003). However, even igneous rocks can offer substantial geochemical heterogeneity such that implementation and interpretation of the geochemical mass balance approach can be compromised (Heimsath and Burke, 2013). Our new statistical model serves as an extension of the geochemical mass balance model

to provide methods to rigorously identify the depth to fresh bedrock and assess immobile element variability.

The mass balance model assumes that the mass of each element (j) in the unweathered parent material (p) is conserved such that any material that is removed can be accounted for (*flux*, where removal is <0 and enrichment is >0 according to the formulation by Chadwick et al. (1990) by comparing weathered material (w) with parent material as shown:

Equation 3.1 $$m_{j,p} + m_{j,flux} = m_{j,w}$$

The mass (m [grams]) of a mobile element (j) can be assessed as the product of the volume (V [cm^3]), the bulk density (ρ [g cm^{-3}]), and the concentration of the element (c_j [ppm or weight percent]). Thus for any given volume of weathered material, the mass balance for mobile elements can be formulated as:

Equation 3.2 $$V_p \rho_p c_{j,p} + m_{j,flux} = V_w \rho_w c_{j,w}$$

The mass balance for immobile elements (i) is:

Equation 3.3 $$V_p \rho_p c_{i,p} = V_w \rho_w c_{i,w}$$

The two unknown and unmeasurable properties in the mass balance for mobile and immobile elements are the original volume of the parent material (V_p) and the total mass of each element that is lost or gained since the initiation of weathering ($m_{j,flux}$). However, we can quantify the fractional mass change of any element ($m_{j,flux}/m_{j,p}$), which is referred to as tau ($\tau_{j,w}$), by combining Equation 3.2 and 3 and rearranging to the form as shown:

Equation 3.4 $$\tau_{j,w} = \frac{m_{j,flux}}{m_{j,p}} = \left(\frac{c_{j,w}}{c_{j,p}} / \frac{c_{i,w}}{c_{i,p}} \right) - 1$$

where $-1 \leq \tau_{j,w} < 0$ represents net elemental loss, or depletion, of the material relative to the parent whereas $0 < \tau_{j,w} < \infty$ represents net elemental gain, or enrichment. Evaluation of tau values has become a ubiquitous tool in the biogeochemical weathering literature in the decades since it was introduced.

Geochemical reactions, however, do not naturally follow patterns that are proportional to fractional mass change as represented by tau, but rather naturally follow patterns that are proportional to the logarithm of the reactant concentration or to the log of a concentration ratio (Buccianti, 2011; Miesch and Chapman, 1977). For example, the thermodynamic chemical potential of a reaction (μ) is proportional to the natural log of the reactant concentration (i.e. $\mu = \mu^{\circ} + RT\,lnC$, where R is the universal gas constant and T the temperature). Therefore, all thermodynamic equilibrium diagrams represent reactant concentrations, or activities, on a log scale (Stumm and Morgan, 1996). Similarly, the first-order chemical rate law, where $dC/dt = kC$, integrates to $\ln C = -kt + \ln C_0$, where a plot of $\ln C$ as a function of time, t, gives a straight line with a slope of $-k$. These natural laws of chemistry lead to log-normal distributions geochemical concentrations that span many orders of magnitude in nature and to geochemical processes that are proportional to concentrations only when viewed on a log scale.

The result of these natural laws of geochemistry is that concentration values and their derivatives such as tau typically have skewed distributions when evaluated on a linear scale, which can constrain biogeochemical interpretation and statistical evaluation

of the trends exhibited in weathering systems. Enrichment values can mathematically extend to infinity, with published tau values of Ca enrichment in lime amended soil extending to $\tau_{j,w}$ >25 (Yoo et al., 2015). Elemental depletion produces a numerically different change in tau because half of element *j* removed (a 2x removal) is $\tau_{j,w}$ = -0.5, and 10x removal is $\tau_{j,w}$ = -0.90, etc. Since chemical depletion commonly spans several orders of magnitude (Oh and Richter, 2005), observed values of tau typically exhibit skewed distributions of tau values that complicate the evaluation of depletion trends.

3.3.2 Features of the Weathering Trends statistical model

The extensive presence of geochemically variable bedrock presents the deep critical zone community with an immense need to objectively distinguish between variability and weathering. Geochemical element concentrations are naturally skewed in every form that we use in studies of bedrock weathering, including raw concentrations, concentration ratios, and tau values. For WT model assessment we log transform concentration ratio data to generate a normal distribution for statistical analysis, which in turn enables us to distinguish elemental depletion from geochemical variability in order to identify the depths where weathering transitions occur. This ability to detect the depth to weathering transitions and to delineate subsurface topographies directly addresses one of the identified research frontiers in critical zone science.

We derive WT from tau by a slight rearrangement of Equation 3.4 into:

Equation 3.5 $$\tau_{j,w} = \left(\frac{c_{j,w}}{c_{i,w}} / \frac{c_{j,p}}{c_{i,p}} \right) - 1,$$

which we log transform into:

Equation 3.6 $$\log(\tau_{j,\tilde{w}}) = \log\left(\frac{c_{j,w}}{c_{i,w}} / \frac{c_{j,p}}{c_{i,p}}\right) - \log(1) = \log\left(\frac{c_{j,w}}{c_{i,w}}\right) - \log\left(\frac{c_{j,p}}{c_{i,p}}\right)$$

We recognize that the weathered material element ratio ($c_{j,w}/c_{i,w}$) is the only depth dependent term in tau and that the element ratio of parent material ($c_{j,p}/c_{i,p}$) is set as a constant value throughout a profile (Equation 3.5). We also recognize that although the tau formulation designates $c_{j,w}/c_{i,w}$ as the weathered element ratio, typical practice is to apply the calculation for all depth intervals, including those within the designated parent material. We proceed by making no prior assumptions about whether material is weathered or not, so we remove the subscript (w) and we apply a generic notation for the element ratio as c_j/c_i. The WT model thus evaluates $\log(c_j/c_i)$ as the dependent variable, y, as a function of depth as the independent variable, x, over the entire measured depth profile with no assumptions or parameter required regarding depth to bedrock. The WT model expects a three-layer weathering system with an upper weathering zone, weathered profile, and fresh bedrock.

3.3.3 Weathering Trends model calculation

The Weathering Trends (WT) model calculates six parameters (d, fd, r, c, s_1, and s_2) identified in Figure 3.1 by fitting Equation 3.7-9, below, to the observed data. The model fits a constant fit in the upper weathering zone ($x < fd$) and in the fresh bedrock zone ($x \geq d$), and a linear fit on the ratio scale for the weathered profile ($fd \leq x < d$), converted here to the log scale, as defined by Equation 3.8. The model assumes a normal distribution of the log of the element concentration ratio around this mean function. As defined by Equation 3.7, the error of i'th data point (ϵ_i) is random and normally

distributed with mean of 0 and a variance described by the function $s^2(x_i)$. The function $s(x_i)$ gives the standard deviation at depth x_i, which is modeled as constant for $x < fd$ and $x \geq d$, and linear for $fd \leq x < d$, as described by Equation 3.9.

Equation 3.7 $$\log(y_i) = m(x_i) + \epsilon_i, \text{where } \epsilon_i \sim N(0, s^2(x_i))$$

Equation 3.8 $$m(x) = \begin{cases} r - c, \text{for } x < fd \\ \log\left(10^r - (10^r - 10^{r-c})\frac{d-x}{d-fd}\right), \text{for } fd \leq x < d \\ r, \text{for } x \geq d \end{cases}$$

Equation 3.9 $$s(x) = \begin{cases} s_1, \text{for } x < fd \\ s_2 - (s_2 - s_1)\frac{d-x}{d-fd}, \text{for } fd \leq x < d \\ s_2, \text{for } x \geq d \end{cases}$$

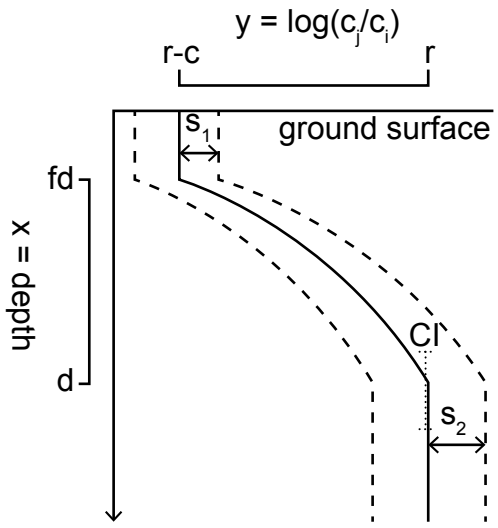

Figure 3.1. The Weathering Trends (WT) model evaluates depth profiles in element concentrations by fitting a piecewise, least-squares regression of the log of an element ratio as a function of the independent variable, depth (x = depth), using three different functions for three different weathering depth zones (Equation 3.7-9). We present the graphical representation in the form of a depletion profile, as an example, with depth plotted vertically and the ground surface (depth = 0) at the top. The solid line is the modeled mean of the element ratio as a function of depth, and the dashed lines are standard deviations of those means. *CI* is the confidence interval

of depth to unweathered bedrock, *d*, indicated by dotted lines. Below are the six parameters that are statistically modeled from observed data.

- *x=d* is the depth of the deepest extent of weathering, or the depth to fresh bedrock.

- *x=fd* is the depth extent of the uppermost weathering zone, where *f* is a fraction of *d*. This boundary may detect a constant concentration value, or an enrichment trend, but most importantly it marks a change from the weathering pattern modeled above depth *d*. Depth *fd* parameter may occur at or near the ground surface.

- $y = \log(c_{j,\tilde{p}}/c_{i,\tilde{p}}) = r$ is the mean log ratio of the mobile to immobile elements for the model identified fresh bedrock, which is where the model finds a mean at depth x ≥ d, and we designate this parent material profile as $\tilde{p}$.

- $y = \log(c_{j,\tilde{u}}/c_{i,\tilde{u}}) = r - c$ is the mean log ratio of the mobile to immobile elements within the upper weathering zone (0 < x < fd). $\log(c_{j,\tilde{u}}/c_{i,\tilde{u}})$ is modeled as a linear constant over this interval, regardless of the shape of the element ratio profile to remain nonspecific to processes in this zone, and we designate this upper profile as $\tilde{u}$.

- s_1 and s_2 are the standard deviations of $log(c_j/c_i)$ around *r-c* and *r*, respectively.

The motivation for the log-ratio approach to WT is not only rooted in the natural laws of geochemistry, but also in common statistical practice. All statistical approaches used by WT are parametric and thus assume a normal distribution. The skewed distributions of our c_j/c_i ratios required log-transformation to meet this requirement. The WT model package also plots data on a log scale such that trends in weathering in $\log(c_j/c_i)$ are proportional to thermodynamic and kinetic processes. The need for log

transformation is supported as a routine convention in geochemical calculations and visualizations, with abundant examples such as log notation, including pH, equilibrium constants, and activity diagrams (Buccianti, 2011; Stanley, 2006; Stumm and Morgan, 1996). For elements that have reported concentrations of zero, the best approach is to state the analytical detection limit, because log of zero values is computationally undefined and it is chemically accurate to report the detection limit rather than assigning a zero value.

The WT model fits a piecewise regression of $\log(c_j/c_i)$ as the dependent variable (labeled y) and depth as the independent variable (labeled x) using three different functions for three different weathering zones (Figure 3.1 and Equation 3.7-9). The deepest zone fits a constant element concentration ratio because we expect fresh bedrock to exhibit minimal variability. The middle zone tracks changes in concentration ratio with depth above fresh bedrock. The WT model allows for enrichment or depletion in the middle zone, but for the present discussion we address the cases where the element concentrations relative to an immobile element decrease due to dissolution and leaching and we term the middle zone the weathered profile. The uppermost zone begins at the depth where the concentration ratio changes in the weathering profile end. Multiple biogeochemical processes can produce similar profile shapes in this zone, which we discuss below. To handle the wide range of possible patterns WT model simplifies the upper zone as the mean of the log element ratio for all depths above the weathered profile. Despite model simplification for the upper zone, log form enables a clear data

display over multiple orders of magnitude of concentration change.

The model parameters *r* and *r-c* are log transformed element concentration ratios and we can use these concentration ratios to estimate a profile mean tau, which is the fractional mass change of the upper weathering zone ($\tau_{j,\tilde{u}}$, for all depths $0 < x < fd$) relative to the model identified parent material ($\tilde{p}$, for all depths $\geq d$). To illustrate the connection we restructure Equation 3.4 as

Equation 3.10 $\tau_{j,w} = \left(\frac{c_{j,w}}{c_{i,w}} / \frac{c_{j,p}}{c_{i,p}} \right) - 1,$

and substitute the WT profile estimates, $\log(c_{j,\tilde{u}}/c_{i,\tilde{u}}) = r - c$ and $\log(c_{j,\tilde{p}}/c_{i,\tilde{p}}) = r$, as

Equation 3.11 $\log(\tau_{j,\tilde{u}}) = \log\left(\frac{c_{j,\tilde{u}}}{c_{i,\tilde{u}}} / \frac{c_{j,\tilde{p}}}{c_{i,\tilde{p}}}\right) - \log(1) = (\mathrm{r} - \mathrm{c}) - \mathrm{r} - \log(1)$

Equation 3.11 reveals that the *WT profile tau* ($\tau_{j,\tilde{u}}$) can be estimated from parameter *c*. The WT estimated profile mean tau is an estimate of the fractional mass change between the mean parent material and upper weathering zone, which in many cases will represent the maximum tau of the profile.

Equation 3.12 $\tau_{j,\tilde{u}} = 10^{-c} - 1$

Both models present the ratio of concentration of elements from the weathered profile and the additional parameter in the geochemical mass balance beyond the ratio of mobile to immobile element, namely the parent material concentration, is constant for all intervals. Tau plots provide an indication of the degree of enrichment or depletion of an element relative to the bedrock for every interval, and as shown in Equation 3.10-

Equation 3.12, an estimated profile mean tau can be calculated from the WT model parameters. We see the log transformation in WT as a beneficial not only as essential for statistical analysis (by creating a log normal distribution), but as a beneficial means to view changes in concentration (and concentration ratios) that are proportional to changes in chemical reaction rates or thermodynamics.

3.3.3.1 Fresh bedrock ($x \geq d$):

If a weathering system has fresh, unweathered bedrock at depth, the WT model will detect this by finding a consistent range of element concentrations. In other words, the depth below which element ratios do not show a statistically significant trend with depth is considered the depth to fresh bedrock. The model uses the least-squares piece-wise linear regression to calculate the mean concentration for fresh bedrock, represented in Figure 1 by the solid vertical line below depth *d*. The mean of the dependent variable at depth *d* is called *r*, where *r* is the mean log ratio of concentrations of a mobile element to an immobile element below depth *d*. Thus the maximum depth extent of weathering or the depth to fresh bedrock occurs at the coordinates (*d, r*). The standard deviation of the data ($\log(c_{j,\tilde{p}}/c_{i,\tilde{p}})$) around the mean for the value of *r* is defined as s_2 and represented by dashed lines in Figure 3.1.

Given the significance of delineating the vertical extent of chemical weathering, it is important to quantify the range of possible model-derived depths to bedrock (*d* in Figure 3.1), the confidence interval. We first quantify the modeled parameters (*d*, *fd*, *r*, *r-c*, s_1, and s_2) using a best fit regression from the observed data by minimizing the least

squares.

Because of the piece-wise and non-differentiable nature of our model, the confidence interval for *d* is asymmetrical, so we calculate it using the profile likelihood instead of the more common Wald method of calculating plus/minus a multiple of the standard error. This method directly evaluates the highest likelihood of observing our data for each value of *d*, and chooses values to be in the confidence interval that have likelihoods close to the likelihood at the best value of *d*.

3.3.3.2 Weathered profile ($fd \leq x < d$):

At depths shallower than *d*, the weathered profile is represented as a least squares regression of the log ratio of concentrations ($\log(c_j/c_i)$) ranging from fresh bedrock at *r* to the maximum extent of weathering at *r-c*. WT models the regression trend for this zone of concentration change by removal (or enrichment) as linear on the ratio scale, though we present the concentration values on the log scale, as described earlier. We have found this linear form to match our data well; other functional forms could be explored in the future as needed. Our plots show plus/minus one standard deviation for the best fit regression line between *r* and *r-c* as a dashed line (Figure 3.1). The upper extent of the weathered profile occurs at coordinates (*fd, r-c*), and estimates the extent of depletion (or enrichment).

3.3.3.3 Upper weathering zone ($0 < x < fd$):

We define the bottom boundary of the upper weathering zone as the point where the zone of concentration change in the weathered profile (1) changes to a constant log

ratio, (2) begins changing in the opposite direction, or (3) reaches the ground surface. When any of these changes occur, the WT model fits the mean of all values above depth *fd* and reports this mean as $\log(c_{j,\tilde{u}}/c_{i,\tilde{u}}) = r - c$ with standard deviation s_1. In the absence of a linear fit above *fd*, the model will plot the weathering profile extending to very near the ground surface. Multiple processes may occur in the upper zone due to influence from surface biogeochemical and atmospheric processes, and we chose to model the upper zone as a linear constant, regardless of the shape of the element ratio profile, to remain non-specific to processes. Future versions of the WT model may choose to fit a variety of different shaped functions to data in this upper zone.

The three different trends in the upper weathering zone represent common processes. Stable elemental concentrations at shallow depths can result from extensive physical mixing by bioturbation or tillage, or possibly from reaching the analytical detection limits for the given element. When element ratio profiles exhibit concentration increases near the ground surface, this result may represent multiple processes, including aeolian inputs (Brimhall et al., 1988; Reynolds et al., 2001), atmospheric dust (Vitousek et al., 1997) or contaminant deposition (Herndon et al., 2011), anthropogenic soil amendments (Yoo et al., 2015), biological nutrient recycling (Hinsinger, 2001), or other allochthonous material. An absence of mixing and a surface source would result in the weathering profile extending to the surface (i.e. *fd* = 0). Proper interpretation of near-surface processes requires a full biogeochemical investigation, and for the upper weathering zone the WT model only seeks to identify the lower boundary of this zone

and display the element ratio data.

3.4 Methods

3.4.1 Site

The Spring Brook watershed, within the Laurels Nature Preserve managed by the Brandywine Conservancy, is the only watershed in the Christina River Basin Critical Zone Observatory (CRB-CZO) that is 100% covered by mature forest. Spring Brook (Figure 3.2) is a first order, 0.096 km^2 catchment, located in southeastern Pennsylvania and within the CRB-CZO. The second growth mixed chestnut, oak, and hickory forest is approximately 120-150 years in age. Spring Brook has soil mantled hillslopes underlain by the Laurels Schist bedrock, a foliated silvery gray-green quartz-plagioclase-muscovite-chlorite-garnet schist with minor biotite (mostly retrograded to chlorite) with accessory magnetite, epidote, tourmaline, apatite, and zircon (Blackmer, 2004) that we analyzed for weathering using two 21-meter deep drill cores. We also sampled a transect of hillslope soil pits that will not be the focus of the present discussion (Fisher et al., n.d.).

The climate in Spring Brook is Humid Continental with mean annual precipitation (MAP) of 1246 mm and a mean annual temperature (MAT) of 10.85°C, which ranges annually from -6 to 29°C (1961-1990, Coatesville, PA www.usclimatedata.com). Paleoclimate records based on pollen type from 18,000-12,000 ybp estimate annual lows of -12°C and highs of 16°C in the region, which was experiencing periglacial conditions until the Laurentide ice sheet began to retreat. By 9,000 ybp the temperatures were -4 to

22°C, with a gradual shift to present day temperature ranges (Prentice et al., 1991).

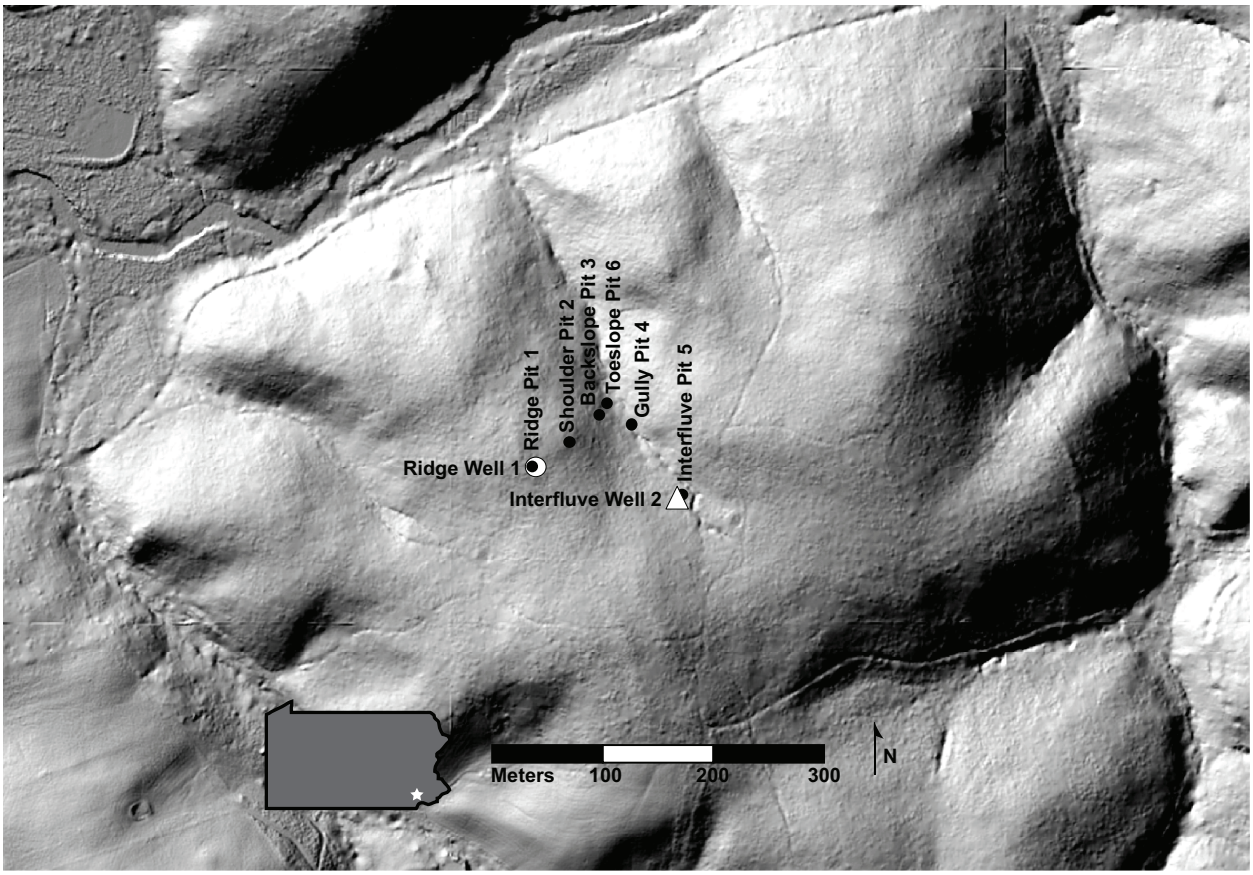

Figure 3.2. Site map of the Spring Brook watershed in the the Laurels Preserve in southeastern, Pennsylvania. In addition to Ridge Well 1 and Interfluve Well 2, we sampled a transect of soil pits to characterize the influence of landscape position on SSA and other biogeochemical properties.

3.4.2 Rotosonic drilling

We sampled two 21-meter deep boreholes at the ridge (Well 1, 143.886 MASL; 39.9195025°, -075.7891562°) and interfluve (Well 2, 134.164 MASL; 39.9194885°, -075.7879179°) using a Geoprobe Rotosonic (model 8140LC) mid-sized track-mounted drilling rig. The drilling method employed was the "4x6" method, which creates a borehole using two hollow bits that yield a 4-inch (10.16 cm) sample diameter and a 6-

inch (15.24 cm) borehole diameter. Most upper sample intervals were drilled with air, while deeper intervals were drilled using EZ-MUD® Polymer Emulsion (by Baroid IDP) to enable drilling to proceed in a timely manner. The drill segments were 152 cm long and were inserted into a plastic sleeve immediately after recovery. While the cores were partially pulverized by the Rotosonic drilling action and broken, the recovered volumes were 68-100% for core segments drilled without fluid. Where EZ-MUD fluid was used, the recoveries ranged from 17-83%. In the lab the cores were opened and photographed and divided into intervals of approximately 10 cm. Samples were oven dried at 60°C, sieved to 2 mm where applicable, and weighed. The drilled wells were maintained with flexible liners (FLUTe™ Blank liners) that can be removed for measurements and future installations. The absence of replicates or denser drilling schemes reflect the challenge in coordinating drilling operation in remote, densely forested, rugged topography.

3.4.3 Elemental analysis

Samples were pulverized on a tungsten carbide ring mill to 6 μm (D_{90}). Elements were analyzed using a Bruker Analytical SRS3000 sequential XRF (at University of Wisconsin-Eau Claire) with major elements measured following fusion in lithium borate and minor elements measured on pucks formed under pressure in a mixture of rock powder with SpectroBlend powder (81.0% C, 2.9% O, 13.5% H, 2.6% N).

3.5 Results and Discussion

3.5.1 Element profiles

The WT model outputs a matrix of element log ratio depth profile plots of all

input mobile elements relative to all chosen immobile elements (Figure 3.3 shows a subset of the plots that are available for each well, which are available in Supplement ##). For each possible combination of mobile/immobile element, WT also outputs tabulated values for all six model parameters and the confidence limits on the depth to unweathered bedrock, *d* (Table 3.1). As shown in the model introduction, WT and tau are derived from the same formulation of elemental data, and as such we compare WT model plots (Figure 3.3) to tau plots for mobile elements Ca, Na, P, Al, Fe, and Si relative to immobile elements Nb and Zr (Figure 3.4) to delineate the cooperative strengths of each model.

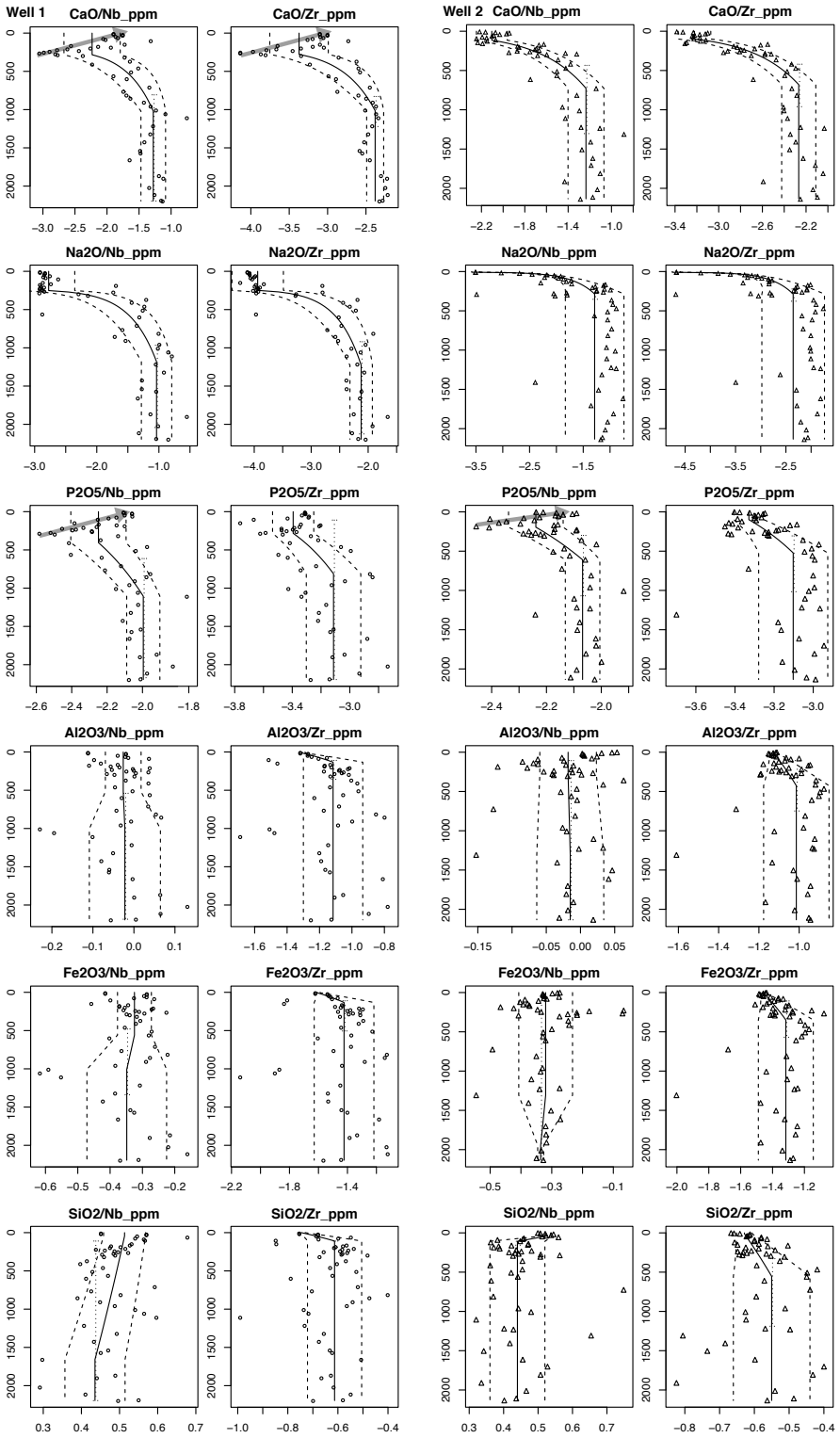
Well 1
CaO/Nb_ppm
CaO/Zr_ppm
Well 2 CaO/Nb_ppm
CaO/Zr_ppm
Na2O/Nb_ppm
Na2O/Zr_ppm
Na2O/Nb_ppm
Na2O/Zr_ppm
P2O5/Nb_ppm
P2O5/Zr_ppm
P2O5/Nb_ppm
P2O5/Zr_ppm
Al2O3/Nb_ppm
Al2O3/Zr_ppm
Al2O3/Nb_ppm
Al2O3/Zr_ppm
Fe2O3/Nb_ppm
Fe2O3/Zr_ppm
Fe2O3/Nb_ppm
Fe2O3/Zr_ppm
SiO2/Nb_ppm
SiO2/Zr_ppm
SiO2/Nb_ppm
SiO2/Zr_ppm

Figure 3.3. Matrix plot of the Weathering Trends model applied to Ca, Na, P, Al, Fe, and Si verses Nb and Zr in both wells, a subset of the full WT model output. For the Laurels Schist samples, Ca and Na exhibited the deepest weathering profiles and thus revealed the maximum depth of weathering influence. Ca and P exhibit enrichment above depth *fd* in profiles marked with gray arrows. Well 2 Na2O had depth *fd* occurring very near the ground surface with no near-surface change in the weathering trend, suggesting that Na has not been completely removed from weatherable minerals in this profile. We note that the depth of influence of weathering (depth *d*) is shallower for Well 2 than Well 1 for Ca, Na, and P. WT profiles for Al, Fe, and Si indicate low mobility of these elements with minimal enrichment or depletion indicated by nearly vertical weathering trends profiles and wide confidence intervals. Solid and dashed lines are least squares regressions and their standard deviations, respectively, as a function of depth following the piecewise model parameterizations in Equation 3.7-9. Confidence intervals on depth *d* are shown with dotted lines. Vertical axes are depth (cm) and the horizontal axes are the log10 of the ratio of elements labeled at the top of each graph. Numerical outputs for these plots are found in Table 3.1.

Table 3.1. Numerical output of six model parameters and confidence intervals for plots in Figure 3.3, a subset of the full WT model outputs. The “lower” and “upper” columns comprise the confidence interval for the estimates of depth to unweathered bedrock for both wells.

mobile	immobile	fd (cm)	d (cm)	CI lower	CI upper	r-c	r	s1	s2
Well 1									
CaO	Zr_ppm	279	1015	828	1221	-3.3719	-2.3803	0.3811	0.1108
CaO	Nb_ppm	283	1020	807	2195	-2.2325	-1.2782	0.4392	0.1920
Na2O	Zr_ppm	249	1227	920	2126	-3.9393	-2.1229	0.4515	0.1965
Na2O	Nb_ppm	251	1182	967	2042	-2.7744	-1.0380	0.4199	0.2442
P2O5	Zr_ppm	283	813	110	2195	-3.3936	-3.1130	0.1432	0.1894
P2O5	Nb_ppm	405	1105	613	2171	-2.2489	-1.9954	0.1562	0.0938
Al2O3	Zr_ppm	14	133	110	357	-1.3071	-1.1165	0.0181	0.1830
Al2O3	Nb_ppm	519	1005	539	2186	-0.0261	-0.0221	0.0435	0.0866
Fe2O3	Zr_ppm	6	133	110	505	-1.6090	-1.4234	0.0201	0.2059
Fe2O3	Nb_ppm	559	1007	480	1340	-0.3247	-0.3485	0.0524	0.1233
SiO2	Zr_ppm	0	110	110	189	-0.7456	-0.6133	0.0146	0.1082
SiO2	Nb_ppm	44	1657	110	2195	0.5131	0.4356	0.0549	0.0788

Well 2									
CaO	Zr_ppm	99	680	420	960	-3.2219	-2.2670	0.1495	0.1562
CaO	Nb_ppm	114	727	434	1304	-2.1047	-1.2354	0.1418	0.1657
Na2O	Zr_ppm	9	287	221	378	-4.6786	-2.3558	0.0781	0.6214
Na2O	Nb_ppm	9	285	209	353	-3.5078	-1.2869	0.0722	0.5465
P2O5	Zr_ppm	99	523	305	1016	-3.3290	-3.1023	0.0764	0.1766
P2O5	Nb_ppm	195	610	299	1069	-2.2387	-2.0682	0.0996	0.0630
Al2O3	Zr_ppm	0	426	107	748	-1.1291	-1.0141	0.0149	0.1625
Al2O3	Nb_ppm	285	1307	107	2134	-0.0181	-0.0149	0.0413	0.0489
Fe2O3	Zr_ppm	0	350	107	569	-1.4606	-1.3167	0.0143	0.1724
Fe2O3	Nb_ppm	1308	1945	107	2134	-0.3198	-0.3360	0.0873	0.0096
SiO2	Zr_ppm	12	554	329	1189	-0.6286	-0.5502	0.0225	0.1101
SiO2	Nb_ppm	44	107	107	157	0.5206	0.4401	0.0163	0.0798

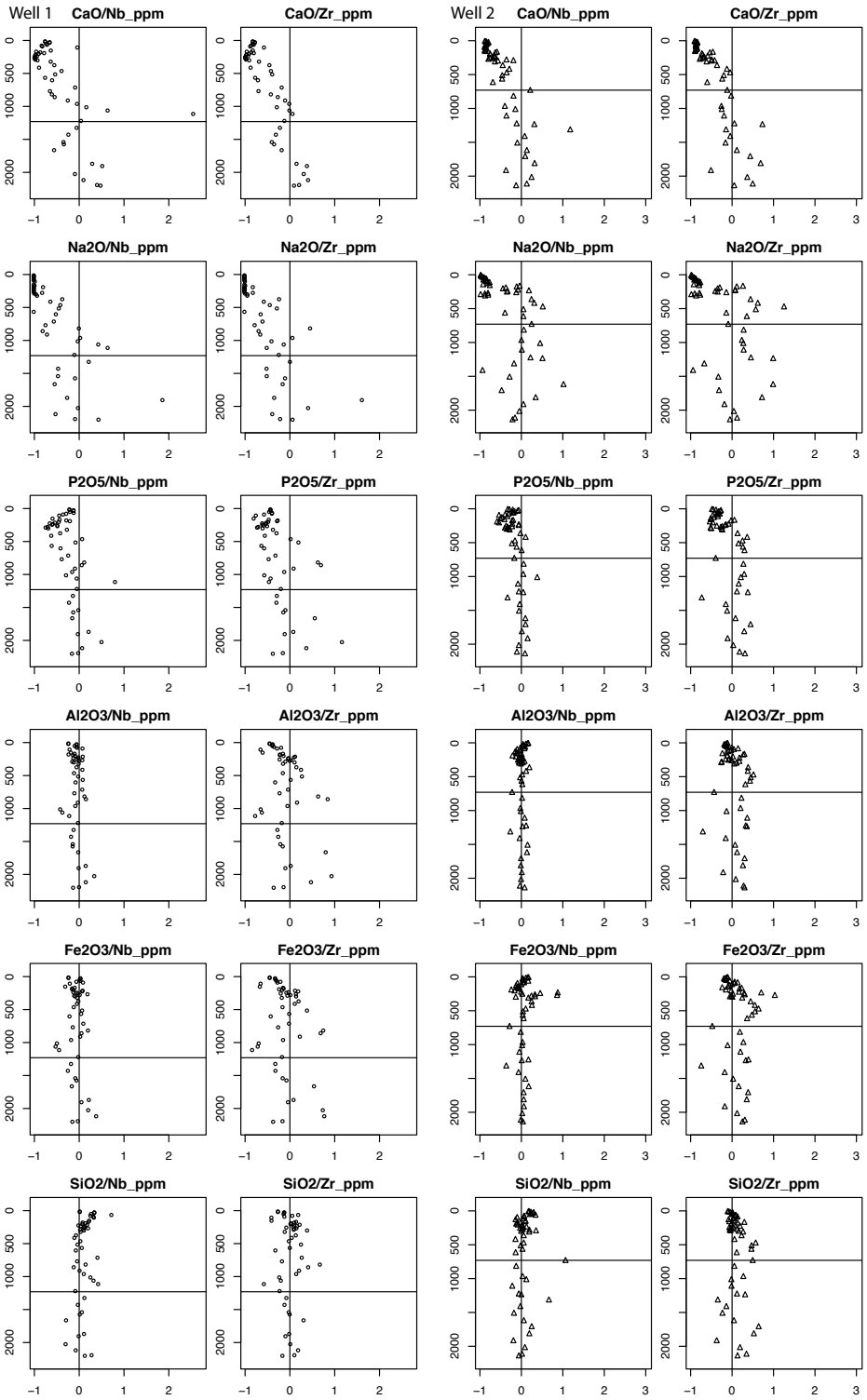
Well 1
CaO/Nb_ppm
CaO/Zr_ppm
Well 2
CaO/Nb_ppm
CaO/Zr_ppm
Na2O/Nb_ppm
Na2O/Zr_ppm
Na2O/Nb_ppm
Na2O/Zr_ppm
P2O5/Nb_ppm
P2O5/Zr_ppm
P2O5/Nb_ppm
P2O5/Zr_ppm
Al2O3/Nb_ppm
Al2O3/Zr_ppm
Al2O3/Nb_ppm
Al2O3/Zr_ppm
Fe2O3/Nb_ppm
Fe2O3/Zr_ppm
Fe2O3/Nb_ppm
Fe2O3/Zr_ppm
SiO2/Nb_ppm
SiO2/Zr_ppm
SiO2/Nb_ppm
SiO2/Zr_ppm

Figure 3.4. Fractional mass change (tau) plots of Ca, Na, P, Al, Fe, Si for Ridge Well 1 and Interfluve Well 2 showing both Nb and Zr as immobile elements. Vertical line represents parent material, which is the average of all concentration values below the horizontal line for each plot, which are the maximum depth of weathering for Ca and Na as estimated using the WT model (12.3 m in Well 1 and 7.2 m in Well 2). Horizontal scales are the same for all plots for each well. Al, Fe, and Si demonstrate that using Zr as the immobile element in this weathering system results in more variability in the range of tau values than Nb.

3.5.2 Lower depth of weathering profile (d) and depth to fresh bedrock

Examination of all of the element profiles identified that the deepest extent of chemical removal occurs in the Na and Ca profiles (Figure 3.3, Table 3.1), which are known to be highly mobile elements. We thus chose the depth of Na and Ca removal as the most conservative estimate for the depth to fresh bedrock for the selection of parent material for the geochemical mass balance. In Ridge Well 1 the deepest extent of weathering is indicated by Na and occurs at 12.3 (CI 95% [9.2, 21.3]) m. For Interfluve Well 2 the deepest influence of weathering is indicated by Ca and occurs at 7.2 (CI 95% [4.3, 13.0]) m deep.

Prior to the development of the WT model, we were challenged to determine the depth to bedrock for the Laurels Schist using mineralogy, geophysical measurements, rock chip density, inspection of hand samples, or plots of element concentrations. The data indicated some weathering trends but identification of the depth to fresh bedrock was difficult to distinguish from geochemical variability. For example, based on the tau plots for Ridge Well 1 Ca (Figure 3.4), bedrock could be identified as the cluster below 18 meters, or it could be assigned at 10 meters, where the tau values begin a depletion

trend to the ground surface. We had no objective method for choosing between these apparent geochemical transitions.

Using the WT model we found clear definition of the depth to bedrock by statistically differentiating between oscillatory variability and changes due to weathering to find the maximum depth extent of removal of each element, with confidence intervals on these depths. For use in the geochemical mass balance model (Figure 3.4), we used the WT model derived depths and calculated the mean of all element concentrations below this depth as the assignment of parent material ($c_{j,\tilde{p}}/c_{i,\tilde{p}}$).

Comparison of depth *d* in the WT model of Ridge Well 1 and Interfluve Well 2 identified that the ridge is more deeply weathered than the interfluve, a lower landscape position, which is a significant result for understanding catchment scale weathering processes. This downslope thinning of the weathered profile is supported by model and empirical expectations (West 2013; Pavich, 1989; Rempe and Dietrich, 2014). We also observe that the depth of Na removal is deeper than the depth of Ca removal at the ridge, but the opposite is true at the interfluve, which suggests different weathering dynamics at these two landscape positions.

Current research on weathering offers that the depth of the groundwater table coincides with the lower boundary of weathering, proposing groundwater equilibrium with bedrock and the penetration of acidity into the formation exhausting at the groundwater table as possible mechanisms for termination of weathering (S. L. Brantley et al., 2013; Rempe and Dietrich, 2014). The Laurels Schist at our study site has deep

groundwater tables that over 12 months in 2014 ranged from 17.7-20.3 meters below the ground surface at Ridge Well 1 and from 6.8-8.3 meters at Interfluve Well 2 (measured using Solinst LevelLogger Edge pressure transducers with post atmospheric correction). The deepest extent of weathering (depth *d*) according to WT statistical analysis of elements appears to coincide with the water table at Interfluve Well 2, but removal of Ca and Na does not appear to extend as deep as the water table at Ridge Well 1. However, in all cases the confidence interval on depth *d* encompasses the water table elevation range.

3.5.3 Features in the weathered profile

WT modeled profiles for Ca, Na, and P display distinct depletion profiles. For WT profiles like those for Na in Ridge Well 1 and Interfluve Well 2, the parameter *r-c* represents a reasonable mean for the concentration ratios at the maximum extent of depletion. Regardless of profile shape, WT profiles do not indicate the extent of chemical depletion. For the type of weathered profiles exhibited by Na, where the upper weathering zone does not deviate beyond *r-c*, the WT estimated profile mean tau (Equation 3.12) quantifies the extent of depletion. The WT weathered profiles for Na exhibit two different shapes, with the profile in Interfluve Well 2 terminating at the ground surface, and the profile in Ridge Well 1 reaching a constant ratio around 2.5 m. We calculate $\tau_{j,\mathrm{w}}$ = -0.98 for Ridge Well 1 and $\tau_{j,\mathrm{w}}$ = -0.99 for Interfluve Well 2, indicating complete removal of Na for both of these profiles, despite the difference in the weathered profile shape.

In contrast, the maximum extent of the weathered profile is not well represented

by *r*-*c* for WT profiles of Ca or P, where the upper weathering zone has a large spread of concentration ratios. For weathered profiles with this shape, WT model effectively finds the depth where the weathered profile transitions to the upper weathering zone, but traditional fractional mass change calculations for each interval are necessary to delineate the extent of removal of Ca and P.

The WT model for elements Al, Fe, and Si display profiles that are low mobility in the Laurels Schist. The WT analysis plotted nearly vertical weathering trends profiles with standard deviations (dotted lines) wider than those for Ca, Na, and P, as well as large confidence intervals for all three elements, with some near-surface decrease for each element indicated by the model when plotted against Zr. We observe less variability for every element when Nb is the immobile element, but when Zr is used oscillations and high variability are dominant.

When modeling traditional geochemical mass balance over the weathered profile (Figure 3.4), tau of Ca varies greatly depending on the selection of immobile element in the Laurels Schist. In particular, we observe high Ca concentrations at ~11 meters deep in Well 1, where we observed a vein of quartz and Ca-plagioclase that we confirmed with XRD (Fisher et al., n.d.). Data from such a hydrothermal feature would most often be removed as an outlier because it might be reasoned that it is external to the bedrock system and is in conflict with the mass balance assumption. However, the quartz/plagioclase vein was certainly intruded prior to the onset of weathering and it could also be reasoned that it has been subjected to the same weathering processes as the

rest of the profile and should remain a part of the bedrock system for the purpose of weathering studies. For the purpose of demonstration, we calculated tau Ca with this sample interval included. When Zr is used as the immobile element, this interval does not indicate enrichment of Ca, but when we calculate the fractional mass change of Ca using Nb as the immobile element for this same interval, we observe that tau Ca=2.5, revealing the drastic enrichment that we expect to observe in a vein with abundant Ca-plagioclase. This observation—that some immobile elements are better than others at normalizing for inherent bedrock variability—demonstrates the value of objectively evaluating all immobile elements.

3.5.4 Upper weathering zone (fd)

WT model identified that the depth of maximum removal of elements Ca, Na, and P (i.e. minimum element concentration ratios) occurs between 2.5-3 meters in Ridge Well 1, and at depths between 1-3 meters in Interfluve Well 2. The WT profiles for Ca and P at Ridge Well 1 (Figure 3.3) show a depletion profile from 10 to 3 meters, then the profiles enrich from 3 meters to the ground surface. These depths correlate with previous findings from this site that reveal a distinct change in the production of mineral surface area at 3 m deep in both wells (Fisher et al., n.d.).

Because the near surface profiles for Ca and P in Well 1 indicate a re-enrichment above 3 meters, and the spread of the concentration ratios in the upper zone are not well approximated by *r*-*c*, calculating tau over every depth interval is the best means to quantify the range of concentration changes for these elements. Figure 3.4 reveals that tau

Ca over the re-enrichment zone goes from approximately -0.9 to -0.5, while the tau values across the re-enrichment of P range from approximately -0.7 to 0. The near-surface enrichment of Ca and P could be the result of biological processing. Although we did not assess the bioavailability of these elements, we understand that plant uptake in the rhizosphere may decrease concentration of bioavailable elements such as P and Ca, and redeposition of plant material can generate an increase of P or Ca at the surface (Hinsinger, 2001). The element behavior of Ca and P are in stark contrast with Na, which is not known to be biologically recycled in soils.

Tau profiles for Al, Fe, and Si exhibit different results over intervals from 0-5 meters for both wells, depending on the immobile element used. When fractional mass change is plotted versus Zr, the result is a near-surface depletion of Al, Fe, and Si, but using Nb as the immobile element results in the opposite. We know that Nb concentration decreases from 5 to 0 meters while Zr concentrations increase (Figure 3.5), so mathematically this means that the concentrations of Al, Fe, and Si remain consistent enough to result in an enrichment tau profile where Nb concentration decreases and a depletion tau profile where Zr concentration increases. This is not to say that Al, Fe, or Si are perfectly refractory in the near-surface interval, but the net concentration change of these elements is small relative to immobile elements, perhaps in part because although these elements undergo weathering they are retained as major components of secondary phyllosilicate and oxide minerals.

3.5.5 Immobile elements

For each field site, we need to select the best immobile element for use in the WT model and the geochemical mass balance. The previous discussion included the use of Nb and Zr for all WT and tau calculations, with some notes indicating where these two immobile elements yielded different results. In the following section we will outline the procedures and considerations for the selection of both Nb and Zr. Given that immobile elements are not perfectly resistant to weathering (Brantley et al., 2008; White et al., 1996) and that immobile elements may also exhibit variability within unweathered bedrock that may or may not correspond to variability in mobile elements in the same unweathered bedrock, this section outlines four procedures that systematically evaluate each potentially immobile element within the Laurels Schist geochemical system. The procedures, detailed in this section, use a combination of WT model functions along with basic statistical analyses (that may be performed in the native R environment alongside WT) to identify the best immobile element.

3.5.6 Immobile element concentration

Plotting the depth profiles of immobile element concentrations provides a first look at overall geochemical variability in the lithology to begin to identify patterns that may indicate mobility and variability (Figure 3.5). Immobile element concentrations should appear enriched relative to the whole rock matrix as mobile elements are lost via dissolution and leaching, and likewise immobiles are residually diluted and appear to deplete where elements like C and N are added. Element concentration profiles for Zr and

Nb in both wells reveal a systematic, oscillating variation below 5 meters (Figure 3.5). The multi-point oscillation patterns indicate that the variability is a bedrock feature rather than element mobility or analytical error, and the pattern suggests that the variability may be inherited from sedimentary parent rock prior to metamorphism because grain size in sedimentary sequences and fractionation during sediment transport results in a range of Zr concentration specific to the sedimentary provenance (Figure 3.5) (De Vos et al., 2006; Hayashi et al., 1997; McLennan, 2001). Given that Zr is expected to be immobile, we expect these concentrations to be preserved to some degree in metamorphically altered products (Rasmussen, 2005). The concentration of Nb mostly follows the patterns of concentration exhibited by Zr, but in some instances the two exhibit an opposite trend. Thus these elements will yield different results when applied as the immobile element in a mass balance.

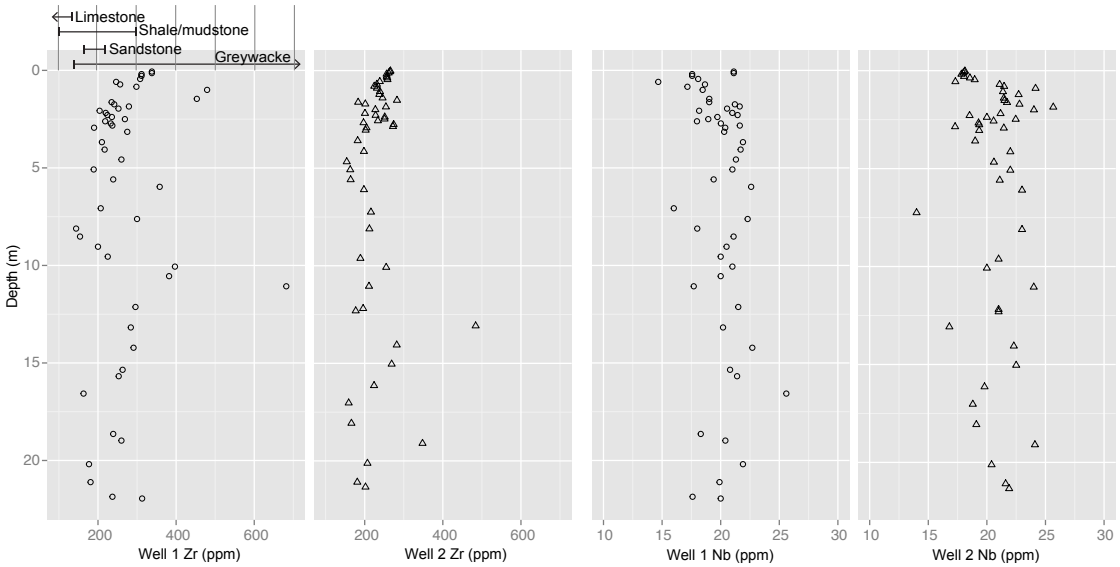

Figure 3.5. Concentration depth profiles for Zr and Nb in both wells. The results reveal some outliers, particularly in the Zr depth profile, where the Well 1 has a vein of quartz and Ca-

plagioclase at ~11 m. Below the plot are ranges of Zr concentrations for several sedimentary rock types (De Vos et al., 2006), which represent potential pre-metamorphosed provenance. The variability of Nb is lower in both wells as shown by the coefficient of variation (Table 3.2).

3.5.7 Coefficient of variation for immobile elements

Calculating the CV of immobile element concentrations quantifies variability of immobile elements, which we expect to remain largely unchanged by weathering. To quantitatively examine inherent geochemical variability, we calculate a coefficient of variation for the immobile elements (CV_i) in the Laurels Schist and compare them in Table 3.2 to data from five additional weathering profiles. The CV is a relative standard deviation (i.e. $CV = standard\ deviation/mean \times 100$, reported as a percentage) that allows comparison of relative variability for data that have different means or have different measurement scales. We see in these results for the Laurels Schist in Well 1 and Well 2, that Zr and Hf have a similar degree of variability that is much higher than the variability of Ti and Nb. The CV_{Zr} in Ridge Well 1 is 33.61%, which is higher than the other metasedimentary rocks (greywacke, shale, and phyllite) in Table 3.2. The CV_{Ti}'s are comparable for the schist, greywacke, and shale profiles that we evaluate in "Analysis of Published Data". The tabulated values of CV for the seven weathering profiles indicate that the variability of the immobile elements in the Laurels Schist appears comparable to the several other published weathering profiles.

Table 3.2. Coefficient of variation (CV_i) of element concentrations for immobile elements in both wells in Laurels Schist along with comparison of data from published data where the geochemical

mass balance was applied, including greywacke (Anderson et al., 2002), shale (Jin et al., 2010), phyllite, gneiss, and diabase (Oh and Richter, 2005).

CV	Well 1 Schist	Well 2 Schist	Graywacke	Shale	Phyllite	Granitic Gneiss	Diabase
Zr	33.61 %	23.00 %	10.48 %	11.64 %	9.00 %	39.30 %	92.04 %
Hf	37.95 %	26.97 %					
Ti	9.20 %	11.41 %	10.28 %	9.93 %	53.98 %	38.58 %	47.08 %
Nb	9.61 %	10.87 %					

3.5.8 Correlation of immobile elements

We assessed the correlation among immobile elements over the entire profile to determine how much of the co-variance is from multiple immobiles residing in the same mineral to determine if some can be ignored (i.e. selecting either Zr or Hf because both reside almost exclusively in zircon). We expect correlation of some immobile elements based on geochemical understanding of which elements occur in each mineral. Because Hf and Zr have nearly identical ionic radii and reside almost exclusively in the mineral zircon (De Vos et al., 2006), we expect these two elements to exhibit the same patterns of concentration with depth. Ti and Nb can occur together in a large number of minerals, including mica group minerals, and the similarity of their ionic radii allows isomorphic substitution (De Vos et al., 2006; Railsback, 2003). Correlations provide information about degree of randomness of variability, which is extremely useful for all bedrock conditions, but particularly for variable bedrock. If two immobile elements exhibit a strong correlation, this evidence that they are behaving similarly in their geochemical environment and may indicate a higher degree of immobility. We test the strength of the

correlation between two immobile elements using a linear correlation (Pearson correlation coefficient). We find that Zr and Hf exhibit a nearly perfect positive correlation in both wells (Zr/Hf Well 1 r=0.99 (n=51, p=<0.00001), and Well 2 r=0.96 (n=52, p=<0.00001)). The correlation between Ti and Nb is not nearly as strong (Ti/Nb Well 1 r=0.39 (n=51, p=0.00418), and Well 2 r=0.50 (n=52, p=0.00019), which indicates that Ti and Nb are more randomly correlated and this agrees with their susceptibility to biogeochemical processes given their presence in mica group minerals, which are more weatherable than zircon.

3.5.9 Immobile elements normalize mobile elements in parent material

Calculating the CV of mobile/immobile element ratios can be meaningful for samples within the parent material because prior to weathering we expect that each mobile element will consistently reside in the same groups of minerals and will thus exhibit a limited amount of variation in fresh bedrock. We calculate the CV using the WT model output parameter s_2, which is the standard deviation of the mean of the log of all element ratios below depth d (fresh bedrock), to test how well the variability of mobile elements is normalized by the immobile elements. The WT model calculates the mean elemental ratio of the parent material (r) and its standard deviation (s_2). We can calculate the CV from these WT parameters as follows: $CV_2 = 10^{(r+s_2)} - 10^{(r)}/10^{(r)} = 10^{(s_2)} - 1$. Doing so for all combinations of mobile to immobile elements shows that normalizing to Zr produces the lowest CV_2 for Ca and Na in parent material from Well 1 (57% and 29%, respectively) and for Ca in parent material from Well 2 (43%), but that normalizing

to Nb produces the lowest CV_2 for the majority of all other mobile elements, with Ti a distant second. Normalizing to Hf never produced a CV_2 lower than for other immobile elements in the Laurels Schist.

3.5.10 Selection of immobile elements

We combine all of the above considerations to determine the best immobile element for our system. Although the CV_i of the concentrations of Ti and Nb as individual elements is much smaller than Zr and Hf, the correlation between Zr and Hf is nearly perfect, which indicates that there is no randomness in their correlation. Thus the high variability of Zr and Hf may be intrinsic to the sedimentary provenance of this bedrock system. The mobile element system exhibits a lower CV_2 for Zr than Hf, and normalization to Zr provides a lower CV_2 for Ca and Na in parent material. Ti and Nb are more loosely correlated with each other than Zr and Hf, but normalizing to Ti and especially Nb generally provides a lower CV_2 for all mobile elements other than Ca (and Na in Well 1). We therefore have chosen to present all Weathering Trends and geochemical mass balance profiles using both Zr and Nb as immobile elements for the Laurels Schist.

3.6 Analysis of published data

Our WT model provides an objective, statistical means to quantitatively determine the significant depths of weathering features, including the depth to fresh bedrock and its mean geochemical composition. This in turn allows an unprecedentedly consistent and systematic way of assigning parent material for the calculation of tau

values for the geochemical mass balance analysis to quantify fluxes of elements over the course of weathering profile development. In this section, we apply our model to several published data sets that had sufficiently deep element profiles for statistical power. We found data from three publications, containing examples of three metasedimentary and two igneous bedrock types. Many published datasets did not offer the opportunity to perform statistical analysis because a common approach to the geochemical mass balance is to delineate only the pedon scale profile. We expect that as the deep critical zone continues to grow as an active research frontier, we will find more deep element profiles, and the Weathering Trends model will facilitate a better understanding of subsurface topographies.

3.6.1 Oregon Coast Range

Anderson et al. (2002) studied a steep headwater catchment in the Oregon Coast Range with erosion rates ranging from 0.05-0.08 $mm \cdot yr^{-1}$ for the past 4-15 ka. The region has shallow soils forming on graywacke, and the catchment was sampled in soil pits and a 35 m deep drill core. Extensive qualitative analysis of the bedrock guided much of the determination of boundaries in the weathering profile. Anderson et al. (2002) delineated the major boundaries in part by the extent of pyrite preservation, defining the rock as pervasively oxidized to 4.5 meters, oxidized from 4.5-9 meters, and below 9 meters the rock is unweathered. They also determined that the permanent groundwater table was at 25 meters, which is much deeper than the depth to fresh bedrock.

Our model analysis of data from Anderson et al. (2002) revealed the deepest

removal of Ca, Na, Mg, and Si (depth *d*) ranging between 3-6 meters (Figure 3.6), which roughly corresponds with the observations by Anderson et al. (2002) of an oxidation front at 4.5 m. Weathering trends identified a depth *fd* for Ca at 2.0 meters, which may indicate a complete removal of Ca between 2-4 meters. However, the change from oxidized to unweathered at 9 meters described by Anderson et al. (2002) was not detected for any element by the Weathering Trends statistical model. WT analysis revealed a change in geochemistry at 1.75 meters, which often emerged as the upper bounds of the confidence interval. The prevalence of this depth in the statistical results may be a sampling artifact from the gap between hand excavated recovery (1.99 m) and the beginning of drilling recovery (3.3 m).

WT showed that Fe is largely retained in this weathering system, despite the oxidation of pyrite. The model showed a slight enrichment of Fe vs. Zr with depth *d* at 3.5 meters (CI 95% [1.75, 6.53]) and a slight depletion of Fe vs. Ti with depth *d* identified at 1.75 meters (CI 95% [1.75, 4.95]) (Figure 3.6). The CV_i for Ti and Zr are 10.28% and 10.48%, respectively, which reveals that neither immobile element indicates a high degree of variability. These results corroborate the finding by Anderson et al. (2002) that there is very little mass change of Fe, thus the oxidation of pyrite must lead to

secondary iron formation in this weathering system.

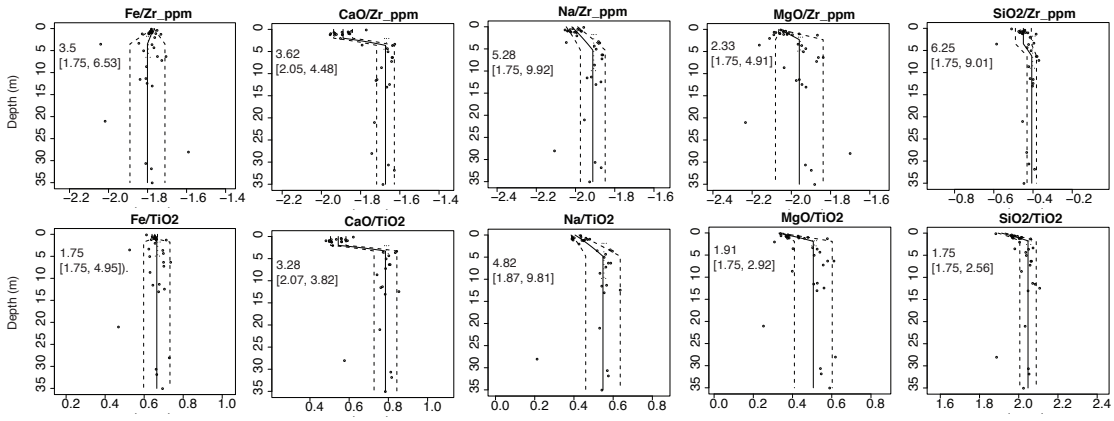

Figure 3.6. Weathering Trends fits for data from Anderson et al. (2002) consistently reveal a weathering front above 5 meters for highly mobile elements (Na, Ca) and less mobile elements (Si). All y-axes span an equivalent numerical range of log ratio values. Depth *d* is reported (in meters) and the 95% confidence interval in brackets.

3.6.2 Pennsylvania Shale Hills

Jin et al. (2010) sampled a 25 m drill core at a ridge top in a first order, forested watershed where soils are extremely thin at the ridge tops (~0.1 m) and forming directly on shale bedrock. The slopes range between 23-28° depending on aspect, and the erosion rates range from 1.61-1.94×10^{-2} mm·yr^{-1} for the past 9-10 ka (West et al., 2013). For their analysis, Jin et al. (2010) averaged all drill core samples from 0.3 to 20 meters (minus outliers) and used these mean values as the parent material for mass balance analysis of soils throughout the watershed.

Weathering Trends, on the other hand, detected deep weathering fronts after outlier removal similar to that done by Jin et al. (2010). WT confirmed that the two deepest samples had “outlier” compositions of most elements, including a vastly higher

Ca concentration, which corroborates the finding in this watershed of minimal carbonate presence above 22 meters (Susan L. Brantley et al., 2013). The CV does not indicate high variability of this shale formation, but when the outliers are removed, the CV_{Ti} decreases from 9.93% to 5.21%, and the CV_{Zr} decreases from 11.64% to 9.93%. WT identified other outliers at 4.5 m with very high Fe, Mn, Mg, and low concentrations of K.

Weathering Trends model generally corroborated the result by Jin et al. (2010) that little change occurred in the elemental concentrations of the ridge drill core profile. However, the Weathering Trends model, with outliers removed, did detect a statistically significant change in Ca at 16-19 m (depending on use of Zr vs. Ti as the immobile element), in Mg at 10-15 m, and in Al, Fe, and Si (vs. Zr) at ~6m (Figure 3.7), although the changes that our model detects generally have wide confidence intervals. Deep weathering at this site is supported by observations of pyrite oxidation extending to 23 m in the same watershed by Brantley et al. (2013a). The lack of distinct weathered profiles and the broad confidence intervals provided by the WT model combined with the published observations of deep removal of Ca and pyrite most likely mean that bedrock weathering extends deeper than 25 m, in contrast to the conclusion of Jin et al. (2010).

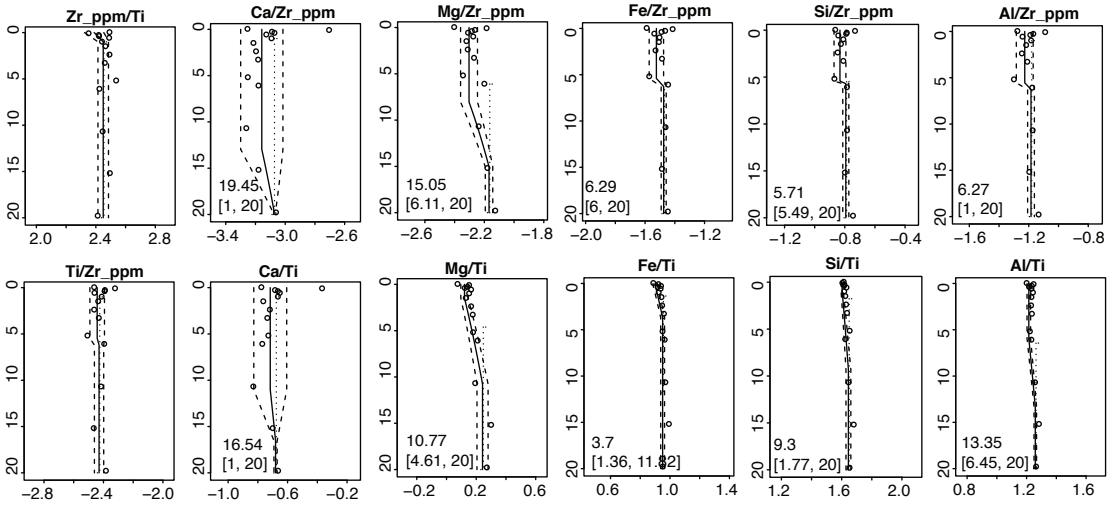

Figure 3.7. Weathering Trends fits for data from Jin et al. (2010) reveals that element ratios do not vary much with depth, which may indicate that the rock is either not highly weathered, or given the depth of change for highly mobile elements such as calcium, the bottom of the drill core may not have reached some weathering fronts. Another consistent trend is that some depletion of Al, Fe, and Si (vs. Zr) occurs at ~6m, which may represent an oxidation front. All y-axes span an equivalent numerical range. Depth *d* is reported (in meters) and the 95% confidence interval in brackets.

3.6.3 North Carolina Piedmont

Oh and Richter (2005) present a comparative weathering study of soils forming on three bedrock types from the Piedmont physiographic province in North Carolina.

The Taurus soil series (fine, kaolinitic, thermic Typic Kanhapludults), forming on phyllite, was sampled from a quarry with 30 m deep exposure. The well drained soils were sampled on nearly level interfluves within an oak forest. The bedrock samples came from multiple levels of the quarry exposure and the concentration values reported were composited from a minimum of 5 samples collected laterally across the outcrop. We tested the variability of this phyllite profile by calculating the CV_i on the two available

immobile elements in the dataset, and the CV_{Zr} indicated low variability at 9.00%, while the CV_{Ti} was 53.98%, indicating that Ti is highly variable in this system. When we apply the WT model to the phyllite (Figure 3.8), we observe clear trends of concentration decrease in Mg, Ca, and Si (depth *d*) that occur between 10-12 meters. Si exhibits a minor depletion and Mg exhibits a substantial depletion, but neither profile exhibits a constant near surface concentration ratio, with no depth *fd*. Ca exhibits a complete depletion profile with depth *fd* occurring at 7.43 meters. Oh and Richter (2005) report that the phyllite samples exhibited a linear depletion pattern for tau Mg, but removal of Ca occurred as a step function, with full concentration (tau=0) at 10 meters and nearly complete loss of weatherable Ca-bearing minerals in the next interval at 7.5 meters, which coincides with the WT modeled depth. Tau profiles from Oh and Richter (2005) also indicate that beginning at 10 meters deep, tau Si exhibited a minor depletion ranging from -0.1 to -0.2.

Cecil soil series (fine, kaolinitic, thermic Typic Kanhapludults) form on granitic gneiss sampled from a quarry under a mixed oak-pine forest, and soil pits were excavated in a broad, gently sloping interfluve. Seven bedrock samples were collected from 4.5 to 90 meters deep within a kilometer from the soil pits, which are averaged and reported as a single sample. To perform WT model analysis, we replicated this sample over five depth intervals (8, 20, 40, 60, and 90 m) to facilitate statistical analysis. Even with this repeated data point, the gneiss exhibits a high degree of variability with CV_i of 39.30% and 38.58% for Zr and Ti, respectively. Weathering trends model analysis (Figure 3.8)

indicates abrupt decreases in concentration for Ca and Si (depth *d*), at 5.3 and 7.61 m, with the upper range of the confidence interval for both occurring at 4.5 m, the shallowest depth we assigned to the bedrock concentration. Stable near surface concentration values (depth *fd*) occur at 3.38 and 4.29 m for Ca and Si, respectively (Figure 3.8). The results from Oh and Richter (2005) report an abrupt loss of Ca, Na, Mg, K, and Si in the top 4 meters, while Al and Fe exhibit variability in the top 4 meters. The WT analysis indicates that the samples that were collected by hand excavation up to 3.38 m are geochemically distinct from the average of seven samples that Oh and Richter (2005) designated as the parent material for their analysis. These observations suggest that the soil may have been forming on a different parent bedrock, which warrants caution in interpreting the elemental mass changes and the variability of the granitic gneiss.

Enon series soils (fine, mixed, active, thermic Ultic Hapludalfs) are forming on diabase in a forested area with gentle slopes that have thick (2.75 m), poorly-drained soils. The bedrock chemistry was taken from a single, least weathered sample selected from boulders within B- and C-horizons that Oh and Richter (2005) estimated as at least 7 m deep. The variability of this sample set is the highest in this report, with CV_i of 92.04% and 47.08% for Zr and Ti, respectively. This extreme variability in Zr concentration raises concern that the bedrock sample is not representative of the rock that soils are forming on or that some other element removal mechanism has acted drastically on this system. Weathering trends identified ubiquitous stable near surface concentration values (depth *fd*) within the top half meter for all elements analyzed (Figure 3.8). Oh and

Richter (2005) describe A, AE, and E horizons up to 0.4 m that are geochemically distinct from the B and C horizons ranging from 0.68-3.38 m, indicating that the WT model identified the depth of this leached E-horizon morphologic boundary within decimeter accuracy over a 7 m deep profile. Apart from the leached horizons, nearly all elemental mass balance profiles from the diabase exhibit a gradual concentration decrease in the upper 4 m. We can conclude that the variability of the Zr concentrations is a product of distinct geochemical transitions, and the WT model reveals that the bedrock sample falls within the same linear trend as the B and C horizon samples.

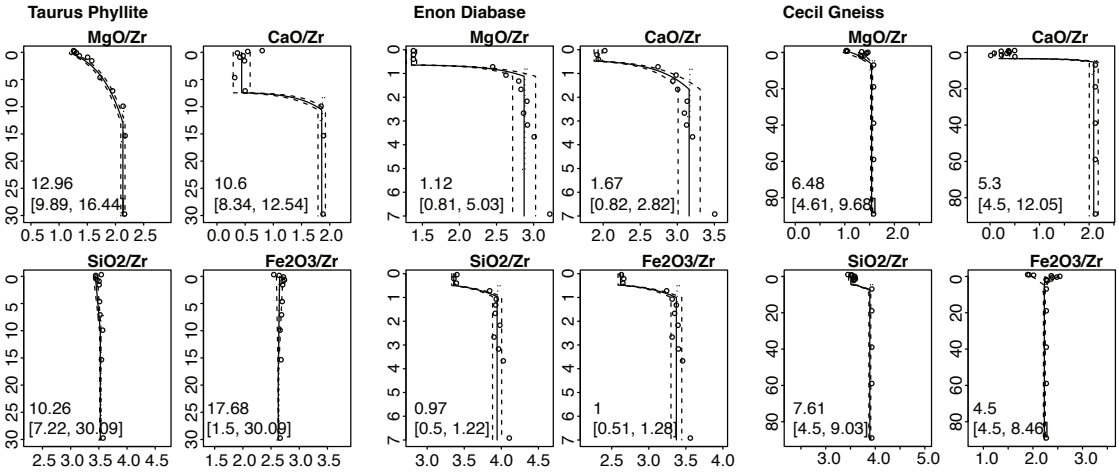

Figure 3.8. Weathering Trends fits for data from the three bedrock types evaluated by Oh and Richter (2005). Most profiles reveal distinct delineation of the depth to bedrock (*d*) and near surface morphologic features or complete elemental removal (*fd*). Y-axes span an equivalent numerical range for each rock type. Depth *d* is reported (in meters) and the 95% confidence interval in brackets.

3.7 Conclusions

The Weathering Trends (WT) model is an extension of the geochemical mass balance that offers a new, enhanced opportunity to characterize and understand

biogeochemical weathering in heterogeneous rock types, such as commonly found in sedimentary and metasedimentary lithologies. Such lithologies with expected high variability cover more than 90% of continental landmasses (Blatt and Jones, 1975; Suchet et al., 2003). As such, many geochemical weathering studies have focused on plutonic settings, which only cover 9% of continental landmasses (Blatt and Jones, 1975; Suchet et al., 2003), because of their expected geochemical homogeneity. The Weathering Trends (WT) model opens the door to studying weathering and soil formation processes in most continental settings.

We present the WT model code and documentation to the scientific community via an open-source R library on GitHub , in order to encourage its widespread use and in order to invite collaborative contributions to improving the model package (https://github.com/AaronRendahl/WeatheringTrends).

The results of the model indicate that weathering in the Laurels Schist is deepest for Ca and Na, which were used to identify a depth to fresh bedrock that is shallower than the groundwater table at Ridge Well 1 and that coincides with the groundwater table at Interfluve Well 2. The upper weathering zone at both landscape positions corroborates previous work in the same weathering system in which mineral surface area exhibited a steep transition in the top 3 meters regardless of landscape position. WT model displayed enrichment of bioavailable elements Ca and P in the upper weathering zone. The WT profiles for Al, Fe, and Si indicated low mobility of these elements.

4 Hillslope soil movement and mixing creates patterns of organic carbon redistribution and organomineral stabilization in a first-order forest watershed

With K. Yoo, UMN—Advisor, A. K. Aufdenkampe, Stroud Water Research Center—Project Lead PI, field site, OC/SA assistance; R. E. Aalto and J. Marquard, University of Exeter—^{210}Pb and ^{137}Cs processing.

4.1 Synopsis

The mobilization of organic carbon (OC) on hillslopes has only recently been recognized as a redistribution of OC, with only some carbon lost to the atmosphere as CO_2. Although we understand that mineral specific surface area (SSA) is a key parameter for protecting OC from microbial consumption, the role of SSA in hillslope redistribution of OC has rarely been explicitly delineated. We assess the changes in OC and mineral surface area (OC/SA) in a hillslope soil transect in a first-order forest watershed and demonstrate that the amount of OC per unit of mineral surface area increases as result of soil mixing, not only due to *in situ* mixing process but also as a result of soil creep and erosional movement. We also report that organic matter properties, including C/N, $\delta^{15}N$, and $\delta^{13}C$, also respond to soil mixing by systematically decreasing C/N, and exhibiting distinctive shifts in stable isotopes as a function of soil profile depth and landscape position. We identify a strong correlation between C/N and the ratio of OC to mineral

surface area (OC/SA), indicating that the processes that associate organic matter and minerals are fundamentally linked with organic matter composition, and both properties may provide a proxy for organic matter stability.

4.2 Introduction

Soil organic matter is the largest active reservoir of carbon on Earth, and understanding the mechanisms of soil organic matter stabilization and feedbacks to climate and other anthropogenic change is a critical need for managing and mitigating atmospheric carbon dioxide (CO_2) (Hartmann et al., 2013). Soil carbon can be rapidly transformed into atmospheric CO_2 unless it is protected from microbial oxidation. In research communities interested in the mechanisms of soil organic carbon stabilization, there has been a growing consensus that interactions between organic matter and minerals—such as occlusion within aggregates or sorption on mineral surfaces (Kleber et al., 2007; Wagai and Mayer, 2007)—may be more critical than molecular structure of organic matter for predicting the stability and turnover time of organic matter in soil (Kleber et al., 2007; Schmidt et al., 2011). The long standing paradigm—that as soil organic matter decomposes, turnover times increase primarily because the intrinsically less reactive and recalcitrant biochemical components are all that remains—was not supported by repeated observations and is currently not the accepted paradigm (Kleber et al., 2010; Schmidt et al., 2011; Sollins et al., 2006). The soil organic biogeochemistry community now understands that environmental conditions that create protective mechanisms—such as freezing (permafrost), burial, anaerobic zones, and organomineral

associations—are key mechanisms for retaining organic matter in soils (Aufdenkampe et al., 2011; Berhe et al., 2007; Van Oost et al., 2007).

Erosion and deposition of soil minerals and organic matter have been widely studied as key processes for understanding soil carbon storage in many settings (e.g. Harden et al., 1999; Liu, 2003; McCarty and Ritchie, 2002; Stallard, 1998; Yoo, 2005; Yoo et al., 2006). We understand that most transported organic matter is redistributed within landscapes instead of being released to the atmosphere as CO_2 upon erosion (Berhe et al., 2007; Van Oost et al., 2007). However, only recently have studies of eroding organic matter considered a mechanism where fresh, reactive organic matter physically mixes with clean, OC-poor minerals from deeper soil horizons to form stable organomineral associations in soils and sediments (Aufdenkampe et al., 2011). This mechanism has been observed at multiple scales, including rivers and drainage basins (Aufdenkampe et al., 2011), hillslopes (Berhe et al., 2012), and soil profiles (Lyttle et al., 2014).

The movement of soil on hillslopes by colluvial soil creep has long been understood to be proportional to the slope, or first derivative of the elevation profile (Carson and Kirkby, 1972; Heimsath et al., 2001). In addition, net change to soil storage (e.g. net erosion loss vs. net depositional accumulation) is related to the curvature, or second derivative of the elevation profile, such that slopes that are convex are net eroding and concave slopes receive net depositional inputs (Gilbert, 1909; Heimsath et al., 1997; Yoo et al., 2007). Although the organic matter associated with hillslope soils must also

erode and be deposited as a function of slope concavity, the research community has debated the fate of colluvially transported soil organic carbon (Foley et al., 2005; Harden et al., 1999; Houghton, 2007; Lal, 2003; Quine and Van Oost, 2007; Schlesinger and Andrews, 2000; Stallard, 1998; Van Oost et al., 2007). Empirical evidence has revealed that: (1) organic matter that is relocated within a landscape largely remains in the soil with net gain in carbon storage during transport (Van Oost et al., 2007); (2) soil organic carbon buried in depositional settings is often protected by various stabilization mechanisms (Harden et al., 1999; McCarty and Ritchie, 2002; Van Oost et al., 2007); and (3) depositional settings provide thick, moist, fertile soils that increase *in situ* plant productivity and carbon input to soils (Yoo, 2005).

Though soil creep movement, by various physical soil perturbations, is unlikely to involve particle size sorting, overland flow erosion may preferentially move fine sediment, promoting organomineral associations during the transport of clay-sized mineral particles. In addition to the potential for the input of reactive minerals in depositional environments, these environments often have higher soil moisture and lower pH, which can protonate mineral surface hydroxyls, rendering them less soluble (Brantley and Olsen, 2013) and more attractive to negatively charged organic substrates (Berhe and Kleber, 2013). Repeated burial episodes may also render the organic matter in each depositional sequence less accessible to degradation (Berhe and Kleber, 2013).

Aquatic scientists have established strong relationships between sediment OC content and mineral specific surface area (SSA) in all depositional settings (Mayer 1994a;

Hedges and Keil 1995; Keil and Mayer 2014) and in riverine suspended sediments (Keil 1997), suggesting that mineral SSA is an effective proxy for the capacity of a mineral matrix to stabilize organic matter (Mayer 1994a; Keil 1994). Very few soil OC studies have considered relationships between mineral SSA and OC storage over a range of landscape positions or as a function of landscape scale processes such as erosion and deposition. Yet one published study found that mineral SSA is a better predictor for mineral associated OC storage than cation exchange capacity, $\Delta^{14}C$, C/N, clay content, exchangeable oxide minerals, or percent of organic carbon (Berhe et al., 2012). Assessing the vertical and lateral distribution of organomineral interactions as they occur at different hillslope positions requires an interdisciplinary understanding of soil mineral and organic matter movement (Yoo, 2005; Yoo et al., 2006), topography-dependent carbon distribution (Quine and Van Oost, 2007; Quinton et al., 2010; Van Oost et al., 2012, 2007), and mechanics of carbon-mineral association (Kleber et al., 2007).

Published ranges of the ratio of organic matter concentration to mineral specific surface area (SSA) are consistently in the range of 0.5-1 mgC m^{-2} of mineral surface for ocean shelf sediments (Mayer, 1994a, 1994b; Wagai and Mayer, 2007), but this ratio is not as well constrained for soils (Wagai et al., 2009). These relationships indicate that SSA has a significant role in determining the potential of soils and sediments to stabilize organic matter (Keil and Mayer, 2014). We know that organic matter attaches to mineral surfaces in patches rather than in smooth, homogeneous layers (Mikutta et al., 2009; Solomon et al., 2012; Thieme et al., 2010) by a number of mechanisms, including cation

bridging, ligand exchange, van der Waals forces, hydrogen bonding, cation and anion exchange, hydrophobic effects, and within soil aggregates (Keil and Mayer, 2014). We also understand that the zone furthest from the mineral surface may turn over more rapidly than the inner zones (Kleber et al., 2007; Sollins et al., 2006). As we consider the meaning of the ratio of organic carbon to mineral surface (OC/SA) and the diversity of mechanisms for associating organic matter with mineral surfaces, we expect that our measurements of bulk SSA and bulk organic carbon will encompass many types of mineral binding sites and organic matter functional groups that interact for the full range of association mechanisms. Thus we describe all of these potential interactions in a general sense as "organomineral associations."

Reviewing these relevant fields led us to hypothesize that erosion driven soil movement on hillslopes results in an increase in organomineral associations and overall organic matter at depositional positions in the landscape. We believe the increase in organomineral associations is the result of a combination of processes, including (1) redistribution of topsoil with a high concentration of fresh organic matter and of subsoil with a high concentration of clean, carbon-poor mineral surfaces, (2) new formation of organomineral associations due to enhanced physical mixing of organic matter with minerals during erosional transport, and (3) soil chemistry of depositional landscapes altering transported minerals and making them attractive to organic matter. Our work looks at the cumulative effects of all of these processes. We assess on a forested hillslope the distribution of organic matter and mineral specific surface area (OC/SA), along with

C/N, $\delta^{15}N$, and $\delta^{13}C$, to show how erosional transport and mixing processes alter organomineral relationships.

4.3 Methods

4.3.1 Study site

The study site is the Spring Brook watershed (Figure 4.1) located in southeastern Pennsylvania and selected as the forested endmember intensive study site for the Christina River Basin Critical Zone Observatory (CRB-CZO) (Fisher et al. 2016a; Fisher et al. 2016b). Spring Brook is a first order watershed that covers 0.096 km^2, with a 250-meter long spring-fed perennial stream. Up gradient from the stream is a 150-meter long, 1-meter deep historic gully that is no longer actively eroding but acts as a depositional swale with a developed A-horizon through the extent of the swale. The soils in Spring Brook are mapped as Manor Series soils (Staff and NRCS, 2012). These Typic Dystrudepts are known for weak structures, coarse loamy textures, and are highly micaceous. Spring Brook is underlain by the Laurels Schist bedrock, a foliated silvery gray-green quartz-plagioclase-muscovite-chlorite-garnet schist with (Blackmer, 2004). Detailed soil and bedrock characteristics are provided by (Fisher et al., n.d.).

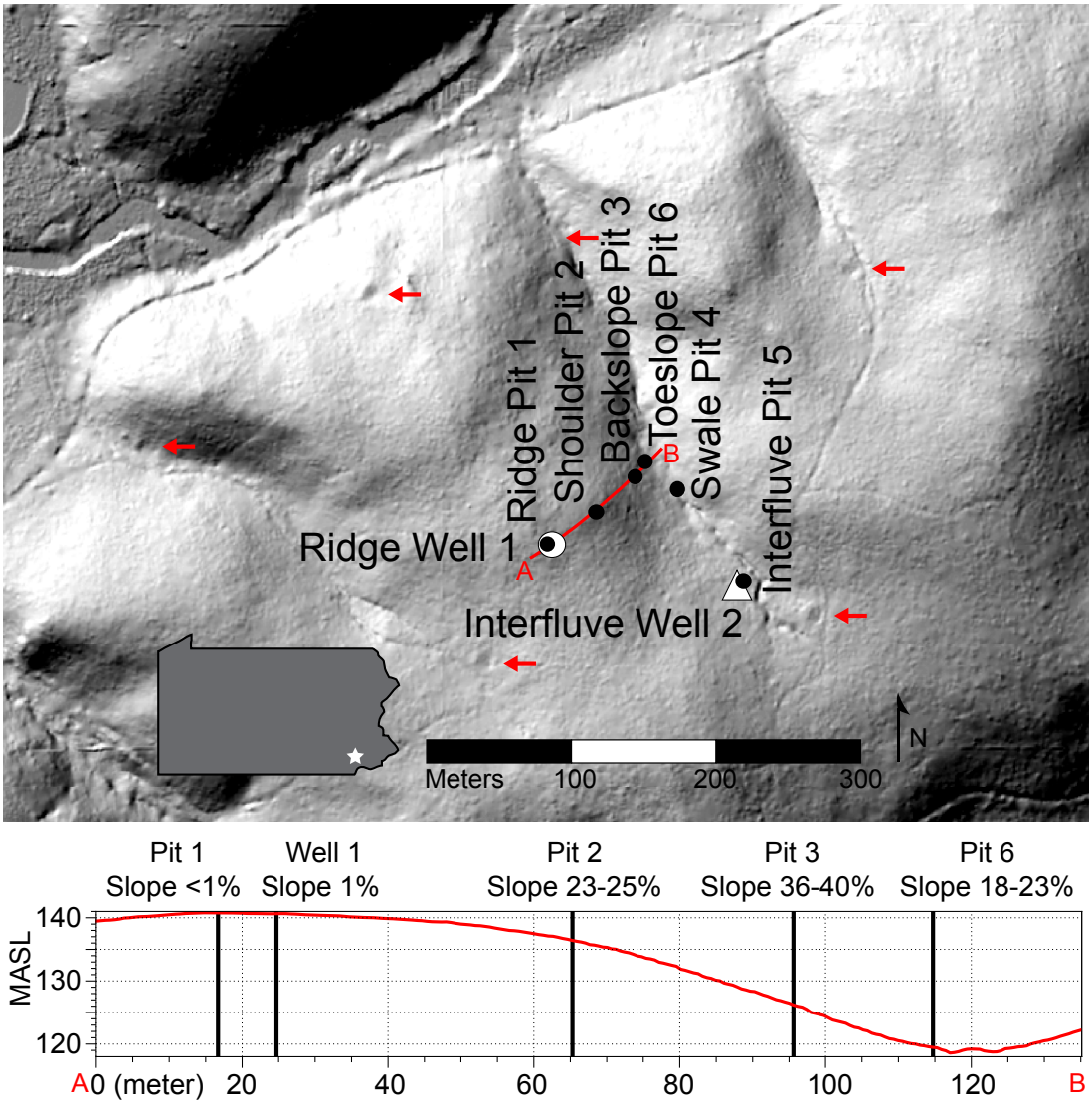

Figure 4.1. Ground returns Lidar hillshade image provides a site map with topographic information of the Spring Brook watershed in the Laurels Preserve in southeastern, Pennsylvania. In addition to Ridge Well 1 and Interfluve Well 2, we sampled a transect of soil pits to characterize the influence of landscape position on SSA and other biogeochemical properties. Arrows indicate flat landforms where charcoal was made during the logging history of this region (Lesley, 1859; Shields and Benson, 2011). A cross-section of the hillslope transect is marked with elevation and slope for each site. LiDAR digital elevation was collected by the National Center for Airborne Laser Mapping (NCALM) and are available at OpenTopography.

The Spring Brook watershed is the only perennial stream watershed in the CRB-CZO that is 100% mature forest and has no tilled agricultural history. The second growth mixed chestnut, oak, and hickory forest is approximately 160-190 years in age, and was likely logged for 1-2 cutting and planting cycles of 25-30 year old hardwood trees to provide charcoal for local smelting operations beginning around 1825 (Lesley, 1859; Shields and Benson, 2011). We see evidence of the former charcoal pits as flat, circular terraces, most of which are visible in the Lidar elevation model (red arrows in Figure 4.1), and confirmed by an exceptionally high abundance of charcoal in the soil. The property was dedicated as preserve land in 1967 (Shields and Benson, 2011) and has had no known grazing since that time.

The climate in Spring Brook is Humid Continental with mean annual precipitation (MAP) of 1246 mm and a mean annual temperature (MAT) of 10.85°C, which ranges annually from -6 to 29°C (1961-1990, Coatesville, PA, http://www.usclimatedata.com). Paleoclimate records from 18,000-12,000 ybp based on pollen type estimate annual lows of -12°C and highs of 16°C in the region during that period, which was experiencing these periglacial conditions until the Laurentide ice sheet began to retreat. By 9,000 ybp the temperatures ranged from -4 to 22°C, with a gradual shift to present day temperature ranges (Prentice et al., 1991).

LiDAR point cloud data and derived digital elevation model (DEM) were collected in April 2010 and processed by the National Center for Airborne Laser Mapping (NCALM). These LiDAR data products are available at OpenTopography

(DOI: 10.5069/G9T43R00;

http://opentopo.sdsc.edu/datasetMetadata?otCollectionID=OT.102011.26918.1).

4.3.2 Soil sampling

Soil pits were hand excavated to ~1-meter deep along a hillslope transect with a north-easterly aspect (40°) as follows:

- Pit 1, flat ridge (<1% slope): 143.932 MASL, 39.9194572°, -075.7892333°, IGSN:IESW10001;
- Pit 2, convex shoulder (23% slope): 139.949 MASL, 39.919783°, -75.7888499°, IGSN:IESW10002;
- Pit 3, planar backslope (36% slope): 129.989 MASL, 39.919926°, -75.7885518°, IGSN:IESW10003;
- Pit 6, concave toeslope (18% slope): 123.096 MASL, 39.9200122°, -75.7883606°, IGSN:IESW10005;
- Pit 4, concave swale (20% slope down valley): <123 MASL, 39.919863°, -75.788162°, IGSN:IESW1001C;
- Pit 5, convex interfluve (16% slope): 133.108 MASL, 39.9195557°, -75.7878866°, IGSN:IESW10004.

After detailed soil description (Staff and NRCS, 2012), sample collection was guided by morphological horizons. Soil materials were sampled across the entire width of the upslope side of the soil pit to integrate heterogeneities. Soil samples were

homogenized in the lab, oven dried, and sieved to 2 mm, and weighed. We did not collect forest litter.

All sites sampled for this project have been registered as sampling features with universally unique International Geo Sample Number (IGSN) identifiers, which are registered with the System for Earth Sample Registration (SESAR, http://www.geosamples.org/ with records available via Universal Record Locators (URL) similar to https://app.geosamples.org/sample/igsn/IESW10001).

4.3.3 Carbon and nitrogen

Samples were oven dried (60°C) and sieved to 2 mm; roots and organic particles were removed by hand and weighed. Coarse rock fragments composed 23-81% of the samples throughout the hillslope transect. Elemental and isotopic organic carbon and nitrogen were analyzed on an Elemental Analyzer (EA, Costech ECS 4010) interfaced with an Isotope Ratio Mass Spectrometer (IRMS, Thermo DeltaPlus XP) after pretreatment by wetting with nanopure water and fuming with hydrochloric acid vapors for 18 hours to remove carbonates and eliminate nitrogen contamination by vapor phase ammonia. Standard curves for the elemental and isotopic analysis were created for each batch using 8 or 9 isotopically depleted and enriched L-glutamic acid standards over a range of carbon and nitrogen masses that encompassed the sample masses.

Stable isotope ratios, reported using $\delta^{13}C$ and $\delta^{15}N$ notation, were normalized relative to the Vienna Peedee Belemnite and Air reference standards respectively using a 2-point approach based on referencing lab standards to USGS 40 ($\delta^{13}C$ = -26.389‰, $\delta^{15}N$

= -4.52) and to USGS 41 ($\delta^{13}C$ = +37.626‰, $\delta^{15}N$ = +47.57) following Coplen et al. (2006).

4.3.4 Specific surface area (SSA)

Fine fraction (<2 mm) oven dried (60°C) samples were degassed at 150°C for a minimum of four hours in an N_2 environment, weighed, and analyzed using N_2 adsorption on a Micromeritics TriStar II 3020. Specific surface area (mineral surface area per unit mass of soil) was calculated using an 11 point isotherm using the BET multipoint isotherm method (Brunauer et al., 1938). For each sample, we measured SSA on two sample treatments to collect information about organomineral associations. Untreated samples that may contain organic matter associated with minerals were measured (SSA_{om}), then the samples were combusted at 350°C for 12 hours to remove organic matter (Keil et al., 1997) and expose organic matter occluded mineral surface for N_2 adsorption of the entire mineral surface (SSA). The ratio of the percent of soil organic carbon (mg OC per 100 mg of soil), measured by elemental analysis (Costech 4010), to the total SSA is given as OC/SA (mgC m^2).

4.3.5 Density fractionation

Dry samples from the <2 mm soil fraction were incorporated into a 2 g cm^{-3} solution of sodium polytungstate solution (SPT) for 2 hours on a shaker at room temperature. After centrifuging at 2500 rpm for 30 minutes, the light soil fraction, primarily composed of detrital organic matter fragments, was carefully removed from the top of the centrifuge tube and centrifuged again at 2500 rpm for 10 minutes to completely

separate SPT from soil. The SPT was separated from the remaining sample to isolate the dense fraction. Light and dense fractions were rinsed with deionized water to reach a conductivity between 50-150 μs cm^{-1}.

4.3.6 Soil texture

We measured soil texture, or the percent sand, silt, and clay of the <2 mm soil fraction, using the hydrometer method (Bouyoucos, 1962; Day, 1965). We allowed 40-50 g of air dried soil to soak for at least 16 hours in a 5% solution of sodium hexametaphosphate. The suspension was mixed with an electric mixer for one minute and transferred to a 1 liter graduated cylinder. At room temperature, samples were carefully stirred to suspend all particles, then cylinders were left undisturbed for particles to settle. Fluid density (ASTM 152H hydrometer) and temperature were measured on soil specimens and a solution of plain sodium hexametaphospate to calibrate for room temperature fluctuations, with all readings taken at 40 seconds and 8 hours. After 40 seconds we expect all of the sand sized particles to have settled out of solution. At 8 hours we expect only clay-sized particles to remain in solution. Thus we convert the density of each solution into a weight percent of sand, silt, and clay.

4.3.7 Soil moisture

Decagon 5TM volumetric soil moisture probes and Decagon MPS-2 water matric potential sensors were installed in the upslope wall of the soil pits at 10, 25, 50, and 90 cm depth in Ridge Pit 1, Shoulder Pit 2, Backslope Pit 3, Toeslope Pit 6, and Interfluve

Pit 5. Measurements are logged at 5 minute intervals using an Arduino based open-source logger system (similar to http://envirodiy.org/mayfly/).

4.3.8 Radio-isotope measurements (^{210}Pb, ^{137}Cs, ^{10}Be, ^{14}C)

We measured ^{137}Cs and ^{210}Pb along the hillslope transect because these two radionuclides work together to track soil movement at the time scale of years to centuries. ^{210}Pb is in the ^{238}U decay series and a daughter isotope of ^{222}Rn gas, which is produced in geologic materials. Thus all soils have a background, steady-state level of ^{210}Pb that is supported by the radioactive decay of *in situ* ^{226}Ra via ^{222}Rn. ^{210}Pb is also continuously produced by atmospheric ^{222}Rn and deposited at a relatively constant rate via precipitation. This meteoric, or fallout, ^{210}Pb has a high affinity for adsorption with fine minerals and organic matter, and decays with a half-life of 22.2 years because it is unsupported by *in situ* ^{226}Ra. The fallout ^{210}Pb is thus in excess to supported ^{210}Pb and is the portion of the total measured ^{210}Pb and is used to understand soil redistribution (Kaste et al., 2007; Matisoff and Whiting, 2012). ^{137}Cs is a radioisotope with a 30.08 year half-life and a high affinity for adsorption with fine minerals and organic matter in soils. In contrast to the continuous deposition of ^{210}Pb, the occurrence of ^{137}Cs in the atmosphere is due to nuclear fallout from accidents and weapons testing, with the largest fallout in the northern hemisphere occurring from 1961-1962. When we combine these two tracers we can learn about the recent movement and mixing of soils using ^{137}Cs and contrast that with the more long-term inventory of ^{210}Pb (Kaste et al., 2007; Matisoff and Whiting, 2012; Ritchie and Mchenry, 1990; Walling and He, 1999).

For ^{210}Pb and ^{137}Cs measurement, cores were sectioned, dried at 100°C, and sieved to <2mm. Bulk density was measured on core sections prior to analysis to calculate final inventory of radio isotopes. Excess ^{210}Pb was directly determined following the method of Aalto and Nittrouer (2012) by equilbrating with its granddaughter ^{210}Po for >60 days in a metal can, dissolving ^{210}Po by digestion in 12N nitric acid followed by 6N HCl, adding ^{209}Po as an internal tracer to determine yield, using an alpha spectrometer (Ortec Ultra-AS, at University of Exeter) for 48-100+h (as needed to record approx. 1000 decays). ^{137}Cs was counted on gamma spectrometer for 40 h on a high-purity Germanium (HPGe) well detector with full digital electronics (Ortec, at University of Exeter). ^{14}C was measured on the <2mm fraction and on density fractions that were separated using sodium polytungstate at specific gravity of 2 g cm^{-3} (Lawrence Livermore National Laboratory). ^{10}Be adsorbed to minerals and organic matter was isolated and extracted from <2mm soil fractions using a series of acidification treatments and ion exchange chromatography, and analyzed by accelerator mass spectrometry (AMS, PRIME Lab).

4.3.9 Inventory of organic carbon and cosmogenic radionuclides

The inventory (I) of soil constituents, including organic carbon and cosmogenic radionuclides (X in generic form) was calculated using $I = \sum_{n=1}^{N}[X_{n,fine} \times \rho_{n,total} \times (1 - f_n) \times h_n]$. Where $X_{n,fine}$ is the measured constituent, measured on the fine fraction (<2mm) from the nth layer of soil, $\rho_{n,total}$ is the bulk density measured for the total soil sample from the nth layer [unit dimensions of M L^{-3}], f_n is the mass fraction of coarse (>2 mm) in

the nth layer determined by dividing the mass of coarse fraction by the mass of bulk soil [unitless, M M^{-1}], h_n is the thickness of the nth soil layer, and N is the total number of sampled soil layers. Due to the high content of rock fragments at all sample sites, this approach is used where term $(1-f_n)$ normalizes for rock content.

4.4 Results

4.4.1 Soil morphology

The soils forming on the Laurels Schist are mapped as Manor Series soils (Staff and NRCS, 2012). These Typic Dystrudepts have weak structures, coarse sandy loam textures, and are highly micaceous. The abundant coarse fragments (> 2mm) in all of the soils in Spring Brook are composed of angular chlorite-mica schist channers. The channers are nearly horizontal throughout the soil pits, with some disruption from root penetration, bioturbation, freeze-thaw processes, and colluvial movement. The easiest path for water movement is through the foliations and fractures in the parent rock, and this continues as the pattern in the soil.

Table 4.1. Soil morphological descriptions for all soil pits, plus pH and soil texture.

Site	Depth (cm)	Horizon	Color	pH DDI	pH $CaCl_2$	>2mm%	Sand%	Silt %	Clay%	Density (g cm^{-3})
Ridge	0-6	A1	10YR 3/2	4.27	3.85	61.17	48.68	25.09	26.24	0.89
Pit 1	6-14	A2	10YR 4/3	4.74	4.26	80.76	51.16	22.59	26.24	1.29
	14-19	BA	10YR 5/3	4.68	4.27	75.48	49.09	23.41	27.51	1.33
	19-28	Bw1	10YR 5/4	4.66	4.24	69.89	53.65	18.85	27.50	1.47
	28-44	Bw2	10YR 6/2	4.62	4.17	60.79	57.28	17.72	25.00	1.55
	44-59			4.61	4.17	68.12	59.28	14.72	26.00	1.67
	59-72			4.65	4.18	57.92	60.64	13.36	26.00	1.75
	72-84			4.68	4.25	79.00	63.64	10.36	26.00	1.74
	84-100	C	10YR 6/3	4.74	4.28	54.42	61.28	8.72	30.00	1.61
	100-146			4.93	4.61	41.06	67.28	10.72	22.00	1.65
Shoulder	0-3	A1	10YR 3/2	4.14	3.87	68.76	50.28	25.72	24.00	0.37

Pit 2	3-7			4.47	4.02	51.89	48.28	27.72	24.00	0.87
	7-11	A2	10YR 4/2	4.68	4.26	57.71	51.28	24.72	24.00	1.38
	11-15			4.74	4.29	49.18	51.28	24.72	24.00	1.50
	15-22	Bw1	10YR 5/4	4.66	4.21	51.62	51.28	22.72	26.00	1.68
	22-31			4.63	4.17	54.71	54.28	17.72	28.00	1.68
	31-41	Bw2	10YR 6/4	4.64	4.18	60.33	54.44	14.30	31.26	1.72
	41-53			4.69	4.25	71.47	61.15	8.85	30.00	1.40
	53-75	C1	10YR 6/1	4.78	4.32	81.40	72.40	3.85	23.75	1.56
	75-135			5.07	4.6	67.09	76.15	1.35	22.50	1.75
Back-slope	0-2	A1	10YR 3/2	4.95	4.64	43.82	60.37	14.64	24.99	1.04
Pit 3	2-5			4.9	4.66	50.86	54.10	20.90	25.00	1.23
	5-8	A2	10YR 4/3	4.92	4.58	34.25	49.13	25.89	24.99	1.35
	8-14			4.92	4.38	50.37	51.60	22.15	26.25	1.58
	14-20	AB	10YR 5/3	4.83	4.35	60.95	49.13	23.39	27.49	1.74
	20-26	Bw1	10YR 6/3	4.85	4.3	68.01	47.85	22.15	30.00	1.48
	26-32			4.64	4.04	71.59	56.63	13.39	29.98	1.96
	32-40	Bw2	10YR 6/3	4.59	4.06	73.39	56.62	12.14	31.23	1.72
	40-48			4.69	4.03	76.52	61.61	9.65	28.74	1.71
	48-60			4.73	4.01	78.89	66.61	5.90	27.49	1.71
	60-75	C	10YR 6/3	4.73	4.03	68.19	67.87	3.40	28.74	1.76
	75-96			4.76	4.04	79.45	70.37	4.65	24.98	1.76
Swale	0-5	A	10YR 4/2	5.46	4.65	40.49	39.61	30.42	29.97	0.82
Pit 4	5-15	BA	10YR 4/3	4.95	4.3	42.92	43.31	25.44	31.24	1.08
	15-25			4.73	4.16	41.11	38.78	31.23	29.99	1.29
	25-35			4.77	4.25	43.78	38.35	31.68	29.98	1.34
	35-47			4.8	4.17	63.90	38.32	30.44	31.24	1.70
	47-60	BA2	10YR 4/2	4.38	3.67	79.08	40.01	27.49	32.49	1.43
	60-84	2Bw1	10YR 6/4	4.7	3.98	64.20	53.74	8.75	37.51	1.41
	84-99	2Bw2	10YR 6/4	4.68	4.11	62.04	53.33	10.44	36.22	1.62
	99-113	2BC	10YR 6/4	4.66	4.16	72.89	59.57	7.95	32.48	1.82
Interfluve	0-2	A1	10YR 3/2	5.2	4.6	25.35	59.44	19.45	21.11	0.84
Pit 5	2-6			5.1	4.2	23.30	49.37	27.30	23.33	0.84
	6-12	A2	10YR 3/3	4.6	4	41.79	47.22	26.12	26.67	1.15
	12-18			4.7	4.1	36.58	47.22	26.12	26.67	1.46
	18-29	AB	10YR 4/3	4.6	4	47.57	46.09	25.01	28.90	1.61
	29-37	Bw1	10YR 5/6	4.5	3.9	55.28	43.98	24.92	31.10	1.61
	37-46			4.4	4	63.35	42.93	23.73	33.33	1.61
	46-56	Bw2	10YR 5/4	4.7	3.8	64.44	43.92	21.66	34.42	1.64
	56-70			4.6	4	55.83	52.69	16.20	31.11	1.58
	70-80	Bw3	10YR 5/6	4.7	4	48.11	55.04	20.54	24.42	1.68
	80-90			5	4	54.85	50.50	22.85	26.65	1.64
	90-107			4.6	4.1	63.63	51.57	20.64	27.78	1.84
	107-122	BC	10YR 6/4	4.4	4	52.21	51.60	22.85	25.54	1.68
Toeslope	0-2	A1	10YR 2/2		4.4	42.46	52.46	25.80	21.74	0.99
Pit 6	2-4				4.2	38.96	52.46	25.80	21.74	1.00
	4-7	A2	10YR 3/2	4.5	4.2	40.25	45.76	32.23	22.01	1.07
	7-10			4.6	4.1	29.71	39.57	35.95	24.49	1.09
	10-15	AB	10YR 3/4	4.7	4.1	23.02	44.12	34.07	21.81	1.19
	15-20			4.6	4.2	39.35	26.46	48.34	25.20	1.36
	20-25	2Ab	7.5YR 3/2	4.6	4.2	34.46	40.61	38.97	20.42	1.68
	25-30			4.5	4.1	75.61	42.46	37.76	19.78	1.52
	30-39			4.5	4.1	61.24	39.66	39.59	20.74	1.90
	39-44	2ABb	10YR 4/4	4.5	4.1	65.84	40.75	38.23	21.03	1.93
	44-60	2Bwb	2.5Y5/4	4.5	4	68.58	39.05	32.47	28.48	2.09
	60-80			4.2	3.9	70.84	45.33	26.37	28.30	1.98
	80-100			4.5	3.7	73.81	44.62	26.79	28.59	1.89

The soils in Spring Brook follow a classic hillslope progression with distinct morphological features in the eroding versus depositional portions of the landscape (Figure 4.2). The eroding portions of the transect, Ridge Pit 1, Shoulder Pit 2, and Backslope Pit 3, are comprised of soils forming directly on bedrock, with depth to C-horizon occurring within the top meter. The channers in the eroding soils occur as tightly fitted plates of rock supported by other rock clasts, mostly in their original orientation, which mimics the foliated structure of the parent schist.

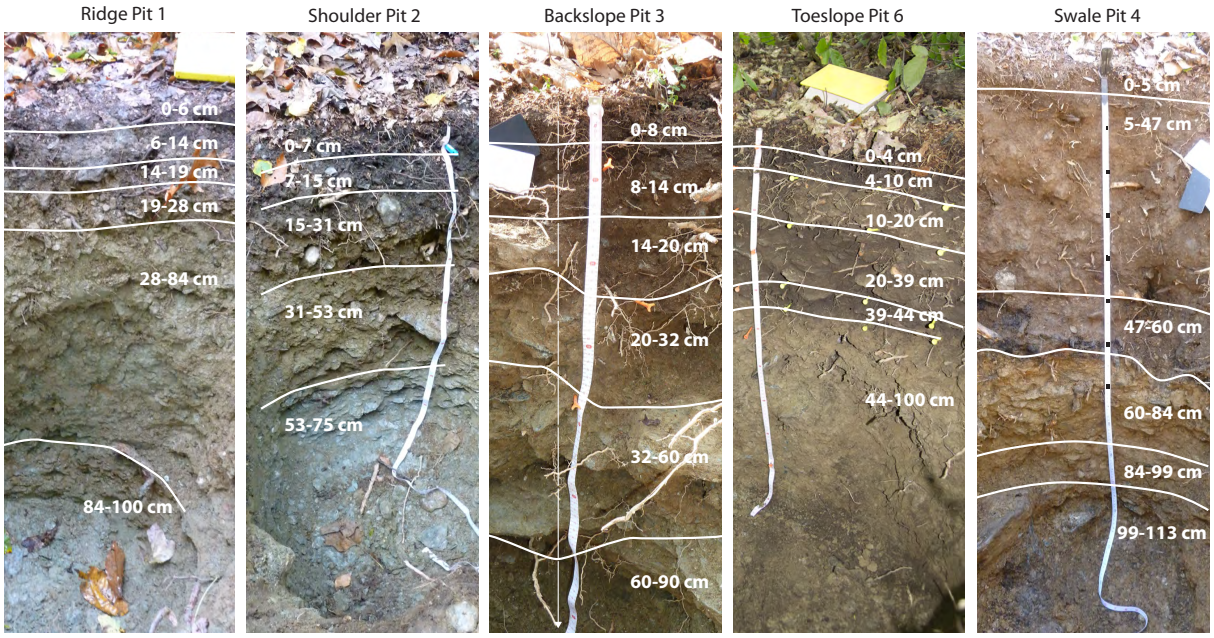

Figure 4.2. Photographs of the soil pit transect with morphological boundaries and depth intervals indicated for each pit. Morphological descriptions are found in Table 4.1.

The depositional portions of the landscape, Toeslope Pit 6, and Swale Pit 4 (Figure 4.2) have features indicating colluvial deposition, including truncation or buried profiles, randomly oriented rock clasts, and a lens of charcoal pieces in Swale Pit 4 at 60

cm deep. The C-horizon in these depositional soil pits occurs below the top meter, beyond our ability to excavate by hand. The Interfluve Pit 5 contains colluvial material to at least 1.24 meters deep, and this colluvial morphology is noted by a lower concentration of rock fragments than the depositional soils with rock clasts supported by a matrix of fine material. This morphology is evidence that this position in the landscape was once a concave zone of depositional collection. This landscape position is currently a convex ridge between two gullies in the valley, which is why we have identified it as an interfluve (Figure 4.3).

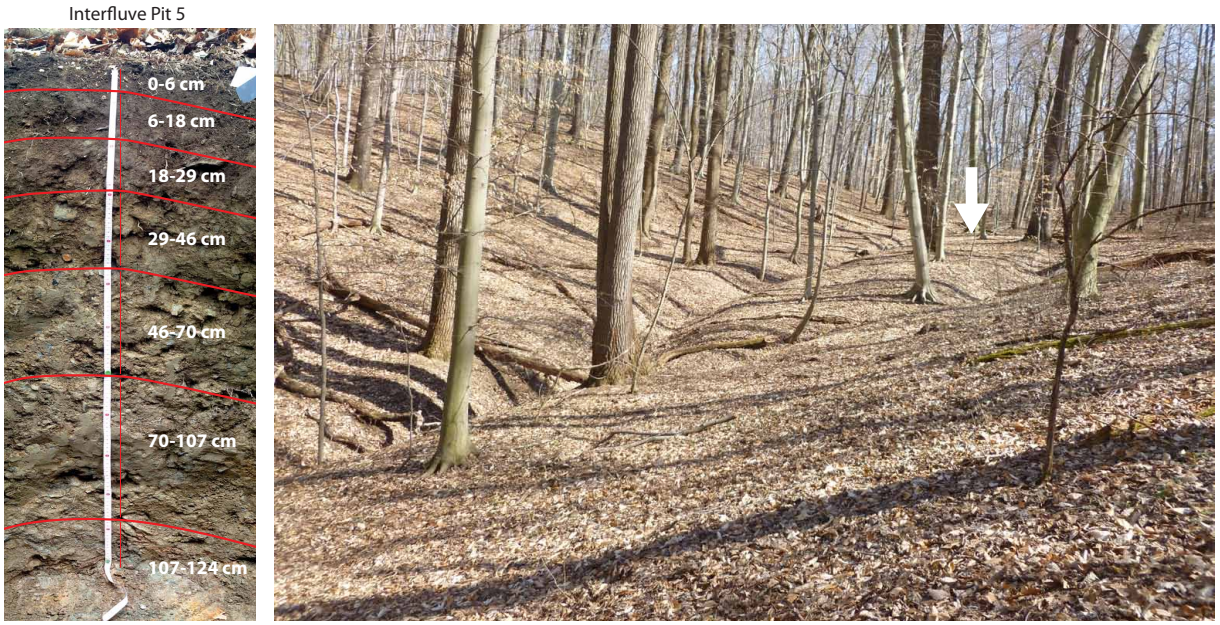

Figure 4.3. Interfluve soil pit and photograph of the interfluve in the landscape with morphological boundaries and depth intervals indicated for each pit. Morphological descriptions are found in Table 4.1. White arrow indicates approximate location of soil pit near the middle of the interfluve, an intermediate convex feature between two hillslopes.

4.4.2 Radio-isotope measurements (^{210}Pb, ^{137}Cs, ^{10}Be)

Measurements of excess ^{210}Pb and ^{137}Cs reveal activity profiles that are smooth with asymptotic decrease with depth to and little activity measured below 10 cm for all profiles (Figure 4.4). The only profiles that have discontinuous activities are the ^{137}Cs profile at Shoulder Pit 2, where the activity in the top 2 cm is lower than the activity from 2-4 cm, and Swale Pit 4 has a discontinuously higher ^{137}Cs activity at 10 cm. The total inventory of ^{210}Pb is highest at the Shoulder Pit 2 followed by Swale Pit 4. The highest ^{210}Pb inventory at Shoulder Pit 2 was unexpected. The inventories of ^{137}Cs were substantially higher in the two depositional sites.

The minimum landscape age determined using meteoric ^{10}Be measured at Ridge Pit 1 is 19 kyr, with an erosion rate of 50 m myr^{-1}.

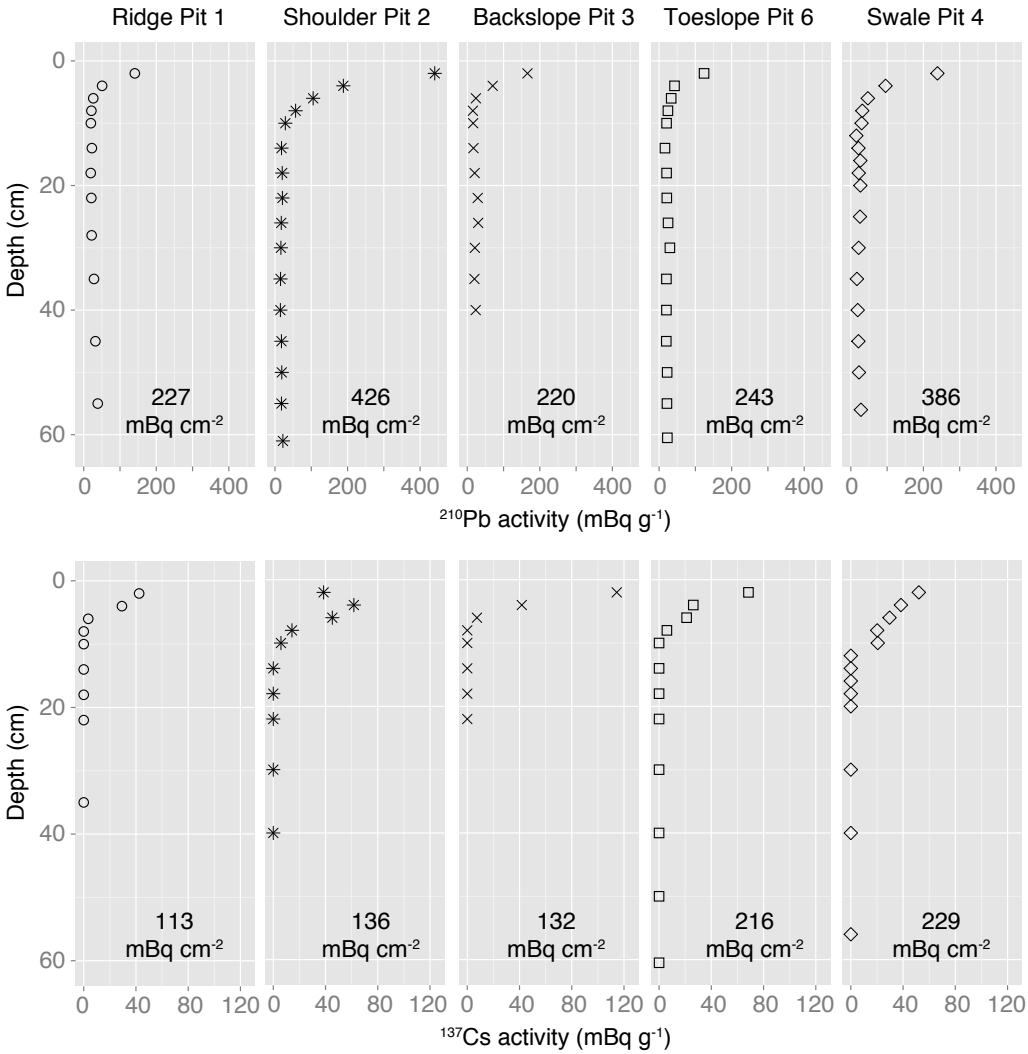

Figure 4.4. Depth profiles of ^{210}Pb and ^{137}Cs activity along the hillslope transect with profile integrated inventories.

4.4.3 Organic matter distribution

Organic carbon profiles decreased from 4-15% OC (weight %) in the upper few cm to <0.25% OC below 60 cm depth (Figure 4.5A). The shape of the profiles were generally similar, with the notable exception where %OC was highly elevated (1.3-2.5% OC) in the 25-50 cm depth interval for profiles at depositional landscape positions

(Toeslope Pit 6 and Swale Pit 4) relative to all other profiles (0.2-0.6% OC from 25-50 cm). Organic carbon cumulative inventory profiles accentuate these differences (Figure 4.5B), with depositional landscape positions continuing to substantially increase from 25 to 50 cm before they asymptote at >12 kg OC m^{-2} for Toeslope Pit 6 and >9 kg OC m^{-2} for Swale Pit 4. Carbon inventory profiles from all other landscape positions began to asymptote at around 25 cm (Figure 4.5B) with maximum inventories about half of those from depositional locations. Planar Backslope Pit 3, which is the steepest location (36% slope) and exhibits the shallowest and rockiest soil profile, had an intermediate inventory value of 6.7 kg OC m^{-2}. Interfluve Pit 5 exhibits a continuous carbon profile like those of the eroding landscapes, but it also contains a higher carbon inventory than Ridge Pit 1 and Shoulder Pit 2.

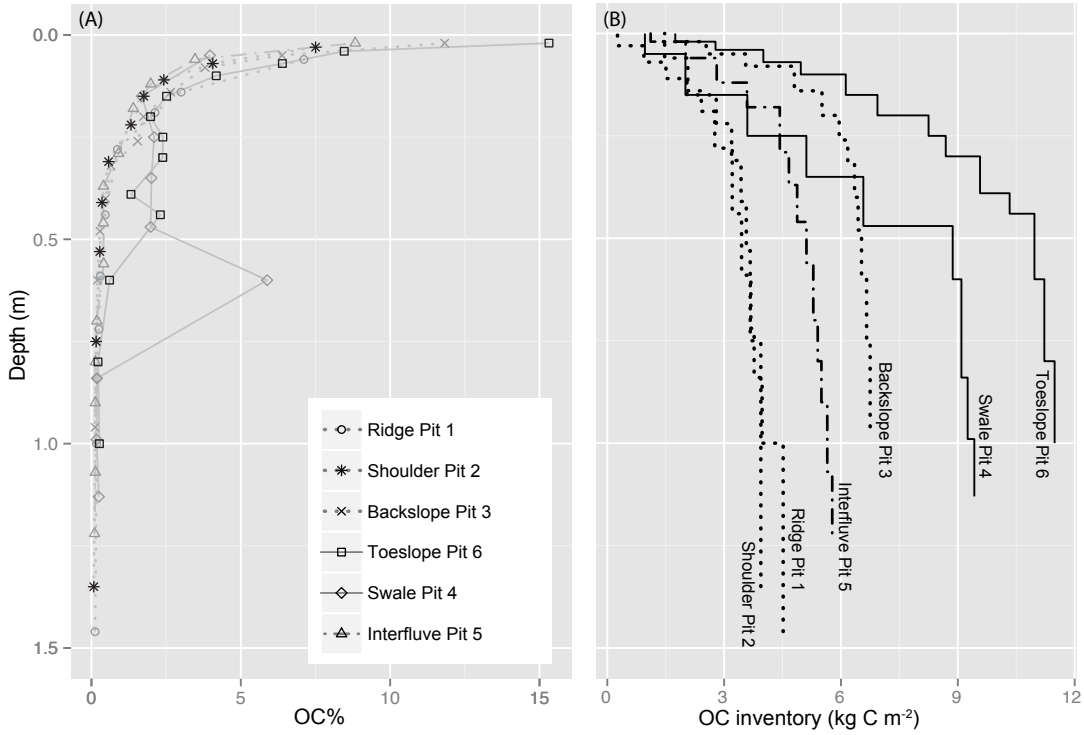

Figure 4.5. Organic carbon profiles in the soil pit transect in Spring Brook. Figure 4.5A is the organic carbon percent with depth, where we highlight an eroding profile, Shoulder Pit 2, and a depositional profile, Toeslope Pit 6. The outlier at 0.6 m deep in Swale Pit 4 was a lens of charcoal. Figure 4.5B calculates a cumulative inventory of organic carbon. Eroding sites Ridge Pit 1 and Shoulder Pit 2 have a lower inventory than depositional sites, where Swale Pit 4 and Toeslope Pit 6, contain nearly double the organic carbon inventory. Interfluve Pit 5 has colluvial depositional morphology, yet features the OC profiles similar to those of soils in eroding parts of the landscape.

4.4.4 Organic matter and mineral surface area

Depth profiles of total organic carbon normalized to total mineral SSA (OC/SA, Figure 4.6) reveal discontinuities in landscape positions. Depositional sites such as Swale Pit 4 and Toeslope Pit 6 have a higher OC/SA ratio for nearly the entire depth profile, and this value is considerably higher for depths above 0.7 m.

The ratio of dense fraction organic carbon, which is physico-chemically associated or sorbed with minerals, to total SSA (OC_{DF}:SA_{tot}, black filled circles and squares, Figure 4.6B), provides an opportunity to test the amount of OC that is directly associated with minerals. The dark filled circles and squares in Figure 4.6B, which are linked to their bulk fraction counterparts using dashed lines, display how the majority of organic matter in these soils occurs in the dense, or mineral-sorbed, fraction. The dense fraction organic matter ranges from 50-100% of the total carbon for measured samples. This test confirms that dense fraction carbon to mineral surface area is comparable to total carbon to mineral surface area, confirming that total OC/SA is a reasonable proxy for mineral-sorbed carbon in this soil system.

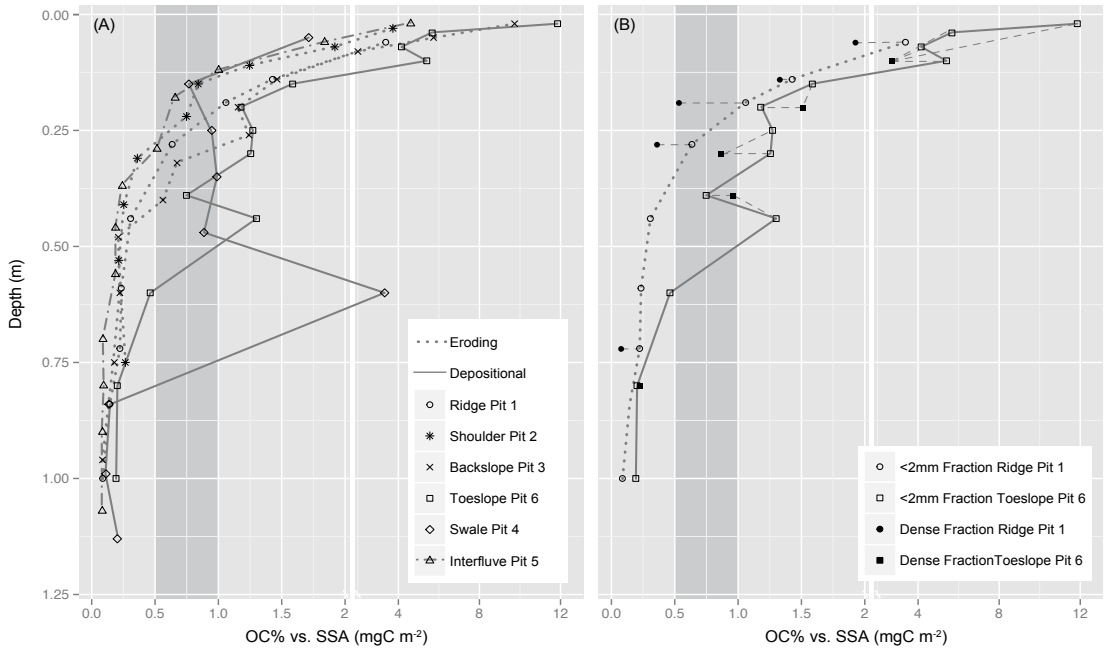

Figure 4.6. The overall depth trend of OC/SA reveals that the ratios display a decrease with increasing depth. Depositional sites Toeslope Pit 6 and Swale Pit 4 deviate from this trend and exhibit higher OC/SA ratios up to 0.5 m deep where deposited material carries a higher OC/SA ratio. The dark gray shaded region from 0.5-1.0 mgC m^{-2} represents the zone where organic matter may be the most stable and is not in extreme excess of either organic carbon or mineral surface area (see text for discussion). Filled symbols are dense fraction organic carbon (OC_{DF}:SA_{tot}) for Ridge Pit 1 and Toeslope Pit 6, revealing that most of the organic matter occurs in the dense fraction, indicating that the use of OC_{tot}:SA_{tot} is a valid approximation of this ratio. Note the scale break on the x-axis. Eroding sites are connected with dotted lines, depositional sites are connected with solid lines, and dashed lines connect dense fraction and total carbon from the same site, indicating composite intervals in Toeslope Pit 6.

4.4.5 Organic matter signatures (C/N, $\delta^{15}N$, $\delta^{13}C$, ^{14}C)

The profiles of C/N ratios display two distinct profile types that characterize better as eroding versus depositional profiles (Figure 7). The eroding, or stable, landscape positions, Ridge Pit 1 and Shoulder Pit 2, display a C/N decrease of approximately 2 that

continuously decreases with depth, and Interfluve Pit 5 exhibits a similar decrease, but in general has the lowest C/N ratio of all of the profiles (9-19, apart from an outlier at 0.5-0.6 m deep, where we identified a large (~5 cm), isolated charcoal piece) (Figure 4.7). Ridge Pit 1 has higher C/N ratios (11-23) throughout the depth profile than the Shoulder Pit 2 (8-20). The C/N ratio of charcoal sample from Swale Pit 4 was 68, which is the primary outlier in the data set.

The C/N ratio of Toeslope Pit 6 and Swale Pit 4 have discontinuous profiles that range from 15-23 up to 0.5 m, and from 11-16 below 0.5 m. Swale Pit 4 had a lens of charcoal approximately 5 cm thick underlain by clay at 0.6 m deep sitting discontinuously above a distinct boundary, above which the peaks in C/N at 0.25 and 0.5 m may also be due to minor amounts of charcoal incorporated into these intervals during transport or by bioturbation or other *in situ* soil mixing.

Dense fraction C/N ratios are very similar to the C/N ratios from the total carbon, ranging from 9-22. Light fraction samples increase dramatically with depth at Ridge Pit 1 and Toeslope Pit 6 and range from 24-89. The range of C/N values in bulk samples for the entire transect is 8-23.

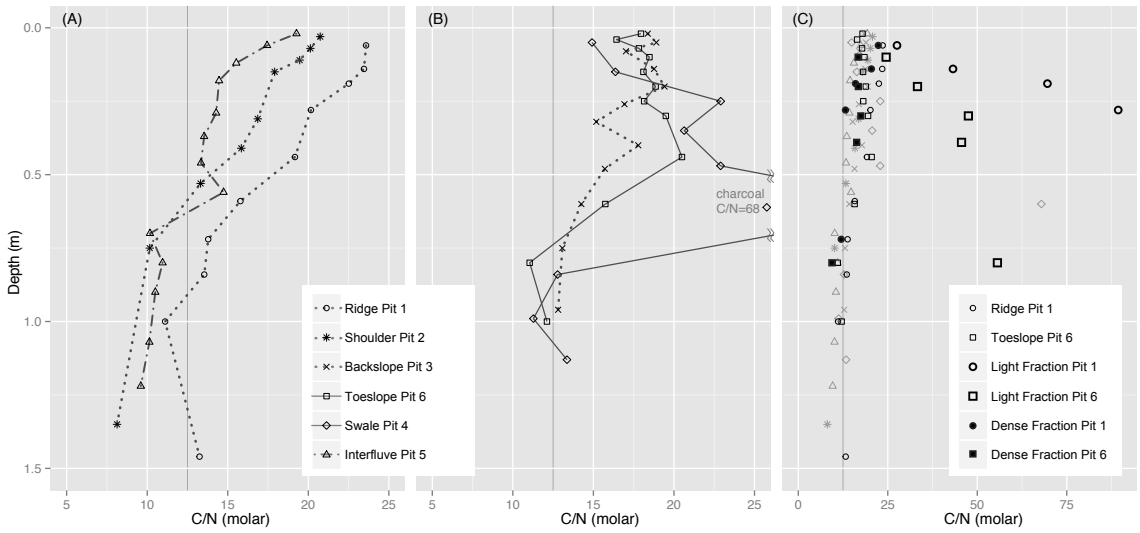

Figure 4.7. Molar ratio of carbon to nitrogen plots categorized by undisturbed (A) and disrupted (B) landscapes, and the C/N of dense and light fractions (2 g cm^{-3}). The data reveal discontinuous depth distribution profiles in soils that have been transported and deposited. We also observe that charcoal occurrence has a much different C/N ratio and the contamination of charcoal may explain outliers in Interfluve Pit 5 at ~0.6 m, as well as in Swale Pit 4 for intervals from 0.25-0.6 m, where we observed a lens of charcoal at 0.6 m. Gray line at C/N=12.5 is solely to aid visual comparison.

The depth profiles of $\delta^{15}N$ (Figure 4.8A) follow similar profile shapes regardless of landscape position, in which $\delta^{15}N$ values are low near the surface, increase by 3-5‰ between 0.25-1 meter, then decrease with depth. However, we also observe systematic differences in the $\delta^{15}N$ values by landscape position, in which $\delta^{15}N$ is substantially higher for nearly every depth interval in the depositional landscapes (Toeslope Pit 6 and Swale Pit 4) than the eroding landscape positions.

The depth profiles of $\delta^{13}C$ (Figure 4.8B) exhibit a variety of profile behaviors. Ridge Pit 1, which decreases between 0-0.12 meter, then increases by ~2‰ to 1 meter

deep. Shoulder Pit 2 and Interfluve Pit 5 increase with depth by ~1.5‰ and maintain that increase between 0.25-1 meter at the shoulder and from 0.25-0.75 meter at the interfluve, then both decrease over the remaining depth intervals measured. Shoulder Pit 3, Toeslope Pit 6, and Swale Pit 4 increase with depth by ~2‰ with some oscillation, and maintain the increase over the depth intervals measured.

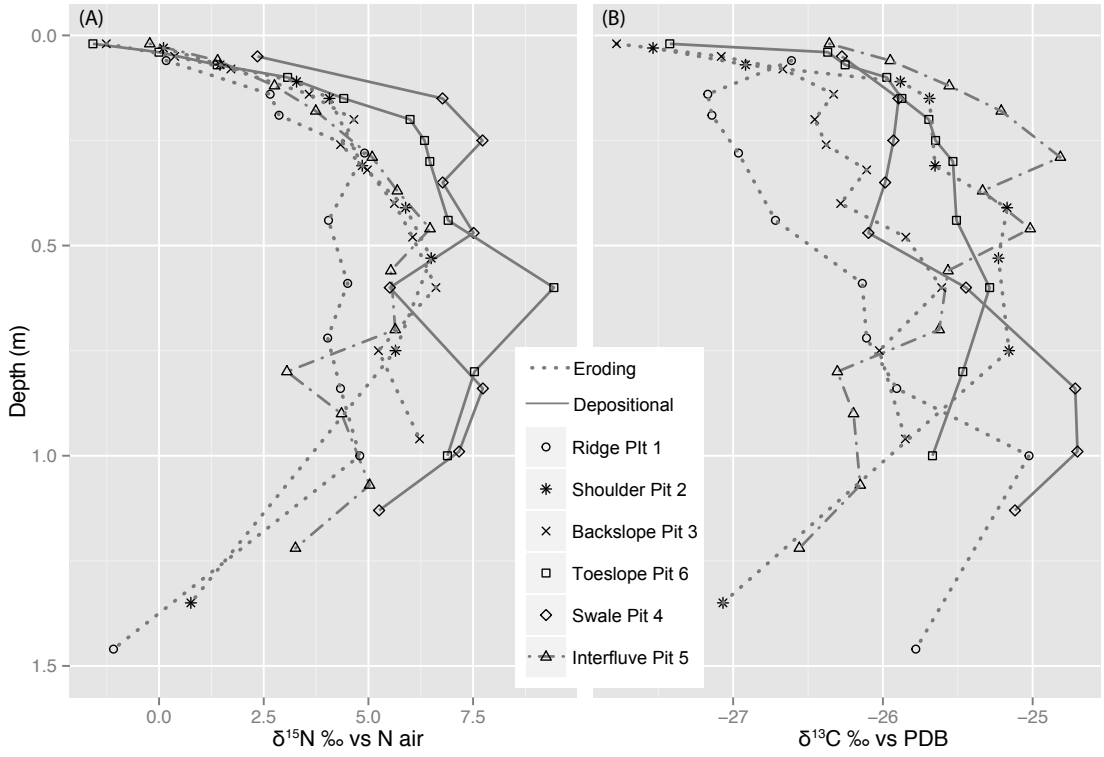

Figure 4.8. Depth profiles of $\delta^{15}N$ and $\delta^{13}C$ for all landscape positions. $\delta^{15}N$ profiles exhibit meaningful differences based on hillslope position, but the $\delta^{13}C$ profiles exhibit more variability by hillslope position.

Measurements of ^{14}C indicate that all dense fraction, or mineral associated carbon in the upper 20 cm at Ridge Pit 1 and Toeslope Pit 6 range in age from modern to 135±25 ybp (Figure 4.9). The dense fraction carbon ages range from 300-370±25 ybp from 20-40

cm in both pits, is 2190±100 ybp from 59-72 cm in Ridge Pit 1, and is 1335±35 ybp from 60-80 cm in Toeslope Pit 6.

Light fraction carbon in Toeslope Pit 6 corresponds well with the dense fraction carbon in the same intervals, with 0-6 cm = modern, 10-20 cm = 155±35, 20-30 cm = 410±25, 30-39 cm = 355±25, and 60-80 cm = 4210±30 ybp. The light fraction carbon in Ridge Pit 1 exhibits much higher ages than the dense fraction, with ages increasing with depth as follows: 0-6 cm = modern, 6-14 cm = 690±30, 14-19 cm = 1125±25, and 19-28 cm = 1690±25 ybp, below which we did not have light fraction sample. The 1-2 millimeter size charcoal distributed throughout the soil in Ridge Pit 1, which went unnoticed until samples were being processed in the laboratory, gives an age of 3035±25 ybp.

The charcoal deposit layer in Swale Pit 4, which contains pieces of charcoal up to 0.5 cm at the base of the colluvium at 55-60 cm, had a radiocarbon age of 145±45 ybp.

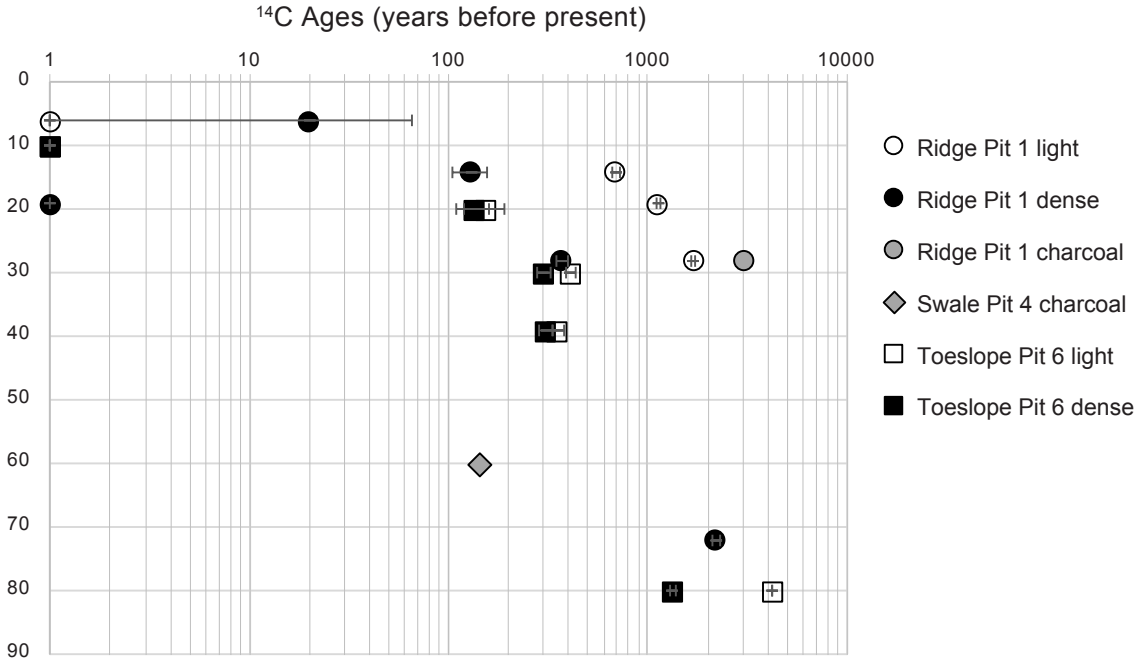

Figure 4.9. 14C ages for the Ridge Pit 1 and Toeslope Pit 6 indicate that radiocarbon ages up to 20 cm of dense fraction (mineral associated) carbon are younger than 200 years, and from 20-40 cm the ages are between 200-400 years before present. The occurrence of charcoal that is visible in hand sample in Ridge Pit 1 gives a date of 3035±25 ybp.

4.5 Discussion

4.5.1 Indications of soil mixing

Depth profiles of ^{137}Cs and ^{210}Pb do not show significant and consistent differences between eroding and depositional soils, indicating that soil mixing rates at decade to century time scales may not vary significantly with topographic position and on these time scales mixing is limited to the top 10 cm of the soils. This agrees with the absence of recent geomorphic soil perturbations such as accelerated erosion, lack of recent gully excavation, and absence of new colluvial deposits that would accentuate topographic variation in soil mixing and erosion. Radiocarbon ages of particulate organic

carbon (as represented by light fractions) and charcoal may also offer insights about soil mixing if we assume that charcoal found at depth in the soil is largely of surficial origin (instead of being originated from combustion of roots). Radiocarbon ages suggest that soil mixing penetrates over virtually the entire soil profile at time scales of several centuries to millennia (Figure 9). This deep soil mixing thus appears to have operated concomitantly with colluvial deposition at Toeslope Pit 6.

The different time frames of soil mixing at 0-0.2 m and 0.2-0.4 m have consequences for other organic matter profiles, including C/N. In the depositional landscapes, depth profiles of C/N in the upper 0.5 m are homogeneous (in contrast to increasing) and suggest greater soil mixing within the depositional soils. This suggests not only that preferential sorption of N enriched organic matter onto mineral surface occurs during the formation of organo-mineral associations in the depositional slope but also that this ratio persists during the soil formation and deposition of the top ~50 cm in the depositional soils. These properties are congruent with mixing and organic matter bonding to minerals, making C/N an indicator of organomineral sorption in this landscape.

4.5.2 Increase in organomineral associations in depositional profiles

The contrast between the OC/SA ratios in eroding and depositional landscapes indicates that there is more organic carbon per unit of mineral surface area in the upper 0.7 m of Toeslope Pit 6 and Swale Pit 4 than any of the eroding sites (Figure 4.6A). Because the majority of this organic carbon occurs in the dense fraction (Figure 4.6B),

the increase in OC/SA in depositional sites thus indicates that the processes involved in erosion and deposition promote new organomineral associations. These positive directions in the changes of the organic carbon per unit of mineral surface area and dense fraction carbon from the eroding to depositional areas also fit nicely with the positive changes in these quantities from eroding soils to Backslope Pit 3. This reasoning is based on the observation that soil disturbance by tree fall and animal burrowing is the major mechanism for colluvial flux and these mechanisms promote mixing, which we hypothesize is an important control on the formation rate of new organomineral associations. Additionally, our radiocarbon ages of dense fractions are evidence that this newly mineral-sorbed carbon is preserved within the landscape on time scales of hundreds of years. This result has substantial implications for how we account for the temporal and spatial scales of carbon in landscape, atmospheric, and ecological models because it showcases the significance of colluvial processes in maintaining the landscape scale inventory of this slowly cycled carbon soil carbon pool. It is notable that this result contrasts with recent geomorphic studies focusing on soil carbon in that most of the previous work focused on the fate of particulate (non-mineral associated) organic carbon through sediment transport chains.

Our observed OC/SA ratios may be viewed in comparison to the same properties measured for materials collected from oceanic shelves and other depositional sediment sinks. We designate the shaded region in Figure 4.6 from 0.5-1 mgC m^{-2} as a range of carbon loading where mineral surfaces are at their capacity to protect organic matter.

Above 1 mgC m^{-2}, we expect organic carbon to occur in excess of the protective capacity of the mineral matrix. Below 0.5 mgC m^{-2}, we expect mineral surface area to occur with excess capacity to protect organic matter and that associated organic carbon is very stable. This relationship was established by Mayer (1994b), where carbon loading of shallow (<75m) ocean shelf sediments over a wide range of locations occurred in the range of 0.86 mgC m^{-2}. Subsequent work corroborated that this range of carbon loading is a reasonable approximation for organic matter protection by mineral surfaces (Hedges and Keil, 1995; Keil et al., 1994), and established that topsoils can contain organic matter in excess of the ranges observed in ocean shelf sediments (Mayer and Xing, 2001; Wagai et al., 2009). Ocean shelves are the ultimate destination of hillslope soils that erode and follow the sediment transport continuum through river systems. Ocean shelf sediments have been subjected to extensive processing in the sediment transport continuum and the carbon associated with these sediments represents organic matter that is stably associated with minerals. We thus expect that topsoils with excess OC will undergo periods of loss and gain of organic carbon while transported in rivers, deltas, and into the ocean (Hedges and Keil, 1995).

Against the background of such continental scale changes in OC/SA ratios from terrestrial upland soils to oceanic depocenters, our work presents significant and systematic changes in the same ratios through a <100 meter distance from convex hillslope sediment source to convergent hillslope colluvial deposits. We observe a relationship between landscape position and depths of transitions from (1) mineral

loadings above their protective capacity for organic carbon, or with excess carbon (>1 mgC m^{-2}), to (2) soil minerals at their protective capacity (0.5-1 mgC m^{-2}), to (3) soil minerals below their protective capacity, or with excess mineral (<0.5 mgC m^{-2}). In eroding landscapes, Ridge Pit 1 and Shoulder Pit 2, the transition from excess organic carbon above mineral protective capacity to soil minerals at their protective capacity (1 → 2) occurs at 12-18 cm, and the subsequent change to OC below mineral protective capacity (2 → 3) is at 25-30 cm depth (Figure 4.6). In eroding landscapes mixing is primarily due to *in situ* processes (e.g. bioturbation, freeze-thaw cycles), where the depth and extent of mixing will depend on the site-specific processes, for example, the influences of tree roots (Gabet and Mudd, 2010), pocket gophers, and earth worms will substantially differ (Lyttle et al., 2014; Yoo et al., 2005). Depositional soils from Toeslope Pit 6 and Swale Pit 4 transition from excess carbon to at protective capacity (1 → 2) at 13-35 cm depth, and from at capacity to excess mineral (2 → 3) at 60-80 cm depth (Figure 4.6). In depositional landscapes the depth of stable and excess organic carbon can be much deeper than the corresponding upslope positions due to the accumulation of transported material that have gone through extensive mixing during colluvial transport. Increased protection of organic matter in depositional landscapes can come not only from an increase in organomineral associations during colluvial transport, but the different soil chemistry in depositional zones can make minerals more attractive to organic matter, and successive depositional sequences make the deeper carbon less accessible to degradation (Berhe and Kleber, 2013). Backslope Pit 3 represents a

transition between these net erosional and net depositional landscape positions, where concurrent soil creep and mixing in this steep portion of the landscape result in enhancing organomineral associations, and where the OC/SA ratios from excess carbon to at protective capacity (1 → 2) occur at 30 cm depth, and from at capacity to excess mineral (2 → 3) at 40 cm depth (Figure 4.6).

4.5.3 Processes that shift C/N values

Shifts in C/N can come from multiple mechanisms, including differences in organic matter sources, which set the starting point of C/N. Typical C/N ratios of forest foliage range from 19-66, with wood having much higher ranges between 250-2500 (Snowdon et al., 2005). Additions of charcoal can vastly increase C/N values because the molecular composition of charcoal is highly aromatic with very low nitrogen content (Lehmann et al., 2005; Skjemstad et al., 1996), and wood charcoal can exhibit a range of very high C/N ratios from 88 to nearly 400 (Hart and Luckai, 2014).

We did not observe a significant difference in vegetation, the aboveground source of organic matter, throughout the landscape, apart from the areas immediately around the stream and seeping springs, where skunk cabbage (Symplocarpus foetidus) was present, but the spring-fed stream is at elevations lower than the studied sites. The only indication for differences in organic matter sources in some soils was the visible presence of charcoal in the upper 0.30 m of Ridge Pit 1, and at 0.6 m in Swale Pit 4. Interfluve Pit 5 has a single piece of 5 cm size charcoal at 0.5 m, but mm-scale pieces of charcoal do not appear to be distributed through this pit, and the absence of distributed charcoal may

contribute to the lower C/N throughout Pit 5. The drastic outlier in C/N (68) in Swale Pit 4 at 0.6 m (Figure 4.7B), where we identified a charcoal lens (Figure 4.2), represents a C/N ratio that has been influenced by charcoal. Additionally, the high values of C/N (25-80) in the light fraction (Figure 4.7C) at Ridge Pit 1 and Toeslope Pit 6 may also be influenced by charcoal at these locations.

This presence of charcoal is corroborated by a radiocarbon age of 3035±25 ybp for a chunk of charcoal from Pit 1 that skews the light-fraction radiocarbon dates ranging from 600-1100 ybp (Figure 4.9), making them older than expected for contemporary plant-derived light fraction carbon. Additionally this charcoal sample is not likely to have been produced during post-settlement deforestation and charcoal production, which is more likely represented by the 145±25 ybp charcoal lens in Swale Pit 4, and which is morphologically tied to an erosional event (Figure 4.2). As a result of charcoal skewing the ages of light fraction carbon in Ridge Pit 1, we cannot indicate light fraction carbon turnover times. In fact, based on extremely high C/N ratios of the light fraction (Figure 4.7C), we expect that charcoal is present in Toeslope Pit 6, but the radiocarbon ages in Pit 6 indicate that the charcoal mixed within this soil pit is more likely from post-settlement charcoal production, which favored the use of trees under 40 years old (Lesley, 1859; Shields and Benson, 2011).

Although we did not visibly identify charcoal at Toeslope Pit 6, this portion of the landscape receives deposition from upslope positions where charcoal was observed in the

soil pits (Ridge Pit 1) and charcoal pits were identified in the Lidar DEM in Figure 4.1 (indicated by red arrows).

Aside from charcoal influences, soil profiles still exhibited systematic differences in C/N ratios, with distinct differences between cumulative soils that have developed from deposited colluvial materials (Figure 4.7B) compared to soils that occur in convex, erosional portions of the current landscape (Figure 4.7A). To explore the potential that these C/N trends are the result of topographic differences in organic matter decomposition, we examined soil temperature and soil moisture data from *in situ* sensors. Though the data is limited to one summer, logged data still shows some differences throughout the transect (Swale Pit 4 is not logged), with slightly lower summer temperatures (by 1-2 °C) and slightly higher soil moisture (by 0.05%) in Toeslope Pit 6 relative to erosional positions. Both soil moisture and temperature are known to be positively correlated with decomposition rates of organic matter, so it appears that our temperature and moisture trends by landscape position might cancel each other out.

We thus propose that association of fresh organic matter with mineral surfaces, facilitated by colluvial processes involving physical soil disturbance, erosion, and deposition, favors sorption of nitrogen rich organic matter. Organic nitrogen enrichment on minerals has been directly shown to occur due to sorptive fractionation mechanisms in aquatic settings, in which proteins are selectively sorbed to minerals over other biochemical classes (Aufdenkampe et al., 2001), and indirectly observed as lower C/N ratios in the dense, mineral-associated fraction of soils (Baldock and Skjemstad, 2000;

Baldock, 2002; Kleber et al., 2010, 2007; Sollins et al., 2009, 2006). The correlation between OC/SA and C/N must be assessed by inverting each to normalize each relative to carbon and avoid a spurious correlation with carbon in the numerators (Berges, 1997). For our soil transect the correlation of the mineral surface area per unit of organic carbon (SA/OC) vs the organic nitrogen per unit of organic carbon (N/C) for all specimen intervals yields a significant positive correlation of r=0.769 (n=65, p=<0.00001), indicating that the relationship between these properties is not random. This can be also shown from the discontinuous profiles in the depositional landscapes (Figure 4.7B) which exhibit the same decreasing profile shape of C/N ratios below ~0.5 m in the eroding profiles (Figure 4.7A). Thus the discontinuity in Figure 4.7B represents a shift to lower C/N in the depth intervals above ~0.5 m than is expected if the C/N profiles followed an eroding profile shape. This discontinuity in C/N ratios mimic the shape of the depth profiles for OC/SA (Figure 4.6), which again highlights that the relationship between these two properties is significant and not random.

The notion that organomineral association accompanies decreases in C/N ratios in the mineral-sorbed carbon pools is somewhat in contrast to the traditional understanding of C/N ratios, which holds that C is preferentially removed (instead of N) via consumption by microbes and lost as respiration of CO_2 (Schmidt et al., 2011). C/N decreases in depth profiles, and a decrease in C/N is traditionally attributed to lower abundance of organic matter with depth. But the majority of organic matter at depth is mineral associated, which is also a reasonable explanation for the decrease in C/N with

depth. In fact, our samples from 0.59-0.72 m in Ridge Well 1 have missing data because there was no light fraction to recover during density separation; all organic matter occurred in the dense fraction at this interval. Microbial processing also decreases with depth due to lower availability of organic matter for processing, lower soil moisture, cooler soil temperatures, and lower microbial abundance (Dick et al., 2005; Schmidt et al., 2011). Given that organic matter and microbial abundance decrease with depth, it is nebulous to attribute the depth decrease in C/N to microbial processing.

4.5.4 Interfluve transition from depositional to eroding landscape

The interfluve in Spring Brook (Figure 4.3) currently appears on the landscape as a convex ridge between two valleys, meaning it is currently an erosional part of the landscape (Gilbert, 1909; Heimsath et al., 1997; Yoo et al., 2007). However, Interfluve Pit 5 clearly displays the morphology of colluvial deposits to the depth of at least 1.24 meters, indicating that this was once a concave zone of depositional collection. Despite the strong evidence for the depositional origin of the Interfluve Pit 5 soil, organic carbon inventory, OC/SA, and C/N ratios of the soil mimic those of eroding landscapes (Figure 4.5, 4.6, and 4.7, respectively). Given its depositional morphology, we expected discontinuities in these depth profiles that reflect transient changes in sediment deposition and interactions between organic matter and minerals as observed in Toeslope Pit 6 and Swale Pit 4.

Despite the depth profile shapes mimicking the eroding landscapes, the overall inventory of organic carbon in Interfluve Pit 5 is higher than the eroding landscapes, and

the C/N ratios are the lowest of any in the transect. We thus postulate that both are lingering signatures of the original depositional context of this interfluve landform. In other words, the current Interfluve soil could be the result of interfluve deposition that occurred prior to the gully incision.

This type of landform may occur by mass wasting during periglacial climatic conditions (Cruickshank and Colhoun, 1965; King and Coates, 1973; Matsuoka, 2001), which prevailed at the study site during the last glacial maximum more than 12-18 kyr (Prentice et al., 1991). Analysis of meteoric ^{10}Be suggests 19 kyr as a minimum age of the landscape. Thus the landscape could have been re-set or re-sculpted at or before19 kyr, which coincides well with the periglacial period. Periglacial mass wasting features are often composed of a matrix of fine material, particularly silt, with or without rock clasts, occurring as a bimodal distribution of sizes. The fine material would form a flowing slurry under the right moisture and temperature conditions with sufficient viscosity to transport larger rocks within the slurry (Matsuoka, 2001). Periglacial mass wasting processes may have been the mechanism of the movement of soil and rock that were deposited at the location of Pit 5 at what is now an intermediate point in this landscape (Steven Peters, personal communication; Dorothy Merritts, personal communication after visiting the field site). We postulate that as glaciers receded and temperatures increased, fluvial processes transformed this depositional feature (swale, lobe, etc.) into an interfluve in this landscape and vegetation began to re-establish after the last glacial maximum.

Periglacial mass movement would provide the opportunity for mixing-derived association of organic matter with mineral surfaces, which would yield both a higher inventory of organic carbon and lower C/N in the depositional profile. Yet the current Interfluve soil profile does not exhibit a significant increase in organic carbon inventory. This may be because the depositional environment fed by the mass wasting was either carbon poor, or the time since the periglacial period was long enough for post-burial degradation of organic matter. Post-burial degradation on the time scale of thousands of years is a well-studied process in ocean shelf sediments, where oxygen exposure can effectively oxidize mineral-sorbed organic carbon over nitrogen on time scales of thousands of years, resulting in reduced total organic carbon and C/N ratios (Cowie et al., 1995; Hedges et al., 1999; Keil et al., 2004). We speculate that similar oxidative decomposition processes at Interfluve Pit 5 could have led to the observed profiles of relatively low organic carbon concentration, low OC/SA, low C/N, enriched $\delta^{13}C$ and low OC inventory that we more commonly observe in eroding landscape positions despite unambiguous soil morphological evidence that the inverfluve at Pit 5 is a colluvial depositional feature.

The challenge in providing an alternative hypotheses for the genesis of the Interfluve soil lies in the conflicts among the soil morphology indicating colluvial deposit, current convex-up interfluve morphology indicating net erosion, and the depth profiles of carbon contents and C/N ratio that are not clearly associated with the other observations from the eroding or depositional soils at the site. Though admittedly

speculative, our observations could be understood in the context of periglacial processes as a crucial mechanism behind the genesis of Interfluve soil.

5 Summary of findings and future work

5.1 Summary of research findings

5.1.1 Organic carbon-mineral associations increase with erosive transport

Carbon-mineral associations and carbon inventories increased down a hillslope transect due to the soil mixing processes that occur during erosion, transport, and deposition. In the minimally-erosive, first-order, forest study watershed, soil mixing occurs by natural processes such as soil creep, bioturbation, freeze-thaw cycles, and rain splash erosion. Measureable properties, including C/N ratio and the ratio of organic carbon to mineral surface area (OC/SA), can indicate changes in organomineral relationships within a landscape and may provide a proxy for the degree of organic matter stability. Analysis of density fractionated samples showed that dense fraction, mineral associated carbon had radiocarbon ages younger than 150 ybp in shallow (<20 cm) samples, indicating that contemporary soil mixing processes are promoting organomineral associations and longevity of soil organic matter in shallow soils. These ages are more than an order of magnitude less than the 8000 years that would be required to erode the upper 40 cm, based on ^{10}Be derived denudation rate at that site of 50 m/m.y., which means that denudation rates do not outpace the time scales of mineral-associated carbon turnover. These findings are significant for quantifying a soil's ability to sequester carbon and demonstrates how carbon sequestration varies through all positions in the landscape and by soil depth, which are critical parameters to improve model carbon fluxes in soil, biomass, and atmospheric models.

5.1.2 Quantifying weathering on geochemically variable rock

The most broadly used quantitative means of assessing rock weathering and depth to unweathered bedrock uses a geochemical mass balance, which requires bedrock homogeneity (Brimhall and Dietrich, 1987). The Laurels Schist is a metasedimentary schist with high geochemical variability, and to assess weathering this bedrock required a new approach to overcome the limitation of homogeneity. In collaboration with a statistician (Dr. Aaron Rendahl), we devised a robust statistical model that enabled objective identification of the depth extent of weathering, or the depth to bedrock, which was often decoupled from geomorphic boundaries, such as the transition from soil to rock and the groundwater table. The statistical model, introduced as an R library, is available as a new method for the weathering community to extend geochemical mass balance assessments in both homogeneous and heterogeneous bedrock. The model leverages a piecewise, least-squares regression and confidence intervals to assess rock variability and weathering trends. This new model overcomes several major limitations to assessing weathering and provides the first major expansion to the geochemical mass balance model in nearly thirty years. The model uses an open-source scripting approach that is accessible on GitHub and can be modified and refined by any author, while preserving previous versions for repeatable results.

5.1.3 Mineral surface area as a weathering indicator

Measuring mineral specific surface area is not currently part of the standard suite of measurements applied in weathering studies, despite its usefulness as a single, easy

laboratory measurement that sums the effect of nearly all physical and mineralogical alterations, and its role in mineral dissolution and organic carbon stabilization. Mineral surface area, when calculated as an inventory, acts as a clear weathering indicator that effectively dampens the "noise" of variable geochemical signatures. Surface area inventory of two 21-meter deep drill cores revealed that changes in surface area were not associated with morphologic boundaries such as the soil-weathered rock interface and the groundwater table. Instead, the major change in surface area occurred between 2-3 m deep, which points to biological processes such as tree rooting depth and oxygen gas ventilation depth as key drivers for the observed change in surface area production for both silicate and Citrate-Dithionate exchangeable oxide minerals. These findings warn against assuming that morphologic boundaries are critical depths where mineral surface characteristics change. Furthermore, our work shows the utility of mineral SSA measurements in identifying and determining the initiation depth and extent of chemical weathering, which is more typically estimated through laboratory measurements of mass change of rock forming elements and their associated minerals, to understand critical hydro-biogeochemical fronts within weathering profiles.

5.2 Future work

5.2.1 Depth of O_2 penetration as a limitation on biogeochemical processes

This dissertation research has inspired me to explore the processes influencing the penetration depth of O_2. We observe that the O_2 ventilation front may determine the depth of the chemical weathering front, but this soil gas also represents the presence and

extent of biological activity. I am motivated to pursue future research that measures *in situ* and laboratory soil gas along with fungal and microbial activity and weathering indicators to fully explore the interplay between belowground organic matter storage, mineral weathering, and nutrient release, and the biogeochemical processes that promote or prohibit soil heath and productivity. I hypothesize that belowground environments are composed of a coupled system where O_2 promotes weathering of iron from primary minerals, then in turn accelerates the silicate weathering engine, both of which provide nutrients for plant productivity and mineral surface area for organic matter stabilization. Supporting this hypothesis are (1) the observation of a strong positive correlation between iron oxide SSA and silicate SSA (Fisher, in submission); (2) the ubiquitous negative correlation of their respective geochemical weathering agents (i.e. O_2 for iron oxides and carbonic acid from elevated pCO_2 for phyllosilicates); (3) the ubiquitous trend of decreasing subsurface O_2 gas with depth to concentrations near zero at the depth where iron oxides appear and reduced iron minerals such as pyrite disappear; and (4) the typical trend of increasing subsurface pCO_2 with depth to concentrations that are typically 1-2 orders of magnitude higher than in the atmosphere. These two dynamic, bioactive gasses are critical controls for chemical weathering, and I wish to pursue future studies to measure subsurface O_2, pCO_2, and SSA to assess the vertical distribution and mechanisms of chemical weathering in all bedrock environments, including highly heterogeneous bedrock.

5.2.2 Iron minerals and organic matter across precipitation and time gradients

I would like to understand how iron minerals stabilize organic matter for carbon storage and sequestration under a variety of soil formation conditions. We believe that detailed characterization of major, minor, and trace iron mineral phases and their surface area will provide a better model for organic matter stabilization than categorizing minerals by orderliness of crystallinity as done in previous work. To test the behavior of iron and organic matter under a variety of soil formation conditions, I have arranged to characterize the composition, concentration, and grain size distribution of Fe-minerals in samples from two well-studied sequences of soils from Hawaii using well-established rock magnetic techniques and electron microscopy. The soil sequences isolate precipitation and time, respectively, to leverage an extraordinary range of natural controls on soil forming factors. Magnetic techniques are exquisitely sensitive to low concentrations (ppm) of minerals and do not require pulverization or chemical alteration, allowing us to preserve the natural state of minerals that are sensitive to changes in moisture, temperature, and redox conditions. We will examine the spatial configuration of Fe-minerals using scanning electron (SEM) and transmission electron microscopy (TEM). Mineral specific surface area (SSA) will be measured using N_2 adsorption and calculated using the BET multipoint isotherm method. For each specimen, we will measure SSA on three treatments to collect information about organomineral associations and the contribution of oxide minerals to SSA.

6 Bibliography

Aalto, R., Nittrouer, C. a, 2012. 210Pb geochronology of flood events in large tropical river systems. Philos. Trans. A. Math. Phys. Eng. Sci. 370, 2040–74. doi:10.1098/rsta.2011.0607

Aitchison, J., J. Egozcue, J., 2005. Compositional Data Analysis: Where Are We and Where Should We Be Heading? Math. Geol. 37, 829–850. doi:10.1007/s11004-005-7383-7

Alexandre, A., Meunier, J.-D., Colin, F., Koud, J.-M., 1997. Plant impact on the biogeochemical cycle of silicon and related weathering processes. Geochim. Cosmochim. Acta 61, 677–682. doi:10.1016/S0016-7037(97)00001-X

Andersen, J.L., Egholm, D.L., Knudsen, M.F., Jansen, J.D., Nielsen, S.B., 2015. The periglacial engine of mountain erosion – Part 1: Rates of frost cracking and frost creep. Earth Surf. Dyn. 3, 447–462.

Anderson, R.S., Anderson, S.P., Tucker, G.E., 2013. Rock damage and regolith transport by frost: An example of climate modulation of the geomorphology of the critical zone. Earth Surf. Process. Landforms 38, 299–316.

Anderson, S.P., Dietrich, W.E., Brimhall, G.H., 2002. Weathering profiles, mass-balance analysis, and rates of solute loss: Linkages between weathering and erosion in a small, steep catchment. Bull. Geol. Soc. Am. 114, 1143–1158.

Andrews, J.A., Schlesinger, W.H., 2001. Soil CO2 dynamics, acidification, and chemical weathering in a temperature forest with experimental CO2 enrichment. Global Biogeochem. Cycles 15, 149–162. doi:10.1029/2000GB001278

Argerich, A., Haggerty, R., Johnson, S.L., Wondzell, S.M., Dosch, N., Corson-Rikert, H., Ashkenas, L.R., Pennington, R., Thomas, C.K., 2016. Comprehensive multi-year carbon budget of a temperate headwater stream. J. Geophys. Res. Biogeosciences. doi:10.1002/2015JG003050

Aufdenkampe, A.K., Hedges, J.I., Richey, J.E., Krusche, A. V, Paulo, S., Llerena, C.A., 2001. Sorptive fractionation of dissolved organic nitrogen and amino acids onto fine sediments within the Amazon Basin. Liminology Oceanogr. 46, 1921–1935.

Aufdenkampe, A.K., Mayorga, E., Raymond, P.A., Melack, J.M., Doney, S.C., Alin, S.R., Aalto, R.E., Yoo, K., 2011. Riverine coupling of biogeochemical cycles between land, oceans, and atmosphere. Front. Ecol. Environ. 9, 53–60. doi:10.1890/100014

Baldock, J.A., 2002. Interactions of organic materials and microorganisms with minerals in the stabilization of soil structure, in: Huang, P.M., Bollag, J.M., Senesi, N. (Eds.), Interactions Between Soil Particles and Microorganisms: Impact on the Terrestrial Ecosystem. pp. 85–131.

Baldock, J.A., Skjemstad, J.O., 2000. Role of the soil matrix and minerals in protecting natural organic materials against biological attack. Org. Geochem. 31, 697–710.

Bazilevskaya, E., Rother, G., Mildner, D.F.R., Pavich, M., Cole, D., Bhatt, M.P., Jin, L., Steefel, C.I., Brantley, S.L., 2014. How Oxidation and Dissolution in Diabase and

Granite Control Porosity during Weathering. Soil Sci. Soc. Am. J. 79, 55. doi:10.2136/sssaj2014.04.0135
Berges, J.A., 1997. Ratios, regression statistics, and spurious correlations. Limnol. Oceanogr. 42, 1006–1007.
Berhe, A.A., Harden, J.W., Torn, M.S., Kleber, M., Burton, S.D., Harte, J., 2012. Persistence of soil organic matter in eroding versus depositional landform positions. J. Geophys. Res. Biogeosciences 117, n/a–n/a. doi:10.1029/2011JG001790
Berhe, A.A., Harte, J., Harden, J.W., Torn, M.S., 2007. The Significance of the Erosion-induced Terrestrial Carbon Sink. Bioscience 57, 337. doi:10.1641/B570408
Berhe, A.A., Kleber, M., 2013. Erosion, deposition, and the persistence of soil organic matter: mechanistic considerations and problems with terminology. Earth Surf. Process. Landforms 38, 908–912. doi:10.1002/esp.3408
Berner, R.A., 1992. Weathering, plants, and the long-term carbon cycle. Geochim. Cosmochim. Acta 56, 3225–3231. doi:10.1016/0016-7037(92)90300-8
Berner, R.A., Cochran, M.F., 1998. Plant-induced weathering of Hawaiian basalts. J. Sediment. Res. 68, 723–726. doi:10.2110/jsr.68.723
Blackmer, G.C., 2004. Bedrock geology of the Coatesville quadrangle, Chester County, Pennsylvania. Pennsylvania Geol. Surv. 4th ser.
Blatt, H., Jones, R.L., 1975. Proportions of Exposed Igneous, Metamorphic, and Sedimentary Rocks. Geol. Soc. Am. Bull. 86, 1085–1088. doi:10.1130/0016-7606(1975)86
Bouyoucos, G.J., 1962. Hydrometer Method Improved for Making Particle Size Analyses of Soils1. Agron. J. 54, 464.
Brantley, S.L., Goldhaber, M.B., Ragnarsdottir, K.V., 2007a. and Scales to Understand the Critical Zone. Earth 307–314.
Brantley, S.L., Goldhaber, M.B., Ragnarsdottir, K.V., 2007b. Crossing Disciplines and Scales to Understand the Critical Zone. Elements 3, 307–314. doi:10.2113/gselements.3.5.307
Brantley, S.L., Holleran, M.E., Jin, L., Bazilevskaya, E., 2013. Probing deep weathering in the Shale Hills Critical Zone Observatory, Pennsylvania (USA): the hypothesis of nested chemical reaction fronts in the subsurface. Earth Surf. Process. Landforms 38, 1280–1298. doi:10.1002/esp.3415
Brantley, S.L., Lebedeva, M., Bazilevskaya, E., 2013. Relating Weathering Fronts for Acid Neutralization and Oxidation to pCO2 and pO2, in: Treatise on Geochemistry: Second Edition. Elsevier Inc., pp. 327–352.
Brantley, S.L., Olsen, A.A., 2013. Reaction Kinetics of Primary Rock-Forming Minerals under Ambient Conditions, in: Treatise on Geochemistry: Second Edition. Elsevier Inc., pp. 69–113.
Brantley, S.L., Wilkinson, B.H., McElroy, B.J., Bellamy, P.H., Brown, E.T., Stallard, R., Larsen, M.C., Raisbeck, G.M., Yiou, F., Blanckenburg, F. Von, Fletcher, R.C., Buss, H.L., Brantley, S.L., Trumbore, S.E., Czimczik, C.I., Olson, J.S., Oost, K.

Van, Parton, W., Turner, M.G., Romme, W.H., Gardner, R.H., O'Neill, R. V., Kratz, T.K., White, A.F., Brantley, S.L., White, A.F., Wardle, D.A., Walker, L.R., Bardgett, R.D., Wiens, J.A., Chadwick, O.A., Chorover, J., Vitousek, P.M., Mooney, H.A., Lubchenco, J., Melillo, J.M., Melillo, J.M., Filippelli, G.M., 2008. Geology. Understanding soil time. Science 321, 1454–5. doi:10.1126/science.1161132

Brimhall, G.H., Dietrich, W.E., 1987. Constitutive mass balance relations between chemical composition, volume, density, porosity, and strain in metasomatic hydrochemcal systems: Results on weathering and pedogenesis. Geochim. Cosmochim. Acta 51, 567–587. doi:10.1016/0016-7037(87)90070-6

Brimhall, G.H., Lewis, C.J., Ague, J.J., Dietrich, W.E., Hampel, J., Teague, T., Rix, P., 1988. Metal enrichment in bauxites by deposition of chemically mature aeolian dust. Nature 333, 819–824.

Brunauer, S., Emmett, P.H., Teller, E., 1938. Adsorption of Gases in Multimolecular Layers. J. Am. Chem. Soc. 60, 309–319. doi:10.1021/ja01269a023

Buccianti, A., 2011. Natural Laws Governing the Distribution of the Elements in Geochemistry: The Role of the Log-Ratio Approach, in: Compositional Data Analysis. John Wiley & Sons, Ltd, Chichester, UK, pp. 255–266. doi:10.1002/9781119976462.ch18

Burt, R., 2004. Soil Survey Laboratory Methods Manual. Soil Surv. Investig. Rep., Soil Survey Investigations Report 42, 735. doi:10.1021/ol049448l

Burt, R., Staff, S.S. (Eds.), 2014. Kellogg Soil Survey Laboratory Methods Manual. Soil Survey Investigations Report No. 42, Version 5. ed. USDA - Natural Resources Conservation Service.

Buss, H.L., Sak, P.B., Webb, S.M., Brantley, S.L., 2008. Weathering of the Rio Blanco quartz diorite, Luquillo Mountains, Puerto Rico: Coupling oxidation, dissolution, and fracturing. Geochim. Cosmochim. Acta 72, 4488–4507.

Carson, M.A., Kirkby, M.J., 1972. Hillslope Form and Process. Cambridge University Press, Cambridge, UK.

Chadwick, O.A., Brimhall, H., Hendricks, D.M., 1990. From a black to a gray box — a mass balance interpretation of pedogenesis. Geomorphology 3, 369–390. doi:10.1016/0169-555X(90)90012-F

Ciolkosz, E.J., Cronce, R.C., Sevon, W.D., 1986. Periglacial Features in Pennsylvania, Agronomy Series Number 92. University Park, PA 16802.

Ciolkosz, E.J., Waltman, W.J., 1995. Cambic Horizons in Pennsylvania Soils, Agronomy Series Number 133. University Park, PA 16802.

Clark, G.M., Ciolkosz, E.J., 1988. Periglacial geomorphology of the Appalachian highlands and interior highlands south of the glacial border - A review. Geomorphology 1, 191–220.

Clarke, B.A., Burbank, D.W., 2011. Quantifying bedrock-fracture patterns within the shallow subsurface: Implications for rock mass strength, bedrock landslides, and erodibility. J. Geophys. Res. Earth Surf. 116.

Clarke, B.A., Burbank, D.W., 2010. Bedrock fracturing, threshold hillslopes, and limits to the magnitude of bedrock landslides. Earth Planet. Sci. Lett. 297, 577–586.
Cochran, M.F., Berner, R.A., 1996. Promotion of chemical weathering by higher plants: field observations on Hawaiian basalts. Chem. Geol. 132, 71–77. doi:10.1016/S0009-2541(96)00042-3
Coplen, T.B., Brand, W.A., Gehre, M., Gröning, M., Meijer, H.A.J., Toman, B., Verkouteren, R.M., 2006. After two decades a second anchor for the VPDBδ13C scale. Rapid Commun. Mass Spectrom. 20, 3165–3166. doi:10.1002/rcm.2727
Cowie, G.L., Hedges, J.I., Prahl, F.G., de Lance, G.J., 1995. Elemental and major biochemical changes across an oxidation front in a relict turbidite: An oxygen effect. Geochim. Cosmochim. Acta 59, 33–46.
Cruickshank, J.G., Colhoun, E.A., 1965. Observations on Pingos and Other LandForms in Schuchertdal, Northeast Greenland. Geogr. Ann. Ser. A, Phys. Geogr. 47, 224. doi:10.2307/520663
Davidson, E.A., Trumbore, S.E., 1995. Gas diffusivity and production of CO2 in deep soils of the eastern Amazon. Tellus 47, 550–565. doi:10.1034/j.1600-0889.47.issue5.3.x
Day, P.R., 1965. Methods of Soil Analysis. Part 1. Physical and Mineralogical Properties, Including Statistics of Measurement and Sampling, Methods of Soil Analysis. Part 1. Physical and Mineralogical Properties, Including Statistics of Measurement and Sampling, Agronomy Monograph. American Society of Agronomy, Soil Science Society of America. doi:10.2134/agronmonogr9.1.c43
De Vos, W., Tarvainen, T., Salminen, R., Reeder, S., De Vivo, B., Demetriades, A., Pirc, S., Batista, M.J., Marsina, K., Ottesen, R.T., O'Connor, P.J., Bidovec, M., Lima, A., Siewers, U., Smith, B., Taylor, H., Shaw, R., Salpeteur, I., Gregorauskiene, V., Halamic, J., Slaninka, I., Lax, K., Gravesen, P., Birke, M., Breward, N., Ander, E.L., Jordan, G., Duris, M., Klein, P., Locutura, J., Bel-lan, A., Pasieczna, A., Lis, J., Mazreku, A., Gilucis, A., Heitzmann, P., Klaver, G., Petersell, V., 2006. Geochemical Atlas of Europe. Part 2 - Interpretation of Geochemical Maps, Additional Tables, Figures, Maps, and Related Publications.
Dick, D.P., Gonçalves, C.N., Dalmolin, R.S.D., Knicker, H., Klamt, E., Kögel-Knabner, I., Simões, M.L., Martin-Neto, L., 2005. Characteristics of soil organic matter of different Brazilian Ferralsols under native vegetation as a function of soil depth. Geoderma 124, 319–333. doi:10.1016/j.geoderma.2004.05.008
Dietrich, W.E., Reiss, R., Hsu, M.L., Montgomery, D.R., 1995. A process-based model for colluvial soil depth and shallow landsliding using digital elevation data. Hydrol. Process. 9, 383–400. doi:10.1002/hyp.3360090311
Dixon, J.L., Heimsath, A.M., Amundson, R., 2009. The critical role of climate and saprolite weathering in landscape evolution. Earth Surf. Process. Landforms 34, 1507–1521. doi:10.1002/esp.1836
Drever, J.I., 1994. The effect of land plants on weathering rates of silicate minerals. Geochim. Cosmochim. Acta 58, 2325–2332. doi:10.1016/0016-7037(94)90013-2

Eberl, D.D., 2003. User's Guide to RockJock - A Program for Determining Quantitative Mineralogy From Powder X-Ray Diffraction Data. U.S. Geol. Surv. Open-File Rep. 03-78 1–47.
Essington, M., 2003. Soil and Water Chemistry: An Integrative Approach, 1st ed, CRC Press. CRC Press, Boca Raton.
Eusterhues, K., Rumpel, C., Kogel-Knabner, I., 2005. Organo-mineral associations in sandy acid forest soils: importance of specific surface area, iron oxides and micropores. Eur. J. Soil Sci. 050912034650049. doi:10.1111/j.1365-2389.2005.00710.x
Fisher, B.A., Yoo, K., Aufdenkampe, A.K., Nater, E.A., Nyquist, J.E., n.d. Vertical and lateral distribution of mineral surface area reveals the importance of iron oxidation and oxygen gas penetration in chemical weathering. J. Geophys. Res. Earth Surf.
Foley, J., Defries, R., Asner, G.P., Barford, C., Bonan, G., Carpenter, S.R., Chapin, F.S., Coe, M.T., Daily, G.C., Gibbs, H.K., Helkowski, J.H., Holloway, T., Howard, E. a, Kucharik, C.J., Monfreda, C., Patz, J. a, Prentice, I.C., Ramankutty, N., Snyder, P.K., 2005. Global consequences of land use. Science 309, 570–4. doi:10.1126/science.1111772
Gabet, E.J., Mudd, S.M., 2010. Bedrock erosion by root fracture and tree throw: A coupled biogeomorphic model to explore the humped soil production function and the persistence of hillslope soils. J. Geophys. Res. Earth Surf. 115.
Gardner, T.W., Ritter, J.B., Shuman, C.A., Bell, J.C., Sasowsky, K.C., Pinter, N., 1991. A periglacial stratified slope deposit in the valley and ridge province of central Pennsylvania, USA: Sedimentology, stratigraphy, and geomorphic evolution. Permafr. Periglac. Process. 2, 141–162. doi:10.1002/ppp.3430020208
Gilbert, G., 1909. The convexity of hilltops. J. Geol. 17, 344–350.
Graham, R., Rossi, A., Hubbert, R., 2010. Rock to regolith conversion: Producing hospitable substrates for terrestrial ecosystems. GSA Today 4–9. doi:10.1130/GSAT57A.1
Haberer, C.M., Muniruzzaman, M., Grathwohl, P., Rolle, M., 2015. Diffusive–Dispersive and Reactive Fronts in Porous Media: Iron(II) Oxidation at the Unsaturated–Saturated Interface. Vadose Zo. J. 14, vzj2014.07.0091. doi:10.2136/vzj2014.07.0091
Hales, T.C., Roering, J.J., 2007. Climatic controls on frost cracking and implications for the evolution of bedrock landscapes. J. Geophys. Res. Earth Surf. 112.
Hancock, G., Kirwan, M., 2007. Summit erosion rates deduced from 10BE: Implications for relief production in the central Appalachians. Geology 35, 89–92.
Harden, J.W., Sharpe, J.M., Parton, W.J., Ojima, D.S., Fries, T.L., Huntington, T.G., Dabney, S.M., 1999. Dynamic replacement and loss of soil carbon on eroding cropland. Global Biogeochem. Cycles 13, 885–901. doi:10.1029/1999GB900061
Hart, S.A., Luckai, N.J., 2014. Charcoal carbon pool in North American boreal forests. Ecosphere 5, 1–14. doi:10.1890/ES13-00086.1

Hartmann, D.L., Tank, a. M.G.K., Rusticucci, M., 2013. IPCC Fifth Assessment Report, Climatie Change 2013: The Physical Science Basis. Ipcc AR5, 31 – 39.
Hasenmueller, E.A., Jin, L., Stinchcomb, G.E., Lin, H., Brantley, S.L., Kaye, J.P., 2015. Topographic controls on the depth distribution of soil CO2 in a small temperate watershed. Appl. Geochemistry 63, 58–69. doi:10.1016/j.apgeochem.2015.07.005
Hayashi, K.I., Fujisawa, H., Holland, H.D., Ohmoto, H., 1997. Geochemistry of approximately 1.9 Ga sedimentary rocks from northeastern Labrador, Canada. Geochim. Cosmochim. Acta 61, 4115–37.
Hedges, J.I., Hu, F.S., Devol, A.H., Hartnett, H.E., Tsamakis, E., Keil, R.G., 1999. Sedimentary organic matter preservation: A test for selective degradation under oxic conditions. Am. J. Sci. 299, 529–555.
Hedges, J.I., Keil, R.G., 1995. Sedimentary organic matter preservation: an assessment and speculative synthesis. Mar. Chem. 49, 137–139. doi:10.1016/0304-4203(95)00013-H
Heimsath, A.M., Burke, B.C., 2013. The impact of local geochemical variability on quantifying hillslope soil production and chemical weathering. Geomorphology 200, 75–88.
Heimsath, A.M., Dietrich, W.E., Nishiizumi, K., Finkel, R.C., 2001. Stochastic processes of soil production and transport: erosion rates, topographic variation and cosmogenic nuclides in the Oregon Coast Range. Earth Surf. Process. Landforms 26, 531–552. doi:10.1002/esp.209
Heimsath, A.M., Dietrich, W.E., Nishiizumi, K., Finkel, R.C., 1997. The soil production function and landscape equilibrium. Nature 388, 21–24.
Heimsath, A.M., Fink, D., Hancock, G.R., 2009. The “humped” soil production function: eroding Arnhem Land, Australia. Earth 1684, 1674–1684. doi:10.1002/esp
Heimsath, A.M., Furbish, D.J., Dietrich, W.E., 2005. The illusion of diffusion: Field evidence for depth-dependent sediment transport. Geology 33, 949. doi:10.1130/G21868.1
Heister, K., 2014. The measurement of the specific surface area of soils by gas and polar liquid adsorption methods-limitations and potentials. Geoderma 216, 75–87. doi:10.1016/j.geoderma.2013.10.015
Herndon, E.M., Jin, L., Brantley, S.L., 2011. Soils reveal widespread manganese enrichment from industrial inputs. Environ. Sci. Technol. 45, 241–7. doi:10.1021/es102001w
Hinsinger, P., 2001. Bioavailability of soil inorganic P in the rhizosphere as affected by root-induced chemical changes: a review. Plant Soil 237, 173–195. doi:10.1023/A:1013351617532
Houghton, R.A., 2007. Balancing the Global Carbon Budget. Annu. Rev. Earth Planet. Sci. 35, 313–347. doi:10.1146/annurev.earth.35.031306.140057
Jackson, M., Hseung, Y., 1952. Weathering sequence of clay-size minerals in soils and sediments: II. Chemical weathering of layer silicates. Soil Sci. Soc. Am. J. 16, 3–6.

Jackson, M.L., 1963. Interlaying of expansible layer sililcates in soils by chemical weathering. Clays Clay Miner.
Jackson, M.L., Barak, P., 2005. Soil Chemical Analysis: Advanced Course. UW-Madison Libraries Parallel Press.
Jackson, M.L., Tyler, S.A., Willis, A.L., Bourbeau, G.A., Pennington, R.P., 1948. Weathering Sequence of Clay-Size Minerals in Soils and Sediments. I. Fundamental Generalizations. J. Phys. Colloid Chem. 52, 1237–1260. doi:10.1021/j150463a015
Jin, L., Ravella, R., Ketchum, B., Bierman, P.R., Heaney, P., White, T., Brantley, S.L., 2010. Mineral weathering and elemental transport during hillslope evolution at the Susquehanna/Shale Hills Critical Zone Observatory. Geochim. Cosmochim. Acta 74, 3669–3691. doi:10.1016/j.gca.2010.03.036
Johnson, M.S., Lehmann, J., Riha, S.J., Krusche, A. V., Richey, J.E., Ometto, J.P.H.B., Couto, E.G., 2008. CO2 efflux from Amazonian headwater streams represents a significant fate for deep soil respiration. Geophys. Res. Lett. 35.
Kaste, J.M., Heimsath, A.M., Bostick, B.C., 2007. Short-term soil mixing quantified with fallout radionuclides. Geology 35, 243–246.
Keil, R.G., Dickens, A.F., Arnarson, T., Nunn, B.L., Devol, A.H., 2004. What is the oxygen exposure time of laterally transported organic matter along the Washington margin?, in: Marine Chemistry. pp. 157–165.
Keil, R.G., Mayer, L.M., 2014. Mineral Matrices and Organic Matter, Treatise on Geochemistry: Second Edition. Elsevier Ltd. doi:doi:10.1016/B978-0-08-095975-7.01024-X
Keil, R.G., Mayer, L.M., Quay, P.D., Richey, J.E., Hedges, J.I., 1997. Loss of organic matter from riverine particles in deltas. Geochim. Cosmochim. Acta 61, 1507–1511. doi:10.1016/S0016-7037(97)00044-6
Keil, R.G., Tsamakis, E., Fuh, C.B., Giddings, J.C., Hedges, J.I., 1994. Mineralogical and textural controls on the organic composition of coastal marine sediments: Hydrodynamic separation using SPLITT-fractionation. Geochim. Cosmochim. Acta 58, 879–893. doi:10.1016/0016-7037(94)90512-6
King, C.A.M., Coates, D.R., 1973. Glacio-periglacial landforms within the Susquehanna Great Bend area of New York and Pennsylvania. Quat. Res. 3, 600–620.
Kleber, M., Nico, P.S., Plante, A., Filley, T., Kramer, M., Swanston, C., Sollins, P., 2010. Old and stable soil organic matter is not necessarily chemically recalcitrant: implications for modeling concepts and temperature sensitivity. Glob. Chang. Biol. 17, 1097–1107. doi:10.1111/j.1365-2486.2010.02278.x
Kleber, M., Sollins, P., Sutton, R., 2007. A conceptual model of organo-mineral interactions in soils: self-assembly of organic molecular fragments into zonal structures on mineral surfaces. Biogeochemistry 85, 9–24. doi:10.1007/s10533-007-9103-5
Lal, R., 2003. Soil erosion and the global carbon budget. Environ. Int. 29, 437–50. doi:10.1016/S0160-4120(02)00192-7

Lebedeva, M.I., Fletcher, R.C., Brantley, S.L., 2010. A mathematical model for steady-state regolith production at constant erosion rate. Earth Surf. Process. Landforms 524, n/a–n/a. doi:10.1002/esp.1954

Lehmann, J., Liang, B., Solomon, D., Lerotic, M., Luiz??o, F., Kinyangi, J., Sch??fer, T., Wirick, S., Jacobsen, C., 2005. Near-edge X-ray absorption fine structure (NEXAFS) spectroscopy for mapping nano-scale distribution of organic carbon forms in soil: Application to black carbon particles. Global Biogeochem. Cycles 19, 1–12.

Lesley, J.P., 1859. The iron manufacturer's guide to the furnaces, forges and rolling mills of the United States: With maps and plates. Wiley.

Liptzin, D., Silver, W.L., Detto, M., 2011. Temporal dynamics in soil oxygen and greenhouse gases in two humid tropical forests. Ecosystems 14, 171–182. doi:DOI 10.1007/s10021-010-9402-x

Liu, S., 2003. Modeling carbon dynamics in vegetation and soil under the impact of soil erosion and deposition. Global Biogeochem. Cycles 17, 1–24. doi:10.1029/2002GB002010

Lowrie, W., 1997. Fundamentals of Geophysics. Cambridge University Press.

Lyttle, A., Yoo, K., Hale, C., Aufdenkampe, A., Sebestyen, S.D., Resner, K., Blum, A., 2014. Impact of Exotic Earthworms on Organic Carbon Sorption on Mineral Surfaces and Soil Carbon Inventories in a Northern Hardwood Forest. Ecosystems 18, 16–29. doi:10.1007/s10021-014-9809-x

Maher, K., 2010. The dependence of chemical weathering rates on fluid residence time. Earth Planet. Sci. Lett. 294, 101–110. doi:10.1016/j.epsl.2010.03.010

Marshall, J.A., Roering, J.J., 2014. Diagenetic variation in the Oregon Coast Range: Implications for rock strength, soil production, hillslope form, and landscape evolution. J. Geophys. Res. Earth Surf. 119, 1395–1417.

Matisoff, G., Whiting, P.J., 2012. Measuring Soil Erosion Rates Using Natural (7Be, 210Pb) and Anthropogenic (137Cs, 239,240Pu) Radionuclides, in: Handbook of Environmental Isotope Geochemistry. Springer Berlin Heidelberg, Berlin, Heidelberg, pp. 487–519. doi:10.1007/978-3-642-10637-8_25

Matsuoka, N., 2001. Solifluction rates, processes and landforms: A global review. Earth-Science Rev. 55, 107–134.

Mayer, L.M., 1994a. Surface area control of organic carbon accumulation in continental shelf sediments. Geochim. Cosmochim. Acta 58, 1271–1284. doi:10.1016/0016-7037(94)90381-6

Mayer, L.M., 1994b. Relationships between mineral surfaces and organic carbon concentrations in soils and sediments. Chem. Geol. 114, 347–363. doi:10.1016/0009-2541(94)90063-9

Mayer, L.M., Xing, B., 2001. Organic Matter – Surface Area Relationships in Acid Soils 65, 567–571.

McCarty, G.W., Ritchie, J.C., 2002. Impact of soil movement on carbon sequestration in agricultural ecosystems. Environ. Pollut. 116, 423–30.

McLennan, S.M., 2001. Relationships between the trace element composition of sedimentary rocks and upper continental crust. Geochemistry, Geophys. Geosystems 2, n/a–n/a. doi:10.1029/2000GC000109
Miesch, A.T., Chapman, R.P., 1977. Log transformations in geochemistry. J. Int. Assoc. Math. Geol. 9, 191–198. doi:10.1007/BF02312512
Mikutta, R., Kleber, M., Kaiser, K., Jahn, R., 2005. Review: organic matter removal from soils using hydrogen peroxide, sodium hypochlorite, and disodium peroxodisulfate. Soil Sci. Soc. Am. J. 69, 120–135.
Mikutta, R., Schaumann, G.E., Gildemeister, D., Bonneville, S., Kramer, M.G., Chorover, J., Chadwick, O. a., Guggenberger, G., 2009. Biogeochemistry of mineral-organic associations across a long-term mineralogical soil gradient (0.3-4100 kyr), Hawaiian Islands. Geochim. Cosmochim. Acta 73, 2034–2060.
Moore, J., Lichtner, P.C., White, A.F., Brantley, S.L., 2012. Using a reactive transport model to elucidate differences between laboratory and field dissolution rates in regolith. Geochim. Cosmochim. Acta 93, 235–261.
Moulton, K.L., 2000. Solute flux and mineral mass balance approaches to the quantification of plant effects on silicate weathering. Am. J. Sci. 300, 539–570. doi:10.2475/ajs.300.7.539
Muggeo, V.M.R., 2008. segmented: An R package to Fit Regression Models with Broken-Line Relationships. R News 8, 20–25.
Navarre-Sitchler, A., Steefel, C.I., Yang, L., Tomutsa, L., Brantley, S.L., 2009. Evolution of porosity and diffusivity associated with chemical weathering of a basalt clast. J. Geophys. Res. 114, F02016. doi:10.1029/2008JF001060
Navarre-Sitchler, A.K., Cole, D.R., Rother, G., Jin, L., Buss, H.L., Brantley, S.L., 2013. Porosity and surface area evolution during weathering of two igneous rocks. Geochim. Cosmochim. Acta 109, 400–413. doi:10.1016/j.gca.2013.02.012
Oh, N., Richter, D., 2005. Elemental translocation and loss from three highly weathered soil-bedrock profiles in the southeastern United States. Geoderma 126, 5–25. doi:10.1016/j.geoderma.2004.11.005
Özdemir, Ö., Dunlop, D.J., Moskowitz, B.M., 2002. Changes in remanence, coercivity and domain state at low temperature in magnetite. Earth Planet. Sci. Lett. 194, 343–358. doi:10.1016/S0012-821X(01)00562-3
Parsekian, A.D., Singha, K., Minsley, B.J., Holbrook, W.S., Slater, L., 2015. Multiscale geophysical imaging of the critical zone. Rev. Geophys.
Pavich, M.J., 1989. Regolith residence time and the concept of surface age of the Piedmont "Peneplain." Geomorphology 2, 181–196.
Prentice, I.C., Bartlein, P.J., Webb III, T., 1991. Vegetation and climate change in Eastern North America since the last glacial maximum. Ecology 72, 2038–2056.
Quine, T.A., Van Oost, K., 2007. Quantifying carbon sequestration as a result of soil erosion and deposition: retrospective assessment using caesium-137 and carbon inventories. Glob. Chang. Biol. 13, 2610–2625. doi:10.1111/j.1365-2486.2007.01457.x

Quinton, J.N., Govers, G., Van Oost, K., Bardgett, R.D., 2010. The impact of agricultural soil erosion on biogeochemical cycling. Nat. Geosci. 3, 311–314.
Railsback, L.B., 2003. An earth scientist's periodic table of the elements and their ions. Geology 31, 737. doi:10.1130/G19542.1
Rasmussen, B., 2005. Zircon growth in very low grade metasedimentary rocks: evidence for zirconium mobility at ~250°C. Contrib. to Mineral. Petrol. 150, 146–155. doi:10.1007/s00410-005-0006-y
Raymo, M.E., Ruddiman, W.F., 1992. Tectonic forcing of late Cenozoic climate. Nature 359, 117 – 122.
Rempe, D.M., Dietrich, W.E., 2014. A bottom-up control on fresh-bedrock topography under landscapes 2014. doi:10.1073/pnas.1404763111
Reynolds, R., Belnap, J., Reheis, M., Lamothe, P., Luiszer, F., 2001. Aeolian dust in Colorado Plateau soils: nutrient inputs and recent change in source. Proc. Natl. Acad. Sci. U. S. A. 98, 7123–7.
Richardson, D.C., Newbold, J.D., Aufdenkampe, A.K., Taylor, P.G., Kaplan, L.A., 2013. Measuring heterotrophic respiration rates of suspended particulate organic carbon from stream ecosystems. Limnol. Oceanogr. Methods 11, 247–261.
Richter, D. de B., Billings, S.A., 2015. "One physical system": Tansley's ecosystem as Earth's critical zone. New Phytol.
Riebe, C.S., Kirchner, J.W., Finkel, R.C., 2004. Erosional and climatic effects on long-term chemical weathering rates in granitic landscapes spanning diverse climate regimes. Earth Planet. Sci. Lett. 224, 547–562. doi:10.1016/j.epsl.2004.05.019
Riebe, C.S., Kirchner, J.W., Finkel, R.C., 2003. Long-term rates of chemical weathering and physical erosion from cosmogenic nuclides and geochemical mass balance. Geochim. Cosmochim. Acta 67, 4411–4427. doi:10.1016/S0016-7037(03)00382-X
Ritchie, J.C., Mchenry, J.R., 1990. Application of Radioactive Fallout Cesium-137 for Measuring Soil Erosion and Sediment Accumulation Rates and Patterns: A Review 233, 215–233.
Roering, J.J., Marshall, J., Booth, A.M., Mort, M., Jin, Q., 2010. Evidence for biotic controls on topography and soil production. Earth Planet. Sci. Lett. 298, 183–190. doi:10.1016/j.epsl.2010.07.040
Schlesinger, W.H., Andrews, J.A., 2000. Soil respiration and the global carbon cycle. Biogeochemistry 48, 7–20. doi:10.1023/A:1006247623877
Schmidt, M.W.I., Torn, M.S., Abiven, S., Dittmar, T., Guggenberger, G., Janssens, I. a, Kleber, M., Kögel-Knabner, I., Lehmann, J., Manning, D. a C., Nannipieri, P., Rasse, D.P., Weiner, S., Trumbore, S.E., 2011. Persistence of soil organic matter as an ecosystem property. Nature 478, 49–56. doi:10.1038/nature10386
Shields, D., Benson, B., 2011. Catalyst for Conservation: the Brandywine Conservancy's success in saving King Ranch lands in Pennsylvania, 1st ed. Pemcor Printing, LLC, USA.

Silver, W.L., Thompson, A.W., McGroddy, M.E., Varner, R.K., Dias, J.D., Silva, H., Crill, P.M., Keller, M., 2005. Fine root dynamics and trace gas fluxes in two lowland tropical forest soils. Glob. Chang. Biol. 11, 290–306. doi:10.1111/j.1365-2486.2005.00903.x

Skjemstad, J.O., Clarke, P., Taylor, J.A., Oades, J.M., McClure, S., 1996. The chemistry and nature of protected carbon in soil. Aust. J. Soil Res. 34, 251–271.

Snowdon, P., Ryan, P., Raison, J., 2005. Review of C:N Ratios in Vegetation, Litter and Soil Under Australian Native Forests and Plantations, National Carbon Accounting System Technical Report No. 45.

Sollins, P., Kramer, M.G., Swanston, C., Lajtha, K., Filley, T., Aufdenkampe, A.K., Wagai, R., Bowden, R.D., 2009. Sequential density fractionation across soils of contrasting mineralogy: evidence for both microbial- and mineral-controlled soil organic matter stabilization. Biogeochemistry 96, 209–231. doi:10.1007/s10533-009-9359-z

Sollins, P., Swanston, C., Kleber, M., Filley, T., Kramer, M., Crow, S., Caldwell, B. a., Lajtha, K., Bowden, R., 2006. Organic C and N stabilization in a forest soil: Evidence from sequential density fractionation. Soil Biol. Biochem. 38, 3313–3324. doi:10.1016/j.soilbio.2006.04.014

Solomon, D., Lehmann, J., Harden, J., Wang, J., Kinyangi, J., Heymann, K., Karunakaran, C., Lu, Y., Wirick, S., Jacobsen, C., 2012. Micro- and nano-environments of carbon sequestration: Multi-element STXM–NEXAFS spectromicroscopy assessment of microbial carbon and mineral associations. Chem. Geol. 329, 53–73. doi:10.1016/j.chemgeo.2012.02.002

Staff, S.S., NRCS, 2012. Official Soil Series Descriptions. Natural Resources Conservation Service, United States Department of Agriculture. [WWW Document]. URL http://www.nrcs.usda.gov/wps/portal/nrcs/detailfull/soils/home/?cid=nrcs142p2_053587 (accessed 5.30.12).

Stallard, R.F., 1998. Terrestrial sedimentation and the carbon cycle: Coupling weathering and erosion to carbon burial. Global Biogeochem. Cycles 12, 231–257.

Stanley, C.R., 2006. Numerical transformation of geochemical data: 1. Maximizing geochemical contrast to facilitate information extraction and improve data presentation. Geochemistry Explor. Environ. Anal. 6, 69–78.

Stone, E.L., Kalisz, P.J., 1991. On the maximum extent of tree roots. For. Ecol. Manage. 46, 59–102.

Strehlau, J.H., Hegner, L.A., Strauss, B.E., Feinberg, J.M., Penn, R.L., 2014. Simple and Efficient Separation of Magnetic Minerals From Speleothems and Other Carbonates. J. Sediment. Res. 84, 1096–1106.

Stumm, W., Morgan, J.J., 1996. Aquatic Chemistry: Chemical Equilibria and Rates in Natural Waters, Environmental science and technology, Environmental science and technology. Wiley-Interscience.

Suchet, P.A., Probst, J.-L., Ludwig, W., 2003. Worldwide distribution of continental rock lithology: Implications for the atmospheric/ soil CO2 uptake by continental weathering and alkalinity river transport to the oceans. Global Biogeochem. Cycles 17. doi:10.1029/2002GB001891

Thieme, J., Sedlmair, J., Gleber, S.-C., Prietzel, J., Coates, J., Eusterhues, K., Abbt-Braun, G., Salome, M., 2010. X-ray spectromicroscopy in soil and environmental sciences. J. Synchrotron Radiat. 17, 149–57. doi:10.1107/S0909049509049905

Thompson, A., Rancourt, D.G., Chadwick, O. a., Chorover, J., 2011. Iron solid-phase differentiation along a redox gradient in basaltic soils. Geochim. Cosmochim. Acta 75, 119–133. doi:10.1016/j.gca.2010.10.005

Van Oost, K., Quine, T.A., Govers, G., De Gryze, S., Six, J., Harden, J.W., Ritchie, J.C., McCarty, G.W., Heckrath, G., Kosmas, C., Giraldez, J. V, Da Silva, J.R.M., Merckx, R., 2007. The impact of agricultural soil erosion on the global carbon cycle. Science (80-.). 318, 626–9. doi:10.1126/science.1145724

Van Oost, K., Verstraeten, G., Doetterl, S., Notebaert, B., Wiaux, F., Broothaerts, N., Six, J., 2012. Legacy of human-induced C erosion and burial on soil-atmosphere C exchange. Proc. Natl. Acad. Sci. U. S. A. 109, 19492–7. doi:10.1073/pnas.1211162109

Vitousek, P., Chadwick, O., Crews, T., Fownes, J., Hendricks, D., Herbert, D., 1997. Soil and ecosystem development across the hawaiian islands. GSA Today 7, 1–10.

Wagai, R., Mayer, L., 2007. Sorptive stabilization of organic matter in soils by hydrous iron oxides. Geochim. Cosmochim. Acta 71, 25–35. doi:10.1016/j.gca.2006.08.047

Wagai, R., Mayer, L.M., Kitayama, K., 2009. Extent and nature of organic coverage of soil mineral surfaces assessed by a gas sorption approach. Geoderma 149, 152–160. doi:10.1016/j.geoderma.2008.11.032

Walling, D.E., He, Q., 1999. Improved models for estimating soil erosion rates from cesium-137 measurements. J. Environ. Qual. 28, 611–622.

West, A., Galy, A., Bickle, M., 2005. Tectonic and climatic controls on silicate weathering. Earth Planet. Sci. Lett. 235, 211–228. doi:10.1016/j.epsl.2005.03.020

West, N., Kirby, E., Bierman, P., Slingerland, R., Ma, L., Rood, D., Brantley, S., 2013. Regolith production and transport at the Susquehanna Shale Hills Critical Zone Observatory, Part 2: Insights from meteoric 10 Be. J. Geophys. Res. Earth Surf. 118, 1877–1896. doi:10.1002/jgrf.20121

White, A.F., Blum, A.E., Schulz, M.S., Bullen, T.D., Harden, J.W., Peterson, M.L., 1996. Chemical weathering rates of a soil chronosequence on granitic alluvium: I. Quantification of mineralogical and surface area changes and calculation of primary silicate reaction rates. Geochim. Cosmochim. Acta 60, 2533–2550. doi:10.1016/0016-7037(96)00106-8

White, A.F., Brantley, S.L., 2003. The effect of time on the weathering of silicate minerals: why do weathering rates differ in the laboratory and field? Chem. Geol. 202, 479–506. doi:10.1016/j.chemgeo.2003.03.001

Yoo, K., 2005. Erosion of upland hillslope soil organic carbon: Coupling field measurements with a sediment transport model. Global Biogeochem. Cycles 19. doi:10.1029/2004GB002271

Yoo, K., Amundson, R., Heimsath, A., Dietrich, W., 2006. Spatial patterns of soil organic carbon on hillslopes: Integrating geomorphic processes and the biological C cycle. Geoderma 130, 47–65. doi:10.1016/j.geoderma.2005.01.008

Yoo, K., Amundson, R., Heimsath, A.M., Dietrich, W.E., 2005. Process-based model linking pocket gopher (Thomomys bottae) activity to sediment transport and soil thickness. Geology 33, 917–920. doi:10.1130/G21831.1

Yoo, K., Amundson, R., Heimsath, A.M., Dietrich, W.E., Brimhall, G.H., 2007. Integration of geochemical mass balance with sediment transport to calculate rates of soil chemical weathering and transport on hillslopes. J. Geophys. Res. 112, F02013. doi:10.1029/2005JF000402

Yoo, K., Fisher, B., Ji, J., Aufdenkampe, A., Klaminder, J., 2015. The geochemical transformation of soils by agriculture and its dependence on soil erosion: An application of the geochemical mass balance approach. Sci. Total Environ. 521-522C, 326–335. doi:10.1016/j.scitotenv.2015.03.084

Yoo, K., Ji, J., Aufdenkampe, A., Klaminder, J., 2011. Rates of soil mixing and associated carbon fluxes in a forest versus tilled agricultural field: Implications for modeling the soil carbon cycle. J. Geophys. Res. 1–10. doi:10.1029/2010JG001304

Yoo, K., Mudd, S.M., 2008. Toward process-based modeling of geochemical soil formation across diverse landforms: A new mathematical framework. Geoderma 146, 248–260. doi:10.1016/j.geoderma.2008.05.029

7 Appendix 1. Laboratory Protocols

7.1 Surface Area of Soils

University of Minnesota-Twin Cities
PI: Kyungsoo Yoo **Room & Building:** Borlaug 181
Department: SWC, LAAS **Current Revision Date:** 09/05/2016
Contributors: Amy Lyttle, Beth Fisher, Marta Roser
Purpose:
Determine the surface area (SA) of soils before and after removal of organic matter.
Method:
Sample preparation:
Measure 5-7 grams of soil sample (most likely from the <2mm fraction) into a small vial and designate for surface area analyses.
'Light' grind sample with mortar and pestle to break up aggregates, pick out organics, and store in crucible.
Dry samples at 60°C in crucible, no cover. After drying, place samples in a desiccator to keep them dry.
Weigh sample fraction to be analyzed. DO NOT use vinyl gloves; these will build up static. However, since fingerprints could affect the mass, wear cloth or anti-static gloves.
For soils in the A and E horizon, measure out 1.5 grams of soil labeled "<2mm" and for soils in the Bt horizon, measure out 1 gram of soil labeled "<2mm".
Tare with test tube holder on scale.
Weigh tube, record weight in lab book.
Tare with weighing paper (creased in half for easy pouring) on scale.
Weigh a well-mixed fraction of soil onto paper using spatula.
Carefully pour sample into test tube.
Brush the inside of the sample tube using a brush slightly wetted with isopropyl alcohol.
Tare test tube holder and weigh tube with soil, record.
Plan and prep a test tube with carbon black and scan one reference carbon black every 1-3 days.
Tare with test tube holder on scale
Weigh tube, record weight in lab book
Tare weighing paper
Measure out 0.5 grams of carbon black
Carefully pour sample into test tube
Brush the inside of the sample tube using a brush slightly wetted with isopropyl alcohol
Tare test tube holder and weigh tube with carbon black, record.
Degassing:
Check pressure on nitrogen and helium gas tanks. If pressure is below 500 Pa, the tanks need to be replaced. The nitrogen tank supplies the degassing station and the analyzer; the helium tank supplies the analyzer.

Degas soil using Nitrogen Flow, at 150°C for 4 hours to overnight.
Set flow control of N2 gas by twisting top of gas probe. Flow should be ~1.5 bubbles per second as measured in a beaker of water.
Clean gas probes with KimWipe making sure there is no soil inside the bottom of the probe.
Tilt test tube almost horizontal (5-10°) while inserting gas probe to the bottom of the tube to make sure no soil enters the bottom of the probe.
Place in heating well and slide aluminum insulator over test tube.
After 4 hours, check tubes. If there is moisture visible on the sides of the tubes, leave samples in the heating well longer. If no moisture is visible, place tubes in the cooling station, and when finally cooled turn the gas off and shake probe to remove any soil stuck to the probe. Leave gas probe in and on while cooling, cork test tube. Be prepared to run in SA analyzer as soon as samples are cool (~20 minutes) because sample will quickly take on moisture in humid conditions.
Weigh the tube and soil again before placing on the surface area analyzer, record in lab book.

Surface area analysis:

Fill large "Cryosafe" Dewar flask with liquid nitrogen using the nitrogen tank. You can test the nitrogen level using a stick, but be sure to fill to a weight that you can safely lift and pour.
Safety Note: When pouring liquid nitrogen, open lab door and wear long pants, shoes, safety glasses, and thick gloves (neoprene insulated).
Fill silver Dewar flask from the analyzer with liquid nitrogen using the "Cryosafe" Dewar. Begin by adding a small amount of liquid nitrogen to cool the jug (it will boil). Fill until the liquid level reaches the hole in the T-shaped indicator when the indicator is resting across the top of the Dewar.
Set silver Dewar aside and cover. Wait to place on analyzer stand until all tubes are in place in the analyzer. Use caution when moving Dewar!

Load samples in analyzer:

Allowing the cooling rack to hold the test tubes, remove stopper and gas probe. Turn off N2 gas flow and stow probe in a heating station well.
Clean a glass filler rod and slide into test tube.
Remove tube from the cooling station and slide isotherm jacket over test tube.
Slide test tube into foam disk in analyzer. (Best load sequence is slot 3, then 2, then 1.)
Add screw top combo (screw top, washer, then O-ring), sliding O-ring ~2cm below the top of tube.
Push test tube into port in analyzer.
Screw into analyzer.
Move silver Dewar onto "elevator" on analyzer being careful to not break the test tubes.
Note, a full Dewar can accommodate two full sample runs (six samples).

Sample analysis:

If Tristar 3020 software is not open, double-click the application on the desktop.

Open new files to run samples
Click on the “Open Sample File” to create a new file.

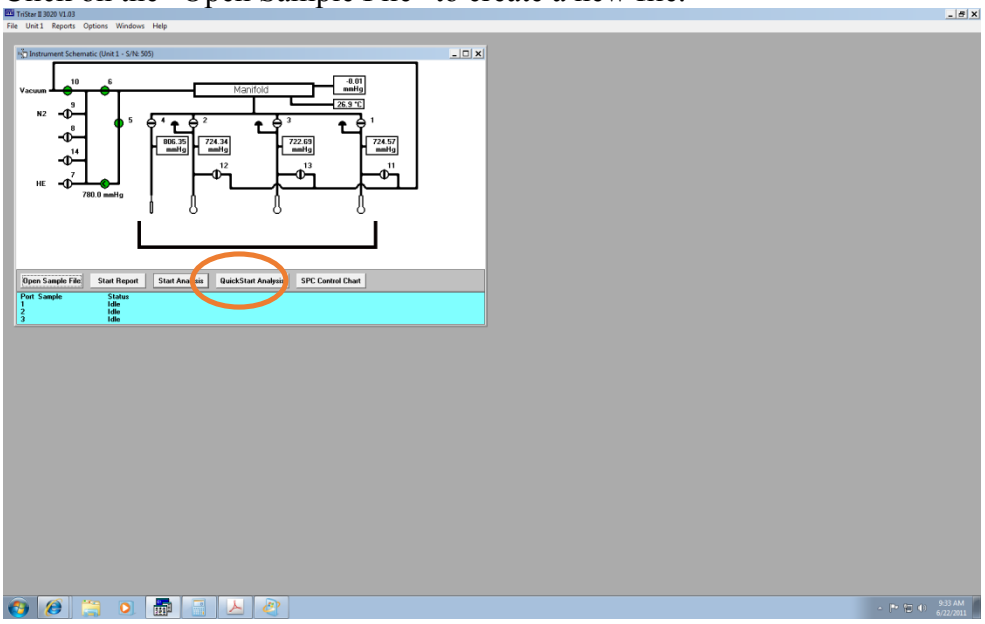

To create a new file, do not select any file, and click “OK”

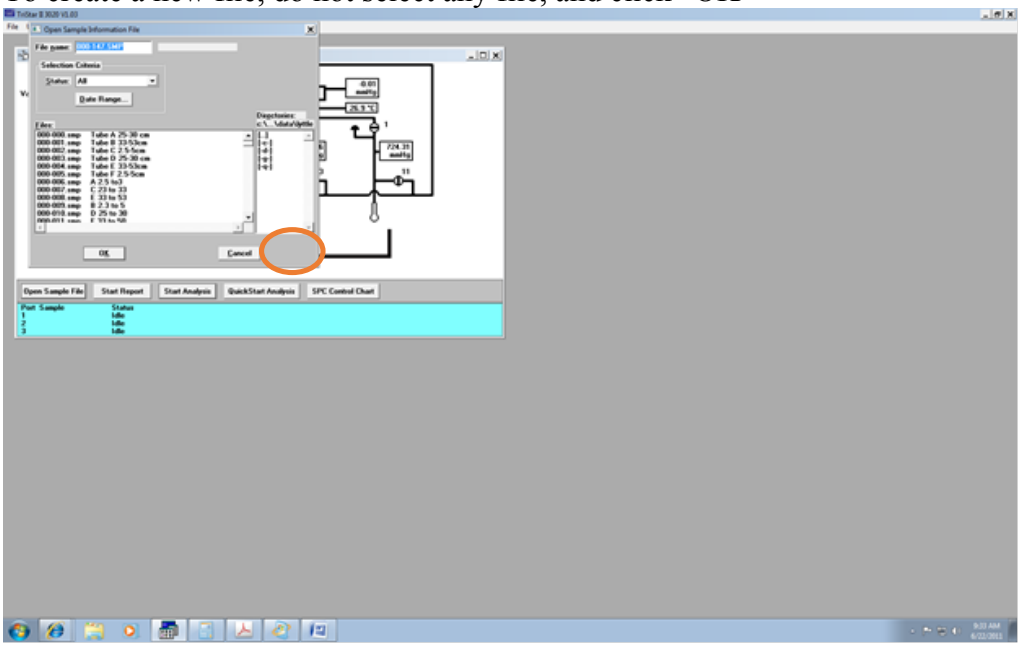

You will be asked if you would like to create a file, click “Yes”

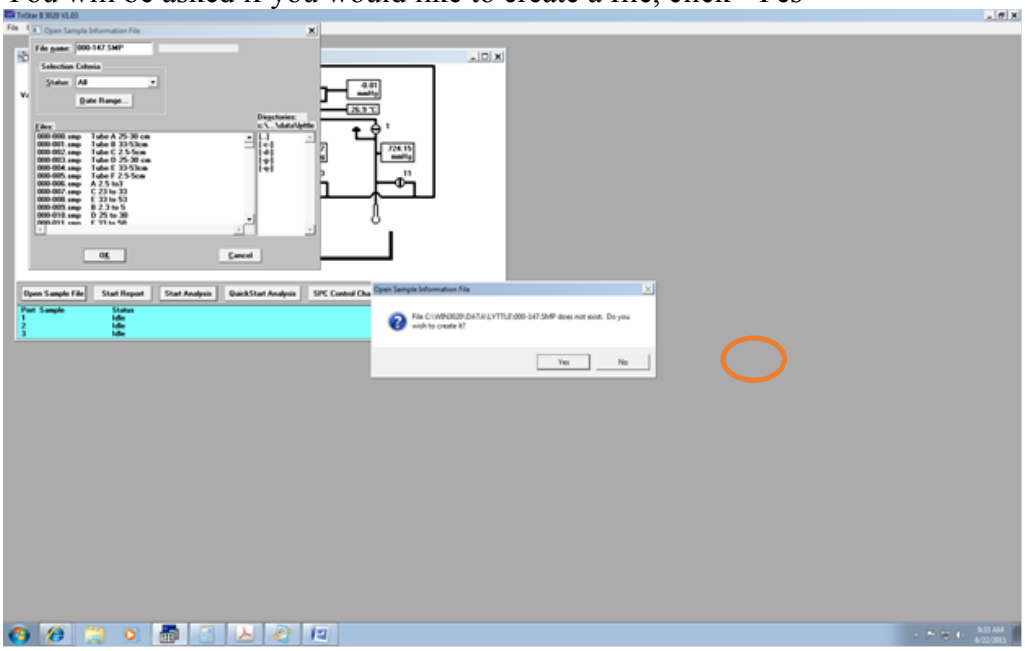

A new .smp file will be created. Fill out sample information – Sample (sample name), Operator (your name), and submitter (where the sample came from, such as soil pit ID). Check the Calculate box under Mass heading and enter the sample weights indicated from your lab book (tube only and degassed tube and soil). Density always = 1. Type any comments in the “Comments” box.

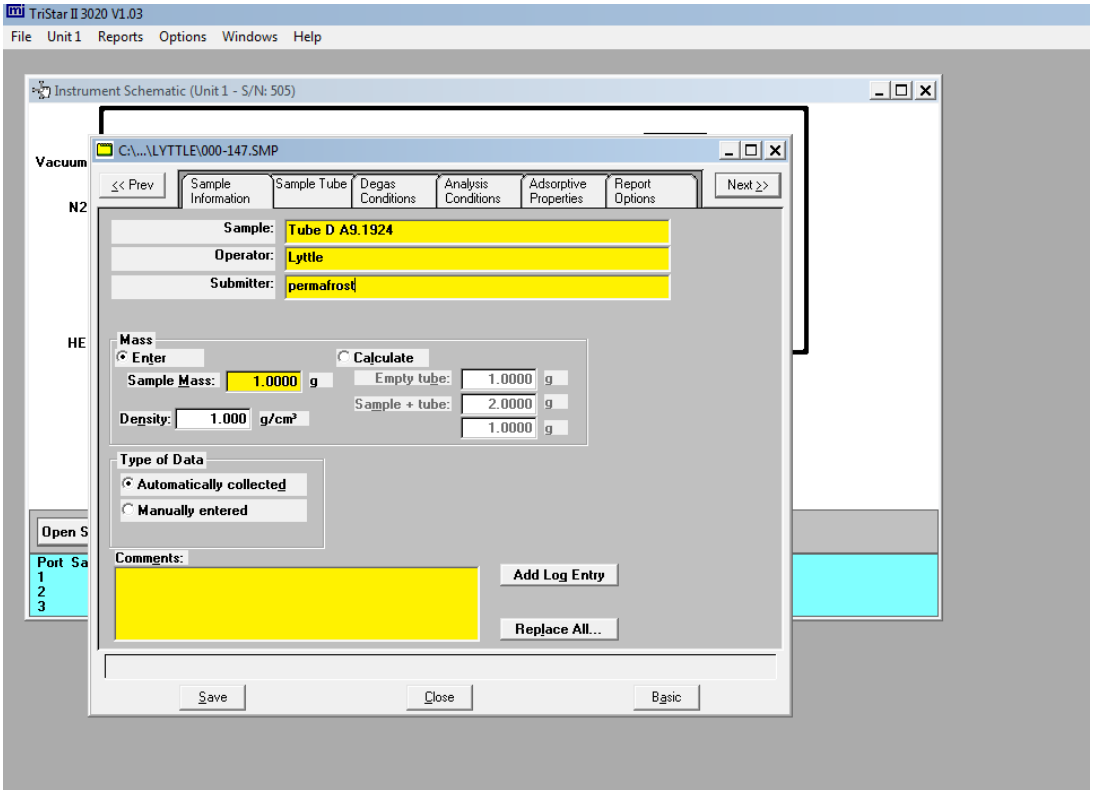
TriStar II 3020 V1.03
File Unit 1 Reports Options Windows Help
Instrument Schematic (Unit 1 - S/N: 505)
Vacuum
N2
HE
Open S
Port Sa
1
2
3
C:\...\LYTTLE\000-147.SMP
<< Prev
Sample Information
Sample Tube
Degas Conditions
Analysis Conditions
Adsorptive Properties
Report Options
Next >>
Sample: Tube D A9.1924
Operator: Lyttle
Submitter: permafrost
Mass
Enter
Sample Mass: 1.0000 g
Density: 1.000 g/cm³
Calculate
Empty tube: 1.0000 g
Sample + tube: 2.0000 g
1.0000 g
Type of Data
Automatically collected
Manually entered
Comments:
Add Log Entry
Replace All...
Save
Close
Basic

Then, click on the “Analysis Conditions” Tab

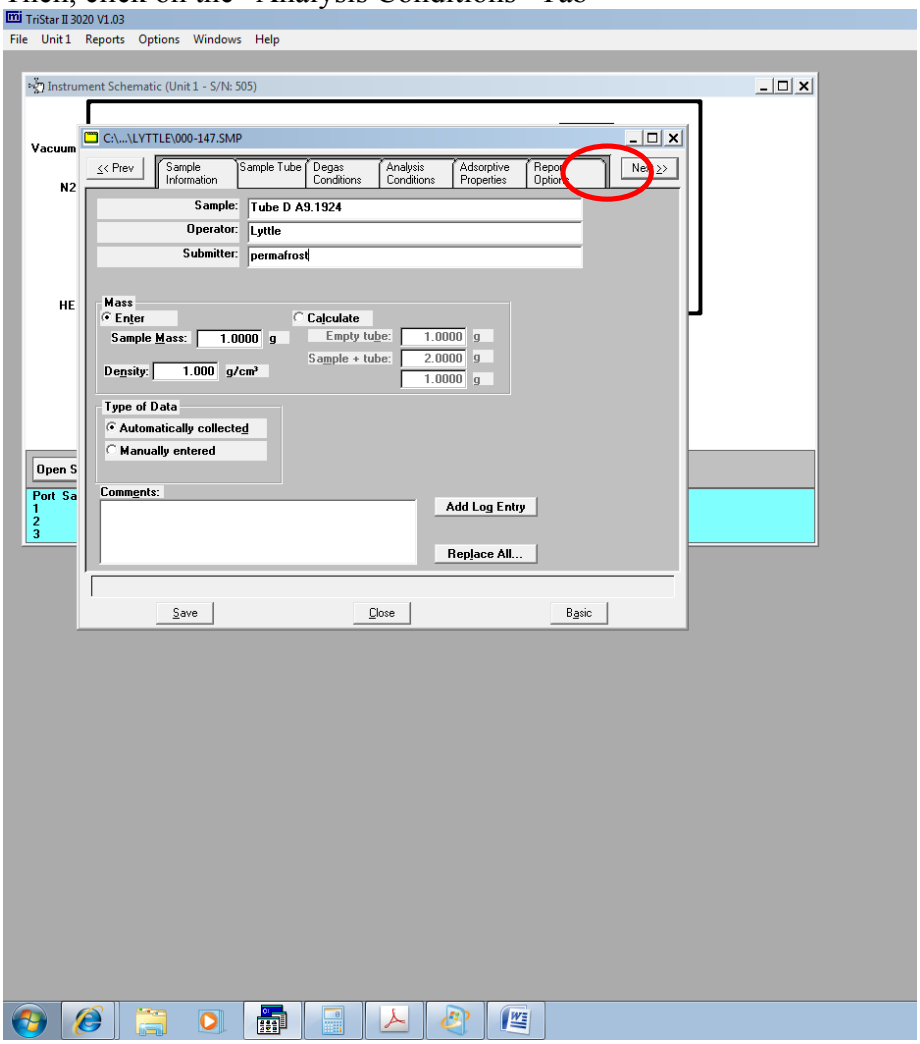

You will be bought to the analysis conditions tab. Click on the “Preparation” box

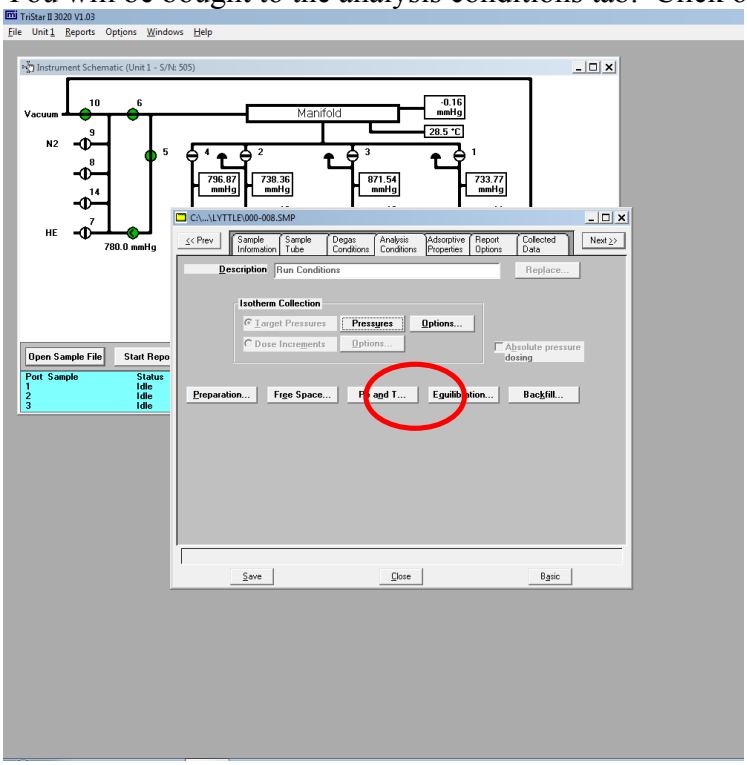

Once you have clicked on the “Preparation” box, check the box next to “Leak Test”. This will perform a leak test on the sample tubes before any analysis has begun.

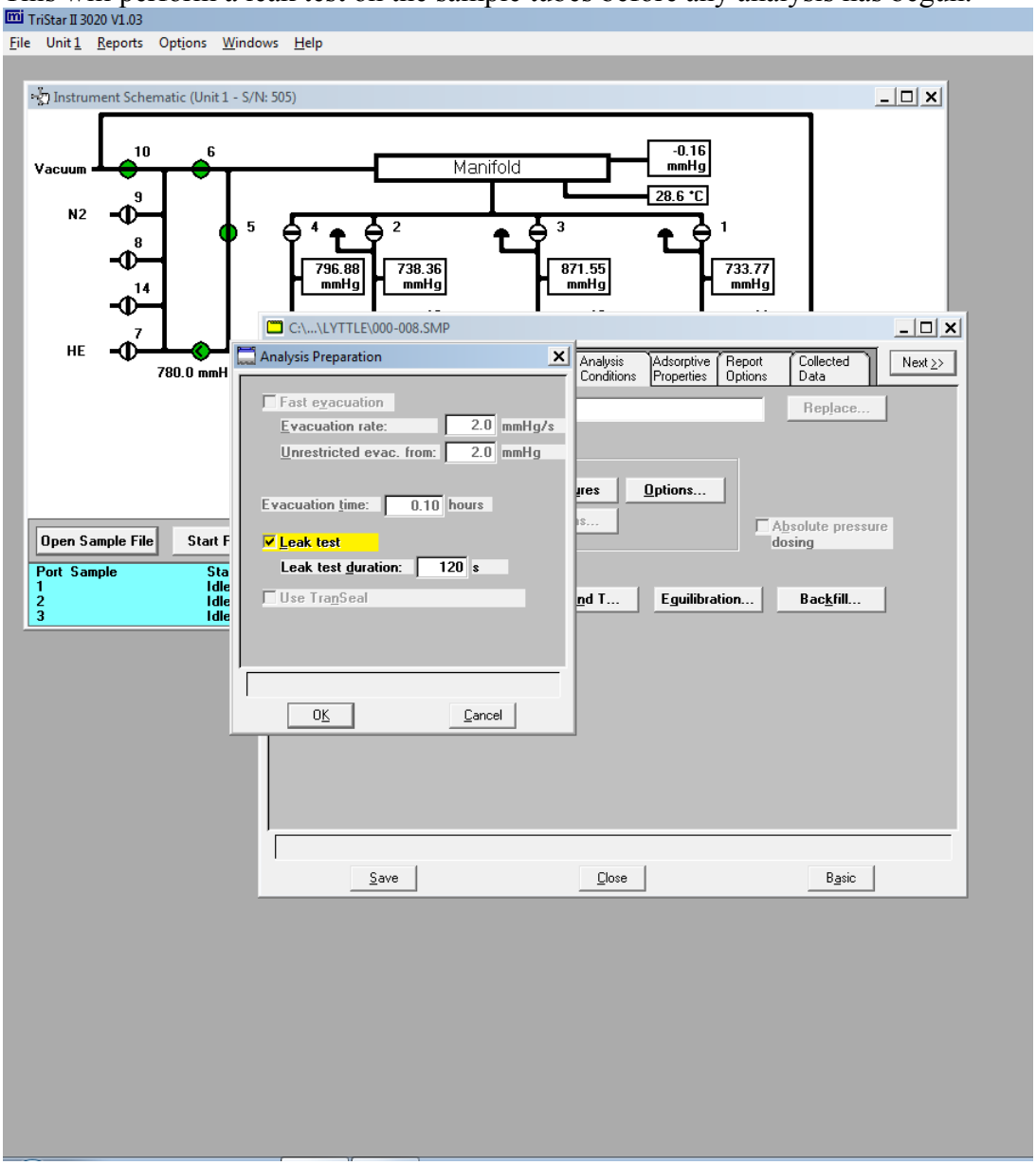

Click “OK” and “Save”.
Once you have saved the file you may close the file
You can create as many new files as needed

When are you read to run analysis click on the “Start Analysis” button.

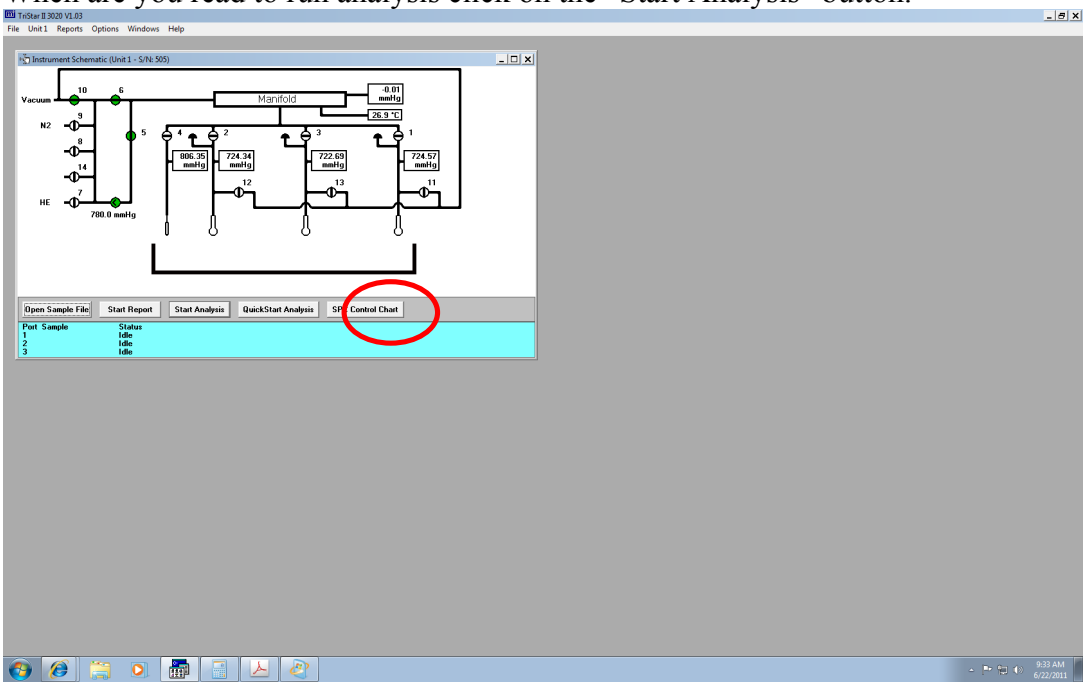

You will then browse for the sample files to be analysed. Only sample files that have NOT yet been analyzed will show when you click the browse botton

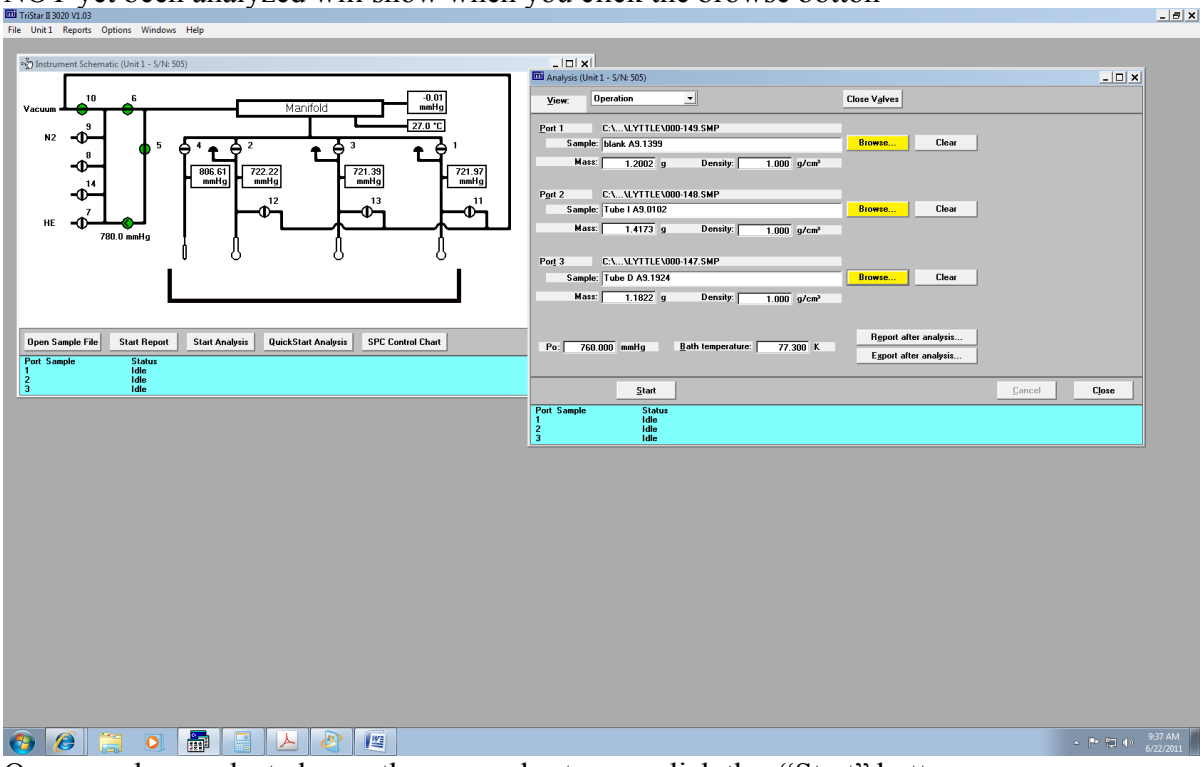

Once you have selected your three samples to run, click the “Start” button.

You will see this screen as analysis starts and evacuation begins:

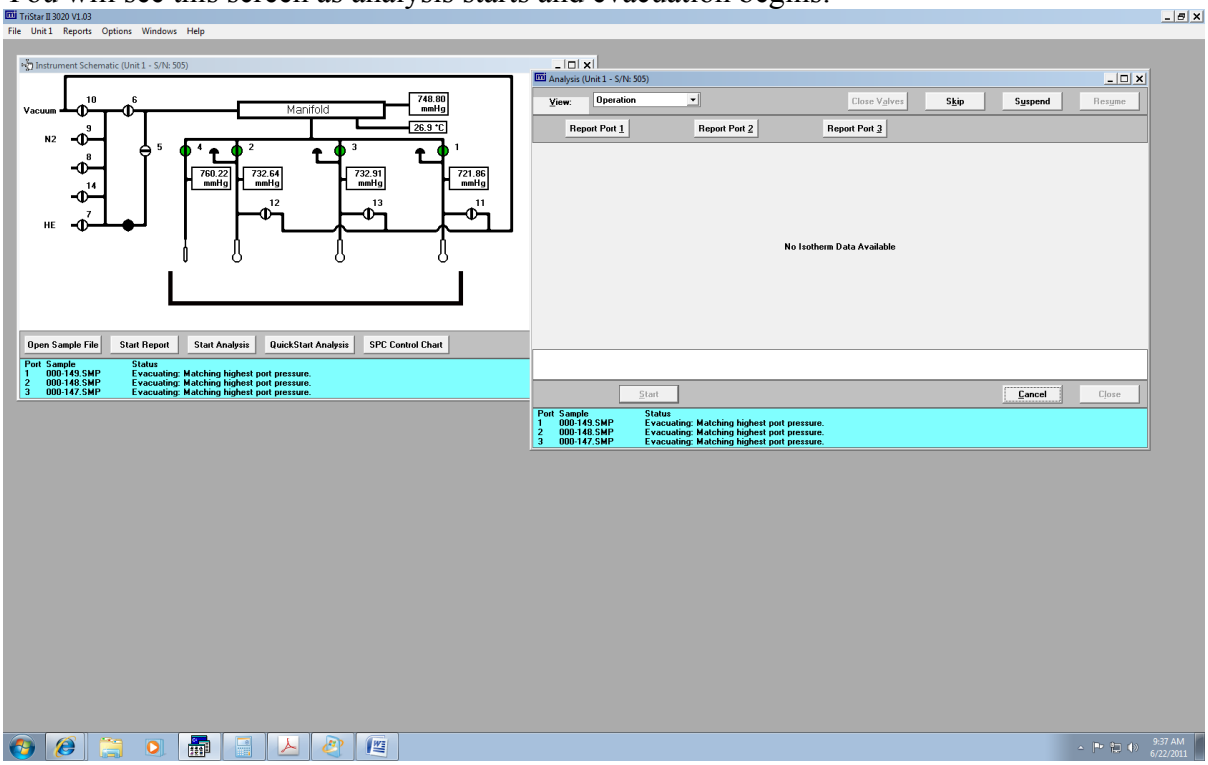

After analysis is complete you will have three individual sample files and data and an isotherm plot for the three samples

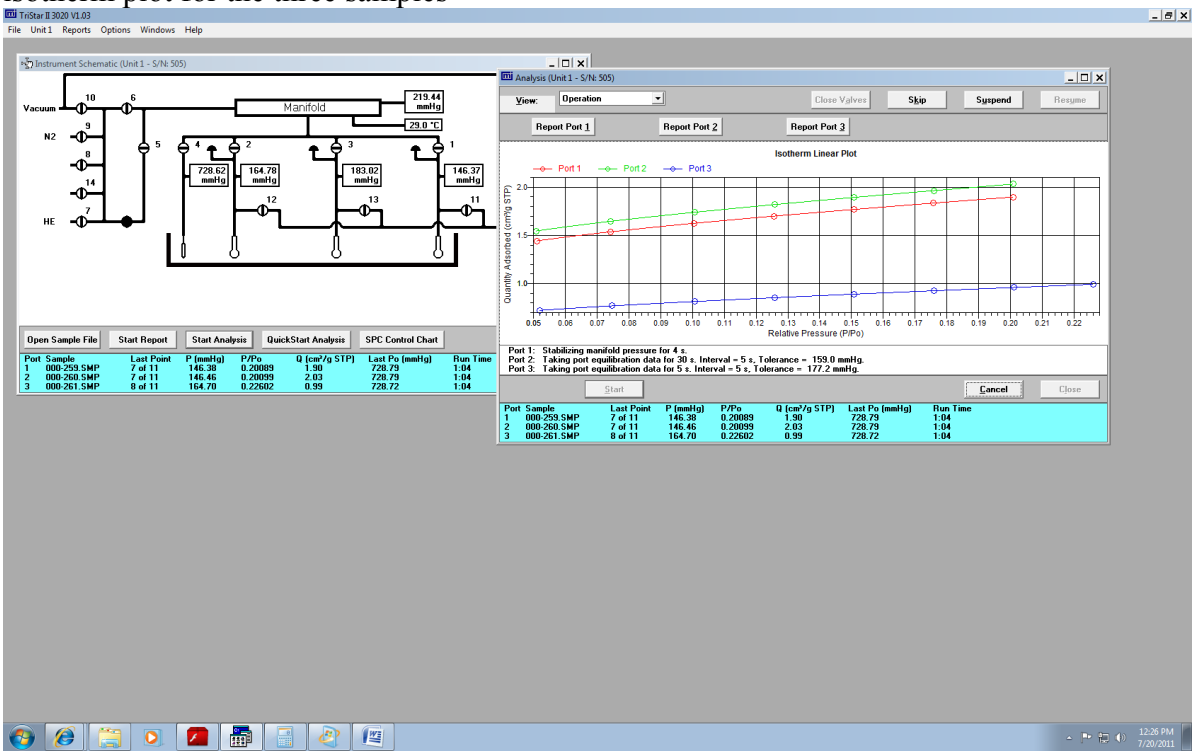

Hazard Identification
Contact with Liquid Nitrogen
Potential Hazards of Liquid Nitrogen:
Explosion: use only equipment approved for cryogenic liquids
Asphyxiation: if sufficient liquid nitrogen is vaporized so as to reduce the oxygen percentage below 19.5%, there is a risk of oxygen deprivation.
Personal Protective Equipment for Liquid Nitrogen
Gloves – in case of accidental splash contact (insulated Neoprene)
Safety glasses
Closed toed shoes
Long pants
Long sleeves or lab coat
Additional Precautions
Always keep container lid on unless in use
Do not use funnel
Emergency and Spill Information
Exposure – in the case of cold burns (frost bite)
Eye: flush eye with cold water for 15 minutes
Skin : flush affected area with cold water for 15 minutes

Inhalation: remove victim from area to fresh air if it is safe to do so
Spills
Minor spills – (a few drops) alert others in the room

7.2 Muffling for Removal of Organics

University of Minnesota-Twin Cities
PI: Kyungsoo Yoo **Room & Building:** Borlaug 181
Department: SWC, LAAS **Current Revision Date:** 09/05/2016
Contributors: Amy Lyttle, Beth Fisher, Marta Roser
Purpose:
Remove organic matter from soil samples by combusting at 350°C for 12 hours after Keil et al. 1997.
Muffling for Removal of Organics
Pour sample into ceramic crucible. Crucibles filled to half-way will burn off organics easier, especially in organic-rich samples. To make sure you have enough sample for surface area measurements, use between 3-5 grams of sample. Label the bottom using a pencil.
Place all crucibles in the Lindberg/Blue 1100°C Box Furnace (Model BF51800) and close the door, making sure it latches.
Turn furnace on. Hold "SET/ENT", click up to "reset" and use the following steps to program the muffling procedure:

Parameter	Value	Meaning
SSP	25	Start setpoint
StC	0	Start code
SP1	350	Segment 1 setpoint
EA1	6.01	Time length for segment 1
SP2	350	Segment 2 setpoint
EA2	12	Time length for segment 2
SP3	50	Segment 3 setpoint
EA3	4.10	Time length for segment 3
SP4	50	Segment 4 setpoint
EA4	4	Time length for segment 4
SP5	25	Segment 5 setpoint
EA5	Off	Time length for segment 5
EV1	0	Event 1
AL1	9	Alarm 1
A 1	510	Temp. at which alarm will go off (?)
HY1	1	Hysteresis for alarm 1
EV2	0	Event 2
AL2	Off	Alarm 2
JC	1	Junction code
wtz	Off	Wait zone

Hold "SET/ENT". This should take you back to the initial screen.
Hold "SET/ENT" again. Click up to "run". You should hear a click and the light should come on. The top number is the temperature that the furnace is currently at, and the bottom number is the programmed temperature. Cycle will be done in 26 hours.
Below is a diagram of the ramp and dwell process of the muffle furnace and an example of a program:

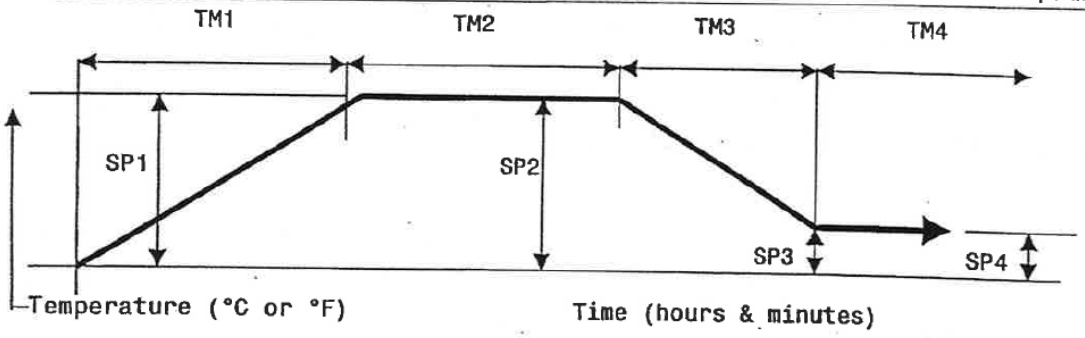

In the table below, '*' denotes values typically set by the user according to the needs of a program.

Parameter	Value	Meaning	Parameter	Value	Meaning
PrG	0	Enters program menu	SP4	*	Segment 4 Setpoint
SSP	25	Start Setpoint	tm3	oFF	Time length for Segment 4
StC	0	Start Code	EV1	0	Event 1
SP1	*	Segment 1 Setpoint	AL1	9	Alarm 1
tm1	*	Time length for Segment 1	HY1	1	Hysteresis for alarm 1
SP2	*	Segment 2 Setpoint	EV2	0	Event 2
tm2	*	Time length for Segment 2	AL2	oFF	Alarm 2
SP3	*	Segment 3 Setpoint	JC	1	Junction code (1=dwell; 0=stop; 2=repeat)
tm3	*	Time length for Segment 3	wtz	oFF	Wait Zone

Figure 6. Typical Program Profile and Table of Parameters

Keil, R.G., Mayer, L.M., Quay, P.D., Richey, J.E., Hedges, J.I., 1997. Loss of organic matter from riverine particles in deltas. Geochim. Cosmochim. Acta 61, 1507–1511. doi:10.1016/S0016-7037(97)00044-6

7.3 Citrate Dithionite Removal of Oxides for SSA

University of Minnesota-Twin Cities
PI: Kyungsoo Yoo **Room & Building:** Borlaug 181
Department: SWC, LAAS **Current Revision Date:** 09/05/2016
Contributors: Janis L. Boettinger, Utah State University, Ed Nater, Beth Fisher, Marta Roser

Purpose:

Removal of exchangeable iron and aluminum oxides to measure SSA of silicate minerals. Crystalline and non-crystalline iron oxides and organically bound Fe and Al are removed using a solution of sodium citrate—sodium bicarbonate—sodium dithionite. This method is commonly referred to as the CBD method of free iron oxide removal. Iron (hydr)oxides are reduced with sodium dithionite ($Na_2S_2O_4$, also known as sodium hydrosulfite); sodium citrate ($Na_3C_6H_5O_7.2H_2O$) chelates the reduced iron to keep it in solution; sodium bicarbonate ($NaHCO_3$) buffers the solution to pH 7.3.

Room Temperature Method. (Holmgren, 1967)

Equipment:

50 mL graduated cylinder
50 mL centrifuge tubes
Wash bottle with distilled H_2O
Small (0.5 g) scoop

Reagents:

0.3 *M* $Na_3C_6H_5O_7.2H_2O$ (sodium citrate)
$Na_2S_2O_4$ (sodium dithionite)
1 *M* $NaHCO_3$ (sodium bicarbonate)
Saturated NaCl solution (or NaCl salt)

Procedure:

Mix sufficient quantity of 0.3 M sodium citrate solution. Add sodium bicarbonate to buffer the solution to pH 7.3.

Place up to 5g of soil in centrifuge tubes.

Add 30 mL of sodium citrate-bicarbonate solution to each sample tube.

In a fume hood, use the scoop to add approximately 1 g Na2S2O4 to the bottle.

Screw the cap tightly on the bottle and shake well. Place sample securely on the shaker and shake overnight (15 h).

If your sample contains an abundance of Fe (hydr)oxides, you may need to treat the sample more than once. The above procedure can be repeated as necessary, with shaking periods of as little as 4 hours.

Centrifuge at 2,000 rpm for 15 min. Add NaCl crystals as necessary to facilitate flocculation.

Remove samples from centrifuge. If supernatant is clear, decant into a waste bottle. If supernatant is cloudy, add NaCl solution or salt, stir, and centrifuge again.

If samples still retain a reddish or yellowish coloration, repeat procedure until the sample is free of coloration by iron oxides.
##The original protocol calls for washing the samples with a 1:1 mixture of 0.3 *M* Na-citrate and saturated NaCl solution. However, we want to also remove residue from the Na-citrate, so we use DDI water. ##
Add ~35 mL of DDI water to each centrifuge tube.
Let samples shake on low for 1-2 hours.
Centrifuge at 2,000 rpm for 15 min
Decant supernatant if clear. If the sample does NOT flocculate, add 0.25 – 1 gram of sodium chloride, shake on vortex mixer, and centrifuge again. Repeat with small increments of sodium chloride until the sample flocculates.
Mix sample with small spatula to make it easier to break up after drying.
Dry samples at 60°C overnight.
Lightly grind samples using a mortar and pestle.

7.4 Pretreatment of clay minerals for XRD

University of Minnesota-Twin Cities
PI: Kyungsoo Yoo **Room & Building:** Borlaug 181
Department: SWC, LAAS **Current Revision Date:** 09/05/2016
Contributors: Janis L. Boettinger, Utah State University, Ed Nater, Beth Fisher

Purpose:

Determine the surface area (SA) of soils before and after removal of organic matter.

Standard Mineral Pretreatments

Mineralogical information can be a valuable aid to the understanding of physical and chemical characteristics and the behavior of soils and geologic materials. Mineral occurrences, distributions, and associations often serve as indications of weathering environments, landform age, and pedogenic and geochemical processes. In addition, mineralogy is used as a criterion for classification of soils and geologic formations and for land evaluation and use.

The full spectrum of analyses available for identification, quantitative estimation, and characterization of minerals and non-crystalline materials extends far beyond the scope of a single course. The procedures provided here are standard methods of sample pretreatment used to prepare clay mineral samples for XRD analysis. A caveat: Standard methods of sample pretreatment prepare samples for standard methods of analysis. In any mineralogical study, the specific analyses to be performed are dictated by the objectives of the investigation, time, and the availability of equipment and facilities. Likewise, the sample pretreatments required are dictated by the methods and objectives of the study.

A procedural outline is provided for the analysis of minerals and non-crystalline inorganic components that commonly occur in soils and geologic materials. Directions for sample preparation and analysis are presented in step-wise outline for convenience of manipulations in the laboratory. The student is expected to understand the principles underlying each procedure, as well as the limitations and applicability of each procedure (treatments and analyses are referenced for this purpose).

Adapted from J.L. Boettinger, Utah State University, 1989 and 1991.

I. Sample Preparation

A. Introduction

Sample preparation includes chemical treatments designed to remove cementing and flocculating agents such as carbonates, organic matter, iron oxides, amorphous material, and other cements, in order to facilitate separation of the different size fractions for mineralogical analyses. Preparatory chemical treatments may also remove certain soil components (Fe_2O_3, light element scatterers such as C and H) that may interfere with subsequent mineralogical analyses.

Depending upon the nature of the samples and the mineralogical information desired, one or more preparatory chemical treatments may be omitted. For example, if a

soil exhibits a pH less than 6.5, removal of carbonates is unnecessary; if identification of iron (hydr)oxide minerals is desired, removal of free iron oxides should be omitted.

The most common chemical treatments used in sample preparation are listed and referenced in this manual. Whether or not any preparatory chemical treatments are omitted, the treatments should be performed in the order presented. The methods described below can all be performed in 250 mL wide-mouth polypropylene bottles.

B. Sample size

The procedures that follow require about 1 to 5 g of clay. In order to extract that quantity from your sample, you will need to know the approximate quantity of clay in the sample. This can be determined more or less accurately by feeling the texture of the sample. From the textural triangle, estimate the quantity of soil (or other material) required to yield 5 g of clay. Weigh sufficient sample to yield approximately 5 g of clay. Distribute the sample evenly such that each bottle contains 20 g. This must be a fairly accurate distribution or the centrifuge will be out of balance and will not run. Do not adjust for uneven distribution of soil sample by adding additional liquid; while this may produce a static balance, the samples will still be out of dynamic balance.

C. Removal of Carbonates (Jackson, 1975)

1.0 *M* sodium acetate (NaOAc) buffered to pH 5.0 with acetic acid

Saturated NaCl solution

Concentrations:

1.0M Na-acetate: 136.08g/L,

Amount required: 100 mL (0.1L) per sample (*12 samples = 1.2L)

136.08 g/L * 1.2L = 163.296g required to make 1.2L of 1.0M Na-acetate

NaCl: The solubility of NaCl in water is 359 g/L, so 359 grams of NaCl will be at saturation point in one liter of deionized water. Some NaCl crystals remaining in the bottom of the container will reveal that the solution is saturated.

Add 50-100 mL to each sample in a 250 mL bottle.

Heat to 90°C in a steam bath for ~1 hour or until samples are no longer fizzing to facilitate carbonate destruction.

Remove bottles from bath. Let cool slightly. Stir each sample and rinse the stirring rod into the tube with distilled water. (If using bottles, swirling the suspension in the bottle is sufficient). If sample does not appear to flocculate, add a small amount of NaCl salt or solution and stir.

Centrifuge at approximately 2,000 rpm for 5 minutes. If supernatant is clear, decant and discard. If supernatant is cloudy, add NaCl solution, shake, and centrifuge again.

D. Removal of Organic Matter

Bleach Method:

This procedure employs sodium hypochlorite (NaOCl; standard household bleach) adjusted to pH 9.5 as an oxidizing agent (Page, 1982).

Reagents:

NaOCl solution (bleach) adjusted to pH 9.5 with HCl (normal pH is 11 to 12). Exposure to air reduces the pH, so you may eventually have to readjust the pH to 9.5 with NaOH. The NaOCl solution is a much more effective oxidizing agent at pH 9.5.
Amount required: 100 mL per sample, but this will require multiple iterations, perhaps more than 7 on the upper horizon samples. Mix a batch of appropriate size to accommodate your storage container and plan to mix extra as required. In my first iterations I discovered that 2 L of bleach required less than 20 mL of HCl.
Procedure:
Add approximately 100 mL of NaOCl solution to each bottle containing soil. Stir.
Place the uncapped bottles into a hot water or sand bath at 70 to 90 C. Leave samples in the water bath for approximately 15 minutes, (this takes much longer! ~1 hour) stirring occasionally.
Remove bottles from bath. Let cool slightly. Stir each sample and rinse the stirring rod into the tube with distilled water. (If using bottles, swirling the suspension in the bottle is sufficient). If sample does not appear to flocculate, add a small amount of NaCl salt or solution and stir.
Centrifuge at approximately 2,000 rpm for 5 minutes. If supernatant is clear, decant and discard. If supernatant is cloudy, add NaCl solution, shake, and centrifuge again.
If using bottles, one or two treatments are normally sufficient unless the soil is high in organic matter. Organic removal should be indicated by loss of the dark color due to organic matter and a lack of bubbling of the sample.

E. Removal of Free Iron Oxides

Crystalline and non-crystalline iron oxides and organically bound Fe and Al are removed using a solution of sodium citrate—sodium bicarbonate—sodium dithionite. This method is commonly referred to as the CBD method of free iron oxide removal. Iron (hydr)oxides are reduced with sodium dithionite ($Na_2S_2O_4$, also known as sodium hydrosulfite); sodium citrate ($Na_3C_6H_5O_7.2H_2O$) chelates the reduced iron to keep it in solution; sodium bicarbonate ($NaHCO_3$) buffers the solution to pH 7.3.
(Jackson, 1975; Klute, 1986)

Equipment:

100 mL graduated cylinder Stirring rods
Steam bath (80°) with beakers of water Wash bottle with distilled H_2O
small (0.5 g) scoop

Reagents:

0.3 *M* $Na_3C_6H_5O_7.2H_2O$ (Na-citrate) $Na_2S_2O_4$ (sodium dithionite)
1 *M* $NaHCO_3$ (sodium bicarbonate) Saturated NaCl solution (or NaCl salt)
Concentrations:
0.3 *M* Na-citrate: 294g/L * 0.3 M = 88.2 g/L
80mL per sample x 12 samples = 960 mL required
Mix 1 liter deionized water with 88.2 g Na-citrate
1 *M* $NaHCO_3$: 84g/L
10mL per sample x 12 samples = 120 mL required

Mix 200 mL with 16.8 g $NaHCO_3$
NaCl: The solubility of NaCl in water is 359 g/L, so 359 grams of NaCl will be at saturation point in one liter of deionized water. Some NaCl crystals remaining in the bottom of the container will reveal that the solution is saturated.

Procedure:

Add approximately 80 mL of Na-citrate to each sample bottle.
Add 10 mL of $NaHCO_3$ to each tube (use the dispenser provided). Stir.
Place sample tubes in steam bath beakers and heat to 75-80°C. Do not let temperature exceed 80°.
Add approximately 0.5 g of Na-dithionite (using calibrated 0.5g scoop) to one sample bottle. Mix thoroughly for about 15 seconds. Repeat with the rest of the samples.
Repeat step 4 above so that each sample receives a total of 1 g Na-dithionite.
Digest samples for 15 minutes with frequent stirring.
Remove samples from steam bath. Add approximately 10 mL saturated NaCl or 1 g NaCl salt to each tube (this step can often be avoided). Stir.
Centrifuge at approximately 2,000 rpm for 5 minutes.
Remove samples from centrifuge. If supernatant is clear, decant into a waste bottle. If supernatant is cloudy, add NaCl solution or salt, stir, and centrifuge again.
If samples still retain a reddish or yellowish coloration, repeat steps 1 through 9 until the sample is free of coloration by iron oxides.
Wash the samples by adding an 80 mL portion of a 1:1 mixture of 0.3 *M* Na-citrate and saturated NaCl solution to each sample tube. Stir. Add NaCl solution or salt if sample does not appear to flocculate. If sample does not again appear to flocculate, add 10 mL of 95% ethanol. Stir. Rinse stirring rod. Centrifuge samples for 2,000 rpm for 5 minutes. Decant supernatant if clear. Repeat.

II. Sample Dispersion

A. Removal of Excess Salts

1. Dialysis

If excess salts are to be washed out of the sample, the simple method of dialysis may be employed. Dialysis tubing is cut into strips of appropriate length and soaked for several minutes (or more) in distilled water. The tubes are opened by rubbing the end of the strip gently. Tie a couple of secure knots around the tubing (or tie a knot in the tubing itself) at one end to close off the bottom of the tube. Open up the rest of the tubing and have another person hold a small funnel in the open end of the tube.
Disperse each sample in the centrifuge tubes/bottles with a small amount of distilled water and stir. Transfer all of the dispersed soil sample from the tubes and stirring rod to the dialysis tube with distilled water. Tie a secure knot around the top of the tube and label the tie string. Keep the dialysis tubes in a tub of distilled water with a small hose constantly circulating fresh distilled water through the tub.
Test for the presence of Cl in the exchanging solution in a sample of water in the tub by adding a few drops of $AgNO_3$ solution and looking for a white AgCl precipitate. If the AgCl precipitate fails to form, the samples should be relatively free of excess salts.

2. Centrifugation

Salts may also be washed from the sample using successive washings of ethanol:distilled water mixtures in the centrifuge tubes. Use 50% ethanol for the initial rinse, 95% ethanol for final washings. The sample supernatant can be tested for Cl as above, or the sample may be washed until it disperses (Jackson, 1975).

B. Dispersion During Fractionation

1. NaCl:

Sodium saturated clays readily undergo dispersion if the ionic strength of the saturating solution becomes sufficiently low. The easiest way to accomplish this is to disperse them in distilled water and centrifuge, then repeat until the sample no longer flocculates. Clay removal has begun.

2. Dilute Na_2CO_3:

A common method of keeping soils dispersed during fractionation is to suspend the soil in a solution of dilute sodium carbonate, pH 9.5 (Klute, 1986). Many variable charge soil surfaces should be negatively charged at this pH, with the repulsion of negatively charged particles facilitating soil dispersion.

3. Dilute HCl

Allophanic, aluminous, or ferruginous soils may be better dispersed in dilute HCl (pH 2.7) instead of Na_2CO_3. Dilute HCl may be used in place of the dilute Na_2CO_3 solution for the duration of fractionation, or for the last wash after initial fractionation with Na_2CO_3, depending on the nature of the soil (Jackson, 1975). At low pH, variable charge surfaces should be positively charged, and repulsion between the positively charged surfaces facilitates dispersion.

3. Physical dispersion

Soils may be dispersed physically by ultrasonic vibration (Busacca et al., 1984). This method is enhanced by sonication in dilute Na_2CO_3.

III. Sample Fractionation

A. Introduction

Particle size fractions

Soil samples are normally separated into various size fractions for mineralogical analysis. The extent of separation may depend upon the objectives of the particular investigation. Soils may be separated into sand, silt, and clay fractions, with each fraction separated into subfractions:

1. Sand (2 mm - 50 μm):
a) very coarse (2.0 - 1.0 mm)
b) coarse (1.0 - 0.5 mm)
c) medium (0.25 - 0.5 mm)
d) fine (0.25 - 0.1 mm)
e) very fine (0.1 mm - 50 μm)
2. Silt (50 - 2 μm):
a) coarse (50 - 20 μm)

b) medium (20 - 5 μm)
c) fine (5 - 2 μm)
3. Clay (<2 μm):
a) coarse (2 - 0.2 μm)
b) medium (0.2 - 0.08 μm)
c) fine (<0.08 μm)

Principles of sedimentation (Stoke's Law)

Particle size fractionation is achieved primarily using the principle of particle sedimentation described by Stoke's Law. The separation of sand from silt and clay employs the use of metal screen sieves, but the separation of the silt and clay fractions uses sedimentation by gravity and accelerated sedimentation by centrifugation (Jackson, 1975).

There are a number of assumptions that must be made in order to apply Stoke's Law to the sedimentation of suspensions of soil and geologic materials. Assumptions include: particles are spherical and smooth, there are no interactions between particles in the suspension, and all particles possess a chosen average particle density. Thus, within the limitations of these assumptions, the time required for particles of a particular size and density to fall a given distance can be calculated. Obviously, these assumptions are violated by soil and geologic materials, but the use of these techniques provides us with working particle size definitions. Derivations for Stoke's Law are given in Klute (1986) and Jackson (1975).

1. Sedimentation by gravity:

$$t = 18\ \nu\ h\ /\ [g\ (d_1 - d_2)\ D^2]$$

where:

t = settling time (seconds);
ν = viscosity of liquid (g cm^{-1} s^{-1}). Viscosity is strongly temperature dependent.
h = depth of fall (cm);
g = gravitational acceleration (980 cm s^{-2});
d_1 = density of spherical particle (g cm^{-3});
d_2 = density of liquid (g cm^{-3});
D = sphere diameter (cm).

2. Sedimentation by centrifugation

$$t = [\nu \log (R_2 / R_1)] / [3.81\ N^2\ r^2\ (d_1 - d_2)]$$

where:

t, ν, d_1, and d_2 are defined above;
R_1 = distance from the axis of rotation (or center shaft) of the centrifuge to the surface of the liquid suspension in the centrifuge tube (cm);
R_2 = distance from the rotation axis to the top of the sediment pad near the bottom of the bottle (cm);
N = revolutions per second;
r = particle radius (cm).

B. Separation of Sand (2 mm - 50 µm)

(If you are only interested in the clay fraction, stop after step 6)

Equipment:

600 mL beakers
1 L plastic bottles or glass beakers
Wash bottles filled with distilled water
Sieves or sieve stack

Reagents:

Distilled water

Procedure:

Carefully transfer samples (dispersed by dialysis or centrifugation) into 600 mL or 1 L beaker with a minimum amount of distilled water.

Position a 50 µm (300 mesh) sieve over a 600 mL beaker.

Disperse sample with stirring rod. Let stand exactly 4 seconds for each centimeter of suspension depth. (This step allows the sands to settle, thus reducing clogging of the sieve in step #4 below).

Decant the supernatant through the sieve, pouring slowly to avoid clogging. Collect suspension in the 600 mL beaker. When beaker gets full, transfer suspension to another container. Label suspension beakers "<50 µm".

Add about 100 mL to the sediment and repeat steps 3 and 4 until most of the fine material has passed through the sieve (usually 2 to 3 times more).

Transfer the sediment to the sieve with a stream of distilled water from the wash bottle. Wash sediment with water until free of silt and clay.

Transfer the sands to a tared glass beaker with water. Be sure to label beaker and record weight before filling. Place beaker in oven and dry overnight at 105° C.

When dry, sands are divided into subfractions using a set of nested sieves. Weigh and record the weight of each sieve in the set. Transfer the sand to the top sieve. Place sieve set on a sieve shaker for 5-10 minutes. Weigh and record weights of each sand filled sieve. Store sands in labeled plastic vials.

C. Separation of coarse silt (50 - 20 µm)

Equipment:

250 mL tall form beakers
1 L plastic bottles or glass beakers
Wash bottles filled with distilled water
Ruler

Reagents:

Dilute Na_2CO_3 solution, pH 9.5 (2.1 g per 20 L)
Distilled water
Dilute HCl (if necessary)

Procedure:

Measure the level of <50 µm suspension. Stir the suspension and allow to settle 3 minutes for each 5 cm suspension depth.

Using a bent glass tube and a vacuum bottle, carefully decant suspension above the line. Do not let any sediment transfer.

Redisperse sediment with dilute Na_2CO_3 and transfer to a 250 mL tall form beaker that has been marked with a line at 5 cm above the inside bottom. Add dilute Na_2CO_3 to the line.

Mix sediment thoroughly. Allow to settle 3 minutes. Carefully decant suspended material into the 1 L bottle without sediment transfer.

Add dilute Na_2CO_3 solution to the 5 cm mark. Mix thoroughly and allow to settle for calculated time for >20 µm particles (see Jackson, 1975, p. 114, Table 3-2). Settling times are 2 min. 20 sec. for 20° C, and 2 min. 5 sec. for 25°C. Decant suspension into bottle.

Repeat step 5 until supernatant is nearly clear. Use distilled water the last two times.

Transfer coarse silt into tared glass beaker. Record weight of beaker before filling. Dry silt overnight at 105°C.

Remove dry silt from oven and let cool in a desiccator. Weigh beaker plus silt. Store coarse silt in labeled plastic vials.

D. Separation of Clay (<2 µm)

Reagents:

Dilute Na_2CO_3 solution, pH 9.5 (0.2 g L^{-1})

Distilled water Dilute HCL (if necessary)

Procedure:

Allow the suspension containing the <20 µm material to stand at least 8 hours for each 10 cm depth (or proceed directly to the centrifugation procedure in step #3 below).

After settling, carefully decant suspended material to another 1 L bottle marked "<2 µm". Avoid transfer of any sediment.

Transfer the sediment (or the suspension, if skipping steps 1 and 2) into a sufficient number of 250 mL bottles. Mark the tubes with a line 9 cm above the top of the estimated sediment pad expected to form after centrifugation (or mark the tube at 10 cm from the bottom, assuming a sediment pad of approximately 1 cm depth).

Bring the volume plus liquid of each tube to the mark with dilute Na_2CO_3 solution.

Disperse by stirring or shaking. Centrifuge for 4 minutes at 750 rpm. Decant supernatant into bottles labeled "<2 µm".

Again bring the contents of each tube to the mark with Na_2CO_3 solution. Disperse.

Centrifuge for the calculated time (see Jackson, 1975, p. 128, Table 3-4). Settling times are 3.3 min. at 20°C, and 2.9 min. at 25°C. Decant suspension into "<2 µm" bottles.

Repeat step 5 until the supernatant suspension after centrifugation is almost clear, using distilled water for the last two centrifugations.

Transfer the fine plus medium silt sediment into a tared glass beaker, recording the beaker weight before filling. Dry in oven overnight at 105°C. Let cool in desiccator. Weigh beaker plus sediment and record. Store silt in labeled plastic vials.

E. Concentration of clay (<2 µm)

Reagents:

95% ethanol Distilled water

NaCl salt $AgNO_3$ solution

Procedure:
Flocculate suspensions of clay (<2 μm) by adding NaCl salt. If suspension fails to flocculate, add additional NaCl, ethanol, or Dilute HCl (gentle heating may also help).
Let suspension stand a few hours (or over night) to allow flocculation to occur.
When flocculation is complete, carefully decant or siphon off as much of the clear supernatant liquid as possible without the loss of any clay.
Excess salt must be washed from the flocculated clay. This can be done using centrifugation.
Centrifugation:
Transfer the flocculated clay suspension to 250 mL polypropylene bottles or 50 mL centrifuge tubes using a minimal amount of 50% ethanol:water mixture. Balance opposing bottles.
Centrifuge at 2,000 rpm for 5-10 minutes. Decant and discard the clear supernatant.
Transfer to 50 mL centrifuge tubes. Add 30 mL of 95% ethanol/water mixture to each tube. Disperse with stirring rod. Centrifuge at 2,000 rpm for 5-10 minutes. Decant and discard the clear supernatant. Do not discard the supernatant if it is not clear!
Repeat step 6 using 95% ethanol until the supernatant is free of Cl^- as determined by the $AgNO_3$ test or the clay starts to disperse.
When the clay is free of Cl, carefully transfer the clay into appropriately-sized sample bottles.

IV. X-ray Diffraction Analysis
Samples of soil and geologic material may be prepared for x-ray diffraction (XRD) analysis using oriented or random powder specimens. Samples containing phyllosilicates, such as the clay fractions from soils and sediments, are usually analyzed using oriented mounts. Sand and silt soil fractions, whole rocks, evaporite deposits, etc. are normally prepared using randomly oriented powder mounts. Any sample may be prepared for XRD analysis as either an oriented or a random powder mount, depending upon the objectives of the research project.
General references for XRD analytical techniques include the chapter by Whittig and Allardice in Klute (1986) and Jackson (1975).

A. Preparation and Analysis of Oriented Specimens
There are a number of ways to prepare oriented aggregates. The following method is simple yet effective because saturation of the exchange complex is achieved by washing the sample directly on porous ceramic plates (Whittig and Allardice, 1986).
Equipment:
Porous ceramic tiles Muffle furnace
Suction apparatus X-ray diffractometer
Pipet
Reagents:
pH 3.5 HCl 0.5 M $MgCl_2$
1 M KCl 1:1 glycerol-water solution

Distilled water
Procedure:
General instructions:
Place 2 ceramic tiles on the suction apparatus for each sample to be analyzed.
Label each tile in pencil with the sample ID. In addition, label one tile with "K", and one with "Mg" to differentiate between samples that will be saturated with K vs. Mg.
Place an aliquot of suspension containing approximately 10-20 mg of mineral material on each tile on the suction appatatus.
Apply suction and allow all of the liquid to pull through the tiles.
Draw the edge of a clean glass slide or spatula across the face of each tile to orient the sample parallel to the tile surface. (If using the same slide for different samples, be sure to clean the slide before orienting each new sample!)
If the sample was not washed free of excess salt before tile preparation, wash each sample tile 5 times with distilled water before proceeding.
For samples to be saturated with Mg:
Wash the sample 2 times with pH 3.5 HCl.
Wash 5 times with 0.5 M $MgCl_2$.
Wash 5 times with distilled water.
Allow sample to dry on the suction apparatus overnight.
Analyze the sample with the x-ray diffractometer, scanning the sample from 2 to 30 degrees 2-theta.
Return the sample to the sucton apparatus.
Wash the sample 2 times with 1:1 glycerol-water solution.
Allow the excess liquid to pull through the tile.
X-ray sample, scanning from 2 to 15 degrees 2-theta.
For sample to be saturated with K:
Wash the sample 5 times with 1 M KCl.
Wash the sample 5 times with distilled water.
Allow sample to dry overnight on the suction apparatus.
Analyze the sample with the x-ray diffractometer, scanning the sample from 2 to 15 degrees 2-theta.
If the sample appears to have any gibbsite (evident from the Mg-saturated 2-30 degree 2-theta analysis) or hydroxy-interlayered 2:1 phyllosilicates, heat the sample in a muffle furnace at 350°C for 2 hours. Cool and x-ray the sample again for the appropriate range in 2-theta values.
Heat the sample in a muffle furnace at 550° for two hours.
Cool and x-ray the sample again, scanning from 2 to 15 degrees 2-theta.

B. Preparation and Analysis of Random Powder Samples

Random powder mounts can be prepared from any size fraction from any material. The sample may or may not be saturated with a particular cation, depending upon the objectives of the experiment. See Jackson (1975) and Whittig and Allardice (1986) for further suggestions and procedures.

Wash excess salts out of sample if necessary.
Dry sample overnight in an oven at 105°C. If sample is <2μm in size, freeze drying is recommended.
Grind the sample into a fine powder using an agate (or other x-ray amorphous material) mortar and pestle.
Pack the powdered material into an appropriate sample holder with a small spatula. Apply pressure (if necessary) to keep sample in place.
Analyze the sample with the x-ray diffractometer, scanning the sample for the appropriate range, usually within 2 to 60 degrees 2-theta.

References

Busacca, A. J., Aniku, J. R., and Singer, M. J. (1984) Dispersion of soils by an ultrasonic method that eliminates probe contact. *Soil Sci. Soc. Am. J.* **48**, 1125-1129.

7.5 Density Fractionation

University of Minnesota-Twin Cities
PI: Kyungsoo Yoo **Room & Building:** Borlaug 181
Department: SWC, LAAS **Current Revision Date:** 09/05/2016
Contributors: Anthony Aufdenkampe, Amy Lyttle, Beth Fisher, Marta Roser
Purpose:
Separation of soil by fractionation based on particle density.
Reagents:
SPT, sodium polytungstate (Sodium metatungstate hydrate, crystalline, Acros Organics)
Choose a glassware item that will allow the water to be deep enough for the hydrometer, such as a graduated cylinder.
Measure 35mL of deionized water in the graduated cylinder.
Dissolve approximately 50g of SPT in the deionized water, stirring with a scoopula or stirring rod. Since the liquid will be thick, a stirring plate and magnet doesn't work very well.
Place hydrometer in liquid. Keep adding SPT until a density of 2g/cm3 is reached.
Equipment
Balance (Mettler Toledo PL602-S & AB104-S)
shaker (New Brunswick Scientific C1 Platform Shaker),
centrifuge (IEC Clinical Centrifuge)
hydrometer (H-B Instrument Company, 1.00 – 2.00 specific gravity)
50mL Falcon test tubes
conductivity meter
pipette and pipette tips
glass stirring rod
Procedure:
If samples have not been oven dried yet, dry them at 60°C overnight. Let cool.
Weigh out 10g of each soil sample and place in an individually labeled bag.
Separate large particles of the plant material from mineral soil (using a 250 or 500 um sieve if necessary).
Weigh all material that has been removed.
Lightly grind samples by rolling a centrifuge tube along the bag, pressing down gently.
Measure 25ml of sodium polytungstate (SPT) at density of 2g/cm3 (refer to Reagents for SPT instructions) and place into Falcon tube. If there is a lot of organic matter – very dark soil – split the soil into two different falcon tubes, each with 25ml of SPT.
Place falcon tubes with soil and SPT on shaker at setting "20" for 2-3 hours at room temperature. The tubes should be parallel to the shaker so that the liquid can go the whole length of the tube.
Centrifuge tubes at setting "5" for 20-30 minutes

After centrifuging the tube should have the heavy soil fraction at the bottom, the SPT in the middle, and the light soil fraction at the top. Carefully pour the light fraction and SPT into a new, labeled 50mL tube.
Centrifuge the light fraction tubes for 10 mins or until the light fraction is floating above the SPT layer. Carefully pipette out the SPT and discard into a labeled container. If there is soil stuck to the pipette tip, rinse off the tip into the centrifuge tube with deionized water.
Rinse heavy and light fraction with deionized water and centrifuge. This is done to rid sample of SPT so conductivity is approximately 50uS/cm (should take ~5 times of rinsing to achieve this).
Dry overnight in a muffle furnace at 60°C in the centrifuge tubes.
Grind each sample using a mortar and pestle. Weigh samples and put into labeled vials.

Sources:

Savage N. 1988. The use of sodium polytungstate for conodont seperations. Journal of Micropaleontology 7: 39-40.
Sollins P, Kramer M, Swanston C, Lajtha K, Filley T, Aufdenkampe A, Wagai R, Bowden R. 2009. Sequential density fractionation across soils of contrasting mineralogy: evidence for both microbial- and mineral-controlled soil organic matter stabilization. Biogeochemistry 96:209-231.

7.6 Measuring soil pH

University of Minnesota-Twin Cities
PI: Kyungsoo Yoo **Room & Building:** Borlaug 181
Department: SWC, LAAS **Current Revision Date:** 09/05/2016
Contributors: Beth Fisher, Charlotte Riggs
Purpose:
Measure pH of soil in deionized water and $CaCl_2$.
Equipment:
10 or more 50 mL centrifuge tubes or similar, tall container with lid to allow for sufficient water height above sample.
pH meter and calibration buffers
small graduated cylinder (for 10-mL)
stirring rod
DI rinse bottle
Kim wipes
stopwatch or timer
Solutions:
deionized water
0.02 M CaCl2
Concentration:
0.02 M CaCl2: 147.02 g/L * 0.02 M = 2.94 g/L
Amount required: 10 mL per sample * 12 samples = 1.2 L
2.94 g/L * 2.5 L (double batch) = 7.35 g of CaCl2
Procedure:
In 50 mL centrifuge tube:
Place ~10 g of soil sample in centrifuge tube.
Add 10 mL of deionized water, cover and stir or shake thoroughly for 30 seconds.
Allow sample to stand for 1 hour, stirring/shaking at approximately every 20 minutes.
With all samples to be measured within reach, stir/shake sample for 30 seconds.
Insert pH electrode (at the same depth for each sample; place lab tape on the probe for your marker) and take pH reading exactly 60 seconds after stirring.
Add 10 mL of 0.02M CaCl2 to the suspension.
Stir/shake sample for 30 seconds.
Insert pH electrode and take second pH reading at exactly 60 seconds after stirring.
Rinse/dry stirring rod between samples.
Repeat steps 1-9 for each sample.
Each iteration, with transition between samples should take ~4 minutes so plan appropriately and run batches of ~10 samples at a time to achieve consistent pH measurements (10 samples would equate to ~1 hour of lab time with pH calibration, prep and cleanup).

7.7 Measuring soil texture/particle size by hydrometer

University of Minnesota-Twin Cities
PI: Kyungsoo Yoo **Room & Building:** Borlaug 181
Department: SWC, LAAS **Current Revision Date:** 09/05/2016
Contributors: Beth Fisher
Purpose:
Measure particle size distribution of fine (<2mm) fraction of soil.
Safety Precautions and Personal Protective Gear Requirements:
Wear lab coat, eye protection and gloves.
Reagents:
Distilled Deionized Water, (DDI).
Sodium Hexametaphosphate, $(NaPO_3)_6$: Dissolve 8.3 + 0.2 g of sodium carbonate (Na_2CO_3) in 1600 mL of DDI in a 4 L nalgene beaker. Slowly add to this solution, in 50 g increments, 100 g of reagent grade sodium hexametaphosphate $(NaPO_3)_6$ and stir well. Check pH of the solution; it should be 8.3 + 0.1. Transfer the solution to a 2 L volumetric flask and make to volume with DDI.
Apparatus:
Standard hydrometer, ATSM 152H, with Bouyoucos scale in g/L
Electrically driven mixer. We use a vintage malt mixer.
Sedimentation cylinder, 1 L, with 1,000 mL mark 36 (+ 2) cm from the inside bottom of the cylinder.
Brass plunger.
Sample Preparation:
Prepare soil samples following normal drying, grinding and sieving procedures. Soil samples should be sieved using a 2mm mesh size.
Procedure:
Stage 1:
Weigh 40.0 or 50.0 g of air-dried, 2 mm sieved soil into a 500 ml flask. Record weight.
Add 100 ml of the 5% solution of sodium hexametaphosphate.
Add about 300 mls of DDI to the suspension in the dispersing cup. The water level should be about 3 inches from the top of the cup.
Allow samples and blank to soak for 16 hours (overnight).
NOTE: It is essential to prepare a blank cylinder for each set of samples. The blank should be prepared exactly the same as the samples (e.g., allowed to sit for 16 hours, mixed, etc).
Stage 2:
Mix the suspension on the electric mixer for 1 minute.
Transfer the suspension to the sedimentation cylinder. Use a wash bottle and rinse down sides of cup to ensure that all soil is transferred.
If the top is covered with foam, add 1 drop of amyl alcohol.

Add sufficient DDI to attain a volume of 1000 mls in the cylinder (the lower mark on the cylinder).

Stage 3:

When temperature is stabilized, measure and record.

Insert the plunger and mix contents thoroughly, taking care not to spill or splash contents of the cylinder. Mix by carefully moving the plunger in short upward strokes to initially disrupt sediments at the bottom of the cylinder. Then proceed to mix by using 3-5 slow, smooth strokes for the length of the cylinder until sediments are clearly suspended.

Upon removing the plunger, begin a 40-second timer.

Note the exact time for each sample (usually 2-minute intervals is a comfortable spacing).

Within 15 seconds after mixing the suspension, carefully lower the hydrometer into the suspension, and at 40 seconds, read the hydrometer value by reading the scale at the top of the meniscus. Record the hydrometer value.

Remove the hydrometer carefully, rinse with DDI and proceed to next sample.

Stage 4:

At exactly 8 hours after suspending the soil in the cylinder, without remixing the suspension, carefully lower the hydrometer into the sedimentation cylinder and record the hydrometer value when it has stabilized. Proceed to the next samples at the same time interval determined in Stage 3.

Record the temperature of the samples and blank at 8 hours.

NOTE: When the hydrometer is floating in a 5% solution of sodium hexametaphosphate (100 mls of 5% sodium hexametaphosphate per liter), it will have a stem reading of 5-7.

It is essential to prepare a blank cylinder for each set of samples. The blank should be prepared exactly the same as the samples (e.g., allowed to sit for 16 hours, mixed, etc).

Special Cleanup:

Pour and rinse out cylinder contents through a sieve and into a sieve with a trap to retain coarse particles.

Calculations:

Temperature correction:

The hydrometer readings must be corrected for deviations from the temperature at which the hydrometer was calibrated (20°C). Care should be taken to avoid extreme temperature variations during this procedure. The temperature should be with in the range of 15 to 25°C.

Corrected Hydrometer Reading = (Sample Reading - Blank Reading) + Correction Factor

Where:

Correction Factor = 0.36*(Measured Temperature - 20°C)

Particle Size Calculations:

% Sand = 100-[(Corrected Hydrometer Reading at 40 sec / Corrected weight of soil)*100]

% Clay = [(Corrected Hydrometer Reading at 2 hours / Corrected weight of soil)*100]

% Silt = 100 - (% Sand + % Clay)

Where:
Corrected weight of Soil = (Oven Dry Weight of Subsample X 50 g)(Air-Dried Weight of Subsample)

References:

Bouyoucos. G.J. 1962. Hydrometer method improved for making particle size analysis of soils. Agron. J. 54:464-465

Day, P.R. 1965. Particle fractionation and particle-size analysisp.545-567. In C.A. Black et al (ed.) Methods of soil analysis, Part 1. Agronomy 9:545-567.

8 Appendix 2. Data

8.1 Major and minor rock forming elements for all sample sites measured by XRF

Site	Upper Depth Cm	Lower Depth Cm	Na2O	MgO	Al2O3	SiO2	K2O	CaO	TiO2	MnO	Fe2O3	P2O5	LOI
LP_Well1	0	6	0.00	1.21	16.38	59.90	2.79	0.27	1.27	0.162	8.16	0.167	12.66
LP_Well1	6	14	0.00	1.21	16.38	59.90	2.79	0.27	1.27	0.162	8.16	0.167	12.66
LP_Well1	14	19	0.00	1.33	16.85	65.57	2.64	0.32	1.21	0.210	9.12	0.155	7.60
LP_Well1	19	28	0.00	1.33	16.85	65.57	2.64	0.32	1.21	0.210	9.12	0.155	7.60
LP_Well1	28	44	0.00	1.29	16.56	63.81	2.72	0.25	1.19	0.146	9.21	0.145	6.69
LP_Well1	44	59	0.00	1.14	14.02	70.15	2.29	0.22	0.94	0.103	7.61	0.130	5.50
LP_Well1	59	72	0.00	1.45	18.14	65.09	3.59	0.17	1.19	0.148	8.84	0.134	5.35
LP_Well1	72	84	0.00	1.64	18.74	63.07	4.10	0.17	1.27	0.152	9.40	0.111	4.97
LP_Well1	84	100	0.05	1.65	14.81	68.35	2.12	0.91	1.32	0.142	7.40	0.104	5.20
LP_Well1	100	146	0.00	1.68	15.86	64.96	2.63	0.37	1.26	0.098	6.66	0.079	5.05
LP_Well1	152	163	0.04	1.86	17.43	64.25	3.36	0.05	1.09	0.187	8.65	0.108	4.52
LP_Well1	163	174	0.00	1.81	16.55	63.96	2.46	0.16	1.14	0.315	9.05	0.153	3.09
LP_Well1	174	185	0.45	1.98	19.05	69.03	3.30	0.25	1.28	0.190	9.23	0.173	4.62
LP_Well1	185	196	0.00	1.85	19.01	61.56	3.76	0.12	1.23	0.162	9.12	0.114	4.42
LP_Well1	196	207	0.00	1.76	19.92	59.70	4.19	0.04	1.20	0.159	9.87	0.085	4.50
LP_Well1	207	218	0.00	1.86	20.95	57.78	4.40	0.04	1.34	0.133	11.29	0.074	4.73
LP_Well1	218	229	0.00	1.80	19.02	62.29	3.87	0.08	1.22	0.112	9.43	0.091	4.09
LP_Well1	229	239	0.00	1.61	19.77	60.73	4.28	0.03	1.22	0.153	9.44	0.080	4.41
LP_Well1	239	250	0.00	1.31	18.22	59.60	3.66	0.02	1.26	0.177	9.31	0.099	4.78
LP_Well1	250	261	0.00	1.48	19.57	60.12	3.97	0.02	1.29	0.126	10.74	0.094	4.81
LP_Well1	261	272	0.38	1.56	20.30	61.28	4.26	0.03	1.30	0.089	10.22	0.061	4.48
LP_Well1	272	283	0.03	1.64	18.65	61.80	3.97	0.04	1.23	0.085	9.73	0.057	3.99
LP_Well1	283	294	0.11	1.77	18.34	63.03	3.75	0.09	1.11	0.081	9.37	0.066	3.91
LP_Well1	305	315	0.15	1.89	20.43	58.68	3.74	0.39	1.19	0.190	9.82	0.149	4.81
LP_Well1	356	368	1.40	1.88	20.99	57.07	4.12	0.51	1.30	0.092	10.86	0.128	4.43
LP_Well1	396	406	0.81	2.27	23.63	54.34	5.32	0.13	1.23	0.113	10.43	0.084	4.75
LP_Well1	445	457	1.27	1.81	19.22	61.16	3.73	0.67	1.28	0.088	9.46	0.228	3.47
LP_Well1	498	508	1.18	1.97	20.91	56.58	4.40	0.51	1.36	0.074	11.29	0.194	3.79
LP_Well1	549	559	0.00	2.06	21.28	57.45	3.87	0.25	1.17	0.182	10.22	0.077	5.03
LP_Well1	589	597	1.12	1.80	21.17	58.62	4.06	0.47	1.31	0.169	8.99	0.134	5.39
LP_Well1	695	707	0.72	1.78	17.39	62.81	2.24	0.75	0.93	0.122	8.81	0.122	4.40
LP_Well1	747	762	0.59	1.86	20.29	59.65	3.66	0.41	1.19	0.171	9.67	0.138	4.66
LP_Well1	800	811	1.82	2.11	20.44	57.51	4.03	0.37	0.98	0.160	10.84	0.201	4.27
LP_Well1	842	852	0.42	2.16	24.68	51.97	5.22	0.50	1.15	0.206	11.21	0.224	4.24
LP_Well1	894	904	0.61	1.94	20.25	57.86	3.63	0.79	1.12	0.133	10.59	0.187	4.02
LP_Well1	948	955	2.08	1.85	18.64	61.69	3.22	0.98	1.04	0.100	8.30	0.170	3.53
LP_Well1	1000	1006	2.07	1.30	12.43	73.26	1.99	1.25	0.97	0.120	5.41	0.150	2.59
LP_Well1	1049	1055	2.89	1.31	12.82	73.64	1.87	1.67	0.96	0.100	4.85	0.190	2.01
LP_Well1	1093	1107	2.93	1.12	14.08	70.18	0.73	3.19	1.20	0.141	4.99	0.318	2.00
LP_Well1	1200	1213	1.96	2.24	21.30	55.07	3.43	1.15	1.26	0.211	10.63	0.205	4.35
LP_Well1	1311	1318	2.49	1.81	18.03	63.05	2.80	0.98	1.09	0.148	8.37	0.175	3.28
LP_Well1	1397	1422	1.24	2.19	18.97	61.75	2.94	0.89	1.21	0.161	8.62	0.177	3.99
LP_Well1	1524	1535	1.13	1.71	18.18	61.66	3.10	0.70	1.16	0.199	9.61	0.205	3.46
LP_Well1	1557	1568	1.98	1.78	18.67	60.64	3.20	0.73	1.13	0.218	10.16	0.187	3.00
LP_Well1	1600	1657	1.20	1.99	25.50	50.98	4.58	0.59	1.24	0.216	10.83	0.218	5.21
LP_Well1	1857	1864	1.37	1.95	21.29	56.63	3.51	1.21	1.24	0.314	11.21	0.222	3.72
LP_Well1	1891	1898	5.88	1.82	20.50	56.46	3.25	1.58	1.18	0.261	10.82	0.199	3.21
LP_Well1	2000	2019	2.17	2.32	29.67	42.98	4.22	1.02	1.40	0.377	13.25	0.328	5.08
LP_Well1	2096	2111	0.97	1.95	23.19	51.42	3.84	1.12	1.21	0.455	13.80	0.213	3.88
LP_Well1	2177	2186	1.63	1.65	17.86	62.69	2.42	1.26	1.02	0.155	8.62	0.173	3.85

Site	Upper Depth Cm	Lower Depth Cm	Total	Ba_ ppm	Ce_ ppm	Co_ ppm	Cr_ ppm	Cu_ ppm	Hf_ ppm	La_ ppm	Nb_ ppm	Nd_ ppm	Ni_ ppm	Pb_ ppm
LP_Well1	0	6	102.17	708	144.9	146	93	32	11.5	45.3	21.1	52.3	54	37.5
LP_Well1	6	14	102.17	708	144.9	146	93	32	11.5	45.3	21.1	52.3	54	37.5
LP_Well1	14	19	102.75	719	168.3	136	87	31	10.5	50.1	17.6	65.5	58	19.7
LP_Well1	19	28	102.75	719	168.3	136	87	31	10.5	50.1	17.6	65.5	58	19.7
LP_Well1	28	44	99.22	715	125.0	138	84	30	10.0	46.2	18.1	60.0	52	15.4
LP_Well1	44	59	100.46	569	105.2	170	73	32	8.0	45.2	14.7	48.0	46	13.7
LP_Well1	59	72	102.06	781	117.7	138	88	42	8.4	50.5	18.7	55.0	53	13.3
LP_Well1	72	84	102.31	810	151.1	138	83	37	10.0	72.1	17.2	78.3	73	13.2
LP_Well1	84	100	101.67	578	114.4	149	77	19	16.8	56.4	18.5	64.1	70	16.8
LP_Well1	100	146	98.63	799	79.4	98	73	14	15.5	31.7	19.0	38.9	63	14.6
LP_Well1	152	163	99.17	671	129.8	113	78	45	7.5	55.6	19.0	61.4	46	14.4
LP_Well1	163	174	97.74	743	221.1	95	98	69	8.0	40.0	21.2	42.7	52	14.8
LP_Well1	174	185	107.80	583	105.8	106	83	49	9.2	29.8	21.6	32.7	35	15.2
LP_Well1	185	196	99.19	688	135.2	106	95	49	8.5	28.8	20.5	36.1	40	15.0
LP_Well1	196	207	99.27	773	157.2	88	91	36	6.6	115.1	18.2	121.1	60	14.8
LP_Well1	207	218	100.57	812	186.0	92	107	28	7.1	43.0	21.0	43.8	56	15.1
LP_Well1	218	229	100.33	707	51.3	85	91	32	7.7	27.4	21.4	27.5	41	14.8
LP_Well1	229	239	99.84	776	123.7	83	93	48	7.7	32.8	19.7	41.0	54	14.6
LP_Well1	239	250	96.98	714	148.0	128	90	59	8.8	90.3	18.9	102.6	59	15.2
LP_Well1	250	261	100.65	803	163.7	87	96	64	7.0	105.1	18.0	112.2	67	13.7
LP_Well1	261	272	102.22	805	176.8	96	93	47	7.9	48.6	20.0	56.2	60	14.7
LP_Well1	272	283	99.83	771	123.8	98	91	38	8.0	25.5	21.6	30.5	49	14.9
LP_Well1	283	294	100.41	763	76.9	100	88	29	6.1	21.5	20.4	26.8	51	14.8
LP_Well1	305	315	101.44	703	429.4	110	92	75	9.0	181.0	20.3	179.7	50	16.6
LP_Well1	356	368	102.78	816	133.6	69	205	32	6.3	23.3	21.9	29.8	52	15.8
LP_Well1	396	406	103.11	870	127.7	50	105	57	6.6	76.0	21.7	77.5	45	15.2
LP_Well1	445	457	102.39	694	216.7	75	89	25	8.0	30.6	21.3	41.4	48	15.1
LP_Well1	498	508	102.26	917	181.0	65	102	30	6.0	99.0	21.0	94.0	60	16.0
LP_Well1	549	559	101.59	749	156.0	78	99	44	7.6	59.8	19.4	64.4	47	16.9
LP_Well1	589	597	103.23	761	165.6	79	91	24	11.6	156.2	22.6	145.0	47	15.8
LP_Well1	695	707	100.07	480	378.4	94	78	65	5.9	221.5	16.0	176.7	59	16.2
LP_Well1	747	762	102.29	610	323.2	79	91	48	9.6	62.0	22.3	70.2	48	17.1
LP_Well1	800	811	102.73	523	85.5	76	89	64	4.4	62.6	18.0	67.7	45	15.4
LP_Well1	842	852	101.98	717	207.6	57	101	48	4.6	66.0	21.1	67.1	50	16.0
LP_Well1	894	904	101.13	760	118.8	77	83	20	5.5	19.2	20.5	25.7	52	15.4
LP_Well1	948	955	101.60	709	127.0	53	93	29	6.0	59.0	20.0	50.0	49	16.0
LP_Well1	1000	1006	101.54	600	106.0	132	65	1	12.0	49.0	21.0	53.0	20	15.0
LP_Well1	1049	1055	102.31	628	102.0	81	52	5	13.0	43.0	20.0	45.0	16	14.0
LP_Well1	1093	1107	100.88	304	102.4	72	57	2	23.7	42.7	17.7	51.5	17	19.8
LP_Well1	1200	1213	101.81	822	163.8	73	112	48	9.7	76.4	21.5	79.6	52	27.3
LP_Well1	1311	1318	102.22	623	142.9	67	94	38	9.5	71.9	20.2	66.0	44	24.1
LP_Well1	1397	1422	102.14	613	110.3	67	95	23	9.6	48.0	22.7	47.9	38	19.0
LP_Well1	1524	1535	101.11	512	141.0	92	86	48	8.1	70.4	20.8	69.7	44	16.6
LP_Well1	1557	1568	101.70	569	145.3	76	92	55	8.0	74.1	21.4	72.6	46	17.1
LP_Well1	1600	1657	102.55	667	97.4	59	125	65	4.6	76.2	25.6	82.2	53	18.6
LP_Well1	1857	1864	102.67	725	178.1	68	97	41	7.2	164.2	18.3	148.5	46	17.1
LP_Well1	1891	1898	105.16	643	158.4	63	95	26	8.4	72.7	20.4	70.6	43	16.4
LP_Well1	2000	2019	102.82	599	153.2	45	134	90	4.9	102.9	21.9	106.1	56	20.5
LP_Well1	2096	2111	102.05	636	140.2	67	125	42	6.0	78.5	19.9	75.3	43	16.5
LP_Well1	2177	2186	101.33	541	147.6	79	93	42	7.5	130.2	17.6	131.0	45	17.0

Site	Upper Depth Cm	Lower Depth Cm	Rb_ ppm	Sc_ ppm	Sr_ ppm	Th_ ppm	V_ ppm	Y_ ppm	Zn_ ppm	Zr_ ppm
LP_Well1	0	6	94	17	79	10.9	147.8	86.6	175	338
LP_Well1	6	14	94	17	79	10.9	147.8	86.6	175	338
LP_Well1	14	19	85	14	73	9.9	144.2	107.9	167	312
LP_Well1	19	28	85	14	73	9.9	144.2	107.9	167	312
LP_Well1	28	44	86	15	75	9.4	148.8	105.1	153	308
LP_Well1	44	59	76	13	62	9.2	124.8	88.7	129	246
LP_Well1	59	72	97	19	60	10.4	144.6	82.3	143	257
LP_Well1	72	84	114	19	64	9.2	148.4	105.7	165	298
LP_Well1	84	100	87	13	79	9.5	132.5	125.8	166	479
LP_Well1	100	146	104	13	50	8.8	123.2	83.7	160	453
LP_Well1	152	163	90	18	65	9.1	135.0	38.6	149	235
LP_Well1	163	174	96	22	69	9.9	151.5	32.9	166	242
LP_Well1	174	185	89	18	83	8.6	140.1	29.1	149	279
LP_Well1	185	196	100	20	78	8.4	143.4	29.2	146	252
LP_Well1	196	207	109	20	67	8.9	145.0	88.8	153	204
LP_Well1	207	218	108	23	68	9.0	167.4	46.4	160	220
LP_Well1	218	229	104	21	75	9.2	149.6	28.3	157	224
LP_Well1	229	239	112	21	68	9.7	147.2	59.3	145	236
LP_Well1	239	250	109	19	57	9.6	151.4	121.5	138	269
LP_Well1	250	261	105	21	59	7.7	160.2	99.7	143	218
LP_Well1	261	272	109	19	72	8.4	161.0	46.4	145	233
LP_Well1	272	283	111	21	71	9.2	150.7	23.4	148	237
LP_Well1	283	294	105	20	81	8.3	155.5	16.7	157	190
LP_Well1	305	315	99	20	112	9.5	141.6	84.2	148	275
LP_Well1	356	368	115	25	126	9.1	159.3	25.1	148	210
LP_Well1	396	406	135	23	103	9.8	143.7	28.6	151	217
LP_Well1	445	457	103	20	133	8.0	143.9	31.8	125	260
LP_Well1	498	508	119	23	124	9.0	161.0	35.0	137	189
LP_Well1	549	559	105	21	88	9.0	142.2	36.6	142	239
LP_Well1	589	597	113	18	120	10.2	144.6	75.4	121	358
LP_Well1	695	707	70	16	201	8.4	112.9	93.3	133	207
LP_Well1	747	762	103	21	140	9.8	135.6	41.9	130	300
LP_Well1	800	811	105	21	133	8.1	134.7	30.8	148	144
LP_Well1	842	852	134	24	144	8.5	151.5	27.4	137	154
LP_Well1	894	904	99	19	146	8.6	129.8	20.2	123	200
LP_Well1	948	955	91	20	173	9.0	113.0	37.0	128	225
LP_Well1	1000	1006	72	10	141	10.0	81.0	40.0	69	397
LP_Well1	1049	1055	68	11	185	10.0	75.0	34.0	71	382
LP_Well1	1093	1107	58	12	321	13.7	83.2	61.7	78	682
LP_Well1	1200	1213	103	22	181	10.8	159.8	56.2	138	296
LP_Well1	1311	1318	96	18	166	9.9	124.5	61.1	129	284
LP_Well1	1397	1422	99	18	157	9.7	125.4	44.6	134	291
LP_Well1	1524	1535	90	18	144	8.0	133.4	48.5	120	263
LP_Well1	1557	1568	95	20	148	8.1	134.4	48.1	125	253
LP_Well1	1600	1657	132	29	178	11.1	163.6	33.3	70	163
LP_Well1	1857	1864	102	19	166	7.9	138.0	100.0	125	239
LP_Well1	1891	1898	92	21	215	9.1	145.5	56.1	123	260
LP_Well1	2000	2019	101	27	271	8.9	179.7	54.1	147	177
LP_Well1	2096	2111	98	30	167	7.7	171.2	57.5	117	181
LP_Well1	2177	2186	82	18	181	8.7	125.0	74.1	118	237

Site	Upper Depth Cm	Lower Depth Cm	Na2O	MgO	Al2O3	SiO2	K2O	CaO	TiO2	MnO	Fe2O3	P2O5	LOI
LP_Well1	2186	2195	2.90	1.44	17.63	62.95	2.44	1.51	1.10	0.174	8.59	0.169	2.94
LP_Well2	0	2	0.00	1.79	20.45	56.97	4.25	0.11	1.33	0.213	9.61	0.104	10.40
LP_Well2	2	6	0.01	1.74	20.06	57.78	3.99	0.12	1.31	0.242	9.41	0.110	10.12
LP_Well2	6	12	0.02	1.63	19.27	59.39	3.47	0.15	1.26	0.298	9.01	0.123	9.55
LP_Well2	12	18	0.04	1.44	17.89	62.22	2.56	0.20	1.18	0.397	8.31	0.144	8.57
LP_Well2	18	29	0.06	1.47	18.15	62.04	2.62	0.19	1.19	0.362	8.44	0.141	8.15
LP_Well2	29	37	0.12	1.54	18.71	61.64	2.74	0.17	1.20	0.284	8.71	0.134	7.23
LP_Well2	37	46	0.17	1.59	19.17	61.31	2.85	0.16	1.21	0.221	8.94	0.128	6.48
LP_Well2	46	56	0.21	1.63	18.26	62.49	2.63	0.14	1.14	0.153	9.12	0.120	6.05
LP_Well2	56	70	0.13	1.82	19.77	60.40	2.92	0.14	1.18	0.155	9.92	0.125	6.07
LP_Well2	70	80	0.24	2.02	22.26	61.05	3.55	0.15	1.27	0.167	10.31	0.111	5.54
LP_Well2	80	90	0.33	1.92	20.87	57.97	3.73	0.14	1.35	0.182	9.85	0.094	5.25
LP_Well2	90	107	0.40	2.02	20.16	59.69	3.35	0.18	1.23	0.185	9.65	0.121	5.14
LP_Well2	107	122	0.35	1.64	18.64	52.08	3.01	0.16	1.14	0.163	8.94	0.102	5.00
LP_Well2	127	140	0.11	1.67	18.27	63.32	2.89	0.12	1.15	0.168	8.92	0.090	5.15
LP_Well2	140	152	0.41	1.77	18.60	63.22	2.85	0.14	1.17	0.168	8.66	0.108	5.53
LP_Well2	152	162	1.78	2.42	20.63	57.23	3.39	0.51	1.14	0.240	9.15	0.150	4.39
LP_Well2	162	171	1.73	2.24	22.20	55.10	4.11	0.49	1.23	0.201	9.63	0.152	4.44
LP_Well2	171	186	1.36	2.02	19.38	60.07	3.69	0.35	1.31	0.196	8.72	0.089	4.75
LP_Well2	186	200	1.13	2.25	20.03	58.50	3.61	0.34	1.22	0.173	9.02	0.093	5.03
LP_Well2	200	219	1.66	2.19	20.47	57.59	3.50	0.43	1.13	0.238	9.49	0.142	4.71
LP_Well2	219	229	1.88	1.58	18.41	55.84	3.59	0.36	1.26	0.281	15.82	0.150	4.17
LP_Well2	229	238	1.13	1.74	18.24	56.30	3.09	0.43	1.17	0.460	13.20	0.161	5.63
LP_Well2	238	248	1.24	1.61	19.81	58.23	3.68	0.30	1.24	0.145	10.35	0.122	5.20
LP_Well2	248	257	1.54	1.56	19.97	55.59	3.93	0.36	1.32	0.232	12.37	0.137	4.69
LP_Well2	257	267	0.30	1.41	20.07	53.32	4.04	0.22	1.34	0.193	16.33	0.110	4.32
LP_Well2	267	276	0.17	1.67	17.56	62.00	3.15	0.73	1.24	0.192	10.88	0.100	3.50
LP_Well2	276	286	0.00	1.74	17.31	62.94	3.21	0.82	1.17	0.149	10.42	0.103	3.61
LP_Well2	286	293	0.34	1.92	19.56	57.08	3.50	0.54	1.07	0.209	8.34	0.118	4.11
LP_Well2	293	305	0.18	2.12	18.48	61.81	3.39	0.40	1.12	0.184	10.23	0.119	3.59
LP_Well2	348	359	2.03	2.34	21.92	53.87	3.23	0.61	1.14	0.290	10.72	0.160	4.43
LP_Well2	403	414	2.48	2.70	23.69	50.29	3.33	0.92	1.32	0.700	12.49	0.210	4.09
LP_Well2	457	467	2.69	2.16	20.30	58.38	3.11	0.78	1.04	0.265	10.28	0.150	3.99
LP_Well2	498	508	1.98	2.13	20.54	57.84	3.38	0.69	1.08	0.233	10.30	0.146	3.92
LP_Well2	549	559	1.08	2.10	20.41	58.01	2.92	0.66	1.18	0.319	9.85	0.161	3.87
LP_Well2	599	610	2.07	2.47	22.69	52.90	3.45	0.41	1.22	0.300	10.96	0.200	4.64
LP_Well2	701	725	1.50	1.39	10.42	78.11	1.38	1.01	0.68	0.110	4.48	0.100	2.16
LP_Well2	799	811	2.09	2.20	22.54	53.68	4.00	1.10	1.28	0.210	10.22	0.210	3.96
LP_Well2	955	962	1.80	2.39	19.73	57.95	3.37	0.74	1.14	0.250	9.77	0.190	3.42
LP_Well2	992	1008	2.50	2.43	19.05	60.11	3.11	1.01	1.14	0.260	9.18	0.240	3.42
LP_Well2	1089	1105	2.08	2.16	25.02	49.94	4.80	0.90	1.31	0.230	10.28	0.190	3.73
LP_Well2	1200	1219	2.20	2.29	22.61	52.68	3.89	1.10	1.21	0.300	11.11	0.170	3.56
LP_Well2	1225	1231	2.73	2.29	20.84	56.08	2.93	1.64	1.05	0.290	9.56	0.190	3.22
LP_Well2	1289	1308	1.18	1.28	11.80	75.39	1.54	2.19	1.02	0.132	4.76	0.096	1.33
LP_Well2	1387	1406	0.09	2.03	20.57	58.14	4.41	1.43	1.35	0.161	9.35	0.185	3.49
LP_Well2	1485	1504	1.37	2.73	24.98	49.26	4.99	1.20	1.50	0.264	11.16	0.183	4.82
LP_Well2	1578	1614	3.45	2.25	21.72	56.25	3.51	1.33	1.19	0.238	10.53	0.188	3.34
LP_Well2	1685	1703	0.83	2.02	17.97	63.05	2.70	1.22	1.01	0.224	8.96	0.179	2.81
LP_Well2	1793	1807	2.21	2.41	18.17	61.14	2.33	1.50	0.95	0.200	9.13	0.167	3.19
LP_Well2	1890	1910	2.17	2.36	23.48	51.95	3.76	0.89	1.55	0.225	11.56	0.240	4.06

Site	Upper Depth Cm	Lower Depth Cm	Total	Ba_ ppm	Ce_ ppm	Co_ ppm	Cr_ ppm	Cu_ ppm	Hf_ ppm	La_ ppm	Nb_ ppm	Nd_ ppm	Ni_ ppm	Pb_ ppm
LP_Well1	2186	2195	101.84	521	103.5	92	81	22	10.1	39.4	20.0	46.7	34	17.6
LP_Well2	0	2	102.38	656	171.9	150	89	55	8.6	70.5	18.1	100.3	70	33.8
LP_Well2	2	6	102.12	664	172.5	145	89	55	8.6	70.7	18.1	101.6	70	31.7
LP_Well2	6	12	101.60	681	173.8	135	91	53	8.5	71.0	18.0	104.2	71	27.5
LP_Well2	12	18	100.70	711	175.9	117	93	50	8.4	71.4	17.8	108.7	72	20.3
LP_Well2	18	29	100.36	713	167.0	117	93	50	8.5	71.2	18.1	102.4	71	20.2
LP_Well2	29	37	99.63	716	147.3	118	94	51	8.6	70.7	18.6	88.4	69	19.9
LP_Well2	37	46	99.02	719	131.1	118	95	51	8.7	70.4	19.0	77.0	68	19.7
LP_Well2	46	56	100.03	630	94.9	120	90	53	7.8	71.5	17.3	75.3	66	18.9
LP_Well2	56	70	99.78	653	100.3	112	96	55	7.6	52.9	21.1	48.2	63	19.5
LP_Well2	70	80	104.19	718	133.0	104	98	58	7.5	49.3	21.5	49.9	62	20.0
LP_Well2	80	90	99.10	760	128.8	96	113	59	8.1	56.1	24.2	59.2	61	17.5
LP_Well2	90	107	99.99	679	142.2	102	97	62	8.2	58.5	21.4	64.6	68	18.4
LP_Well2	107	122	89.32	666	133.3	96	100	58	7.9	54.6	22.7	64.6	67	19.1
LP_Well2	127	140	99.38	604	145.0	118	91	57	8.0	47.3	21.4	49.1	59	18.5
LP_Well2	140	152	100.63	613	151.2	105	89	61	9.4	55.6	21.5	64.3	65	18.3
LP_Well2	152	162	97.98	661	124.6	90	103	73	5.7	71.6	21.7	82.1	67	17.4
LP_Well2	162	171	98.63	793	146.1	73	113	48	6.5	73.2	22.8	78.5	62	17.5
LP_Well2	171	186	99.61	810	157.4	93	110	51	7.8	80.7	25.7	83.4	53	15.6
LP_Well2	186	200	99.79	775	178.7	90	100	56	6.7	101.0	24.0	103.7	63	16.0
LP_Well2	200	219	99.18	686	166.2	97	100	57	7.0	89.4	21.2	99.1	61	16.2
LP_Well2	219	229	99.23	783	103.1	92	147	43	6.0	48.7	18.5	47.7	44	13.0
LP_Well2	229	238	99.39	692	128.7	99	128	47	6.6	59.9	20.0	59.8	56	14.0
LP_Well2	238	248	99.30	742	129.3	91	123	49	7.5	60.6	22.5	60.4	52	15.9
LP_Well2	248	257	98.47	818	103.1	91	143	50	6.4	49.4	20.6	54.0	48	15.1
LP_Well2	257	267	99.76	860	107.7	74	144	45	6.8	41.9	19.3	44.1	48	15.4
LP_Well2	267	276	99.81	704	128.9	97	91	44	9.5	46.5	19.3	51.0	46	16.6
LP_Well2	276	286	100.05	719	108.5	94	86	36	9.1	51.0	17.3	55.5	46	16.6
LP_Well2	286	293	95.14	700	123.3	94	96	71	6.6	53.9	21.4	58.8	59	19.1
LP_Well2	293	305	100.17	619	121.6	100	91	42	6.1	34.9	19.3	37.4	53	16.6
LP_Well2	348	359	100.74	679	176.0	79	106	54	6.0	98.0	19.0	100.0	68	17.0
LP_Well2	403	414	102.22	683	210.0	69	124	31	6.0	56.0	22.0	31.0	73	16.0
LP_Well2	457	467	103.15	586	197.5	99	92	51	4.4	28.5	20.6	28.1	68	18.9
LP_Well2	498	508	102.24	641	140.0	74	88	0	5.0	35.0	22.0	37.0	67	17.0
LP_Well2	549	559	100.56	644	137.3	76	91	44	5.0	37.8	21.1	42.7	67	17.9
LP_Well2	599	610	101.31	728	388.0	100	120	151	5.0	400.0	23.0	412.0	62	17.0
LP_Well2	701	725	101.34	513	61.0	134	55	20	7.0	29.0	14.0	37.0	33	13.0
LP_Well2	799	811	101.49	720	174.0	60	116	48	6.0	84.0	23.0	80.0	54	17.0
LP_Well2	955	962	100.75	620	192.0	76	116	68	6.0	93.0	21.0	85.0	55	15.0
LP_Well2	992	1008	102.45	556	126.0	109	95	25	7.0	53.0	20.0	54.0	53	16.0
LP_Well2	1089	1105	100.64	855	196.0	50	134	42	7.0	100.0	24.0	96.0	57	19.0
LP_Well2	1200	1219	101.12	661	186.0	83	158	26	6.0	96.0	21.0	91.0	54	17.0
LP_Well2	1225	1231	100.82	544	159.0	79	123	56	5.0	79.0	21.0	73.0	61	17.0
LP_Well2	1289	1308	100.72	568	71.3	115	51	2	15.8	26.2	16.8	38.8	20	17.3
LP_Well2	1387	1406	101.21	769	122.4	76	83	13	9.0	53.5	22.3	59.0	41	16.8
LP_Well2	1485	1504	102.46	931	168.3	51	105	71	8.7	75.5	22.5	72.4	60	19.8
LP_Well2	1578	1614	104.00	695	150.3	64	96	43	7.1	72.9	19.8	75.8	51	18.9
LP_Well2	1685	1703	100.97	585	133.3	56	88	38	4.6	50.5	18.8	56.2	50	16.6
LP_Well2	1793	1807	101.40	498	121.0	94	75	161	4.6	58.0	19.1	58.1	53	16.6
LP_Well2	1890	1910	102.25	753	176.4	68	108	36	11.8	81.6	24.1	80.5	61	20.4

Site	Upper Depth Cm	Lower Depth Cm	Rb_ ppm	Sc_ ppm	Sr_ ppm	Th_ ppm	V_ ppm	Y_ ppm	Zn_ ppm	Zr_ ppm
LP_Well1	2186	2195	79	16	204	9.0	119.9	41.2	104	313
LP_Well2	0	2	96	16	101	9.4	147.2	125.7	170	266
LP_Well2	2	6	97	16	103	9.3	146.2	128.2	169	264
LP_Well2	6	12	98	16	105	9.3	144.2	133.3	167	261
LP_Well2	12	18	100	16	110	9.1	140.7	142.3	165	256
LP_Well2	18	29	102	17	111	9.2	143.3	139.6	162	256
LP_Well2	29	37	105	18	114	9.3	149.1	133.7	156	258
LP_Well2	37	46	107	18	116	9.5	153.7	128.8	151	258
LP_Well2	46	56	98	17	106	10.7	150.5	152.0	146	239
LP_Well2	56	70	102	18	112	10.5	161.9	65.3	149	231
LP_Well2	70	80	110	21	122	11.0	160.5	34.9	146	224
LP_Well2	80	90	118	22	116	11.0	161.2	37.0	141	231
LP_Well2	90	107	107	21	128	10.8	150.4	41.9	151	239
LP_Well2	107	122	106	22	138	10.4	160.6	44.1	144	237
LP_Well2	127	140	99	19	116	10.6	149.7	37.6	132	246
LP_Well2	140	152	98	18	114	11.9	146.3	44.8	143	283
LP_Well2	152	162	100	24	151	10.0	129.0	65.5	163	183
LP_Well2	162	171	115	24	154	9.5	142.0	68.5	152	201
LP_Well2	171	186	104	22	105	9.4	138.8	129.1	134	254
LP_Well2	186	200	105	23	119	9.3	135.8	132.0	155	227
LP_Well2	200	219	101	22	137	9.4	135.1	76.3	156	201
LP_Well2	219	229	85	23	78	5.5	211.1	65.3	123	228
LP_Well2	229	238	80	22	78	6.6	195.4	71.5	131	251
LP_Well2	238	248	98	22	109	8.5	165.0	54.6	118	251
LP_Well2	248	257	96	26	95	6.6	187.9	43.1	118	234
LP_Well2	257	267	100	24	95	5.9	226.8	27.1	103	197
LP_Well2	267	276	99	17	126	9.1	154.7	38.0	116	274
LP_Well2	276	286	102	15	123	8.3	148.0	40.7	114	272
LP_Well2	286	293	120	22	155	11.9	139.6	39.4	145	205
LP_Well2	293	305	107	18	128	9.6	148.6	24.6	142	202
LP_Well2	348	359	96	26	168	8.0	146.0	58.0	163	182
LP_Well2	403	414	93	29	167	8.0	162.0	57.0	179	198
LP_Well2	457	467	101	23	162	10.1	132.4	38.6	139	154
LP_Well2	498	508	113	23	149	10.0	138.0	37.0	141	163
LP_Well2	549	559	112	24	149	9.5	139.8	38.1	140	164
LP_Well2	599	610	98	26	181	8.0	156.0	147.0	170	198
LP_Well2	701	725	60	8	152	9.0	65.0	27.0	74	216
LP_Well2	799	811	111	25	194	8.0	149.0	62.0	151	212
LP_Well2	955	962	96	23	162	8.0	131.0	59.0	155	189
LP_Well2	992	1008	89	18	156	8.0	130.0	46.0	146	255
LP_Well2	1089	1105	128	29	195	10.0	159.0	68.0	143	211
LP_Well2	1200	1219	99	26	181	8.0	155.0	62.0	150	196
LP_Well2	1225	1231	82	26	211	8.0	137.0	58.0	147	177
LP_Well2	1289	1308	101	8	161	11.0	85.0	30.7	69	484
LP_Well2	1387	1406	124	19	148	10.0	138.4	38.0	107	282
LP_Well2	1485	1504	140	23	193	10.4	150.0	47.3	153	269
LP_Well2	1578	1614	105	22	212	9.3	146.8	46.3	138	224
LP_Well2	1685	1703	88	21	179	8.7	139.3	41.9	139	159
LP_Well2	1793	1807	78	18	184	8.7	111.1	39.8	156	166
LP_Well2	1890	1910	110	23	218	10.8	156.8	48.3	155	348

Site	Upper Depth Cm	Lower Depth Cm	Na2O	MgO	Al2O3	SiO2	K2O	CaO	TiO2	MnO	Fe2O3	P2O5	LOI
LP_Well2	1991	2012	1.66	2.48	19.51	59.36	2.98	1.51	1.08	0.109	9.40	0.165	3.90
LP_Well2	2093	2109	1.56	2.14	20.07	58.78	2.87	1.45	1.03	0.272	9.61	0.166	3.74
LP_Well2	2109	2134	1.47	1.86	22.81	55.00	3.84	1.13	1.17	0.143	10.26	0.206	3.64
LP1	0	6	1.10	1.66	21.49	50.19	0.20	4.08	0.37	0.220	8.71	1.340	12.33
LP1	6	14	1.24	1.86	25.54	44.96	0.19	4.89	0.24	0.170	13.59	1.360	8.59
LP1	14	19	1.23	1.68	25.30	49.63	0.22	5.01	0.43	0.130	9.31	1.310	6.69
LP1	19	28	1.60	1.72	23.69	52.68	0.14	4.32	0.20	0.130	10.04	1.240	6.02
LP1	28	44	1.18	1.83	20.24	55.06	0.13	3.66	0.24	0.090	10.20	1.080	5.05
LP1	59	72	1.81	2.33	20.14	57.10	0.17	2.98	0.29	0.100	10.12	1.040	6.27
LP1	100	146	1.23	2.15	21.46	53.97	0.17	3.97	0.43	0.110	11.30	1.180	6.67
LP2	3	7	1.17	1.60	16.01	60.43	0.25	2.43	0.89	0.370	7.95	1.080	8.26
LP2	15	22	0.87	1.90	17.05	62.34	0.19	2.35	0.59	0.160	8.08	1.160	4.95
LP2	31	41	1.04	2.01	19.17	57.74	0.19	2.89	0.95	0.170	9.20	1.300	4.92
LP2	53	75	1.32	2.24	21.53	56.16	0.19	4.32	0.72	0.110	9.33	1.140	4.70
LP2	75	135	1.37	2.46	19.61	60.98	0.24	2.87	0.96	0.110	9.11	1.080	4.27
LP3	2	5	2.31	1.62	15.92	65.08	0.19	2.00	1.12	0.320	7.06	0.720	4.79
LP3	14	20	1.12	1.52	15.15	60.49	0.21	2.18	0.46	0.310	7.21	0.940	5.98
LP3	32	40	1.23	1.79	19.26	56.88	0.23	2.70	0.60	0.390	8.22	1.110	4.69
LP3	48	60	2.56	2.20	20.13	57.68	0.12	2.90	0.66	0.170	9.35	1.000	4.05
LP3	60	75	1.93	2.09	20.29	56.89	0.11	2.86	0.97	0.190	9.40	1.230	16.56
LP3	75	96	1.78	2.00	22.03	53.94	0.33	3.26	2.05	0.210	10.11	1.170	4.07
LP4	5	15	1.94	1.80	24.51	49.36	0.14	4.15	0.62	0.530	11.30	1.490	7.38
LP4	25	35	1.38	1.52	20.16	57.33	0.13	3.67	0.30	0.300	9.09	1.110	7.86
LP4	47	60	1.43	1.99	24.22	47.86	0.11	4.28	0.39	0.390	11.04	1.400	9.96
LP4	60	84	1.27	2.17	23.96	47.62	0.09	4.40	0.42	0.270	13.29	1.720	5.19
LP4	99	113	1.46	1.82	22.73	51.89	0.13	4.27	0.37	0.220	12.19	1.270	4.42
LP6	0	10	1.37	2.02	19.25	57.11	0.20	2.72	0.56	0.260	9.36	1.160	11.61
LP6	10	20	1.56	2.25	21.80	54.19	0.15	3.30	0.62	0.160	10.21	1.170	8.36
LP6	20	30	1.77	1.75	20.31	54.89	0.29	2.35	0.56	0.430	8.69	1.150	8.79
LP6	30	39	1.59	2.04	24.18	51.20	0.21	3.55	0.57	0.400	9.88	1.320	7.39

Site	Upper Depth Cm	Lower Depth Cm	Total	Ba_ ppm	Ce_ ppm	Co_ ppm	Cr_ ppm	Cu_ ppm	Hf_ ppm	La_ ppm	Nb_ ppm	Nd_ ppm	Ni_ ppm	Pb_ ppm
LP_Well2	1991	2012	102.15	570	139.7	83	79	151	6.0	61.0	20.4	68.8	57	17.6
LP_Well2	2093	2109	101.69	574	123.7	63	83	85	5.1	63.1	21.6	63.7	57	18.1
LP_Well2	2109	2134	101.53	724	160.5	57	95	60	5.7	75.3	21.9	80.0	52	19.3
LP1	0	6	101.69	849	149.0	114	124	59	8.0	90.0	36.0	91.0	48	26.0
LP1	6	14	102.63	929	181.0	121	99	54	6.0	105.0	19.0	115.0	62	26.0
LP1	14	19	100.94	953	160.0	111	106	54	7.0	78.0	17.0	76.0	52	26.0
LP1	19	28	101.78	801	160.0	106	128	54	6.0	82.0	15.0	79.0	57	24.0
LP1	28	44	98.76	893	201.0	106	101	71	6.0	113.0	17.0	112.0	61	23.0
LP1	59	72	102.35	870	356.0	113	90	75	6.0	176.0	17.0	167.0	64	23.0
LP1	100	146	102.64	952	244.0	118	99	51	6.0	111.0	15.0	114.0	66	21.0
LP2	3	7	100.44	780	212.0	129	142	37	9.0	115.0	37.0	99.0	50	22.0
LP2	15	22	99.64	861	232.0	110	112	51	9.0	126.0	17.0	113.0	55	22.0
LP2	31	41	99.58	878	177.0	119	94	56	8.0	115.0	16.0	126.0	52	22.0
LP2	53	75	101.76	983	190.0	110	125	20	7.0	87.0	15.0	79.0	51	22.0
LP2	75	135	103.06	768	230.0	110	125	67	7.0	126.0	14.0	126.0	53	21.0
LP3	2	5	101.13	626	83.0	82	305	94	5.0	46.0	20.0	45.0	42	15.0
LP3	14	20	95.57	801	213.0	136	116	55	7.0	108.0	18.0	106.0	57	24.0
LP3	32	40	97.10	825	179.0	135	111	74	6.0	92.0	18.0	98.0	59	24.0
LP3	48	60	100.82	687	246.0	220	183	70	6.0	104.0	16.0	92.0	53	19.0
LP3	60	75	112.52	659	111.0	103	74	49	7.0	61.0	17.0	57.0	53	24.0
LP3	75	96	100.95	862	224.0	140	143	44	8.0	111.0	16.0	108.0	43	23.0
LP4	5	15	103.22	893	221.0	121	133	47	8.0	127.0	19.0	151.0	61	28.0
LP4	25	35	102.85	875	220.0	162	204	44	8.0	131.0	17.0	154.0	61	24.0
LP4	47	60	103.07	970	113.0	120	254	44	7.0	62.0	18.0	63.0	60	24.0
LP4	60	84	100.40	887	152.0	129	111	72	8.0	78.0	18.0	74.0	61	25.0
LP4	99	113	100.77	909	138.0	120	120	33	7.0	56.0	18.0	47.0	64	23.0
LP6	0	10	105.62	612	163.0	88	116	43	7.0	97.0	39.0	103.0	53	20.0
LP6	10	20	103.77	710	282.0	89	101	56	8.0	147.0	18.0	172.0	60	24.0
LP6	20	30	100.98	677	301.0	97	151	46	8.0	176.0	17.0	189.0	61	26.0
LP6	30	39	102.33	838	203.0	113	65	47	8.0	124.0	18.0	132.0	54	26.0

Site	Upper Depth Cm	Lower Depth Cm	Rb_ ppm	Sc_ ppm	Sr_ ppm	Th_ ppm	V_ ppm	Y_ ppm	Zn_ ppm	Zr_ ppm
LP_Well2	1991	2012	96	19	168	9.4	121.6	47.8	163	207
LP_Well2	2093	2109	97	19	179	8.0	128.9	45.6	143	181
LP_Well2	2109	2134	122	24	200	9.6	150.9	45.8	121	202
LP1	0	6	116	26	173	10.0	146.0	92.0	256	203
LP1	6	14	127	30	190	10.0	146.0	117.0	217	245
LP1	14	19	132	28	189	10.0	150.0	101.0	224	184
LP1	19	28	112	26	167	9.0	146.0	85.0	207	192
LP1	28	44	111	27	158	10.0	135.0	85.0	198	211
LP1	59	72	107	31	176	11.0	133.0	102.0	196	241
LP1	100	146	109	30	146	9.0	145.0	79.0	191	206
LP2	3	7	97	21	138	11.0	130.0	98.0	284	174
LP2	15	22	97	22	122	10.0	140.0	98.0	274	182
LP2	31	41	98	26	153	10.0	146.0	70.0	289	179
LP2	53	75	123	27	160	9.0	138.0	64.0	228	168
LP2	75	135	96	26	192	9.0	130.0	72.0	238	178
LP3	2	5	76	19	171	7.0	99.0	35.0	151	131
LP3	14	20	99	25	175	9.0	139.0	93.0	235	186
LP3	32	40	108	27	199	10.0	142.0	52.0	209	177
LP3	48	60	92	24	187	9.0	126.0	48.0	182	165
LP3	60	75	89	21	186	6.0	138.0	55.0	220	141
LP3	75	96	102	27	232	10.0	144.0	66.0	264	145
LP4	5	15	109	26	172	10.0	146.0	182.0	260	183
LP4	25	35	104	21	116	9.0	128.0	189.0	228	160
LP4	47	60	119	29	168	9.0	178.0	80.0	242	165
LP4	60	84	116	29	146	11.0	163.0	59.0	264	192
LP4	99	113	124	29	162	10.0	166.0	46.0	220	152
LP6	0	10	84	17	143	8.0	119.0	95.0	210	174
LP6	10	20	94	20	142	9.0	122.0	169.0	234	191
LP6	20	30	81	19	183	8.0	131.0	244.0	246	176
LP6	30	39	104	24	213	9.0	144.0	165.0	273	171

8.2 SSA, densities, color, and sample weights for wells

Site	Upper Depth cm	Lower Depth cm	<2mm %	>2mm %	Munsell Hue	Munsell Value	Munsell Chroma	SSA un-treated	SSA total	SSA post CBD	Rock density g/cm3
LP_Well1	0	6	38.83	61.17	10YR	3	2	4.08	21.06	5.96	2.64
LP_Well1	6	14	19.24	80.76	10YR	4	3	9.59	21.04	6.05	2.65
LP_Well1	14	19	24.52	75.48	10YR	5	3	11.28	20.05	5.33	2.65
LP_Well1	19	28	30.11	69.89	10YR	5	4	10.51	13.69	4.29	2.68
LP_Well1	28	44	39.21	60.79	10YR	5	4	6.93	15.09	4.00	2.70
LP_Well1	44	59	31.88	68.12	10YR	6	2	7.55	12.81	5.20	2.69
LP_Well1	59	72	42.08	57.92	10YR	6	2	4.33	11.20	4.88	2.69
LP_Well1	72	84	21.00	79.00	10YR	6	3	7.50	13.31	4.87	2.70
LP_Well1	84	100	45.58	54.42	10YR	6	3	9.61	20.13	10.55	2.79
LP_Well1	100	146	58.94	41.06	GLEY 1	6	2	3.90	10.20	3.51	--
LP_Well1	152	163	44.43	55.57	2.5Y	5	3	4.03	5.19	2.46	--
LP_Well1	163	174	47.55	52.45	2.5Y	5	3	5.26	5.87	1.78	--
LP_Well1	174	185	49.37	50.63	2.5Y	5	3	6.37	7.83	2.26	--
LP_Well1	185	196	50.92	49.08	2.5Y	5	3	5.15	3.84	1.28	--
LP_Well1	196	207	50.95	49.05	2.5Y	5	4	6.19	3.14	0.99	--
LP_Well1	207	218	57.40	42.60	2.5Y	6	4	5.92	3.54	1.53	--
LP_Well1	218	229	60.65	39.35	2.5Y	6	4	4.41	3.81	1.68	--
LP_Well1	229	239	56.15	43.85	2.5Y	5	4	6.80	3.63	--	--
LP_Well1	239	250	64.69	35.31	10YR	5	4	8.88	6.55	2.61	--
LP_Well1	250	261	61.84	38.16	2.5Y	5	4	8.80	10.11	1.95	--
LP_Well1	261	272	60.09	39.91	2.5Y	6	4	6.81	3.18	1.38	--
LP_Well1	272	283	62.32	37.68	2.5Y	7	2	5.90	2.61	--	--
LP_Well1	283	294	62.46	37.54	5Y	7	2	5.12	4.83	2.01	--
LP_Well1	294	305	65.04	34.96	2.5Y	6	3	5.57	3.60	1.84	--
LP_Well1	305	315	--	--	5Y	6	2	4.36	4.36	--	2.76
LP_Well1	356	368	--	--	5Y	6	2	4.14	2.23	--	--
LP_Well1	396	406	--	--	5Y	6	2	--	3.06	--	--
LP_Well1	445	457	--	--	5Y	6	2	3.89	3.89	--	--
LP_Well1	498	508	--	--	GLEY 1	7	2	3.48	2.99	2.83	2.74
LP_Well1	549	559	--	--	2.5Y	6	4	5.21	5.21	--	--
LP_Well1	589	597	--	--	5Y	6	2	4.72	4.72	--	--
LP_Well1	695	707	--	--	5Y	6	2	5.89	5.05	4.20	2.74
LP_Well1	747	762	--	--	5Y	6	2	3.63	3.63	--	2.60
LP_Well1	800	811	--	--	5Y	6	2	3.85	3.85	--	2.78
LP_Well1	842	852	--	--	5Y	7	2	2.66	2.69	2.04	2.86
LP_Well1	894	904	--	--	5Y	6	2	2.91	2.91	--	2.66
LP_Well1	948	955	--	--	GLEY 1	7	10Y	4.93	4.93	--	--
LP_Well1	1000	1006	--	--	5Y	7	2	3.42	3.42	--	2.51
LP_Well1	1049	1055	--	--	5Y	7	2	4.17	3.46	3.28	2.62
LP_Well1	1093	1107	--	--	5Y	7	2	2.80	2.80	--	--
LP_Well1	1200	1213	--	--	5Y	7	2	--	4.03	--	--
LP_Well1	1311	1318	--	--	5Y	7	2	5.27	5.27	--	--
LP_Well1	1397	1422	--	--	5Y	7	3	3.16	3.46	3.01	2.70
LP_Well1	1524	1535	--	--	5Y	6	2	3.81	3.81	3.32	--
LP_Well1	1557	1568	--	--	5Y	6	3	4.49	4.49	--	--
LP_Well1	1600	1657	--	--	5Y	7	2	--	4.05	--	2.77
LP_Well1	1829	1838	--	--	GLEY 1	7	5GY	3.62	3.62	--	2.69
LP_Well1	1857	1864	--	--	5Y	8	1	--	3.57	--	--
LP_Well1	1891	1898	--	--	5Y	8	1	3.93	3.51	--	--

Site	Upper Depth cm	Lower Depth cm	<2mm %	>2mm %	Munsell Hue	Munsell Value	Munsell Chroma	SSA un-treated	SSA total	SSA post CBD	Rock density g/cm3
LP_Well1	2000	2019	--	--	5Y	7	1	--	3.51	--	2.86
LP_Well1	2096	2111	--	--	GLEY 1	7	3	--	3.51	--	2.81
LP_Well1	2177	2186	--	--	2.5Y	6	4	--	3.51	--	--
LP_Well1	2186	2195	--	--	2.5Y	7	2	--	3.51	--	2.44
LP_Well2	0	2	74.65	25.35	10YR	3	2	3.68	19.16	6.33	--
LP_Well2	2	6	76.70	23.30	10YR	3	2	9.73	18.85	6.33	--
LP_Well2	6	12	58.21	41.79	10YR	3	3	13.11	19.81	6.33	--
LP_Well2	12	18	63.42	36.58	10YR	3	3	15.25	21.29	7.55	2.77
LP_Well2	18	29	52.43	47.57	10YR	4	3	13.91	17.59	7.25	--
LP_Well2	29	37	44.72	55.28	10YR	5	6	14.87	16.77	6.94	2.66
LP_Well2	37	46	36.65	63.35	10YR	5	6	18.60	21.20	8.19	2.86
LP_Well2	46	56	35.56	64.44	10YR	5	4	18.51	21.75	8.57	2.75
LP_Well2	56	70	44.17	55.83	10YR	5	4	15.86	20.12	7.40	--
LP_Well2	70	80	51.89	48.11	10YR	5	6	10.96	13.84	5.84	2.82
LP_Well2	80	90	45.15	54.85	10YR	5	6	12.99	14.92	5.42	2.71
LP_Well2	90	107	36.37	63.63	10YR	5	6	13.54	15.83	4.42	2.73
LP_Well2	107	122	47.79	52.21	10YR	6	4	12.77	13.04	4.10	2.75
LP_Well2	127	140	62.10	37.90	2.5Y	6	3	11.47	8.74	5.62	--
LP_Well2	140	152	32.08	67.92	2.5Y	6	4	12.36	11.01	--	--
LP_Well2	152	162	53.64	46.36	5Y	6	2	3.29	2.99	2.60	--
LP_Well2	162	171	58.38	41.62	5Y	7	2	4.06	2.11	1.77	--
LP_Well2	171	186	66.15	33.85	2.5Y	6	3	5.97	6.07	2.17	--
LP_Well2	186	200	61.11	38.89	5Y	6	2	5.37	7.15	2.79	--
LP_Well2	200	219	47.69	52.31	2.5Y	6	3	4.01	4.42	--	--
LP_Well2	219	229	58.01	41.99	10YR	5	4	7.47	8.74	2.67	--
LP_Well2	229	238	53.95	46.05	10YR	5	4	9.41	11.15	3.59	--
LP_Well2	238	248	42.77	57.23	10YR	5	4	9.96	10.18	3.76	--
LP_Well2	248	257	55.58	44.42	10YR	5	4	9.00	10.32	2.73	--
LP_Well2	257	267	60.53	39.47	10YR	5	4	8.12	11.81	4.52	--
LP_Well2	267	276	56.91	43.09	2.5Y	6	3	4.76	5.14	2.14	--
LP_Well2	276	286	57.06	42.94	2.5Y	6	4	4.42	4.91	1.33	--
LP_Well2	286	293	55.38	44.62	2.5Y	6	3	3.55	3.32	1.55	--
LP_Well2	293	305	54.79	45.21	2.5Y	6	3	2.94	2.78	0.81	--
LP_Well2	348	359	--	--	2.5Y	6	2	3.24	3.24	--	--
LP_Well2	403	414	--	--	10YR	6	4	1.38	1.38	--	2.88
LP_Well2	457	467	--	--	5Y	6	1	2.43	2.43	--	2.81
LP_Well2	498	508	--	--	2.5Y	8	1	2.29	2.29	--	2.83
LP_Well2	549	559	--	--	5Y	7	1	2.13	2.13	--	2.79
LP_Well2	599	610	--	--	10YR	5	4	3.13	3.13	--	2.29
LP_Well2	701	725	--	--	10YR	6	3	--	--	--	2.65
LP_Well2	799	811	--	--	GLEY 1	6	5GY	3.36	3.36	--	2.77
LP_Well2	955	962	--	--	GLEY 1	7	5GY	3.77	3.77	--	2.77
LP_Well2	992	1008	--	--	5Y	5	2	--	--	--	2.75
LP_Well2	1089	1105	--	--	GLEY 2	6	10G	--	--	--	2.85
LP_Well2	1200	1219	--	--	GLEY 1	4	10G	--	--	--	--
LP_Well2	1225	1231	--	--	GLEY 1	7	5G	--	--	--	--
LP_Well2	1237	1244	--	--	GLEY 1	6	N	2.33	2.33	--	--
LP_Well2	1289	1308	--	--	5Y	6	1	--	--	--	2.83
LP_Well2	1387	1406	--	--	GLEY 1	7	10Y	--	--	--	2.74

Site	Upper Depth cm	Lower Depth cm	<2mm %	>2mm %	Munsell Hue	Munsell Value	Munsell Chroma	SSA un-treated	SSA total	SSA post CBD	Rock density g/cm3
LP_Well2	1485	1504	--	--	GLEY 1	7	10Y	--	--	--	2.75
LP_Well2	1578	1614	--	--	5Y	6	1	--	--	--	2.80
LP_Well2	1685	1703	--	--	GLEY 1	8	N	--	--	--	2.85
LP_Well2	1793	1807	--	--	GLEY 1	8	N	--	--	--	2.80
LP_Well2	1890	1910	--	--	GLEY 1	8	N	--	--	--	2.83
LP_Well2	1991	2012	--	--	GLEY 1	8	N	--	--	--	2.84
LP_Well2	2093	2109	--	--	GLEY 1	7	N	--	--	--	2.80
LP_Well2	2109	2134	--	--	GLEY 1	8	N	--	--	--	2.82

Site	Upper Depth cm	Lower Depth cm	Bulk density g/cm3
LP_Well1	0	6	0.89
LP_Well1	6	14	1.29
LP_Well1	14	19	1.33
LP_Well1	19	28	1.47
LP_Well1	28	44	1.55
LP_Well1	44	59	1.67
LP_Well1	59	72	1.75
LP_Well1	72	84	1.74
LP_Well1	84	100	1.61
LP_Well1	100	146	1.65
LP_Well1	152	163	1.73
LP_Well1	163	174	1.46
LP_Well1	174	185	1.55
LP_Well1	185	196	1.71
LP_Well1	196	207	1.82
LP_Well1	207	218	1.91
LP_Well1	218	229	1.91
LP_Well1	229	239	1.68
LP_Well1	239	250	1.69
LP_Well1	250	261	1.66
LP_Well1	261	272	1.83
LP_Well1	272	283	1.67
LP_Well1	283	294	1.51
LP_Well1	294	305	1.98
LP_Well1	305	315	1.84
LP_Well1	356	368	1.93
LP_Well1	396	406	1.93
LP_Well1	445	457	1.86
LP_Well1	498	508	1.86
LP_Well1	549	559	1.86
LP_Well1	589	597	1.86
LP_Well1	695	707	1.86
LP_Well1	747	762	1.76
LP_Well1	800	811	1.89
LP_Well1	842	852	1.95
LP_Well1	894	904	1.81
LP_Well1	948	955	1.76
LP_Well1	1000	1006	1.71
LP_Well1	1049	1055	1.78
LP_Well1	1093	1107	1.81
LP_Well1	1200	1213	1.72
LP_Well1	1311	1318	1.81
LP_Well1	1397	1422	1.84
LP_Well1	1524	1535	1.86
LP_Well1	1557	1568	1.86
LP_Well1	1600	1657	1.89
LP_Well1	1829	1838	1.89
LP_Well1	1857	1864	1.89
LP_Well1	1891	1898	1.89

Site	Upper Depth cm	Lower Depth cm	Bulk density g/cm3
LP_Well1	2000	2019	1.94
LP_Well1	2096	2111	1.91
LP_Well1	2177	2186	1.79
LP_Well1	2186	2195	1.66
LP_Well2	0	2	0.84
LP_Well2	2	6	0.84
LP_Well2	6	12	1.15
LP_Well2	12	18	1.46
LP_Well2	18	29	1.61
LP_Well2	29	37	1.61
LP_Well2	37	46	1.61
LP_Well2	46	56	1.64
LP_Well2	56	70	1.58
LP_Well2	70	80	1.68
LP_Well2	80	90	1.64
LP_Well2	90	107	1.84
LP_Well2	107	122	1.68
LP_Well2	127	140	1.69
LP_Well2	140	152	1.68
LP_Well2	152	162	1.68
LP_Well2	162	171	1.87
LP_Well2	171	186	1.94
LP_Well2	186	200	2.05
LP_Well2	200	219	1.95
LP_Well2	219	229	1.95
LP_Well2	229	238	1.95
LP_Well2	238	248	1.95
LP_Well2	248	257	1.95
LP_Well2	257	267	1.95
LP_Well2	267	276	1.95
LP_Well2	276	286	1.95
LP_Well2	286	293	1.95
LP_Well2	293	305	1.95
LP_Well2	348	359	1.96
LP_Well2	403	414	1.96
LP_Well2	457	467	1.91
LP_Well2	498	508	1.92
LP_Well2	549	559	1.90
LP_Well2	599	610	1.56
LP_Well2	701	725	--
LP_Well2	799	811	1.88
LP_Well2	955	962	1.88
LP_Well2	992	1008	--
LP_Well2	1089	1105	--
LP_Well2	1200	1219	--
LP_Well2	1225	1231	--
LP_Well2	1237	1244	1.89
LP_Well2	1289	1308	1.86
LP_Well2	1387	1406	1.87

Site	Upper Depth cm	Lower Depth cm	Bulk density g/cm3
LP_Well2	1485	1504	1.90
LP_Well2	1578	1614	1.94
LP_Well2	1685	1703	1.90
LP_Well2	1793	1807	1.93
LP_Well2	1890	1910	1.93
LP_Well2	1991	2012	1.90
LP_Well2	2093	2109	1.92
LP_Well2	2109	2134	1.93

8.3 SSA, densities, color, and pH for soil pits

Site	Upper Depth cm	Lower Depth cm	Horizon	Munsell Hue	Munsell Value	Munsell Chroma	pH DDI	pH CaCl2	SSA untreated	SSA total	SSA post CBD	Bulk density g/cm3
LP1	0	6	A1	10YR	3	2	4.27	3.85	4.08	21.06	6.33	0.89
LP1	6	14	A2	10YR	4	3	4.74	4.26	9.59	21.04	6.33	1.29
LP1	14	19	BA	10YR	5	3	4.68	4.27	11.28	20.05	6.33	1.33
LP1	19	28	B1	10YR	5	4	4.66	4.24	10.51	13.69	7.55	1.47
LP1	28	44	B2	10YR	5	4	4.62	4.17	6.93	15.09	7.25	1.55
LP1	44	59	B2	10YR	6	2	4.61	4.17	7.55	12.81	6.94	1.67
LP1	59	72	B3	10YR	6	2	4.65	4.18	4.33	11.20	8.19	1.75
LP1	72	84	B3	10YR	6	3	4.68	4.25	7.50	13.31	8.57	1.74
LP1	84	100	C1	10YR	6	3	4.74	4.28	9.61	20.13	7.40	1.61
LP1	100	146	SAP	GLEY 1	6	2	4.93	4.61	3.90	10.20	5.84	1.65
LP2	0	3	A1	10YR	3	2	4.14	3.87	3.64	20.11	8.32	0.37
LP2	3	7	A1	10YR	4	2	4.47	4.02	6.08	21.16	--	0.87
LP2	7	11	A2	10YR	4	2	4.68	4.26	9.38	19.45	7.19	1.38
LP2	11	15	A2	10YR	4	3	4.74	4.29	10.38	20.85	7.21	1.50
LP2	15	22	B1	10YR	5	4	4.66	4.21	9.49	17.69	9.80	1.68
LP2	22	31	B1	10YR	6	4	4.63	4.17	9.39	15.93	10.09	1.68
LP2	31	41	B2	10YR	6	4	4.64	4.18	8.87	14.01	6.89	1.72
LP2	41	53	B2	10YR	6	4	4.69	4.25	8.13	13.14	6.70	1.40
LP2	53	75	Cr1	10YR	6	1	4.78	4.32	2.59	5.94	2.68	1.56
LP2	75	135	SAP	GLEY 1	6	2	5.07	4.6	2.55	2.91	1.27	1.75
LP3	0	2	AO	10YR	3	2	4.95	4.64	7.24	12.15	6.52	1.04
LP3	2	5	AO	10YR	3	2	4.9	4.66	4.12	11.13	7.27	1.23
LP3	5	8	AB	10YR	4	3	4.92	4.58	6.77	19.00	--	1.35
LP3	8	14	AB	10YR	4	3	4.92	4.38	9.40	18.13	--	1.58
LP3	14	20	Bt	10YR	5	3	4.83	4.35	8.94	15.08	5.97	1.74
LP3	20	26	Bt	10YR	6	3	4.85	4.3	8.10	12.50	5.41	1.48
LP3	26	32	Bt	10YR	6	3	4.64	4.04	6.42	9.75	4.07	1.96
LP3	32	40	B1	10YR	6	3	4.59	4.06	6.83	8.42	4.60	1.72
LP3	40	48	B1	10YR	6	3	4.69	4.03	7.28	13.60	5.26	1.71
LP3	48	60	B2	10YR	6	3	4.73	4.01	--	9.08	4.31	1.71
LP3	60	75	B2	10YR	6	3	4.73	4.03	7.02	8.71	5.11	1.76
LP3	75	96	B2	10YR	6	3	4.76	4.04	4.83	14.03	4.04	1.76
LP4	0	5	A1	10YR	4	2	5.46	4.65	9.80	23.16	--	0.82
LP4	5	15	A1	10YR	4	3	4.95	4.3	13.55	22.01	8.79	1.08
LP4	15	25	A1	10YR	4	3	4.73	4.16	13.79	22.13	8.11	1.29
LP4	25	35	A1	10YR	4	3	4.77	4.25	13.44	20.33	9.30	1.34
LP4	35	47	A2	10YR	4	3	4.8	4.17	14.66	22.36	--	1.70
LP4	47	60	Ag	10YR	4	2	4.38	3.67	12.67	17.71	7.71	1.43
LP4	60	84	B1	10YR	6	4	4.7	3.98	11.28	13.60	6.54	1.41
LP4	84	99	B2	10YR	6	4	4.68	4.11	12.00	15.30	6.78	1.62
LP4	99	113	CB	10YR	6	4	4.66	4.16	8.93	12.22	--	1.82
LP5	0	2	A1	10YR	3	2	5.2	4.6	3.68	19.16	--	0.84
LP5	2	6	A1	10YR	3	2	5.1	4.2	9.73	18.85	--	0.84
LP5	6	12	A2	10YR	3	3	4.6	4	13.11	19.81	--	1.15
LP5	12	18	A2	10YR	3	3	4.7	4.1	15.25	21.29	--	1.46
LP5	18	29	AB	10YR	4	3	4.6	4	13.91	17.59	--	1.61
LP5	29	37	Bw1	10YR	5	6	4.5	3.9	14.87	16.77	--	1.61
LP5	37	46	Bw1	10YR	5	6	4.4	4	18.60	21.20	--	1.61
LP5	46	56	Bw2	10YR	5	4	4.7	3.8	18.51	21.75	--	1.64
LP5	56	70	Bw2	10YR	5	4	4.6	4	15.86	20.12	--	1.58

Site	Upper Depth cm	Lower Depth cm	Horizon	Munsell Hue	Munsell Value	Munsell Chroma	pH DDI	pH CaCl2	SSA untreated	SSA total	SSA post CBD	Bulk density g/cm3
LP5	70	80	Bw3	10YR	5	6	4.7	4	####	13.84	--	1.68
LP5	80	90	Bw3	10YR	5	6	5	4	12.99	14.92	--	1.64
LP5	90	107	Bw3	10YR	5	6	4.6	4.1	13.54	15.83	--	1.84
LP5	107	122	BC	10YR	6	4	4.4	4	12.77	13.04	--	1.68
LP6	0	2	A1	10YR	2	2	--	4.4	1.43	12.92	6.67	0.99
LP6	2	4	A1	10YR	2	2	--	4.2	2.34	14.93	6.86	1.00
LP6	4	7	A2	10YR	3	2	4.5	4.2	5.44	15.39	6.82	1.07
LP6	7	10	A2	10YR	3	2	4.6	4.1	7.36	--	7.18	1.09
LP6	10	15	AB	10YR	3	4	4.7	4.1	13.17	15.86	7.07	1.19
LP6	15	20	AB	10YR	3	4	4.6	4.2	14.04	16.79	7.42	1.36
LP6	20	25	2Ab	7.5YR	3	2	4.6	4.2	16.78	18.80	8.17	1.68
LP6	25	30	2Ab	7.5YR	3	2	4.5	4.1	16.89	18.99	8.32	1.52
LP6	30	39	2Ab	7.5YR	3	2	4.5	4.1	16.35	17.71	8.51	1.90
LP6	39	44	2Ab	10YR	4	4	4.5	4.1	14.25	17.74	9.14	1.93
LP6	44	60	Bw	2.5Y	5	4	4.5	4	12.23	13.14	5.95	2.09
LP6	60	80	Bw	2.5Y	5	4	4.2	3.9	12.67	10.90	11.61	1.98
LP6	80	100	Bw	2.5Y	5	4	4.5	3.7	13.90	13.87	5.25	1.89
LP6	0	10	A1-A2	10YR	2	2	4.55	4.225	--	14.41	--	1.04
LP6	10	20	AB	10YR	3	4	4.65	4.15	--	16.33	--	1.27
LP6	20	30	2Ab	7.5YR	3	2	4.55	4.15	--	18.89	--	1.60

Site	Upper Depth cm	Lower Depth cm	<2mm %	>2mm %	Sand%	Silt %	Clay%
LP1	0	6	38.83	188.36	48.68	25.09	26.24
LP1	6	14	19.24	482.13	51.16	22.59	26.24
LP1	14	19	24.52	359.90	49.09	23.41	27.51
LP1	19	28	30.11	368.27	53.65	18.85	27.50
LP1	28	44	39.21	345.05	57.28	17.72	25.00
LP1	44	59	31.88	453.05	59.28	14.72	26.00
LP1	59	72	42.08	269.62	60.64	13.36	26.00
LP1	72	84	21.00	608.42	63.64	10.36	26.00
LP1	84	100	45.58	1147.55	61.28	8.72	30.00
LP1	100	146	58.94	137.62	67.28	10.72	22.00
LP2	0	3	31.24	262.38	50.28	25.72	24.00
LP2	3	7	48.11	130.50	48.28	27.72	24.00
LP2	7	11	42.29	194.90	51.28	24.72	24.00
LP2	11	15	50.82	156.65	51.28	24.72	24.00
LP2	15	22	48.38	277.44	51.28	22.72	26.00
LP2	22	31	45.29	258.77	54.28	17.72	28.00
LP2	31	41	39.67	394.55	54.44	14.30	31.26
LP2	41	53	28.53	538.09	61.15	8.85	30.00
LP2	53	75	18.60	2365.63	72.40	3.85	23.75
LP2	75	135	32.91	343.82	76.15	1.35	22.50
LP3	0	2	56.18	281.30	60.37	14.64	24.99
LP3	2	5	49.14	505.27	54.10	20.90	25.00
LP3	5	8	65.75	328.12	49.13	25.89	24.99
LP3	8	14	49.63	712.71	51.60	22.15	26.25
LP3	14	20	39.05	1111.40	49.13	23.39	27.49
LP3	20	26	31.99	1492.50	47.85	22.15	30.00
LP3	26	32	28.41	1408.86	56.63	13.39	29.98
LP3	32	40	26.61	1570.35	56.62	12.14	31.23
LP3	40	48	23.48	1922.65	61.61	9.65	28.74
LP3	48	60	21.11	1938.35	66.61	5.90	27.49
LP3	60	75	31.81	1450.20	67.87	3.40	28.74
LP3	75	96	20.55	1326.06	70.37	4.65	24.98
LP4	0	5	59.51	321.58	39.61	30.42	29.97
LP4	5	15	57.08	519.28	43.31	25.44	31.24
LP4	15	25	58.89	510.51	38.78	31.23	29.99
LP4	25	35	56.22	485.29	38.35	31.68	29.98
LP4	35	47	36.10	1082.78	38.32	30.44	31.24
LP4	47	60	20.92	1082.78	40.01	27.49	32.49
LP4	60	84	35.80	1082.78	53.74	8.75	37.51
LP4	84	99	37.96	1082.78	53.33	10.44	36.22
LP4	99	113	27.11	1082.78	59.57	7.95	32.48
LP5	0	2	74.65	148.23	59.44	19.45	21.11
LP5	2	6	76.70	219.75	49.37	27.30	23.33
LP5	6	12	58.21	488.94	47.22	26.12	26.67
LP5	12	18	63.42	447.12	47.22	26.12	26.67
LP5	18	29	52.43	716.58	46.09	25.01	28.90
LP5	29	37	44.72	934.27	43.98	24.92	31.10
LP5	37	46	36.65	1046.73	42.93	23.73	33.33
LP5	46	56	35.56	1091.65	43.92	21.66	34.42
LP5	56	70	44.17	859.06	52.69	16.20	31.11

Site	Upper Depth cm	Lower Depth cm	<2mm %	>2mm %	Sand%	Silt %	Clay%
LP5	70	80	51.89	816.27	55.04	20.54	24.42
LP5	80	90	45.15	954.82	50.50	22.85	26.65
LP5	90	107	36.37	1167.23	51.57	20.64	27.78
LP5	107	122	47.79	2496.48	51.60	22.85	25.54
LP6	0	2	57.54	193.75	52.46	25.80	21.74
LP6	2	4	61.04	279.39	52.46	25.80	21.74
LP6	4	7	59.75	334.05	45.76	32.23	22.01
LP6	7	10	70.29	243.28	39.57	35.95	24.49
LP6	10	15	76.98	227.38	44.12	34.07	21.81
LP6	15	20	60.65	491.54	26.46	48.34	25.20
LP6	20	25	65.54	363.14	40.61	38.97	20.42
LP6	25	30	24.39	1672.66	42.46	37.76	19.78
LP6	30	39	38.76	1433.83	39.66	39.59	20.74
LP6	39	44	34.16	1049.48	40.75	38.23	21.03
LP6	44	60	31.42	1325.97	39.05	32.47	28.48
LP6	60	80	29.16	1435.89	45.33	26.37	28.30
LP6	80	100	26.19	1163.75	44.62	26.79	28.59
LP6	0	10	62.16	262.62	47.56	29.94	22.49
LP6	10	20	68.81	359.46	35.29	41.20	23.51
LP6	20	30	44.96	1017.90	41.53	38.37	20.10

8.4 Carbon and Nitrogen of <2mm fraction for soil pits

Site	Upper Depth cm	Lower Depth cm	C inv kgC/m2 fine	C wt%	C%SE	C Conf Lim 1 wt%	C Conf Lim 2 wt%	δ13C‰ PDB	δ13C ‰SE	13C Conf Lim 1 wt%	13C Conf Lim 2 wt%	N wt%
LP1	0	6	1.473	7.112	0.016	7.096	7.128	-26.611	0.650	-27.261	-25.962	0.352
LP1	6	14	2.068	3.002	0.025	2.976	3.027	-27.169	0.650	-27.821	-26.520	0.149
LP1	14	19	2.414	2.125	0.020	2.105	2.144	-27.142	0.650	-27.793	-26.493	0.110
LP1	19	28	2.760	0.870	0.009	0.860	0.879	-26.964	0.650	-27.615	-26.315	0.050
LP1	28	44	3.209	0.464	0.014	0.450	0.477	-26.718	0.650	-27.368	-26.069	0.028
LP1	44	59	3.448	0.299	0.011	0.288	0.310	-26.137	0.649	-26.788	-25.489	0.022
LP1	59	72	3.686	0.249	0.015	0.235	0.264	-26.110	0.649	-26.760	-25.462	0.021
LP1	72	84	3.770	0.190	0.011	0.179	0.202	-25.908	0.649	-26.558	-25.260	0.016
LP1	84	100	3.975	0.174	0.013	0.161	0.188	-25.024	0.648	-25.673	-24.377	0.018
LP1	100	146	4.516	0.121	0.015	0.106	0.135	-25.780	0.649	-26.430	-25.133	0.011
LP2	0	3	0.263	7.503	0.039	7.464	7.542	-27.535	0.274	-27.810	-27.261	0.422
LP2	3	7	0.940	4.063	0.030	4.033	4.093	-26.917	0.274	-27.192	-26.643	0.235
LP2	7	11	1.507	2.425	0.022	2.403	2.447	-25.883	0.274	-26.157	-25.609	0.145
LP2	11	15	2.043	1.753	0.019	1.734	1.772	-25.689	0.274	-25.963	-25.416	0.114
LP2	22	31	3.192	0.574	0.010	0.564	0.585	-25.652	0.274	-25.926	-25.379	0.040
LP2	31	41	3.434	0.354	0.012	0.342	0.367	-25.171	0.273	-25.444	-24.898	0.026
LP2	41	53	3.569	0.281	0.013	0.268	0.294	-25.228	0.273	-25.502	-24.955	0.025
LP2	53	75	3.670	0.158	0.011	0.147	0.169	-25.158	0.273	-25.432	-24.885	0.018
LP2	75	135	3.943	0.079	0.010	0.069	0.089	-27.068	0.274	-27.342	-26.794	0.011
LP3	0	2	1.379	11.826	0.055	11.772	11.881	-27.779	0.275	-28.053	-27.504	0.751
LP3	2	5	2.539	6.385	0.036	6.349	6.421	-27.079	0.274	-27.354	-26.805	0.394
LP3	5	8	3.554	3.805	0.025	3.781	3.830	-26.668	0.274	-26.942	-26.394	0.261
LP3	8	14	4.803	2.653	0.016	2.637	2.669	-26.329	0.274	-26.603	-26.055	0.165
LP3	14	20	5.512	1.743	0.013	1.731	1.756	-26.455	0.274	-26.729	-26.181	0.105
LP3	20	26	5.954	1.553	0.014	1.539	1.567	-26.379	0.274	-26.653	-26.105	0.107
LP3	26	32	6.175	0.657	0.011	0.646	0.669	-26.109	0.274	-26.382	-25.835	0.051
LP3	32	40	6.348	0.474	0.013	0.461	0.486	-26.282	0.274	-26.556	-26.008	0.031
LP3	40	48	6.440	0.286	0.010	0.277	0.296	-25.847	0.274	-26.121	-25.574	0.021
LP3	48	60	6.528	0.202	0.010	0.192	0.212	-25.608	0.274	-25.881	-25.334	0.017
LP3	60	75	6.658	0.156	0.012	0.144	0.168	-26.024	0.274	-26.298	-25.750	0.014
LP3	75	96	6.749	0.120	0.012	0.108	0.132	-25.850	0.259	-26.109	-25.592	0.011
LP4	0	5	0.966	3.967	0.019	3.948	3.986	-26.274	0.259	-26.533	-26.015	0.310
LP4	5	15	2.006	1.688	0.021	1.668	1.709	-25.895	0.259	-26.154	-25.637	0.120
LP4	15	25	3.596	2.098	0.018	2.080	2.116	-25.929	0.259	-26.188	-25.671	0.107
LP4	25	35	5.112	2.010	0.021	1.988	2.031	-25.985	0.259	-26.244	-25.726	0.114
LP4	35	47	6.575	1.981	0.019	1.962	2.000	-26.097	0.259	-26.356	-25.838	0.101
LP4	47	60	8.868	5.884	0.018	5.866	5.901	-25.445	0.258	-25.704	-25.187	0.101
LP4	60	84	9.093	0.185	0.012	0.173	0.197	-24.716	0.258	-24.974	-24.458	0.017
LP4	84	99	9.252	0.172	0.012	0.160	0.185	-24.701	0.258	-24.959	-24.443	0.018
LP4	99	113	9.423	0.247	0.013	0.235	0.260	-25.118	0.258	-25.377	-24.860	0.022
LP5	0	2	1.113	8.830	0.019	8.811	8.849	-26.357	0.569	-26.927	-25.789	0.534
LP5	2	6	2.011	3.466	0.011	3.456	3.477	-25.951	0.569	-26.521	-25.383	0.232
LP5	6	12	2.809	1.987	0.010	1.977	1.996	-25.557	0.569	-26.128	-24.989	0.149
LP5	12	18	3.588	1.404	0.010	1.393	1.414	-25.210	0.570	-25.780	-24.641	0.113
LP5	18	29	4.429	0.907	0.006	0.901	0.913	-24.815	0.570	-25.385	-24.245	0.074
LP5	29	37	4.663	0.406	0.006	0.400	0.412	-25.334	0.570	-25.905	-24.765	0.035
LP5	37	46	4.875	0.399	0.004	0.395	0.404	-25.016	0.570	-25.587	-24.447	0.035
LP5	46	56	5.114	0.409	0.005	0.405	0.414	-25.566	0.569	-26.136	-24.997	0.032
LP5	56	70	5.289	0.180	0.005	0.175	0.185	-25.624	0.569	-26.194	-25.055	0.021

Site	Upper Depth cm	Lower Depth cm	C inv kgC/m2 fine	C wt%	C%SE	C Conf Lim 1 wt%	C Conf Lim 2 wt%	δ13C‰ PDB	δ13C ‰SE	13C Conf Lim 1 wt%	13C Conf Lim 2 wt%	N wt%
LP5	70	80	5.403	0.130	0.005	0.126	0.135	-26.304	0.569	-26.874	-25.736	0.014
LP5	80	90	5.498	0.128	0.005	0.123	0.133	-26.196	0.569	-26.766	-25.628	0.014
LP5	90	107	5.648	0.132	0.005	0.128	0.137	-26.151	0.569	-26.721	-25.583	0.015
LP5	107	122	5.776	0.105	0.004	0.101	0.109	-26.558	0.569	-27.128	-25.990	0.013
LP6	0	2	1.746	15.316	0.017	15.299	15.333	-27.423	0.152	-27.576	-27.271	0.995
LP6	2	4	2.779	8.463	0.020	8.444	8.483	-26.369	0.153	-26.521	-26.216	0.600
LP6	4	7	4.007	6.392	0.011	6.381	6.403	-26.252	0.153	-26.405	-26.100	0.418
LP6	7	10	4.968	4.178	0.010	4.167	4.188	-25.974	0.153	-26.127	-25.822	0.264
LP6	10	15	6.123	2.515	0.007	2.509	2.522	-25.873	0.153	-26.026	-25.721	0.162
LP6	15	20	6.936	1.979	0.006	1.973	1.985	-25.694	0.153	-25.846	-25.541	0.122
LP6	20	25	8.249	2.391	0.009	2.382	2.400	-25.648	0.153	-25.801	-25.496	0.154
LP6	25	30	8.690	2.383	0.006	2.377	2.389	-25.532	0.153	-25.685	-25.380	0.143
LP6	39	44	10.330	2.307	0.006	2.301	2.313	-25.509	0.153	-25.661	-25.356	0.131
LP6	44	60	10.967	0.607	0.004	0.603	0.611	-25.287	0.153	-25.440	-25.135	0.045
LP6	60	80	11.221	0.220	0.004	0.216	0.224	-25.467	0.153	-25.619	-25.314	0.023
LP6	80	100	11.485	0.266	0.004	0.263	0.270	-25.669	0.153	-25.822	-25.516	0.026

Site	Upper Depth cm	Lower Depth cm	N%SE	N Conf Lim 1 wt%	N Conf Lim 2 wt%	δ15N‰ N-air	δ15N ‰SE	15N Conf Lim 1 wt%	15N Conf Lim 2 wt%	C/N molar	C/N SE	C/N Conf Lim 1 wt%
LP1	0	6	0.004	0.348	0.356	0.170	0.387	-0.217	0.556	23.585	0.265	0.011
LP1	6	14	0.005	0.144	0.154	2.653	0.384	2.268	3.037	23.457	0.785	0.033
LP1	14	19	0.004	0.106	0.114	2.866	0.384	2.481	3.249	22.514	0.777	0.034
LP1	19	28	0.002	0.049	0.052	4.908	0.382	4.525	5.290	20.162	0.712	0.035
LP1	28	44	0.002	0.026	0.030	4.047	0.383	3.663	4.429	19.171	1.548	0.081
LP1	44	59	0.002	0.020	0.024	4.504	0.382	4.122	4.886	15.787	1.352	0.086
LP1	59	72	0.002	0.019	0.023	4.027	0.383	3.644	4.410	13.786	1.661	0.121
LP1	72	84	0.002	0.015	0.018	4.333	0.383	3.950	4.716	13.543	1.632	0.120
LP1	84	100	0.002	0.016	0.020	4.793	0.382	4.411	5.175	11.113	1.457	0.131
LP1	100	146	0.002	0.008	0.013	-1.089	0.388	-1.478	-0.701	13.250	3.104	0.234
LP2	0	3	0.014	0.408	0.436	0.106	0.176	-0.070	0.282	20.737	0.696	0.034
LP2	3	7	0.014	0.221	0.250	1.456	0.175	1.281	1.631	20.130	1.229	0.061
LP2	7	11	0.011	0.134	0.157	3.284	0.174	3.110	3.458	19.464	1.533	0.079
LP2	11	15	0.010	0.104	0.124	4.070	0.174	3.896	4.244	17.913	1.622	0.091
LP2	22	31	0.006	0.034	0.046	4.853	0.174	4.679	5.026	16.864	2.512	0.149
LP2	31	41	0.007	0.019	0.033	5.889	0.173	5.716	6.062	15.842	4.313	0.272
LP2	41	53	0.007	0.017	0.032	6.500	0.173	6.327	6.673	13.314	4.024	0.302
LP2	53	75	0.006	0.012	0.024	5.647	0.173	5.473	5.820	10.157	3.595	0.354
LP2	75	135	0.006	0.006	0.017	0.759	0.175	0.584	0.935	8.130	4.156	0.511
LP3	0	2	0.017	0.734	0.767	-1.260	0.176	-1.437	-1.084	18.375	0.421	0.023
LP3	2	5	0.014	0.380	0.408	0.373	0.176	0.198	0.549	18.904	0.686	0.036
LP3	5	8	0.011	0.250	0.272	1.715	0.175	1.540	1.890	17.021	0.727	0.043
LP3	8	14	0.007	0.158	0.172	3.584	0.174	3.410	3.759	18.764	0.794	0.042
LP3	14	20	0.006	0.099	0.111	4.654	0.174	4.481	4.828	19.415	1.128	0.058
LP3	20	26	0.007	0.100	0.114	4.336	0.174	4.162	4.509	16.928	1.112	0.066
LP3	26	32	0.006	0.044	0.057	4.976	0.174	4.803	5.150	15.177	1.909	0.126
LP3	32	40	0.007	0.024	0.038	5.620	0.173	5.447	5.794	17.785	4.131	0.232
LP3	40	48	0.006	0.016	0.027	6.056	0.173	5.883	6.229	15.713	4.190	0.267
LP3	48	60	0.006	0.011	0.023	6.613	0.173	6.440	6.786	14.250	5.216	0.366
LP3	60	75	0.007	0.007	0.021	5.239	0.173	5.065	5.412	13.073	6.705	0.513
LP3	75	96	0.001	0.010	0.012	6.221	0.232	5.989	6.454	12.811	1.725	0.135
LP4	0	5	0.002	0.308	0.312	2.350	0.234	2.115	2.584	14.916	0.131	0.009
LP4	5	15	0.002	0.118	0.122	6.771	0.232	6.539	7.003	16.366	0.332	0.020
LP4	15	25	0.002	0.105	0.109	7.726	0.232	7.494	7.958	22.904	0.440	0.019
LP4	25	35	0.002	0.111	0.116	6.773	0.232	6.541	7.005	20.636	0.440	0.021
LP4	35	47	0.002	0.099	0.103	7.513	0.232	7.281	7.744	22.895	0.481	0.021
LP4	47	60	0.002	0.099	0.103	5.512	0.233	5.279	5.745	67.911	1.636	0.024
LP4	60	84	0.001	0.016	0.018	7.734	0.232	7.502	7.966	12.777	1.072	0.084
LP4	84	99	0.001	0.017	0.019	7.167	0.232	6.934	7.398	11.276	1.009	0.089
LP4	99	113	0.001	0.021	0.023	5.256	0.233	5.023	5.489	13.360	0.946	0.071
LP5	0	2	0.006	0.529	0.540	-0.222	0.433	-0.656	0.211	19.265	0.204	0.011
LP5	2	6	0.003	0.229	0.235	1.398	0.432	0.966	1.829	17.442	0.226	0.013
LP5	6	12	0.003	0.147	0.152	2.757	0.430	2.326	3.186	15.529	0.273	0.018
LP5	12	18	0.003	0.111	0.116	3.743	0.429	3.313	4.172	14.462	0.342	0.024
LP5	18	29	0.002	0.073	0.076	5.091	0.428	4.662	5.518	14.280	0.316	0.022
LP5	29	37	0.001	0.034	0.036	5.690	0.428	5.262	6.118	13.535	0.577	0.043
LP5	37	46	0.001	0.034	0.036	6.472	0.427	6.045	6.899	13.340	0.443	0.033
LP5	46	56	0.001	0.031	0.034	5.535	0.428	5.107	5.963	14.741	0.548	0.037
LP5	56	70	0.001	0.020	0.022	5.641	0.428	5.213	6.068	10.171	0.610	0.060

Site	Upper Depth cm	Lower Depth cm	N%SE	N Conf Lim 1 wt%	N Conf Lim 2 wt%	δ15N‰ N-air	δ15N ‰SE	15N Conf Lim 1 wt%	15N Conf Lim 2 wt%	C/N molar	C/N SE	C/N Conf Lim 1 wt%
LP5	70	80	0.001	0.013	0.015	3.053	0.430	2.623	3.482	10.955	1.000	0.091
LP5	80	90	0.001	0.013	0.015	4.357	0.429	3.928	4.785	10.502	0.888	0.085
LP5	90	107	0.001	0.014	0.016	5.029	0.428	4.601	5.457	10.135	0.808	0.080
LP5	107	122	0.001	0.012	0.014	3.258	0.430	2.828	3.687	9.604	0.797	0.083
LP6	0	2	0.018	0.977	1.013	-1.580	0.362	-1.943	-1.218	17.953	0.320	0.018
LP6	2	4	0.023	0.578	0.623	-0.003	0.360	-0.364	0.357	16.436	0.618	0.038
LP6	4	7	0.012	0.406	0.431	1.389	0.359	1.029	1.747	17.825	0.528	0.030
LP6	7	10	0.012	0.252	0.276	3.070	0.357	2.713	3.427	18.479	0.846	0.046
LP6	10	15	0.008	0.154	0.170	4.411	0.356	4.055	4.766	18.104	0.879	0.049
LP6	15	20	0.007	0.115	0.129	5.995	0.354	5.641	6.349	18.862	1.092	0.058
LP6	20	25	0.011	0.143	0.164	6.340	0.354	5.986	6.694	18.151	1.289	0.071
LP6	25	30	0.007	0.136	0.149	6.466	0.354	6.112	6.820	19.495	0.948	0.049
LP6	39	44	0.007	0.124	0.139	6.905	0.353	6.551	7.258	20.496	1.146	0.056
LP6	44	60	0.005	0.040	0.050	9.430	0.351	9.078	9.781	15.741	1.682	0.107
LP6	60	80	0.005	0.018	0.028	7.533	0.353	7.179	7.885	11.044	2.304	0.209
LP6	80	100	0.004	0.021	0.030	6.887	0.353	6.533	7.240	12.117	2.032	0.168

Site	Upper Depth cm	Lower Depth cm	C/N Conf Lim 2 wt%
LP1	0	6	23.321
LP1	6	14	22.671
LP1	14	19	21.737
LP1	19	28	19.451
LP1	28	44	17.623
LP1	44	59	14.435
LP1	59	72	12.125
LP1	72	84	11.911
LP1	84	100	9.655
LP1	100	146	10.146
LP2	0	3	20.041
LP2	3	7	18.901
LP2	7	11	17.931
LP2	11	15	16.291
LP2	22	31	14.352
LP2	31	41	11.530
LP2	41	53	9.290
LP2	53	75	6.563
LP2	75	135	3.975
LP3	0	2	17.954
LP3	2	5	18.218
LP3	5	8	16.294
LP3	8	14	17.970
LP3	14	20	18.287
LP3	20	26	15.816
LP3	26	32	13.268
LP3	32	40	13.654
LP3	40	48	11.523
LP3	48	60	9.034
LP3	60	75	6.368
LP3	75	96	11.085
LP4	0	5	14.785
LP4	5	15	16.034
LP4	15	25	22.463
LP4	25	35	20.196
LP4	35	47	22.414
LP4	47	60	66.275
LP4	60	84	11.705
LP4	84	99	10.267
LP4	99	113	12.414
LP5	0	2	19.061
LP5	2	6	17.216
LP5	6	12	15.256
LP5	12	18	14.121
LP5	18	29	13.964
LP5	29	37	12.958
LP5	37	46	12.897
LP5	46	56	14.193
LP5	56	70	9.561
LP5	70	80	9.955
LP5	80	90	9.613
LP5	90	107	9.327
LP5	107	122	8.807
LP6	0	2	17.633
LP6	2	4	15.818
LP6	4	7	17.297
LP6	7	10	17.633
LP6	10	15	17.225
LP6	15	20	17.771
LP6	20	25	16.862
LP6	25	30	18.547
LP6	39	44	19.350
LP6	44	60	14.060
LP6	60	80	8.740
LP6	80	100	10.085

8.5 Carbon and Nitrogen of dense, light, and >2mm fraction for soil pits

Site	Upper Depth cm	Lower Depth cm	LFC wt%	LFC% SE	LFC Conf Lim 1 wt%	LFC Conf Lim 2 wt%	LFδ13C ‰ PDB	LFδ13C ‰SE	LF13C Conf Lim 1 wt%	LF13C Conf Lim 2 wt%	LFN wt%
LP1	0	6	22.870	0.026	22.844	22.896	-27.462	0.568	-28.031	-26.894	0.967
LP1	6	14	23.797	0.033	23.764	23.830	-27.800	0.568	-28.369	-27.233	0.642
LP1	14	19	25.747	0.029	25.719	25.776	-27.263	0.568	-27.832	-26.695	0.431
LP1	19	28	31.400	0.033	31.367	31.433	-28.106	0.568	-28.675	-27.539	0.410
LP6	0	10	27.135	0.027	27.108	27.162	-25.854	0.569	-26.424	-25.285	1.289
LP6	10	20	25.183	0.026	25.157	25.209	-26.919	0.569	-27.489	-26.352	0.882
LP6	20	30	29.752	0.029	29.724	29.781	-26.821	0.569	-27.391	-26.253	0.730
LP6	30	39	28.938	0.030	28.909	28.968	-26.659	0.569	-27.229	-26.091	0.740
LP6	60	80	35.927	0.045	35.882	35.972	-26.561	0.569	-27.131	-25.993	0.753

Site	Upper Depth cm	Lower Depth cm	DFC wt%	DFC% SE	DFC Conf Lim 1 wt%	DFC Conf Lim 2 wt%	DFδ13C‰ PDB	DFδ13C ‰SE	DF13C Conf Lim 1 wt%	DF13C Conf Lim 2 wt%	DFN wt%
LP1	0	6	4.058	0.011	4.047	4.069	-26.434	0.569	-27.003	-25.866	0.212
LP1	6	14	2.797	0.011	2.785	2.808	-26.256	0.569	-26.825	-25.688	0.160
LP1	14	19	1.069	0.007	1.061	1.076	-26.090	0.569	-26.660	-25.521	0.078
LP1	19	28	0.493	0.007	0.485	0.500	-25.579	0.569	-26.149	-25.011	0.044
LP1	59	72	0.086	0.004	0.081	0.090	-25.477	0.569	-26.047	-24.908	0.008
LP6	0	10	3.843	0.010	3.833	3.852	-26.013	0.569	-26.582	-25.444	0.268
LP6	10	20	2.464	0.007	2.457	2.471	-25.724	0.569	-26.294	-25.155	0.171
LP6	20	30	1.635	0.006	1.629	1.640	-25.733	0.569	-26.303	-25.165	0.109
LP6	30	39	1.705	0.006	1.699	1.712	-25.549	0.569	-26.119	-24.981	0.122
LP6	60	80	0.245	0.006	0.239	0.250	-25.170	0.570	-25.740	-24.601	0.030

Site	Upper Depth cm	Lower Depth cm	>2mm C wt%	>2mm C%SE	>2mm C Conf Lim 1 wt%	>2mm C Conf Lim 2 wt%	>2mmδ 13C‰ PDB	>2mm δ13C ‰SE	>2mm1 3C Conf Lim 1 wt%	>2mm1 3C Conf Lim 2 wt%	>2mm N wt%
LP1	6	14	0.237	0.010	0.227	0.247	-24.949	0.648	-25.598	-24.302	0.015
LP1	59	72	0.061	0.010	0.050	0.071	-25.846	0.649	-26.496	-25.198	0.005
LP1	84	100	0.071	0.013	0.058	0.084	-26.328	0.274	-26.602	-26.054	0.009
LP1	100	146	0.078	0.011	0.067	0.089	-26.514	0.274	-26.788	-26.240	0.010
LP4	5	15	0.270	0.012	0.258	0.282	-26.122	0.259	-26.381	-25.864	0.018
LP4	25	35	0.789	0.009	0.779	0.798	-26.392	0.259	-26.651	-26.134	0.038
LP4	47	60	1.701	0.021	1.679	1.722	-26.567	0.259	-26.826	-26.308	0.022
LP4	60	84	0.048	0.012	0.036	0.059	-25.806	0.259	-26.065	-25.548	0.005
LP4	99	113	0.029	0.011	0.018	0.039	-28.419	0.260	-28.679	-28.159	0.003

Site	Upper Depth cm	Lower Depth cm	LFN% SE	LFN Conf Lim 1 wt%	LFN Conf Lim 2 wt%	LFδ15 N‰ N-air	LFδ15 N ‰SE	LF15N Conf Lim 1 wt%	LF15N Conf Lim 2 wt%	LFC/N molar	LFC/N SE
LP1	0	6	0.007	0.960	0.975	-2.270	0.436	-2.706	-1.834	27.573	0.210
LP1	6	14	0.010	0.632	0.652	0.920	0.432	0.487	1.352	43.217	0.657
LP1	14	19	0.008	0.423	0.439	0.488	0.433	0.054	0.920	69.596	1.283
LP1	19	28	0.009	0.401	0.418	-1.383	0.435	-1.819	-0.949	89.366	1.902
LP6	0	10	0.006	1.283	1.296	-1.368	0.435	-1.804	-0.934	24.541	0.126
LP6	10	20	0.007	0.875	0.889	1.966	0.431	1.534	2.397	33.293	0.267
LP6	20	30	0.005	0.725	0.735	3.562	0.429	3.132	3.991	47.515	0.341
LP6	30	39	0.008	0.732	0.748	3.265	0.430	2.835	3.694	45.598	0.476
LP6	60	80	0.013	0.740	0.766	0.974	0.432	0.542	1.406	55.620	0.968

Site	Upper Depth cm	Lower Depth cm	DFN% SE	DFN Conf Lim 1 wt%	DFN Conf Lim 2 wt%	DFδ15 N‰ N-air	DFδ15 N ‰SE	DF15N Conf Lim 1 wt%	DF15N Conf Lim 2 wt%	DFC/N molar	DFC/N SE
LP1	0	6	0.003	0.209	0.215	0.267	0.433	-0.166	0.700	22.343	0.338
LP1	6	14	0.003	0.157	0.163	2.586	0.430	2.155	3.016	20.421	0.389
LP1	14	19	0.002	0.076	0.080	3.701	0.429	3.271	4.130	15.989	0.391
LP1	19	28	0.002	0.042	0.045	5.561	0.428	5.133	5.988	13.178	0.569
LP1	59	72	0.001	0.007	0.009	3.912	0.429	3.482	4.341	12.000	1.620
LP6	0	10	0.003	0.265	0.271	2.251	0.431	1.820	2.681	16.713	0.173
LP6	10	20	0.002	0.169	0.173	5.058	0.428	4.630	5.486	16.780	0.195
LP6	20	30	0.002	0.108	0.111	7.446	0.426	7.020	7.872	17.474	0.251
LP6	30	39	0.002	0.120	0.124	7.101	0.426	6.674	7.527	16.310	0.235
LP6	60	80	0.001	0.029	0.032	7.911	0.426	7.485	8.336	9.394	0.477

Site	Upper Depth cm	Lower Depth cm	>2mm N%SE	>2mm N Conf Lim 1 wt%	>2mm N Conf Lim 2 wt%	>2mm δ15N ‰ N-air	>2mm δ15N ‰SE	>2mm 15N Conf Lim 1 wt%	>2mm 15N Conf Lim 2 wt%	>2mm C/N molar	>2mm C/N SE
LP1	6	14	0.002	0.013	0.016	2.613	0.384	2.229	2.997	18.853	2.139
LP1	59	72	0.001	0.003	0.006	0.497	0.386	0.110	0.883	15.717	5.866
LP1	84	100	0.007	0.002	0.016	6.896	0.173	6.723	7.068	9.329	7.890
LP1	100	146	0.006	0.004	0.017	4.996	0.174	4.823	5.170	8.736	5.376
LP4	5	15	0.001	0.017	0.019	5.324	0.233	5.091	5.557	17.655	1.284
LP4	25	35	0.001	0.037	0.039	7.145	0.232	6.913	7.377	24.006	0.631
LP4	47	60	0.002	0.020	0.024	5.469	0.233	5.236	5.702	90.799	8.535
LP4	60	84	0.001	0.004	0.006	11.045	0.231	10.815	11.276	11.452	3.581
LP4	99	113	0.001	0.003	0.004	7.029	0.232	6.796	7.261	9.637	4.405

Site	Upper Depth cm	Lower Depth cm	LFC/N Conf Lim 1 wt%	LFC/N Conf Lim 2 wt%
LP1	0	6	0.008	27.363
LP1	6	14	0.015	42.561
LP1	14	19	0.018	68.313
LP1	19	28	0.021	87.464
LP6	0	10	0.005	24.415
LP6	10	20	0.008	33.026
LP6	20	30	0.007	47.174
LP6	30	39	0.010	45.122
LP6	60	80	0.017	54.652

Site	Upper Depth cm	Lower Depth cm	DFC/N Conf Lim 1 wt%	DFC/N Conf Lim 2 wt%
LP1	0	6	0.015	22.005
LP1	6	14	0.019	20.032
LP1	14	19	0.024	15.598
LP1	19	28	0.043	12.609
LP1	59	72	0.135	10.380
LP6	0	10	0.010	16.540
LP6	10	20	0.012	16.585
LP6	20	30	0.014	17.224
LP6	30	39	0.014	16.076
LP6	60	80	0.051	8.917

Site	Upper Depth cm	Lower Depth cm	>2mm C/N Conf Lim 1 wt%	>2mm C/N Conf Lim 2 wt%
LP1	6	14	0.113	16.714
LP1	59	72	0.373	9.852
LP1	84	100	0.846	1.439
LP1	100	146	0.615	3.360
LP4	5	15	0.073	16.371
LP4	25	35	0.026	23.375
LP4	47	60	0.094	82.264
LP4	60	84	0.313	7.871
LP4	99	113	0.457	5.232

8.6 Morphological descriptions of soil pits

Site	Position	Depth	Horizon	Color	Color name
LP1	Ridge	0-6 cm	A1	10YR 3/2	dark grayish brown
LP1	Ridge	6-14 cm	A2	10YR 4/3	brown
LP1	Ridge	14-19 cm	BA	10YR 5/3	brown
LP1	Ridge	19-28 cm	Bw1	10YR 5/4	yellowish brown
LP1	Ridge	28-84 cm	Bw2	10YR 6/2	light brownish gray
LP1	Ridge	84-100 cm	C	10YR 6/3	pale brown
LP2	Shoulder	0-7 cm	A1	10YR 3/2	brownish black
LP2	Shoulder	7-15 cm	A2	10YR 4/2	grayish yellow brown
LP2	Shoulder	15-31 cm	Bw1	10YR 5/4	dull yellowish brown
LP2	Shoulder	31-53 cm	Bw2	10YR 6/4	dull yellow orange
LP2	Shoulder	53-75 cm	C1	10YR 6/1	brownish gray
LP3	Backslope	0-5 cm	A1	10YR 3/2	dark grayish brown
LP3	Backslope	5-14 cm	A2	10YR 4/3	dull yellowish brown
LP3	Backslope	14-20 cm	AB	10YR 5/3	dull yellowish brown
LP3	Backslope	20-32 cm	Bw1	10YR 6/3	light brownish gray
LP3	Backslope	32-60 cm	Bw2	10YR 6/3	pale brown
LP3	Backslope	60-90 cm	C	10YR 6/3	pale brown
LP4	Swale	0-5 cm	A	10YR 4/2	dark grayish brown
LP4	Swale	5-47 cm	BA	10YR 4/3	brown
LP4	Swale	47-60 cm	BA2	10YR 4/2	dark grayish brown, 55-60 cm contains many fine-medium charcoal fragments and few distinct fine-coarse mottles
LP4	Swale	60-84 cm	2Bw1	10YR 6/4	light yellowish brown
LP4	Swale	84-99 cm	2Bw2	10YR 6/4	light yellowish brown
LP4	Swale	99-113 cm	2BC	10YR 6/4	light yellowish brown

Site	Position	Depth	Soil type	Structure
LP1	Ridge	0-6 cm	extremely channery sandy clay loam	weak fine subangular structure
LP1	Ridge	6-14 cm	extremely channery sandy clay loam	weak fine granular structure, single grain, very rocky
LP1	Ridge	14-19 cm	extremely channery sandy clay loam	weak very fine subangular blocky structure
LP1	Ridge	19-28 cm	extremely channery sandy clay loam	weak very fine subangular blocky structure, very rocky
LP1	Ridge	28-84 cm	extremely channery sandy clay loam	weak very fine subangular blocky structure, very rocky
LP1	Ridge	84-100 cm	very channery sandy clay loam	structureless single grain
LP2	Shoulder	0-7 cm	extremely to very channery sandy clay loam	weak fine grainy structure, very rocky
LP2	Shoulder	7-15 cm	very channery sandy clay loam	weak fine subangular blocky structure, very rocky
LP2	Shoulder	15-31 cm	very channery sandy clay loam	weak very fine subangular blocky structure, very rocky
LP2	Shoulder	31-53 cm	extremely channery sandy clay loam	weak very fine subangular blocky, weak fine granular structure, very rocky
LP2	Shoulder	53-75 cm	extremely gravelley sandy clay loam	structureless single grain
LP3	Backslope	0-5 cm	very channery sandy clay loam	structureless
LP3	Backslope	5-14 cm	very channery sandy clay loam	structureless, rocky
LP3	Backslope	14-20 cm	very channery sandy clay loam	structureless, rocky
LP3	Backslope	20-32 cm	extremely channery sandy clay loam	weak subangular blocky structure, very rocky
LP3	Backslope	32-60 cm	extremely channery sandy clay loam	weak subangular blocky structure, very rocky
LP3	Backslope	60-90 cm	extremely channery sandy clay loam	structurless single grain structure, very rocky
LP4	Swale	0-5 cm	very channery sandy clay loam	weak very fine subangular blocky
LP4	Swale	5-47 cm	very channery sandy clay loam	weak fine-very fine subangular blocky
LP4	Swale	47-60 cm	extremely channery sandy clay loam	weak medium-fine angular blocky structure, very rocky
LP4	Swale	60-84 cm	extremely channery sandy clay loam	weak fine to very fine subangular blocky structure, very rocky
LP4	Swale	84-99 cm	extremely channery sandy clay loam	weak fine to very fine subangular blocky structure, very rocky
LP4	Swale	99-113 cm	extremely channery sandy clay loam	weak very fine subangular blocky structure, very rocky

Site	Position	Depth	Roots	Rocks
LP1	Ridge	0-6 cm	common very fine, very few medium roots	61% angular schist channers
LP1	Ridge	6-14 cm	common very fine, very few medium roots	81% angular schist channers
LP1	Ridge	14-19 cm	few very fine, few medium roots	75% angular schist channers
LP1	Ridge	19-28 cm	few fine roots	70% angular schist channers
LP1	Ridge	28-84 cm	very few very fine, few medium, few coarse roots (decreasing downward)	58-79% angular schist channers
LP1	Ridge	84-100 cm	--	54% angular schist channers
LP2	Shoulder	0-7 cm	few fine, few medium roots	52-69% angular schist channers
LP2	Shoulder	7-15 cm	few fine, few medium roots	49-58% angular schist channers
LP2	Shoulder	15-31 cm	few fine, few medium roots	52-55% angular schist channers
LP2	Shoulder	31-53 cm	very few fine, very few medium roots	60-71% angular schist channers
LP2	Shoulder	53-75 cm	--	81% angular schist channers
LP3	Backslope	0-5 cm	common very fine roots	44-51% angular schist channers
LP3	Backslope	5-14 cm	common very fine-fine roots	50-61% angular schist channers
LP3	Backslope	14-20 cm	common very fine-fine roots	50-61% angular schist channers
LP3	Backslope	20-32 cm	moderately few fine-medium roots	68-72% angular schist channers
LP3	Backslope	32-60 cm	moderately few fine-medium roots	73-79% angular schist channers
LP3	Backslope	60-90 cm	very few fine roots	68-79% angular schist channers
LP4	Swale	0-5 cm	common very fine to medium roots	40% angular schist channers
LP4	Swale	5-47 cm	common fine to medium roots	41-44% angular schist channers
LP4	Swale	47-60 cm	common fine-medium roots, coarse massive roots	79% angular schist channers
LP4	Swale	60-84 cm	moderately few fine-medium roots	64% angular schist channers
LP4	Swale	84-99 cm	moderately few fine-medium roots	62% angular schist channers
LP4	Swale	99-113 cm	--	>73% angular schist channers with boulders

Site	Position	Depth	Boundary
LP1	Ridge	0-6 cm	clear smooth boundary
LP1	Ridge	6-14 cm	clear smooth boundary
LP1	Ridge	14-19 cm	clear smooth boundary
LP1	Ridge	19-28 cm	gradual smooth boundary
LP1	Ridge	28-84 cm	clear smooth boundary
LP1	Ridge	84-100 cm	--
LP2	Shoulder	0-7 cm	clear smooth boundary
LP2	Shoulder	7-15 cm	clear smooth boundary
LP2	Shoulder	15-31 cm	clear smooth boundary
LP2	Shoulder	31-53 cm	clear smooth boundary
LP2	Shoulder	53-75 cm	--
LP3	Backslope	0-5 cm	very abrupt smooth boundary
LP3	Backslope	5-14 cm	abrupt wavy boundary
LP3	Backslope	14-20 cm	abrupt wavy boundary
LP3	Backslope	20-32 cm	clear wavy boundary
LP3	Backslope	32-60 cm	clear smooth boundary
LP3	Backslope	60-90 cm	--
LP4	Swale	0-5 cm	clear smooth boundary
LP4	Swale	5-47 cm	clear smooth boundary
LP4	Swale	47-60 cm	clear wavy boundary
LP4	Swale	60-84 cm	clear smooth boundary
LP4	Swale	84-99 cm	clear smooth boundary
LP4	Swale	99-113 cm	--

Site	Position	Depth	Horizon	Color	Color name
LP5	Interfluve	0-6 cm	A1	10YR 3/2	very dark grayish brown
LP5	Interfluve	6-18 cm	A2	10YR 3/3	dark brown
LP5	Interfluve	18-29 cm	AB	10YR 4/3	brown
LP5	Interfluve	29-46 cm	Bw1	10YR 5/6	dark brown
LP5	Interfluve	46-70 cm	Bw2	10YR 5/4	yellowish brown, Very few black (10YR 2/1 charcoal pieces of 3-7 cm in this interval)
LP5	Interfluve	70-107 cm	Bw3	10YR 5/6	yellowish brown
LP5	Interfluve	107-124 cm	BC	10YR 6/4	light yellowish brown primary matrix, secondary matrix color is olive (5Y 5/3), with common fine-medium brownish yellow (10YR 6/6) and dark brown (10YR 3/3) mottles at field moisture
LP6	Toeslope	0-4 cm	A1	10YR 2/2	very dark brown
LP6	Toeslope	4-10 cm	A2	10YR 3/2	very dark grayish brown
LP6	Toeslope	10-20 cm	AB	10YR 3/4	dark yellowish brown
LP6	Toeslope	20-39 cm	2Ab	7.5YR 3/2	dark brown
LP6	Toeslope	39-44 cm	2ABb	10YR 4/4	dark yellowish brown
LP6	Toeslope	44-100 cm	2Bwb	2.5Y5/4	olive

Site	Position	Depth	Soil type	Structure
LP5	Interfluve	0-6 cm	channery sandy clay loam	weak very fine granular structure, rocky
LP5	Interfluve	6-18 cm	very channery sandy clay loam	weak very fine-medium subangular blocky structure, very rocky
LP5	Interfluve	18-29 cm	very channery sandy clay loam	moderate very fine-medium angular blocky structure, very rocky
LP5	Interfluve	29-46 cm	very channery sandy clay loam	weak very fine-medium subangular blocky structure, very rocky
LP5	Interfluve	46-70 cm	very channery sandy clay loam.	moderate medium angular blocky structure, very rocky
LP5	Interfluve	70-107 cm	very channery sandy clay loam	weak fine-medium angular blocky structure, very rocky
LP5	Interfluve	107-124 cm	very channery sandy clay loam	weak fine-medium subangular blocky structure, very rocky
LP6	Toeslope	0-4 cm	very channery sandy clay loam	weak fine granular structure
LP6	Toeslope	4-10 cm	very channery sandy clay loam	weak fine-very fine subangular blocky structure
LP6	Toeslope	10-20 cm	channery sandy clay loam	weak very fine-medium subangular blocky structure
LP6	Toeslope	20-39 cm	very channery sandy clay loam	weak very fine-medium subangular blocky structure, very rocky
LP6	Toeslope	39-44 cm	extremely channery sandy clay loam	weak very fine-medium subangular blocky structure, very rocky
LP6	Toeslope	44-100 cm	extremely channery sandy clay loam	weak fine-medium subangular blocky structure, very rocky

Site	Position	Depth	Roots	Rocks
LP5	Interfluve	0-6 cm	common fine-very fine roots	24% angular schist channers
LP5	Interfluve	6-18 cm	common fine roots, common coarse roots	39% angular schist channers
LP5	Interfluve	18-29 cm	few fine-very fine, few medium-coarse roots	48% angular schist channers
LP5	Interfluve	29-46 cm	few fine-very fine, common med-coarse roots	59% angular schist channers
LP5	Interfluve	46-70 cm	few fine-very fine roots	60% angular schist channers
LP5	Interfluve	70-107 cm	few very fine-fine, few medium roots	56% angular schist channers
LP5	Interfluve	107-124 cm	very few fine roots	52% angular schist channers, channers sub-horizontal, some vertical channers present
LP6	Toeslope	0-4 cm	many fine-very fine, few medium roots	42% angular schist channers
LP6	Toeslope	4-10 cm	common fine-very fine, common medium-coarse roots	35% angular schist channers
LP6	Toeslope	10-20 cm	few fine-very fine, common medium-coarse roots	31% angular schist channers
LP6	Toeslope	20-39 cm	very few fine-very fine, few med-coarse, common very coarse roots	57% angular schist channers
LP6	Toeslope	39-44 cm	very few fine, very few medium-coarse roots	65% angular schist channers
LP6	Toeslope	44-100 cm	very few fine, very few medium-coarse roots	71% angular schist channers, most channers sub-horizontal, some vertical channers present

Site	Position	Depth	Boundary
LP5	Interfluve	0-6 cm	clear smooth boundary
LP5	Interfluve	6-18 cm	clear smooth boundary
LP5	Interfluve	18-29 cm	clear smooth boundary
LP5	Interfluve	29-46 cm	clear smooth boundary
LP5	Interfluve	46-70 cm	clear smooth boundary
LP5	Interfluve	70-107 cm	--
LP5	Interfluve	107-124 cm	boundary to C not detected
LP6	Toeslope	0-4 cm	clear smooth boundary
LP6	Toeslope	4-10 cm	clear smooth boundary
LP6	Toeslope	10-20 cm	clear smooth boundary
LP6	Toeslope	20-39 cm	gradual boundary
LP6	Toeslope	39-44 cm	gradual boundary
LP6	Toeslope	44-100 cm	boundary to C not detected